STATIC AND RECONFIGURABLE DEVICES FOR NEAR-FIELD AND FAR-FIELD TERAHERTZ APPLICATIONS

by

Silvia Tofani
Department of Information Engineering, Electronics and Telecommunications
Istituto per la Microelettronica e Microsistemi

A thesis submitted in partial fulfillment of the requirements for the degree of
Doctor of Philosophy in Information and Communication Engineering

at

Sapienza University of Rome

February 2018

Cycle XXX

Certified by Thesis Supervisors:

Prof. Alessandro Galli
Department of Information Engineering,
Electronics and Telecommunications
Sapienza University of Rome

Dr. Romeo Beccherelli
Istituto per la Microelettronica e Microsistemi
Consiglio Nazionale delle Ricerche

This thesis was evaluated by the two following external referees:

Gaetano Bellanca, Professor, University of Ferrara, Ferrara, Italy

Marco Peccianti, Reader, University of Sussex, Brighton, United Kingdom

The time and effort of the external referees in evaluating this thesis, as well as their valuable and constructive suggestions, are very much appreciated and greatly acknowledged.

CONTENTS

CONTENTS III

LIST OF FIGURES...VIII

LIST OF TABLES XVII

ABSTRACT XIX

ACKNOWLEDGMENTS XXI

LIST OF SYMBOLS, ABBREVIATIONS AND ACRONYMS XXII

Symbols XXII

Units of measurements XXVI

Chemical symbols and formulas XXVII

Abbreviations.. XXVIII

Acronyms.. XXVIII

INTRODUCTION XXXII

CHAPTER I

Terahertz radiation 1

1. Introduction to terahertz radiation 1

  1.1 Terahertz in the electromagnetic spectrum... 2

  1.2 Terahertz applications and challenges.. 3

2. Terahertz sources... 7

3. Terahertz detectors 9

4. Terahertz passive components... 11

  4.1 Terahertz waveguides... 12

  4.2 Quasi-optical components 13

    4.2.1 Polarizers 13

4.2.2 Waveplates 14
4.2.3 Filters 15
4.2.4 Lenses 16

CHAPTER II

Passive devices for terahertz radiation: zone plates as planar diffractive lenses 17
1. Introduction 17
2. Planar diffractive lenses: zone plates 18
3. Zone plates for terahertz radiation and their applications 21
4. Zone plates theoretical background 23
4.1 Diffraction efficiency 24
4.2 Comparison between properties of zone plates and traditional lenses 24
4.3 Zone plates aberrations 25
5. Materials for terahertz diffractive devices 26
6. Fabrication methods and techniques 29

CHAPTER III

Methods for numerically design and fabricate polymeric zone plates 31
1. Introduction 31
2. Numerical methods in computational electromagnetic 33
3. Numerical investigation of zone plates for terahertz focusing 35
3.1 Material choice 37
3.2 Number of zones 37
3.3 Frequency behavior 38
3.4 Comparison with a conventional refractive lens 39
4. Fabrication 39

CHAPTER IV

Numerical investigation and fabrication of terahertz zone plates 42
1. Material choice 42
2. Number of zones 43
3. Frequency behavior 45

4. Comparison with a conventional refractive lens 46
5. Conclusions about the numerical investigation and zone plates fabrication 47

CHAPTER V

Methods for the experimental characterization of diffractive lenses at terahertz frequencies 49
1. Introduction 49
2. Set-ups for terahertz metrology 50
  2.1 Set-ups employing time-domain methods 51
  2.2 Set-ups employing frequency-domain methods..................................... 51
3. Terahertz diffractive lenses characterization: measurements set-up............... 53
4. Terahertz beam characterization: knife-edge technique................................. 56
  4.1 Knife-edge set-up.. 56
  4.2 Knife-edge measurements automation 59
  4.3 Post-processing of data from knife-edge measurements: terahertz imaging 61
5. Iris sampling method: focal length characterization...................................... 62
6. Terahertz spectrometer calibration 63
  6.1 Near-field antenna images on cross-sections of emitted radiation........... 64
  6.2 Distribution of the field intensity employed as lenses excitation 64

CHAPTER VI

Experimental characterization of polymeric zone plates.......................................67
1. Introduction 67
2. Zone plates focal length 67
3. Zone plates focal plane 69
4. Focal plane experimental comparison between ideal and real illumination: multilevel zone plate case of study... 72
5. Conclusions 73

CHAPTER VII

Future perspectives in developing planar diffractive lenses..................................74

1. Introduction......74
2. Tunable zone plates......74
  2.1 Material with tunable properties: liquid crystals......75
    2.1.1 Effects of an external electric field on nematic liquid crystals......77
    2.1.2 Q-tensor formulation......79
  2.2 Double-sided zone plate with two focal lengths......81
3. Metal zone plates......88
  3.1 Zone plates in reflection mode......89

CHAPTER VIII

Leaky-wave antennas for terahertz far-field applications......92
1. Introduction......92
2. Historical path in the development of a leaky-wave theory......93
3. Classification of leaky-wave antennas......95
  3.1 One-dimensional uniform leaky-wave antennas......95
  3.2 One-dimensional periodic leaky-wave antennas......97
  3.3 Two-dimensional leaky-wave antennas......98
4. Operation principles of leaky waves......99
5. Leaky-wave antenna analysis and design techniques overview......102
  5.1 Transverse resonance technique......104
6. Leaky-wave antennas at terahertz frequencies......105
7. Conclusions......109

CHAPTER IX

Fabry-Perot cavity leaky-wave antennas based on liquid crystals for terahertz beam-steering......110
1. Introduction......110
2. Liquid crystals for the design of a tunable leaky-wave antenna......111
3. Tunable Fabry-Perot cavity leaky-wave antenna design......114
4. Terahertz implementation of a Fabry-Perot cavity leaky-wave antenna with liquid crystals: numerical results......116
  4.1 Dispersion analysis of fundamental leaky modes: lossless case of study117

4.2 Terahertz Fabry-Perot cavity leaky-wave antenna radiation patterns: lossless case of study 120

4.3 Terahertz Fabry-Perot cavity leaky-wave antenna: dispersion curves and radiation patterns in the case of materials with dielectric losses 122

5. Conclusions 125

CHAPTER X

Terahertz leaky-wave antennas based on homogenized metasurfaces 126

1. Introduction 126

2. Design constraints of terahertz metasurface leaky-wave antennas 127

3. Impedance synthesis of three partially reflective sheet geometries 130

4. Radiating behavior of Fabry-Perot cavity leaky-wave antennas based on fishnet-like metasurface 134

4.1 Full-wave analysis of the truncated structure 138

5. Conclusions 141

REFERENCES 142

LIST OF PUBLICATIONS 167

Journal papers 167

Conference proceedings 167

Doctoral school book and e-book contributions 168

LIST OF FIGURES

Fig. 1 Electromagnetic spectrum. 2

Fig. 2 Path loss in line-on-site communications at THz frequencies for different distances. It takes into account both attenuation due to molecular absorption of gases in atmosphere both the spreading losses. Three bands are marked as promising ranges: 0.38 – 0.44 THz, 0.45 – 0.52 THz, 0.62 – 0.72 THz, and 0.77 – 0.92 THz [29]. 4

Fig. 3 Comparison between novel polarizers (red) and commercially available polarizers (blue) at the frequency of 1 THz. Figure is taken from [91] where a description of the polarizers in the legend is driven in detail. 14

Fig. 4 Behavior of some filter categories widely employed at THz frequencies [88]. . 16

Fig. 5 Huygens-Fresnel principle for zone plate construction. A plane wave is propagating towards the point of the space P_0. O, R_1, and R_2 are point of the wave front, which have a fixed distance with respect to P_0. 18

Fig. 6 a) Fresnel ZP for a microlight emitting diode [119]; b) ZP constructed for 12-cm waves [120]. 20

Fig. 7 Multiple and virtual foci in a ZP. Undiffracted radiation is commonly called zero-order of diffracted radiation. The focus “+1” is associated to the first order of diffraction. The focus “+3” represents a higher-order focus, corresponding to i = 2 in equation II.8. Foci “-1” and “-3” are the equivalent virtual foci of the positive ones... 25

Fig. 8 Diffraction efficiency by increasing the number of discretization of zones phase step [117]. 32

Fig. 9 Overview of the numerical approaches to the electromagnetic problems. 35

Fig. 10 Comparison between sources in terms of frequency and output power. This plot is from [5] and it is based on data until the year 2011. For additional information about THz sources until the year 2017, compare *Table 1*. 38

Fig. 11 Milling cutters used throughout this work for ZP fabrication. The diameter of each cutter is indicated. 41

Fig. 12 Comparison between the focusing properties of a binary ZP made of a) Zeonex E48R and b) HRFZ-Si. A plane wave of 1 V/m is incident perpendicularly to both lenses. The E-field modulus is represented in a 3-D space, filled by air. Both ZPs, ending at *z* = 2 mm, have same external diameter, number of zones and thickness. ... 42

Fig. 13 Comparison between the focusing properties of a binary ZP made of Zeonex E48R (blue line) or HRFZ-Si (red line). A plane wave of 1 V/m is incident perpendicularly to both lenses. *z*-axis is the perpendicular one to the ZP plane. *z* = 0 mm corresponds to the end of the lens, where a free space, filled by air, starts. Both ZPs have the same external diameter, number of zones and thickness. 43

Fig. 14 Focusing behavior of a binary ZP with a fixed diameter and an increasing number of ring zones. A plane wave of 1 V/m is incident perpendicularly to the lens. All color maps represents ZP central section and optical axis, *z*, where THz radiation, coming from *z* = 0, is focused. 45

Fig. 15 Frequency behavior of a multilevel ZP from 0.5 THz to 1.1 THz with a step of 0.1 THz. z-axis is the perpendicular one to the ZP plane. Minor peaks in the square modulus of the E-field for z from 1 mm to 3 mm are related to multiple reflections within the 2 mm thick slab in which ZP is fabricated (no antireflection coating is used). For *z* < 1 mm and *z* > 3 mm, a free space filled by air for THz waves propagation is considered. 46

Fig. 16 Frequency behavior of a biconvex refractive lens from 0.5 THz to 1.1 THz with a step of 0.1 THz. z -axis is the lens optical axis. Extremely short peaks in the square modulus of the E-field for z from 2 mm to 4 mm are related to few multiple reflections inside the lens. For *z* < 2 mm and *z* > 4 mm, a free space, filled by air, for THz waves propagation is considered. 47

Fig. 17 Fabricated ZP lenses: a) multilevel ZP, b) double-sided ZP, c) binary ZP. The little roughness perceived in visible light is introduced by milling process, but it does not affect the lens behavior at THz because it is several orders of magnitude below the wavelength at 1 THz. 48

Fig. 18 Overview of the experimental approaches to the THz measurements. 50

Fig. 19 Schematic representation of photoconductive antennas in their a) emitting and b) receiving configuration. PI is the photogenerated current. 54

Fig. 20 Standard configuration of the commercial TDS TERA K15 by Menlo Systems. PAT: photoconductive antenna in transmission mode; L_1 and L_3: convex-plane lenses; L_2 and L_4: plano-convex lenses; PAR: photoconductive antenna in receiving mode [180]. 55

Fig. 21 TDS set-up configurations for the characterization of the THz beam emitted by the lens antenna (PAT). Three planes are imaged by knife-edge technique: a) plane 1, at a distance of 3 mm from the PAT; b) plane 2, at a distance of 9 mm from the PAT; c) plane 3, at the position in which the test ZPs will be located. PAT: photoconductive antenna in transmission mode; L_1 and L_3: convex-plane lenses; L_2 and L_4: plano-convex lenses; KE: knife-edge blade; PAR: photoconductive antenna in receiving mode. 57

Fig. 22 Schematic representation of a THz TDS for focal spot measurements. PAT: photoconductive antenna in transmission mode; L_1 and L_3: convex-plane lenses; L_4: plano-convex lens; KE: knife-edge blade; PAR: photoconductive antenna in receiving mode. 58

Fig. 23 Experimental set-up for standard knife-edge measurements. PAT: photoconductive antenna in transmission mode; L_1 and L_3: convex-plane lenses; L_4: plano-convex lens; KE: knife-edge blade; PAR: photoconductive antenna in receiving mode. 59

Fig. 24 LabVIEW front panel for knife-edge measurements automation. It employs drivers for the instruments and puts them in communication. The user can choose several parameters. Program also shows an updated plot of saved data and blade position. 60

Fig. 25 Schematic representation of a THz TDS for focal length measurements. PAT: photoconductive antenna in transmission mode; L_1 and L_3: convex-plane lenses; L_4: plano-convex lens; I: iris; PAR: photoconductive antenna in receiving mode. 62

Fig. 26 Field distribution at 1 THz at a) 3 mm and b) 9 mm from the hemispherical lens of the emitting photoconductive antenna.. 64

Fig. 27 THz field distribution collimated by a commercial lens and imaged on a planar surface by knife-edge technique. 65

Fig. 28 Experimental and numerical evaluation of the focal length of three ZPs by means of the optical axis sampling of a) binary ZP, b) double-sided ZP, and c) multilevel ZP. Measurements are performed with the iris sampling method, which is also reproduced in the simulation environment. 69

Fig. 29 Acquired data for a) a conventional binary ZP, b) a double-sided ZP, and c) a multilevel ZP; their difference quotient for d) a conventional binary ZP, e) a double-sided ZP, and f) a multilevel ZP; and focal plane images obtained by knife-edge measurements for g) a conventional binary ZP, h) a double-sided ZP, and i) a multilevel ZP. Negative values of the $|E|/|E|_{\max}$ are due to diffraction and scattering among the components in the THz optical path. 71

Fig. 30 Normalized amplitude of the electric field in the focal plane for the multilevel ZP acquired with knife-edge technique by rotating a) the lens, or b) the blade........... 73

Fig. 31 Liquid crystals mesophases: a) nematic, b) cholesteric, and c) smectic.......... 76

Fig. 32 Orientation of rod-like molecules in a nematic LC cell without any applied voltage or in presence of a voltage with strength higher than Freedericksz threshold. Typically, an alternating voltage in the few kilohertz range is chosen for preventing electrochemical degradation. 78

Fig. 33 a) A ZP configuration with a uniform electrode on top and a ZP-patterned electrode on bottom substrate. The rest condition of the LC is tilted 2° from the *y*-axis. b) tilt angle and c) *y*-component of refractive index tensor distributions in a LC cell 387 μm thick, 2 ms after the application of a 70 V step voltage (steady state). 83

Fig. 34 a) A ZP configuration with a uniform electrode on top and a ZP-patterned electrode on bottom substrate. The rest condition of the LC is tilted 2° from the *y*-axis. b) tilt angle and c) *y*-component of refractive index tensor distributions in a LC cell 193 μm thick, 2 ms after the application of a 35 V step voltage (steady state). 84

Fig. 35 Cross section of geometrical radial-symmetric model and data for the materials chosen for a dual-focus double-sided ZP. The ZP is symmetric and only the profile along the radius of the lens is represented in the picture..86

Fig. 36 Computed square modulus of the electric field component along the optical axis (*z*-component) at 1 THz for a dual-focus double-sided phase-reversal ZP lens. The green line is for zero applied voltage (rest), while the blue line is for LC molecules parallel to the lens optical axis (V_∞). 86

Fig. 37 Computed normalized square modulus of the *z*-component of the electric field at 0.5 THz along the optical axis of a Fresnel ZP working in transmission (red) or in reflection mode (blue). 90

Fig. 38 Comparison between the computed square module of the electric field normalized to the square module of the incident electric field, at 0.5 THz, along the optical axis of a Fresnel ZP reflector and a multilevel phase-reversal ZP (compare Ch. IV). 90

Fig. 39 A rectangular waveguide, as an example of 1-D uniform LWAs. The electromagnetic field propagates in *z*-direction. An infinite ground plane surrounds the slot [222]. 96

Fig. 40 An example of periodic 1-D LWA. This antenna configuration has a width, *w*, larger than the operative wavelength. The electric field is in y-direction and the electromagnetic wave propagates in *z*-direction. 97

Fig. 41 An example of a 2-D LWA: the substrate-superstrate LWA. It can produce a) a pencil beam at broadside or b) a conical beam with an angle θ with respect to the broadside direction. 98

Fig. 42 Ray diagram of a forward leaky-wave. The intensity of the field is given by arrows separation: closer arrows correspond to a stronger field [222].......................100

Fig. 43 Ray diagram of a backward leaky-wave. The intensity of the field is given by arrows separation: closer arrows correspond to a stronger field [222].......................101

Fig. 44 Ray diagram of a leaky-wave excited by a source located in z = 0 [222]. 101

Fig. 45 Terminated equivalent network representing a waveguide cross-section [223]. 104

Fig. 46 LC cell driven by a gold fishnet electrode..111

Fig. 47 Real part of the three main components of the LC permittivity tensor mapped in the *xy*-plane, in the middle of the LC cell (*z* = 0). The LCs behavior is show in absence of an external field (first row), for a voltage above the threshold (last row), and for an intermediate value of driving voltage (middle row) [with courtesy of Dr. W. Fuscaldo]. 112

Fig. 48 Real and the imaginary part of the LC dielectric permittivity along a line perpendicular to the *xy*-plane and passing through three selected points of the LC cell [with courtesy of Dr. W. Fuscaldo]..113

Fig. 49 Schematic representation of the proposed FPC-LWA and its equivalent transmission line model..115

Fig. 50 Dispersion curves of the fundamental TM for different THz FPC-LWA with LC: a) Layout 1, b) Layout 2, c) Layout 3, d) Layout 4. Colors gradually shade from blue to red as the applied external voltage decreases from V_∞ to zero [with courtesy of Dr. W. Fuscaldo]..118

Fig. 51 Radiation patterns predicted by leaky-wave theory (dashed lines) or by means of reciprocity theorem (solid lines): a) Layout 1, b) Layout 2, c) Layout 3, and d) Layout 4 (see Table 3.5). The condition of the THz beam pointing at broadside (blue lines) and the radiation at the maximum pointing angle (red lines) are presented [with courtesy of Dr. W. Fuscaldo]. 121

Fig. 52 Dispersion curves of the fundamental TM when losses of the materials are taken into account: a) Layout 2, and b) Layout 4. Colors gradually shade from blue to red as the applied external voltage decreases from V_∞ to zero [with courtesy of Dr. W. Fuscaldo]. 122

Fig. 53 THz FPC-LWA unit cell model, as implemented in CST full-wave simulation. A probe for evaluating the tangential magnetic field at the ground plane is added as a light blue arrow. 123

Fig. 54 Radiation patterns of a) Layout 2 and b) Layout 4 for radiation at broadside (solid) and at the maximum pointing angle (dashed). Radiation patterns are calculated by means of reciprocity theorem in the lossless (in red) and the lossy (in black) case. Patterns from leaky-wave theory are also shown (blue). Full-wave simulations with CST are reported, in the lossy case, for radiation at broadside (filled green circles) and at the maximum pointing angle (empty green circles) [with courtesy of Dr. W. Fuscaldo]. 124

Fig. 55 Directivity at broadside as a function of the characteristic impedance of a PRS (see equation X.1). Black, blue, green, and red dashed lines selects the reactance values required for achieving theoretical directivities of 15, 20, 25 and 30 dB, respectively. 128

Fig. 56 A model for evaluating the surface impedance of a periodic PRS. A Floquet wave impinges on the PRS. The impedance matrix is obtained in correspondence of the PRS, fixing a suitable de-embedding distance. An equivalent circuit model can be derived for retrieving the value of the surface impedance from the impedance matrix parameters. 129

Fig. 57 Illustrative example of a FPC-LWA based on PRS with three different elements geometry. 130

Fig. 58 Surface reactance X_s of a) a patch-based PRS, as a function of the normalized gap *g* between the patches, and b) a strip-based PRS, as a function of the normalized width *w* of the strips. 131

Fig. 59 Surface reactance X_s of a fishnet-based PRS as a function of both *g* and *w*. The iso-lines of the reactance at 15, 25, 45, and 75 Ω are reported in white dashed lines. 132

Fig. 60 Surface reactance of a fishnet-like unit cell as a function of frequency. The family of curves is obtained changing the angle of incidence from 0° to 80° (the color shades from blue to red, respectively). 133

Fig. 61 a) Surface reactance as a function of the frequency for the four layouts presented in *Table 14*: behavior at 15 Ω is in red, at 25 Ω is in blue, at 45 Ω is in green, and at 66 Ω is in black. b) Section of the proposed FPC-LWA and its equivalent circuit model. Z_0 and Z_1 are the modal impedances in the air and in the medium, respectively, whereas k_{x0} and k_{x1} are the vertical wavenumbers in the air and in the medium, respectively. 135

Fig. 62 Dispersion curves β_z/k_0 (solid lines) and α_z/k_0 (dashed lines) as a function of the frequency. In the insets, the frequency range is limited to 0.8 – 1.2 THz to highlight the behavior around the operative frequency of the dominant leaky modes for both TE (in green) and TM (in blue) polarizations. 135

Fig. 63 Radiation patterns normalized to broadside radiation calculated with the leaky-wave approach (black solid lines) and reciprocity theorem (black dashed lines) are reported over the *E*-plane for the four layouts of *Table 14*. 136

Fig. 64 Radiation patterns normalized to broadside radiation calculated with the leaky-wave approach (black solid lines) and reciprocity theorem (black dashed lines) are reported over the H-plane for the four layouts of *Table 14*. 137

Fig. 65 Radiation patterns normalized to broadside radiation calculated with the leaky-wave approach (red solid lines) and reciprocity theorem (blue asterisks), and validated with full-wave simulations (black circles) are reported over the *E*-plane for the four layout of *Table 14*. 139

Fig. 66 Radiation patterns normalized to broadside radiation calculated with the leaky-wave approach (red solid lines) and reciprocity theorem (blue asterisks), and validated with full-wave simulations (black circles) are reported over the H-plane for the four layout of *Table 14*. 140

LIST OF TABLES

Table 1 Comparison between the main THz radiation sources. 7

Table 2 Comparison between some techniques employing optical and near-infrared lasers for generating THz radiation by optical pumping. 8

Table 3 Commercially available THz time-domain spectrometers generating THz radiation by photoconductive antennas (readapted from [76]). 9

Table 4 Commercial available detectors for THz radiation [25]. 10

Table 5 Comparison of THz conventional materials refractive index and absorption coefficient at 1 THz. 27

Table 6 Dependence of the number of operations to the frequency *f* and the number of iterations N_{it} [161]. 33

Table 7 Comparison between lenses fabrication techniques [167]. 40

Table 8 Leaky-wave antennas typologies and examples, working in the frequency range of 0.3 - 3 THz. In the headers, *f* is the frequency at which the antennas are investigated, while η is the radiation efficiency. 106

Table 9 Metasurfaces FPC-LWAs in the frequency range 0.3 - 3 THz. In the headers, *f* is the frequency at which the antennas are investigated, while η is the radiation efficiency. 107

Table 10 Leaky-wave antennas with a reconfigurable pointing angle, working in the frequency range between about 0.3 THz and 3 THz. In the headers, *f* is the frequency at which the antennas are investigated, η is the radiation efficiency, and $\Delta\theta$ is the maximum variation of the pointing angle. 108

Table 11 Design parameters for different THz FPC-LWA layouts. 117

Table 12 Figure of merits for radiating performance of different layouts of a FPC-LWA with LCs: beam reconfigurability (θ_p^M), directivity (D_0) and beamwidth ($\Delta\theta$). 119

Table 13 Comparison between radiation properties of Layout 2 and 4, with and without dielectric material losses 124

Table 14 Relevant geometrical parameters and radiating properties of the FPC-LWAs based on the considered PRSs with fishnet-like elements 134

ABSTRACT

The terahertz frequency electromagnetic radiation has gathered a growing interest from the scientific and technological communities in the last 30 years, due to its capability to penetrate common materials, such as paper, fabrics, or some plastics and offer information on a length scale between 100 µm and 1 mm. Moreover, terahertz radiation can be employed for wireless communications, because it is able to sustain terabit-per-second wireless links, opening to the possibility of a new generation of data networks.

However, the terahertz band is a challenging range of the electromagnetic spectrum in terms of technological development and it falls amidst the microwave and optical techniques. Even though this so-called “terahertz gap” is progressively narrowing, the demand of efficient terahertz sources and detectors, as well as passive components for the management of terahertz radiation, is still high. In fact, novel strategies are currently under investigation, aiming at improving the performance of terahertz devices and, at the same time, at reducing their structure complexity and fabrication costs.

In this PhD work, two classes of devices are studied, one for near-field focusing and one for far-field radiation with high directivity. Some solutions for their practical implementation are presented.

The first class encompasses several configurations of diffractive lenses for focusing terahertz radiation. A configuration for a terahertz diffractive lens is proposed, numerically optimized, and experimentally evaluated. It shows a better resolution than a standard configuration. Moreover, this lens is investigated with regard to the possibility to develop terahertz diffractive lenses with a tunable focal length by means of an electro-optical control. Preliminary numerical data present a dual-focus capability at terahertz frequencies.

The second class encompasses advanced radiating systems for controlling the far-field radiating features at terahertz frequencies. These are designed by means of the formalism of leaky-wave theory. Specifically, the use of an electro-optical material is considered for the design of a leaky-wave antenna operating in the terahertz range, achieving very promising results in terms of reconfigurability, efficiency, and radiating capabilities. Furthermore, different metasurface topologies are studied. Their analytical and numerical investigation reveals a high directivity in radiating performance. Directions for the fabrication and experimental test at terahertz frequencies of the proposed radiating structures are addressed.

ACKNOWLEDGMENTS

The work described in this PhD thesis has been possible thanks to the help and the support of several people.

At first, I would like to thank my supervisors, prof. Alessandro Galli and Dr. Romeo Beccherelli, for their suggestions and patience during these three years.

I thank prof. Renato Cicchetti, prof. Emanuele Piuzzi, and prof. Antonio d'Alessandro from Department of Information Engineering, Electronics and Telecommunications of "Sapienza" University, who have been members of my Advisory Board, for their valuable doubts and questions.

I thank Alfonso Morbidini from Istituto Nazionale di Astrofisica (INAF) for his willingness and the time he spent for the lenses fabrication.

I thank Dr. Mauro Missori from Istituto dei Sistemi Complessi of Consiglio Nazionale delle Ricerche (ISC-CNR) and prof. Renato Fastampa from Physics Department of "Sapienza" University for their precious supervision and help during terahertz experimental measurements.

I thank Dr. Dimitrios Zografopoulos from Istituto per la Microelettronica e Microsistemi of Consiglio Nazionale delle Ricerche (ISC-CNR) for the time he spent teaching me the numerical tools employed in the study of liquid crystals.

I thank Dr. Walter Fuscaldo from Department of Information Engineering, Electronics and Telecommunications of "Sapienza" University for introducing me, with patience and dedication, in the field of leaky-wave antennas.

I thank my labmates for the stimulating discussions and for all the fun we have had together.

Last but not the least, I would like to thank my family, my boyfriend and my friends for supporting me spiritually throughout this PhD and my life in general.

LIST OF SYMBOLS, ABBREVIATIONS AND ACRONYMS

Symbols

α	angle between the optical axis and the principal ray
α_{loss}	attenuation constant due to material losses
α_r	radial attenuation constant
α_z	attenuation constant in *z*-direction
$\hat{\alpha}_z$	normalized attenuation constant
$\boldsymbol{\beta}$	phase constant vector
β_r	radial phase constant
β_x	phase constant in *x*-direction
β_z	phase constant in *z*-direction
$\hat{\beta}_z$	normalized phase constant
γ	ratio between the viscosity of a nematic liquid crystal and the order parameter
γ_{s}	scattering frequency
$\Delta\varepsilon$	dielectric anisotropy
$\Delta\theta$	beamwidth
$\Delta\lambda$	interval of wavelengths
Δk_{t}	transverse wavenumber perturbation
Δn	birefringence
Δr	width of the outermost ring of a zone plate
$\bar{\bar{\varepsilon}}$	dielectric permittivity tensor
$\varepsilon_{\perp}$	dielectric permittivity in direction perpendicular to the polarization direction of an applied electric field
$\varepsilon_{\parallel}$	dielectric permittivity in direction parallel to the

	polarization direction of an applied electric field
ε_0	vacuum dielectric permittivity
ε_e	extraordinary dielectric permittivity
ε_eq	average dielectric anisotropy
ε_o	ordinary dielectric permittivity
$\tilde{\varepsilon}_\mathrm{r}$	relative dielectric permittivity
η	radiation efficiency
η_d	diffraction efficiency
η_0	vacuum impedance
θ	azimuthal angle
θ_0	angle between the z-axis and the phase vector
θ_m	angle between the long molecular axes of a liquid crystal and its director
${\theta_p}^M$	beam reconfigurability
λ	wavelength
λ_0	wavelength in vacuum
$\lambda_{1,2,3}$	eigenvalues of the Q-tensor
λ_Al	wavelength in an alumina layer
λ_d	arbitrary wavelength value in a wavelength range
λ_LC	wavelength in a liquid crystal layer
λ_sub	wavelength in a polymeric substrate
μ_0	vacuum permeability
σ	electric conductivity
φ	phase shift
ω	angular frequency
ω_p	plasma frequency
A	arbitrary constant
a	radius of the central circle of a zone plate
a_th	thermotropic coefficient
b_th	thermotropic coefficient
c_th	thermotropic coefficient
d	distance

$\boldsymbol{D}$	electromagnetic displacement vector
D	dissipation function
D_0	directivity
E	electric field
E_F	electric field for the Freedericksz transition
E_m	average electric field
E_max	maximum electric field
e_r	efficiency
$e_{r,\infty}$	efficiency contribution due to the substrate losses
ER	extinction ratio
f	frequency
$f/\#$	f-number of a lens
f_0	design frequency
F_b	free energy density
F_d	elastic energy density
F_em	electromagnetic energy density
f_op	operating frequency
F_th	thermotropic energy density
G	gain
g	gap
$\hat{h}$	convolution kernel
h_air	distance between the unit cell and the waveguide port
h_i	thickness of the i-th layer
i	positive integer
$\bar{\bar{I}}$	identity matrix
K	local field factor
k_0	free-space wavenumber
k_r	radial wavenumber
k_z	propagation wavenumber
k_t	transverse wavenumber
k_{t0}	transverse wavenumber of an unperturbed mode
l	focal length

L	straight line
L_1	collimating refractive lens
$L_{1,2,6}$	elastic parameters
L_2	focalizing refractive lens
L_3	collimating refractive lens
L_4	focalizing refractive lens
m	number of Fresnel zones
m	integer (only in chapters VIII, IX, and X)
$\boldsymbol{m}$	director of the short molecular axis
N	number of layers in a multistack
n	refractive index
n	integer (only in chapter IX)
$\boldsymbol{n}$	director of the long molecular axis
n_e	extraordinary refractive index
n_o	ordinary refractive index
N_it	number of iterations
p	object distance
p	period (only in chapters VIII and X)
p	integer (only in chapters IX)
$p_{1,2}$	polarization coefficients
$\boldsymbol{P}$	polarization vector
P_d	diffracted power
PI	photogenerated current
P_in	incident power
q	image distance
$\bar{\bar{Q}}$	Q-tensor
q_i	i^th element of the Q-tensor
R_V	responsivity
S	order parameter
S_eq	order parameter in the equilibrium state
t	thickness
T^TE	transverse-electric component of transmitted power

T^{TM}	transverse-magnetic component of transmitted power
V_∞	asymptotic value of the voltage for an infinite time
V_F	voltage for the Freedericksz transition
V_i	voltage signal of the i^{th} pixel of a detector array
v_n	voltage spectral dentisity
w	width
X_s	surface reactance
Y	admittance
Y'	normalized admittance
Y_0	admittance in vacuum
Z	impedance
Z'	normalized impedance
Z_0	impedance in vacuum
$Z_{i,j}$	elements of the impedance matrix of a two-port network
Z_{in}	input impedance
Z_L	characteristic impedance of the Floquet port in the substrate
Z_s	surface impedance

Units of measurements

μm	micrometers
μW	microwatt
cm	centimeter
dB	decibel
fps	foot per second
fs	femtosecond
GB	gigabyte
GHz	gigahertz
Hz	hertz
K	kelvin

kΩ	kiloohm
kHz	kilohertz
km	kilometer
kW	kilowatt
m	meters
mm	millimeter
mPa	millipascal
ms	millisecond
MW	megawatt
mW	milliwatt
nm	nanometer
ns	nanosecond
nW	nanowatt
pN	piconewton
ps	picosecond
pW	picowatt
rad	radian
s	second
S	siemens
THz	terahertz
V	volt
W	watt

Chemical symbols and formulas

Au	gold
Al	aluminum
Al_2O_3	alumina
CF_4	tetrafluoromethane
Cr	chromium
GaAs	gallium arsenide
HfO_2	hafnium dioxide

InGaAs	indium gallium arsenide
$LiTaO_3$	lithium tantalite
Ni	nickel
p-Ge	germanium doped with an acceptor
SF_6	sulfur hexafluoride
Si	silicon
SiN_x	silicon nitride
SiO_2	silica
Ti	titanium
VO_x	vanadium oxide

Abbreviations

c.w.	continuous wave
e.g.	*exempli gratia*
Fig.	figure
i.e.	*id est*
min	minutes
viz.	*videlicet*

Acronyms

1D, 1-D	one-dimensional
2D, 2-D	two-dimensional
3D, 3-D	tridimensional
ABS	acrylonitrile butadiene styrene
AF	array factor
CAD	computer-aided drafting
CMOS	complementary metal-oxide semiconductor
CNT	carbon nanotubes
COP	cyclo-olefin polymer

DBR	distributed Bragg reflector
DC	direct current
DNA	deoxyribonucleic acid
EBG	electronic bandgap
FBW	fractional bandwidth
FD	frequency domain
FDTD	finite difference time domain
FEM	finite element method
FET	field-effect transistor
FF	filling factor
FIT	finite integration technique
FPA	focal-plane array
FPC	Fabry-Perot cavity
FTIR	Fourier transform infrared spectrometer
FTS	fast tool servo (only in chapter III)
FTS	Fourier transform spectroscopy
FWHM	full width at the half maximum
Gbps	gigabit-per-second
GDS	grounded dielectric slab
HD	high definition
HDPE	high-density polyethylene
HEMT	high electron mobility transistor
HMD	horizontal magnetic dipole
HPBW	half power beamwidth
HRFZ	high resistivity floating zone
HSS	high-speed steel
IR	infrared
ITO	indium tin oxide
KE	knife-edge
LC	liquid crystals
LEO	low Earth orbit
LOS	line-on-site
LWA	leaky-wave antenna

MM	micro-milling
MMW	millimeter-waves
MoM	method of moments
MOSFET	metal-oxide-semiconductor field-effect transistor
MPIE	mixed-potential integral equation
NEP	noise equivalent power
QCL	quantum cascade laser
QW	quantum well
PAR	photoconductive antenna in reception mode
PAT	photoconductive antenna in transmission mode
PEDOT:PSS	poly(3,4-ethylenedioxythiophene):poly(4-styrenesulfonate)
PEC	perfect electric conductor
PET	polyethylene terephthalate
PGF	periodic Green's function
PMMA	poly(methyl methacrylate)
PP	polypropylene
PRS	partially reflective sheet
PS	polystyrene
PTFE	polytetrafluoroethylene
RAM	random access memory
RIE	reactive ion etching
RT	Radon transform
SNR	signal-to-noise ratio
SPDT	single point diamond turning
STS	slow tool servo
Tbps	terabit-per-second
TD	time domain
TDS	time domain spectrometer, time domain spectroscopy
TE	transverse-electric
TEN	transverse equivalent network
TM	transverse-magnetic
TPX	polymethylpentene

TRT	transverse resonance technique
US$	USA dollars
UV	ultraviolet
VGA	video graphics array
VIS	visible
VNA	vector network analyzer
WG	waveguide
WP	waveplate
ZP	zone plate

INTRODUCTION

> *"Since we have become accustomed to think of waves of electrical energy and light waves as forming component parts of a common spectrum, the attempt has often been made to extend our knowledge over the wide region which has separated the two phenomena, and to bring them closer together, either by cutting down the wave length of electrical oscillations […] or by the discovery and measurement of longer heat waves.*"
>
> ― H. Rubens and E.F. Nichols[1], 1897.

This statement is the opening of a significant paper for the development of a terahertz science. Even though this was only a first stage, it was clear that there were two approaches for the development of a terahertz technology: the optical and the electronic route. The terahertz range has been associated for long time to its lack in technical capabilities. It was only during 1970s that the first terahertz benchtop set-ups suitable for spectroscopic investigations have been developed. This was the starting point for the experimental test of passive components and detectors, which have been allowed for reducing the technological gap.

Nowadays, terahertz radiation has become crucial in several fields, such as, for example, the objects inspection for industrial and security applications or the wireless communications. Thus, there is a high requirement of affordable high-performance terahertz devices, suitable for mass production and for the integration in complex systems.

The Chapter I introduces the terahertz radiation, starting from a definition of the frequency band and its main application fields, passing through the state-of-art of terahertz generation and detection, and concluding with a brief overview of the most employed passive components for terahertz radiation. Among them, this PhD thesis is devoted to the development of planar diffractive lenses. Thus, the Chapter II discusses

---

[1] H. Rubens and E.F. Nichols, "Heat rays of great wave length," *Phys. Rev. (Series I)*, vol. 4, no. 4, pp. 314-323, 1897.

this choice, comparing the diffractive lenses with the most conventional refractive lenses and parabolic mirrors for terahertz focusing. Moreover, the Chapter II provides the theoretical background of diffractive lenses design, as well as an overview of the materials and the fabrication processes suitable for their practical implementation.

The numerical investigation of the diffractive lenses is described in Chapter III. It aims at optimizing the lenses geometry and comparing their behavior with the one of a refractive lens of equal diameter. The numerical data coming from this analysis are reported and discussed in Chapter IV and constitute the design basis for their fabrication. The available experimental techniques for terahertz characterization are introduced in Chapter V, which also includes the description and the calibration of the available instrument and of the set-up built for the lenses measurements. The data resulting from the experimental characterization of the fabricated lens prototypes are reported in Chapter VI.

The design and the experimental characterization presented in Chapters III-VI are the starting point for a preliminary study on advanced diffractive lens configurations, such as a tunable dual-focus diffractive lens and a diffractive lens working in reflection mode (Chapter VII). This last device opens also the possibility to design terahertz lens antennas employing such diffractive lenses.

In terms of radiating systems for terahertz applications, an interesting device is the Fabry-Perot cavity leaky-wave antenna. It has the advantage to be scalable from microwaves to optical frequencies, due to the ubiquity of the leaky-wave phenomena (introduced in Chapter VIII). Thus, two main configurations of Fabry-Perot cavity leaky-wave antenna are presented for working at terahertz frequencies. In Chapter IX, a leaky-wave antenna based on a multistack of isotropic and anisotropic material layers is theoretically investigated for steering the THz beam. In Chapter X, leaky-wave antennas made with different metasurface topologies are theoretically studied for the design of high directivity terahertz antennas. Furthermore, their practical implementation is discussed.

CHAPTER I

Terahertz radiation

1. Introduction to terahertz radiation

The so-called terahertz (THz) radiation is an electromagnetic radiation with a frequency between 100 GHz and 10 THz [1]–[5]. However, this definition is not completely accepted and the THz range is sometimes extended from 100 GHz to 30 THz [6] or limited to a narrower region, between 300 GHz and 3 THz. About this issue, in 2002 Siegel wrote [7]: “Below 300 GHz, we cross into the millimeter-wave bands (best delimited in the author’s opinion by the upper operating frequency of WR-3 waveguide — 330 THz). Beyond 3 THz, and out to 30 µm (10 THz) is more or less unclaimed territory, as few if any components exist. The border between far-IR and submillimeter is still rather blurry and the designation is likely to follow the methodology (bulk or modal — photon or wave), which is dominant in the particular instrument.”

Sometimes, the designation of a range as THz frequencies band is influenced by the specific field of application. For example, the technological interest towards THz radiation arose in connection with the development of space-based instruments for astrophysics and Earth missions. The 98% of total photons emitted in the history of the Universe since the Big Bang has a frequency below 30 THz, with a peak emission at around 3 THz (cosmic microwave background radiation, which have a spectral radiance peak at about 160 GHz [8], is excluded) [3], [5]. For this reason, in this field, 30 THz can be considered the upper limit of the THz band. However, most of the scientific and technological community refers as THz the radiation between 300 GHz and 10 THz.

1.1 Terahertz in the electromagnetic spectrum

A first experimental effort towards material characterization by THz radiation was in 1897 [9], [10]. It consisted of measurements of black body radiation employing a bolometer. In [10], the authors wrote: “since we have become accustomed to think of waves of electrical energy and light waves as forming component parts of a common spectrum, the attempt has often been made to extend our knowledge over the wide region that separates the two phenomena, and bring them closer together”. It appears as a first explicit reference to the fact that a technological gap exists in the electromagnetic spectrum. It is set between photonics and electronics (*Fig. 1*).

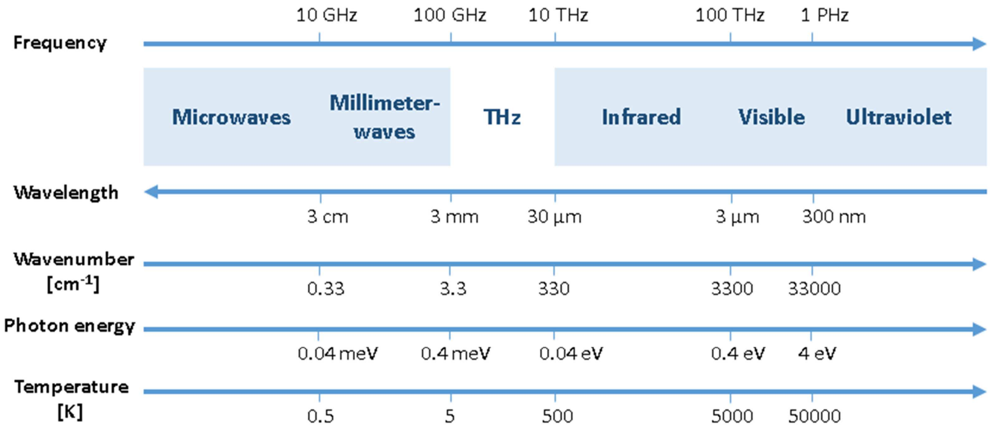

Fig. 1 Electromagnetic spectrum.

A summary of the historical developments in this range of the spectrum is beyond the aim of the preset work. An interesting review can be found in [11]. However, it may be worthy to mention the key discoveries that contribute to the establishment of a THz technology. The first THz detectors were initially proposed for FIR radiation sensing. In 1959, the first carbon bolometer [12] as well as a photoconductive detector [13] were developed. During 1960s, several progresses were achieved in the field of detection: germanium bolometer [14], pyroelectric [15] and tunable FIR detectors [16] were introduced. With regard to the generation of THz radiation, in 1962, optical rectification mechanism was experimentally demonstrated for the first time [17]. It is still now one of the main THz generating mechanism [18]. In 1971, the first THz pulse was generated using a benchtop resource [19]. Finally, in 1984, the first laser operating between 390 – 1000 μm was constructed, with a peak power up to 10 kW [20], whereas, in 1986, a THz emitting antenna was demonstrated for the first time [21].

Several progresses have been made until now in the field of THz sources and detectors. Starting from the 1950s, many attractive applications have been developed, as will be described in the following sections.

1.2 Terahertz applications and challenges

Historically, THz detection was conceived for interstellar dust sensing between 100 GHz and 3 THz. Nowadays, space-borne THz sensors have been developed both for interstellar and Earth observation. Associated payload can be located at different orbits. Low Earth orbit (LEO, *i.e.*, an orbit around Earth with an altitude of 2000 km or less, and an orbital period of about 84 – 127 min) allows for astronomy research [22] and Earth control [23]. Large space observatories [24] have more distant and relatively stable dislocation points and are usually devoted to deep space astronomy. In this situation, there are important limitations in terms of maximum mass (few tens of kilograms) and power supply availability (tens of watts) per instruments. Miniaturization, integration, and the employment of materials able to guarantee sensitivity and responsivity (see Ch. I Sec. 3) at high temperatures, are the main goal of THz technology for space application [25].

The THz measurements for Earth observations from LEO suffer from radiation attenuation due to water molecules absorption. Generally, water molecules in atmosphere create small clusters by means of hydrogen bonds. The rotation and vibration of water molecules in clusters determine absorptions in THz radiation spectrum. The number of molecules in the cluster establishes at which THz frequency there will be radiation absorption. For example, a cluster of 38 water molecules causes absorption at 20 THz [26], a cluster of 8 water molecules is responsible of absorption at 1.4 THz [27], while a mixture of ring clusters of 4, 5 and 6 molecules gives absorption lines at 0.56 THz, 0.76 THz, 0.98 THz, 1.1 THz, 1.17 THz, and 1.41 THz [28].

Due to water absorption, THz radiation can be exploited only in specific spectral bands for wireless communication. Most promising bands, for line-on-site (LOS) data transmission at distances over 1 m, are in the ranges 0.38 – 0.44 THz, 0.45 – 0.52 THz, 0.62 – 0.72 THz, and 0.77 – 0.92 THz [29], as shown in *Fig. 2*. In these frequency windows, absorption losses due to atmosphere gases are below 10 dB/km, but spreading losses are high, motivating the requirement of high directivity and high gain antennas.

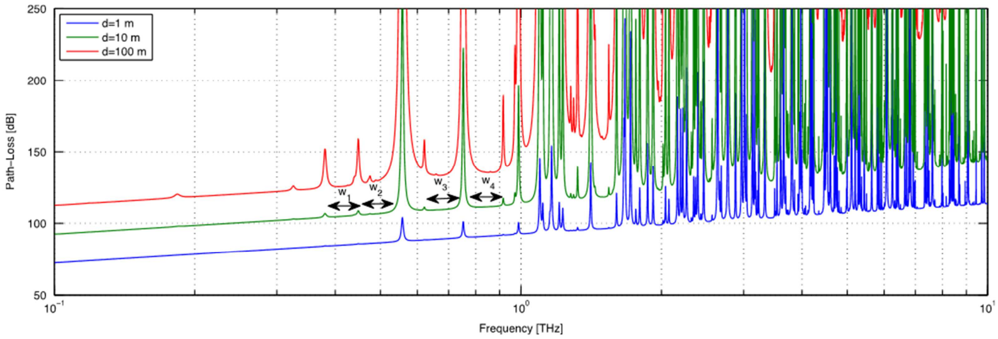

Fig. 2 Path loss in line-on-site communications at THz frequencies for different distances. It takes into account both attenuation due to molecular absorption of gases in atmosphere both the spreading losses. Three bands are marked as promising ranges: 0.38 – 0.44 THz, 0.45 – 0.52 THz, 0.62 – 0.72 THz, and 0.77 – 0.92 THz [29].

The main advantage of wireless communication at THz is that wireless technology below 0.1 THz and above 10 THz is not able to sustain Terabit-per-second links (Tbps) [29]. In fact, below 0.1 THz, the available bandwidth is not sufficient and confines the feasible data rates. At millimeter waves (~ 60 GHz), 10 Gbps within 1 m are currently reachable [30], but they are of two orders of magnitude below the estimated demand in wireless communications of next future. On the other hand, above 10 THz, large bandwidth are available, but several limitations compromise the feasibility: (i) low transmission power due to eyes health safety; (ii) influence of atmospheric weather conditions on waves propagation; (iii) high reflection losses; (iv) losses due to emitter-receiver misalignment [31]. At THz frequencies, the main challenges for commercial realization of Tbps wireless technology are: (i) the realization of compact THz sources able to supply an output power in continuous wave mode up to 100 mW, and (ii) the availability of electronically steerable antenna arrays able to minimize link losses [25]. The THz technology is not completely mature yet, but these goals are reachable in the future.

From the point of view of biological applications, strong absorptions due to water molecules allow for the monitoring of water content in human tissues or the hydration level of plants [32]. Water allows for high contrast imaging at THz frequencies. With more detail, THz absorption depends on: (i) salts concentration; (ii) protein and DNA content; (iii) macromolecules structural changes, due to bonds with ligand or denaturing processes. Because all of these factors are also involved in the cellular metabolism, it is possible to distinguish between a healthy tissue and a tissue with a disease by means of THz radiation measurements [33]–[36]. Moreover, THz is a non-ionizing radiation and can be exploited for *in vivo* measurements. For example, one of the first applications in this field was presented in [37], where a change in skin hydration is detected *in vivo* by means of THz radiation. After that, THz radiation allowed for a high contrast imaging of hidden margins of basal cell carcinoma, a skin cancer, before a surgery intervention [38]. The THz radiation is able to penetrate under the skin in a non-invasive way and has a negligible scattering inside tissues. Moreover, time-domain systems (see next section) can offer quasi-3D information [25]. However, the availability of sources with yet limited power, when compared to the power required to cope with absorption due to water, confines THz penetration depth inside aqueous systems, such as human body. For this reason, at the present, THz radiation can be employed only for the diagnosis of superficial skin cancers.

The THz radiation has the great advantage to penetrate into non-metallic materials and to distinguish between them, thanks to specific band absorptions which provide a fingerprint for the material. In fact, THz radiation can be exploited for security applications and non-destructive packaging inspection. Examples of security applications are body-scanning imager [39] and explosives detection by spectrometer analysis [40]. Commercially available body-scanners work in the frequency range of 0.15 – 0.68 THz [41], [42] and have the advantages of being compatible with compact hardware systems, such as wearable devices. Moreover, they could combine imaging with spectroscopic information for the identification of dangerous substances. In fact, every molecule has its own fingerprint at THz frequencies, *i.e.* a unique spectrum of absorption due not only to the bounds between atoms in functional groups, but to the bound between atoms constituting a molecule [40]. However, in body-scanning, THz imaging detectors need to have an extremely large area, able to cover the dimensions of a human body. It constitutes a big issue, especially in the maintaining of good imaging performance (compare Ch. I Sec. 3) with low times for image acquiring and affordable costs of the whole technology.

Penetrative capability of THz radiation in several common materials such as plastics, fabrics, ceramics, and paper, linked to the possibility to distinguish between them, can be applied in non-destructive and non-contact test of several objects and coatings. For example, marine structures are protected from environmental corrosion agents by specific coatings. The corrosive process is able to modify both chemical and physical properties of materials causing defects, as bubbles or cracks, which are usually located under the external surface of objects [43]. THz radiation is able to penetrate inside coatings and discloses every defect larger than the incident wavelength [44], [45]. In this way, it is possible to check coatings and prevent failures by substituting them before compromising the covered structure or object. By applying the same principles, it is also possible to employ THz radiation for monitoring and preserving the cultural heritage [46], [47]. Moreover, it is also possible to investigate under the surface of paintings or frescos and discover details hidden by their creator. THz spectroscopic imaging complements the information obtained by other consolidated techniques, such as the imaging at near-infrared frequencies. For example, in [48] a Pablo Picasso painting on canvas was analyzed by THz pulsed time-domain imaging. Different areas of this painting show different numbers of layer, confirming that the author repainted some parts of his artwork.

From a technological point of view, the main effort in the THz field is to provide a suitable source of radiation [49]. Available sources are usually expensive, bulky, and emit weak radiation. This problem can be approached from the millimeter-wave (MMW) side or from the infrared (IR) side [50]. From a MMW point of view, it is difficult at THz to create circuits for high-frequency waves. From an IR point of view, THz optical systems are challenging due to the fact that optical elements have dimensions comparable to the wavelength [51]. Some solutions and the state-of-art about THz sources will be discussed in the next section.

Table 1 Comparison between the main THz radiation sources.

	Frequency [THz]	**Output power**	**Advantages**	**Disadvantages**	**Reference**
Direct generation					
Quantum cascade lasers	0.85 - 5	< 250 mW (pulsed) < 139 mW (c.w.)	• high output power • can operate in c.w. and in pulsed mode	• require cooling (<199.5 K) • limited bandwidth	[52]
Semiconductor laser	1 - 10	~ mW	• broadband multimode emission • can operate in c.w. and in pulsed mode	• applications of p-Ge laser are mainly restricted to research laboratories • require cooling	[53]
Free electron laser	1.25 – 7.5	< 20 W (Novosibirsk: 500 W)	• broadband • high output power	• relatively low efficiency • large and heavy	[54]
THz vacuum tube sources (in strong magnetic field)	0.1 - 0.3	~ mW	• high power and frequency tuning range	• large and heavy • expensive • high power requirement • narrowband	[55]–[57]
Up-converters					
Frequency multipliers	0.84 - 1.9 (commercial available: 1.1 – 1.7)	< 2 mW (commercial available: 60 µW – 1.6 mW)	• low levels of dc power • inherently phase lockable • can work at room temperature	• cooling can be required • very narrowband	[58], [59] (commercially available: [60])
Transistors (InGaAs HEMT, Si MOSFET, FET)	0.3 - 3	-	• possible integration in a single chip	• require cooling • two peaks of emission	[61], [62]
Down-converters					
IR-pumped gas lasers	0.5 – Far-IR (discrete)	1–400 mW	• extremely high power	• not all frequencies covered • narrowband • bulky	[63]–[65]
Sources pumped by visible or Near-IR lasers	See *Table 2*				

2. Terahertz sources

Sources are the most difficult components to realize in the THz band. Conventional electronic sources of power, such as amplifiers or oscillators, are limited by several factors: (i) their components, *i.e.* transistors and Gunn diodes, have characteristic transit times that cause a frequency roll-off, even at the lower THz range; (ii) carriers in device components have a saturation velocity, typically of about 10^5 m/s; (iii) there are contact parasitic effects; (iv) there is a maximum electric field that materials are able to sustain before breakdown [7], [51].

These factors are the main cause of the fact that the output power falls as the square root of the frequency [66]. However, electronic sources are relatively compact and could open to the possibility of creating integrated devices.

Sources inspired by photonics, such as lasers, produce coherent powers in the order of tens of milliwatts until several watts, and they enable broadband emission. On the other hand, they are usually heavy instruments or require large apparatus for working (such as, for example, the cooling systems), can be often expensive, and difficult to use in outdoor applications.

A comparison of some of the most used sources and generation techniques for THz radiation can be found in *Table 1*, where features of (i) direct generation, (ii) up-conversion (*i.e.* frequency multiplication) and (iii) down-conversion (*i.e.* frequency difference generation) approaches are reviewed.

Optical and near-IR lasers generating THz radiation by optical pumping are the most employed sources, especially for spectroscopy applications, because they do not need cooling and are enough compact to be portable. They can operate in pulsed or continuous wave mode (c.w.). A comparison of properties for some examples of these two operational modes can be found in *Table 2*.

Table 2 Comparison between some techniques employing optical and near-infrared lasers for generating THz radiation by optical pumping.

	Laser operation	Frequency [THz]	Bandwidth [THz]	Output	Reference
Photomixer	c.w.	0.1 – 10 (tunable)	0.9	Power: < mW	[67]
Mechanical resonance	c.w.	0.2 – 0.9	0.54	Power: < 7 mW	[68]
Photoconductive antenna	pulsed	0.1 – 10	> 20	Power: 3.8 mW (in a band of 5 THz)	[69], [70]
Gas photoionization	pulsed	0.1 – 10	> 20	$\|E\|$ peak: 21 MW/cm	[71]
Optical rectification in crystals	pulsed	0.1 – 6	~ 6	$\|E\|$ peak: 200 kW/cm to 6.3 MW/cm	[72]

Continuous lasers can be mixed for generating radiation in the THz band. This kind of sources are called photomixers and generate THz radiation by optical heterodyning [73]. They have a better spectral resolution than pulsed emitters and output powers in the order of milliwatts [74]. Moreover, they can be employed as sources for spectroscopy as well as for THz communications. However, they operate in narrowband and have limited tuning ranges.

Pulsed lasers are employed for exciting a photoconductive switch or antenna. They are also able to produce THz by three different mechanism: (i) gas photoionization, (ii) optical rectification in a non-linear crystal, and (iii) drift or diffusion of transient currents in a semiconductor with high charge mobility [75]. Pulsed lasers generation technology is the base of time-domain spectroscopy (TDS). The configuration of a typical TDS set-up with photoconductive antennas will be described in detail in chapter V. In *Table 3*, properties of several commercial available TDS with photoconductive antennas are compared.

Table 3 Commercially available THz time-domain spectrometers generating THz radiation by photoconductive antennas (readapted from [76]).

Company	Model	Bandwidth [THz]	Output power	Peak dynamic range [dB]
Teraview	TPS Spectra 3000	4	~ 1 µW	80
Teraview	TeraPulse 4000	6	-	80
Picometrix	T-ray 5000	4	~ 0.5 µW	80
Advantest	TAS	4	-	60
Toptica	TeraFlash	5	~ 30 µW	90
Ekspla	T-Spec	4.5	-	70
NTT Electronics	OD-PMAN-13001	2.2	< 1 µW	20
Menlo System	TERA ASOPS	3	-	60
Menlo System	TERA K8	3.5	-	70
Menlo System	**TERA K15**	**4**	**> 60 µW**	**75**

3. Terahertz detectors

Unlike detectors for visible and infrared radiation, detectors for THz waves have not reached the quantum limit yet [77]. In fact, detector characteristics are not limited by noise due to photons, except for measurements at some frequencies or at sub-kelvin temperatures [78].

The performance of a THz set-up is influenced by sensitivity, responsivity, and frame rate of its detector(s). The sensitivity is expressed by a figure of merit, the noise equivalent power (NEP). NEP is defined as the incident power that gives a signal-to-noise ratio (SNR) equal to one in an output bandwidth of 1 Hz. Low values of NEP express a high sensitivity. Mathematically [79]:

$$\mathrm{NEP} = \frac{v_{\mathrm{n}}}{R_{\mathrm{v}}} \qquad \text{(I.1)}$$

where, v_n is the noise voltage spectral density, *i.e.* the noise power per unit of bandwidth, and R_v is the responsivity, *i.e.* the input-output gain of the detector.

For an imaging detector, constituted by a certain number of pixels, a $\mathrm{NEP_{camera}}$ is usually indicated, where: $\mathrm{NEP} = \mathrm{NEP_{camera}}/\sqrt{\mathrm{bandwidth}}$. NEP is expressed in $\mathrm{W}/\sqrt{\mathrm{Hz}}$. The $\mathrm{NEP_{camera}}$ is expressed in W and can be computed as [79]:

$$\mathrm{NEP_{camera}} = \frac{v_{\mathrm{n}} P_{\mathrm{in}}}{\sum_{\mathrm{array}} V_i} \qquad \text{(I.2)}$$

where P_in is the total incident THz power and V_i is the signal of the i$^{\mathrm{th}}$ pixel of the detector array.

Table 4 Commercial available detectors for THz radiation [25].

	Frequency [THz]	**Responsivity [V/W]**	**NEP or $\mathrm{NEP_{camera}}$**	**Frame rate or response time**	**Number of pixels**	**Company**
Schottky barrier diode	0.11 – 0.17	2000	13.2 pW/Hz$^{1/2}$	42 ns	Single detector	VDI
Photoconductive antenna	0.1 – 4.0	-	-	-	Single detector	EKSPLA
Photoconductive folded dipole antenna	0.6 – 1.0	800	66 pW/Hz$^{1/2}$	-	Single detector	STM
Photoconductive antenna	0.3 – 4.5	-	-	-	Single detector	Menlo System
FET array	0.7 – 1.1	$115\cdot10^{3}$	12 nW	25 Hz	32x32	STM
Bolometer	4.25	-	24.7 pW	50 Hz	384x288	INO
Golay cell	0.2 – 20	$10\cdot10^{3}$	10 nW/Hz$^{1/2}$	25 ms	Single detector	Microtech
Micro-bolometer	1.0 – 7.0	-	< 100 pW	30 Hz	320x240	NEC
$\mathbf{LiTaO_3}$ pyroelectric	0.1 – 300	-	96 nW	50 Hz	320x320	Ophir photonics
Pyroelectric	0.3 1.0 3.010	$18.3\cdot10^{3}$	440 pW/Hz$^{1/2}$	10 Hz	Single detector	QMC
α-Si micro-bolometer	2.4	$14\cdot10^{6}$	30 pW	-	320x240	CEA-Leti
VOx micro-bolometer	2.8	$200\cdot10^{3}$	35 pW	30 Hz	160x120	Infrared Systems
VOx micro-bolometer	3.1	-	280 pW	16 ms (each pixel)	640x480	NEC
Antenna QW cavity	2.0 – 4.0	126	32 pW	25 Hz	320x240	CEA-Leti

In *Table 4*, parameters of several commercially available THz detectors are compared. According to *The 2017 terahertz science and technology roadmap* [25], detectors based on CMOS technology, such as photoconductive antennas and FET arrays, are the most promising tools for THz sensing and imaging. In fact, they are suitable for miniaturization and integration in compact devices and are able to operate at room temperature. However, improvements are needed for increasing responsivity, sensitivity and response times, as well as, in imaging, the number of available pixels [25]: "Future expectations for terahertz imaging systems include video rate imaging (at least 25 fps) at VGA resolution. Further into the future, HD format will be the normal expectation for any imaging system. Image resolution (as opposed to display resolution), noise and dynamic range are all expected to improve. These improvements will rely on advancement in source, detector and optical/system design technology. Specifically, compact, room temperature terahertz sources in the region of 10 mW average power are essential in order to enable stand-off imaging at distances greater than 1 m. Such sources when coupled with a Si CMOS FPA would render a low-cost THz camera (we estimate < US$ 5000 per unit) that could find wide spread use in applications such as stand-off detection of hidden objects and non-invasive medical (*e.g.* oncology) and dental diagnostics."

It means that the development of THz detection tools cannot ignore a progress of the whole THz components technology, included not only sources and detectors, but passive THz devices too, as discussed in the next section.

4. Terahertz passive components

Generally, when the availability of high power is fundamental for a specific application, quasi-optical devices are preferred to guided-wave structures. For example, in a commercially available metallic rectangular waveguide (WG) losses are equal to 1 dB/cm at 1 THz (Virginia Diodes VM250 (WR-1.0) [80]). In fact, at microwaves, metals behave as perfect conductors, while they are lossy at THz. Additionally, most of dielectrics extremely transparent at optical frequencies absorb THz waves (compare Ch. II Sec. 5). Guided structures, however, offer several advantages. They (i) allow for the integration of compact and light THz systems; (ii) provide better isolation; (iii) do not need optical alignment accuracy [25].

4.1 Terahertz waveguides

Metallic WGs are mainly suitable for transmission of THz waves at distances of the order of millimeters because they cannot guarantee both mode confinement and negligible metallic losses [81]. For example, parallel-plate WGs show low losses: if plates are made of copper and are located at a distance of 0.1 mm each other, the loss is approximately 1.2 dB/cm at 1 THz [82]. Moreover, their group velocity dispersion can be considered negligible. However, they offer no confinement in lateral directions.

Co-planar WGs and co-planar strip-lines are employed in photoconductive transmitters and receivers for propagation distances in the order of millimeters. In fact, they suffer from strong attenuations of 40 dB/cm or higher [83], [84], but they continue to be attractive because their small dimensions and planar geometry [82].

At THz frequencies, most dielectric materials suffer from high absorption coefficient or from frequency dispersion in refractive index value, except for high-resistivity silicon and few polymeric materials (compare Ch. II Sec. 5). These properties need to be taken into account in the design of dielectric WGs. Optical fibers are an example of possible dielectric guiding structure largely studied at THz frequencies. Three core structures can be compared [81]:

1) Solid-core fibers: they are reasonably simple to fabricate and offer a wide bandwidth in single mode operation. On the other hand, they are deeply influenced by material absorption. Example [85]: a fiber with a diameter of 0.42 mm, made of TOPAS polymer (compare Ch. II Sec. 5), has losses of 0.78 dB/cm over 0.35 – 0.65 THz and a dispersion of less than 1 ps/THz·cm over 0.5 – 1.5 THz.
2) Porous-core fibers: they reduce losses due to material losses and show low THz dispersion. Because porous are filled by air, they are sensitive to waveguide perturbations. Example [86]: a fiber with a diameter of 0.445 mm, made of polyethylene (compare Ch. II Sec. 5), with circular holes filled by air

in its core, has losses below 0.17 dB/cm over 0.1 – 0.5 THz and a dispersion of less than 1 ps/THz·cm over 0.1 – 0.5 THz.

3) Hollow-core fibers: they show the lowest losses and dispersion, but they work in a limited frequency band, are difficult to fabricate, and have a larger diameter than the other fiber typologies. Example [87]: a fiber with a diameter of 2 mm, made of Teflon (compare Ch. II Sec. 5), with a core made of air, has losses below 0.17 dB/cm at 1 THz.

The main drawback of dielectric WGs is that they are subjected to diffraction limit and the mode propagation area cannot be reduced beyond it. Because of dimensions, their integration inside extremely compact THz devices could be a critical issue.

4.2 Quasi-optical components

The most encountered way to propagate THz radiation is the quasi-optical one. THz transmission in free space is possible when the electromagnetic beam is collimated and is not completely warped by diffraction. However, the maximum beam size is restricted to a moderate number of wavelengths. For this reason, diffraction is a significant issue in the design of quasi-optical components. Diffraction theory can be successfully applied as design tool, but its formulation is quite complex. In most cases, however, THz radiation has a Gaussian amplitude distribution, which is transverse to beam propagation axis. Gaussian optics is widely employed in the THz propagation theoretical analysis, because it is accurate and allows for a rapid design of passive components [88].

4.2.1 Polarizers

A Gaussian beam can have, in principle, any polarization state. Many THz emitters have both vertical and horizontal polarization components because of the antenna structure [89] or bulk contributions to optical rectification [90]. Sometimes, THz antennas are not characterized in terms of polarization and it can affect set-up optical properties [91]. Polarizers are able to separate polarization components by means of a grating with different geometries and made of different materials. The power transmitted across a linear polarizer is given by two components: T^{TM}, which is the component parallel to the grating vector, and T^{TE}, which is perpendicular. A figure of merit is the extinction ratio, defined as: $\mathrm{ER} = 10\log(T^{\mathrm{TE}}\,/\,T^{\mathrm{TM}})$. For an ideal polarizer, $T^{\mathrm{TE}} = 0$ and $\mathrm{ER} = 0$. *Fig. 3* shows the state of art of polarizers comparing them with commercial ones in terms of transmitted power and extinction ratio at 1 THz. A description of different structures and materials for THz polarizers goes beyond the aim of this works and can be found in [91]. Commercially available polarizers have high transmittance and good extinction ratio. However, they are well-known metallic wire grid polarizers and could be substituted in the next future by polarizers made of novel materials, such as carbon nanotubes (CNT).

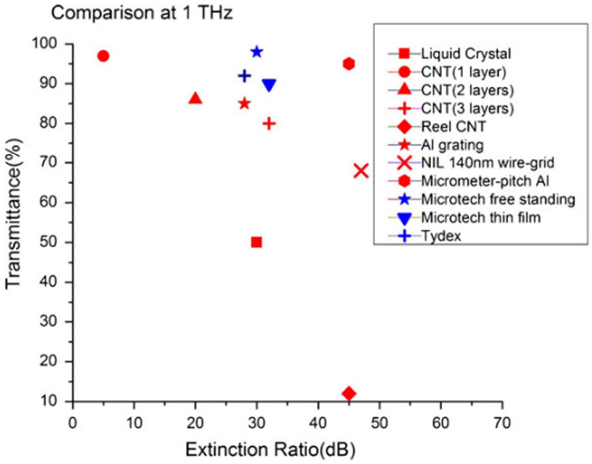

Fig. 3 Comparison between novel polarizers (red) and commercially available polarizers (blue) at the frequency of 1 THz. Figure is taken from [91] where a description of the polarizers in the legend is driven in detail.

4.2.2 Waveplates

Waveplates (WPs) are material slabs able to introduce a differential phase shift between the components of a linearly polarized radiation. A quarter WP introduces a phase shift of 90°, transforming a linear polarization into a circular polarization [92]. A half WP leads to a phase shift of 180°, rotating the polarization plane of a linear polarized beam [88].

At THz, the main issue is the availability of a transparent material, with low frequency dispersive refractive index. Natural or artificial anisotropic dielectrics are both suitable.

As will be discussed in detail in Ch. II Sec. 5, some anisotropic polymeric materials are transparent and affordable choices.

4.2.3 Filters

There are several different filters at THz frequencies that can be employed for various applications. According to [88], THz filters can be divided in four categories:

1) Two-dimensional structures: planar structures with a pattern of conductors that is periodic in two dimensions. Simple geometries, such as strips with spacing higher than a half of the operational wavelength, behave as high-pass filters in transmission. According to the Babinet principle [93], a complementary geometry, *i.e.* patches, acts as a low-pass filter in transmission. Rings, crosses or other geometries [94] exhibit a resonant behavior.
2) Three-dimensional structures: planar structures with a pattern of conductors that is periodic in two dimensions and with an arbitrary size in the third direction. Examples are perforated plates and dichroic plates [95]. They work as high-pass filters in transmission.
3) Dual-beam interferometers: devices that, employing a dielectric slab or a wire grid structure, divide the incident beam into two parts, introduce a delay in one of them and recombine the two parts in a single beam [96]. They are the THz counterparts of the Michelson interferometer widely used in optics or in the IR region. The output spectrum is a sinusoid with properties depending on the introduced delay and on the imperfections in the two beams recombination.
4) Multi-beam interferometers: stacks of partially reflective mirrors. They are also called Fabry-Perot interferometers [97]. Dielectric slabs as well as planar structures with periodic conductors can act as mirrors. The frequency response is deeply influenced by reflectivity of the mirrors and by their thickness. The amplitude of transmitted radiation can be compromised by absorption losses in materials constituting the mirrors.

A summary of filters behavior described above can be found in *Fig. 4.*

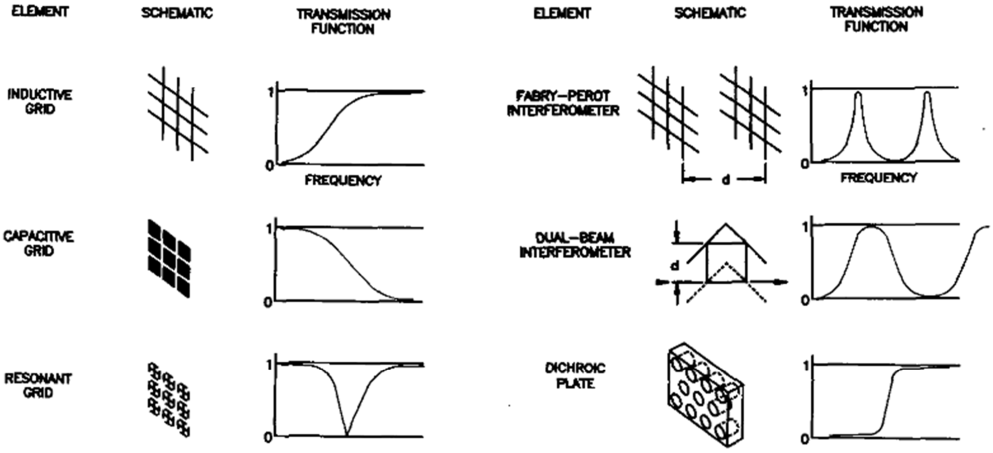

Fig. 4 Behavior of some filter categories widely employed at THz frequencies [88].

4.2.4 Lenses

Lenses are important passive components for the manipulation of THz beams. They are devices able to focus incident radiation in a small area, ideally of circular shape and with a diameter comparable to the wavelength. In practice, however, it is hard to focus THz waves at the diffraction limit. Several solutions for increasing THz lenses resolution without losing radiation power in the focal area are possible and they will be discussed in the following chapters.

CHAPTER II

Passive devices for terahertz radiation: zone plates as planar diffractive lenses

1. Introduction

Electromagnetic radiation can be focused by refraction, reflection, diffraction and interference of waves. At THz frequencies, most common choices are refraction or reflection.

Plano-convex or biconvex lenses [98]–[100] are usually employed in broadband THz set-ups, because they are compact, light and highly familiar to those skilled in visible optics. However, in contrast to visible optics, material losses, finite thickness and low power of THz sources limit the effectiveness of refractive lenses. Off-axis parabolic mirrors do not introduce significant absorption loss, but they are rather bulky and require significant space in the free-space electromagnetic path. Furthermore, they suffer from comatic aberration and from the presence of various polarization states of the THz wave in the focal area [101]. Therefore, for example, when an off-axis parabolic mirror is employed for performing polarization-resolved terahertz time-domain spectroscopy experiments, the sample has to be set exactly in focus to prevent changes in the radiation polarization state.

Another way to focalize electromagnetic radiation is by diffraction [102]–[104]. Diffractive lenses introduce lower absorption losses than refractive lenses, because they can be thinner. However, they are highly chromatic devices and are not suitable for broadband applications. This capability of a diffractive lens to focus different electromagnetic wavelengths at different focal lengths has been used for tomographic applications [105]. Among diffractive lenses, the zone plate (ZP) is a thin and ideally planar device, which introduces one of the lowest absorption losses.

2. Planar diffractive lenses: zone plates

A ZP is a circular grating able to focalize electromagnetic waves by interference instead of refraction or reflection. It has been introduced in 1875 by Soret [106], who described it as an alternation between ring-shaped zones completely opaque or transparent to an incident radiation.

Zone construction follows the Huygens-Fresnel principle [93]. It can be explained from *Fig. 5*, where a plane wave is travelling in free space.

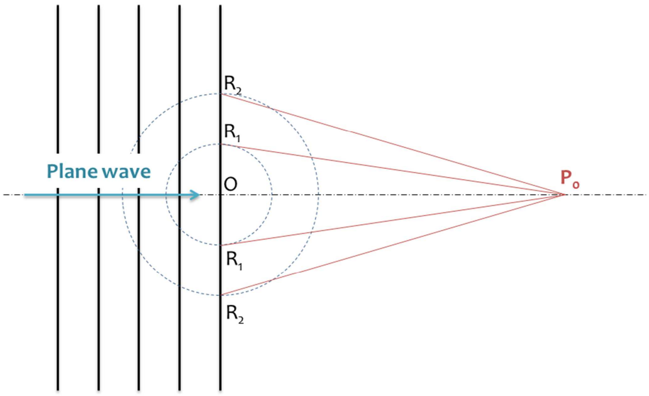

Fig. 5 Huygens-Fresnel principle for zone plate construction. A plane wave is propagating towards the point of the space P_0. O, R_1, and R_2 are point of the wave front, which have a fixed distance with respect to P_0.

P_0 is a point at distance OP_0 from the wave front of the plane wave. According to Huygens principle, every point of the wave front acts as a source of electromagnetic waves. These secondary waves (i) have same amplitude, (ii) are in phase and (iii) are propagating to P_0. The wave front can be divided in zones by constructing circles centered in O. The first circle radius is such that the distance OP_0 differs from R_1P_0 by $\lambda/2$; for the second circle radius, the distance OP_0 differs from R_2P_0 by $2\lambda/2$; and so on. In this way, the radiation passing through a single zone arrives in phase at the point P_0. If only the radiation coming from alternate zones is collected, it constructively interferes in P_0. A ZP is a screen, which stops wave propagation only in alternated half-period zones for a point of the space.

Developments and applications of ZP lenses, similar to those in electromagnetics, have also been made in acoustics. Acoustical Fresnel zones are, sometimes, called Huygens' zones [107].

Fresnel ZPs are not often employed because their efficiency in radiation collection is poor for two main reasons: (i) only $1/\pi^2$ of incident power on a ZP can be focused in its primary focus; (ii) 1/4 of the incident light is not diffracted and creates a continuous background in the image plane. Moreover, ZP focal length is proportional to $1/\lambda$ and changes according to the operational frequency (highly chromatic lenses). ZPs can be difficult to fabricate when, for example, the ZP has to focus electromagnetic radiation at high frequencies (UV and higher).

To overcome difficulties linked to ZP efficiency, Lord Rayleigh proposed a phase-reversal ZP in 1888 [108]. The main difference between a conventional and a phase-reversal ZP is that in the phase-reversal ZPs all zones are, ideally, made of a low-absorbing material. The phase-reversal device continues to consist of an alternation of concentric ring-shaped zones: some zones are open; the others retard the incident radiation phase by the amount of π radians by adding $\lambda/2$ to the optical path of radiation rays. The simplest way to implement such retardation is by employing a dielectric material with an appropriate thickness. In this way, at the ZP primary focus, the power intensity could be increased four times.

Starting from 1898, Wood further developed Lord Rayleigh idea. He demonstrated phase-reversal ZPs advantages over conventional Fresnel ZPs. In fact, in [109] he wrote: "In a paper published in Poggendorff's Annalen (1875) Soret showed that if we describe a number of small concentric circles on a glass plate, with radii proportional to the square roots of the natural numbers, and blacken the spaces between the alternate rings, the plate will have the property of bringing parallel rays of light to a focus, like a condensing-lens. […] [Soret] showed that such a plate forms real images of luminous objects and could be used as the objective of a telescope or as the eyepiece. He also showed that in addition to acting as a condensing lens, the zone plate acted as a concave or dispersing lens. Moreover, he pointed out that the plate has multiple foci at distances a^2/λ, $a^2/3\lambda$, $a^2/5\lambda$, where a is the radius of the central circle. […] It has been pointed out by Lord Rayleigh that if it were possible to provide that the light stopped alternate zones were replaced by phase-reversal, a fourfold effect would be produced. After some experimenting I have succeeded in producing such a zone plate, perfectly transparent over its entire extent. […] Using one of the new plates as the objective of a telescope in connection with a low-power eyepiece, I have distinctly seen the lunar craters and have constructed telescopes in which both objective and eyepiece were zone-plates.”. Wood proposed several ways for realizing phase-reversal ZPs [109], [110] and also suggested some possible and successful applications for these devices at visible frequencies. However, ZPs are of little practical use in this range of the electromagnetic spectrum where refractive lenses and mirrors are available. Until the first half of the 20th century, optical ZPs were considered by most scientific literature only a mean for experimentally demonstrating the Huygens-Fresnel principle [111], [112].

Because ZPs operation principle is valid at any wavelength, it is applicable beyond the visible range. Starting from 1950s, ZPs were reconsidered for the focusing of X-rays [113], [114] and extreme UV radiation [115], [116] and their fabrication constrains were actively discussed. At these frequencies, mirrors can efficiently focus radiation, with a small spot size and achromatic behavior, but ZPs offer the advantage to be more compact, lighter and easier to align, even if they have a relatively low efficiency. Some strategies have been recently developed for increasing the intensity in the first-order focus area, such as the binary ZPs stacking [117], [118].

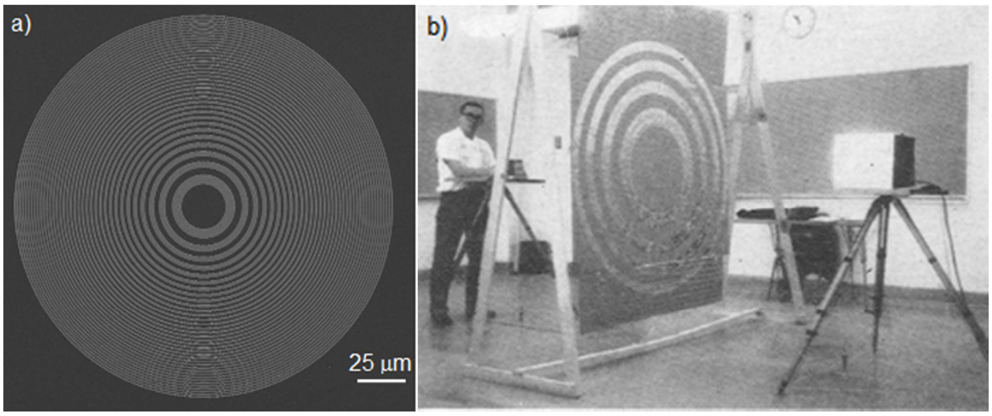

Fig. 6 a) Fresnel ZP for a microlight emitting diode [119]; b) ZP constructed for 12-cm waves [120].

On the contrary, at microwaves, ZPs show some differences compared to their optical counterpart (*Fig. 6*). In the visible, the zone number is high; Wood’s plate had 100 ring-shaped zones, for example. Moreover, the relative aperture, *i.e.* the ratio of aperture diameter to focal length, is small. On the other hand, a microwave ZP has usually few zones and a large relative aperture. In [120], Brown wrote: “Assume one [ZP] for 12-cm waves and having an aperture of *f*/4. Computations show that its primary focal length is 16 m, its aperture 11.5 m! Dimensions suitable for lecture room apparatus can be attained only with much larger relative apertures. It then follows that a microwave zone plate can be designed exactly for only a single pair of conjugate foci, this restriction being the same as for a lens of large relative aperture.”

For wavelengths in the order of centimeters or lower, ZPs can be used as antennas [121]–[123]: as emitting antenna, they have small gain, but good bandwidth; as receiving antenna, they behave as converging lenses [122].

3. Zone plates for terahertz radiation and their applications

Along with emerging of a THz technology, ZPs have also been developed for this frequency region. However, common materials at optical and microwave frequencies are not suitable for THz ZPs due to THz absorption. Thus, ZP fabrication process needs to be different as well.

From the point of view of ZPs applications, they take inspiration from both optics and microwaves: ZPs could be used to focus electromagnetic radiation, for example in THz spectroscopy or imaging, or they can be coupled with antennas for increasing directivity. It is important to underline that, in most cases, when ZPs are employed as lens antenna, they usually work in reflection mode, while, when ZPs are developed for quasi-optical applications, they mainly work in transmission mode.

The use of ZPs as lens antennas can be found in [124]–[127]. For example, a ZP designed for a specific microwave frequency is effective also at its odd harmonic frequencies [125]. A ZP lens antenna was designed for operation at 90 GHz, but it was also investigated at 0.27 THz, 0.45 THz, until 1.35 THz. The authors have showed that for all these odd harmonics of the design frequency, the gain peak has the same shape, top value, and bandwidth. It opens up the opportunity to create a multiple band THz lens antenna, by simply employing a suitable emitting source. However, antenna resolution and efficiency of a ZP designed for microwave but operated at higher odd harmonics up to THz frequency are not comparable to those achievable by a ZP antenna designed specifically to operate at THz with the first harmonic. Moreover, all applications of a ZP as lens antenna in the THz range have been mainly investigated analytically or numerically; experimental evidences have been present so far only at sub-THz frequencies, between 0.1 THz and 0.28 THz [128].

The ZPs can be slightly modified in their shape for obtaining interesting features. For example, in [129] a sensor was integrated on the bottom side of a substrate and a spiral-shape ZP is designed on the top side of the same substrate. This device behaved as a receiving antenna at 28 THz. In fact, it was designed in the way that the spiral ZP focal length at 28 THz corresponds to the substrate thickness. Moreover, at the same time, the whole device has been able to work as lens for waves at 0.4 THz. In this way, if a detector was placed at a distance corresponding to spiral ZP focal length at 0.4 THz, a dual-band detection could be operated.

In the THz central frequency band, ZPs are mainly employed as focusing elements. In [102], [130], [131] two Fresnel ZPs have been compared: a conventional one and a ZP made by cross-shaped resonant elements. The two ZP lenses have been designed to have the same focal length and numerical aperture, but it has been shown that they also have the same beam waist. The main difference is the maximum intensity of the THz beam in the focus area: this is almost twice as high for the conventional Fresnel ZP with respect to the ZP with resonant elements. Both ZPs considered in [102], [130], [131] were metallic lenses and they induced the presence of standing waves when other metallic elements were present in the same THz radiation path. A phase-reversal ZP could prevent it since it is made with a dielectric material. An application suggested by the same authors for their ZPs has been the coupling of the metallic ZPs [132] or the phase reversal ZP [133] with InGaAs-based THz detectors for enhancing their detection power.

The refractive nature of ZPs implies that they behave as highly chromatic lenses. However, it is possible to tune (i) the frequency at which they are optimized for, or (ii) their focal length at a fixed frequency. Currently, the only way known at THz to operate a tuning of ZP focal length is to photo-induce a ZP pattern on a silicon substrate and change the number of the photo-induced ring zones, for a fixed overall lens diameter [134], [135].

4. Zone plates theoretical background

A ZP has a geometry composed of concentric rings with an increasing radius. When a plane wave impinges on the ZP, the path of the rays contributing to the focus grows as the distance from the center of the lens increases. Considering two adjacent zones, the path increases by λ from the beginning of the first zone to the end of the second one. The phase, in the first ring of these two zones, increases from 0 to π. In the second zone, the phase increases from π to 2π. For this reason, radiation coming from the second zone destructively interferes with radiation from first zone. In a Fresnel zone plate, radiation from second zone is completely stopped by a non-transmitting material. In phase reversal zone plates, radiation phase is changed by choosing an opportune difference of thickness between two adjacent zones. Since the path difference between two adjacent zones is required to be λ/2, the zone radius is given by

$$r_m^2 = ml\lambda + \frac{m^2\lambda^2}{4} \qquad \text{(II.1)}$$

where r_m is the radius of the m^{th} zone, and l is the focal length. ZPs are not usually employed for finite object distances, because they introduce spherical aberrations. When $m\lambda \ll l$, the expression calculating the radius is simplified to

$$r_m \approx \sqrt{ml\lambda} \qquad \text{(II.2)}$$

In this approximation, all zones occupy the same area and contribute equally to the focus. The expression II.2 is accurate only for objects or images at infinity. If object p and image q distances are finite, equation II.1 has to be expanded in powers of $m\lambda$ [109]:

$$r_m^2 = ml\lambda + \frac{m^2\lambda^2}{4}\left(1 - \frac{3l(q-l)}{q^2}\right) + O\left(\frac{m^3\lambda^3}{q}\right) \qquad \text{(II.3)}$$

The second term in equation II.3 becomes significant if $m^2 > l/\lambda$. Higher-order terms remain negligible for all object distances unless the following constrain holds $m^{3/2} \geq 5l/\lambda$.

In a phase-reversal ZP, the zone thickness is a critical parameter. It can be derived from the phase shift φ that a material introduces in the ray path:

$$\varphi = \frac{2\pi}{\lambda} t(n-1) \qquad \text{(II.4)}$$

where n is the ZP material refractive index and t is the ZP thickness. In the case of a half-period zone plate, $\varphi = \pi$ and thus zone thickness equals

$$t = \frac{\lambda}{2(n-1)} \tag{II.5}$$

A more rigorous geometrical construction of all the formulas presented in this section can be found in [112], [113].

4.1 Diffraction efficiency

ZP diffraction efficiency is an important parameter for evaluating the ZPs focusing performance in terms of power throughput. It is defined as the ratio between the power diffracted by the ZP, P_d, and the power incident onto the ZP, P_in:

$$\eta_\mathrm{d} = \frac{P_\mathrm{d}}{P_\mathrm{in}} \tag{II.6}$$

In a ZP, the diffraction efficiency can be analytically evaluated by Fresnel-Kirchhoff theory and corresponds to about 40.5%. In a phase-reversal ZP, if the zone thickness t is lower than the ratio between the square value of the width of the narrowest and outermost ring, Δr, and the wavelength, λ, *i.e.*

$$t < \frac{\Delta r^2}{\lambda} \tag{II.7}$$

the Fresnel-Kirchhoff theory is valid and the diffraction efficiency of the phase-reversal ZP is the same of a conventional ZP. On the contrary, for high values of zone thickness, a more rigorous analytical calculation is needed. Details can be found in [136].

4.2 Comparison between properties of zone plates and traditional lenses

The resolving power of a ZP is very similar to that of a conventional lens of the same diameter [137]. However, the image of a ZP can suffer from both chromatic and spherical aberrations when this lens is used at a frequency different from the one for which it was designed [138].

On the other hand, a ZP has higher-order foci in addition to the primary real focus (with a focal length l) at distances

$$l_i = l/(2i+1),\, i = 1, 2, \ldots \tag{II.8}$$

It also has an identical series of virtual foci, allowing the use of the ZP as a diverging element as well as a converging one (*Fig. 7*).

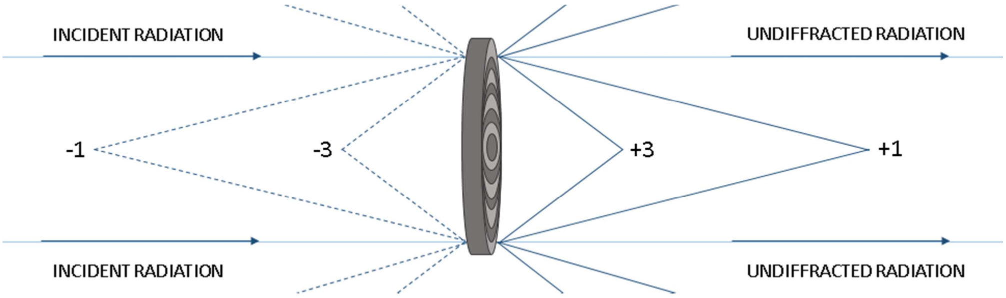

Fig. 7 Multiple and virtual foci in a ZP. Undiffracted radiation is commonly called zero-order of diffracted radiation. The focus “+1” is associated to the first order of diffraction. The focus “+3” represents a higher-order focus, corresponding to i = 2 in equation II.8. Foci “-1” and “-3” are the equivalent virtual foci of the positive ones.

4.3 Zone plates aberrations

Aberrations of a ZP have the same form as those of a conventional refractive lens. The discussion of this topic follows the work in [139]. It will be limited, for convenience, only at one dimension, but it is possible to extend it at a bidimensional case by multiplying each term by the appropriate power of cosθ, where θ is the azimuthal angle.

To obtain an image free from aberrations up to the third order, it must hold that:

$$m \leq \sqrt{2l/\lambda} \qquad \text{(II.9)}$$

However, for a fixed ZP external diameter, it is important to maximize the number of zones because this influences lens resolution, which corresponds to the minimum zone width, *i.e.* to the width of the more external ring.

The ZPs focus by interference and diffraction of waves, so they suffer from chromatic aberration. However, there is a short frequency range in which a ZP is achromatic. The full width at the half maximum (FWHM) of this band, $\Delta\lambda$, can be estimated by considering that the optical path of focalized radiation at the design wavelength λ has to be close to the one at a different wavelength λ_d, *i.e.* $m\lambda/2 = m\lambda_d/2 \pm \lambda_d/4$:

$$\Delta\lambda \cong \lambda/m \qquad \text{(II.10)}$$

Off-axis aberrations can be considered as a sum of coma, astigmatism and field curvature. If α is the angle between the principal ray and the optical axis, off-axis aberrations become manifest when their sum equals $\lambda/4$:

$$r_m^3\,\alpha/2l^2 - 3r_m^2\,\alpha^2/4\,l = \lambda/4 \qquad \text{(II.11)}$$

Fixing the value of a ZP external radius, the first zone diameter increases as the number of zones decreases. Thus, the angle between the principal ray and the optical α is high when the number of zones is low. In this condition, the second term of the sum, linked to astigmatism and field curvature, is dominant on the first term, due to coma aberration. The half field over which the image is diffraction limited can be set by

$$\alpha = (3m)^{-\frac{1}{2}} \qquad \text{(II.12)}$$

If coma dominates, the half field can be evaluated by

$$\alpha = (m\lambda/l)^{-\frac{1}{2}}(1/2m) \qquad \text{(II.13)}$$

It is worth pointing out that formulas II.9-13 describe wave front aberrations in terms of deviation from a diffraction-limited situation, as analyzed in [139], and not in terms of distribution of light according to geometrical optics.

5. Materials for terahertz diffractive devices

In most cases, THz sources emit radiation with a power in the order of tens of microwatts. Thus, lenses for THz waves should not absorb incoming radiation. Moreover, they should be hydrophobic because water exhibits several absorption bands in the THz spectrum. High resistivity floating zone silicon (HRFZ-Si) is a single-crystal silicon, with a resistivity exceeding 10 kΩ/cm. Below 1.5 THz, silicon resistivity is important because the presence of carriers due to impurities deeply influences absorption coefficient. In THz range, HRFZ-Si shows a refractive index essentially constant and equal to 3.418, which changes less than ±0.001 for frequencies between 100 GHz and 2 THz [140]. In the same frequency range, absorption coefficient is less than 0.05 cm^{-1}.

The THz high refractive index of the HRFZ-Si allows for thin devices. However, the high cost and crystalline nature of the material makes it suitable only for some applications. Additionally, the high refractive index results in significant Fresnel losses and pronounced Fabry-Perot effects.

In general, materials showing properties analogous to those of glasses or transparent polymers at optical frequencies are highly desirable for THz refractive optics. However, conventional glasses presents significant losses [141]. For example, highly disordered glasses, such as Pyrex and BK7, have an absorption coefficient of 13 cm^{-1} and 16 cm^{-1}, with a refractive index of 2.1 and 2.5 at 0.9 THz, respectively. In fact, ionic network modifiers, especially alkali oxides, are present in these glasses, increasing the microscopic polarizability of the glass. High purity amorphous silica and polycrystalline quartz (refractive index of 2.05 between 0.5 and 1.5 THz) are better, but losses as high as 1.2 cm^{-1} are found at 1 THz. Additionally, the requirement of a high purity affects the final price of devices fabricated in pure silica.

Table 5 Comparison of THz conventional materials refractive index and absorption coefficient at 1 THz.

Material	Refractive index	Absorption coefficient [cm^{-1}]	Reference
ABS	1.57	17.3	[142]
BK7	2.50	16	[141]
Dolomite (stone)	2.70	8	[143]
HDPE	1.53	13.9	[144]
HRFZ-Si	3.42	0.05	[140]
Paper (black)	1.54	11.14	[145]
Paper (green)	1.42	8.7	[145]
PET (Mylar)	1.712	20	[146]
PMMA	1.60	15.1	[144]
PP	1.51	2.09	[146]
PS	1.59	3	[144]
Pyrex	2.10	13	[141]
Silica	2.05	1.2	[141]
Teflon	1.45	1.76	[144]
TOPAS	1.52	0.4	[144]
TPX	1.46	0.6	[147]
Zeon COP	1.52	0.4	[148]

Therefore, there is a need of alternative materials showing the following properties: (i) low absorption losses, (ii) suitable refractive index, typically 1.4 - 1.7 to limit Fresnel losses, (iii) no dispersion, (iv) hydrophobicity, to prevent absorption of atmospheric vapor; (iv) processability, also in limited volumes for low cost affordable components.

A few polymers have been considered in the literature to fulfill some of these requirements. Between polymeric materials, there are, for example, high-density polyethylene (HDPE) [149], polytetrafluoroethylene (PTFE) or Teflon [150], polymethylpentene (TPX), TOPAS [151], and Zeonex® [148], [152] , two cyclo-olefin polymers.

Currently, 3D printable materials are employed in the low-THz spectrum, like HDPE, acrylonitrile butadiene styrene (ABS) or other plastics [142]. Paper [145], [153] and natural stone [143] are interesting alternatives in very dry environments where water absorption is not an issue. In *Table 5* a comparison of refractive index and absorption coefficient value, between the discussed materials, is presented.

In the design of ZPs and, in general, of lenses for THz frequencies, the choice of the material is often influenced by the refractive index value. A high refractive index increases Fresnel losses due to the huge difference of refractive index between the lens material and air. In this situation, an antireflection coating is needed. These coatings, in their simplest form, are thin films with two main characteristics: (i) their refractive index is equal to the square root of the refractive index of the material to be coated; (ii) their optical thickness corresponds to the ¼ of a chosen wavelength that will determine an antireflection operative band. This means that an ideal antireflection coating has an optical thickness of 75 μm at a frequency of 1 THz. Assuming the lens material is HRFZ-Si (refractive index of about 3.418), the coating material needs to have a refractive index of 1.849 and a physical thickness of 40.56 μm. Such material should also have low absorption at the operating wavelength. Moreover, the deposition process of the antireflection coating has not to introduce water molecules in the materials because water induces high THz absorptions.

Polymeric materials with a refractive index lower than 2 are often convenient choices as THz devices substrates. In this situation, losses due to material absorption have to be as low as possible. In fact, in most applications, the materials thickness has to be set proportional to the wavelength in the medium (*i.e.*, $t \propto \lambda_0/n$, where λ_0 is the wavelength in the vacuum and n is the material refractive index). Thus, as low the refractive index is as high the thickness of the structure will be, inducing an increment of absorption losses. The preferred range of refractive index for the UV-VIS-IR-THz is, usually, between 1.4 and 1.7.

6. Fabrication methods and techniques

Until the 1960s, lens technology was essentially based on three fabrication techniques: cutting, grinding and polishing. The main reason is that lenses were mainly manufactured for optics and were made of glass. A grinding process allows for obtaining a surface profile that is as close as possible to the desired shape. A final surface quality with tolerances in the nanometer range, *i.e.* deeply sub-wavelength, can be reached by polishing, which is a mechanical or chemical process. This level of control is needed to avoid scattering induced by roughness. The optimized form of these techniques is still used today for creating macroscopic devices with an excellent surface quality, in absence of micrometric features.

Meanwhile, with the massive progress of semiconductor processing and photolithografic techniques, (i) the mass production, (ii) the integration of different elements in the same device, and (iii) a reduction of production expenses became feasible. However, until 1960s, the minimum feature size was of the order of tens of micrometers [154].

For all these reasons, the first method to produce a ZP for optical applications was to draw a ZP on a white sheet of paper, filling alternate zones with black. Its photograph negative works as a ZP device [113]. This technique has serious limitations linked to the quality of the photographic film. Sizes and other characteristics of silver salt crystals and the quality of emulsion in the photographic film determine the sensitivity, contrast and resolution of the negative image. For example, a Velvia RVP100 from Fujifilm has fundamental particles between 200 nm and 2 μm of diameter and a corresponding film resolution of about 8 μm [155], which is more than 10 times higher than the optical wavelength.

It was only during 1980s that standard lithography became to offer feature size of about one micrometer. Moreover, dry etching techniques started to be employed to make micro-optical devices like, in particular, diffractive optical elements in glass or silicon. Lithography and etching are consolidated steps in ZP fabrication, but some issues remain in the fabrication of diffractive optics [156]: “The simplicity of repeated masking and etching makes it possible to fabricate complex binary optical elements cheaply and in volume, but the manufacturing technique does leave its traces in one significant drawback. It produces not the curved and angled surfaces of conventional optics but rather a series of flat steps that approximates the desired shape. Deviations from the ideal shape scatter light out of its intended path. Losses of even 5 percent at the surface of each binary optical element can seriously degrade the performance of optical trains containing half a dozen elements or more.”

In recent years, technology has definitely entered in the era of sub-micrometer features. The ZPs for X-rays or extreme ultraviolet radiation are, now, able to nano-focus waves by means of novel diffractive optical elements, such as photon sieve and modified Fresnel ZP [157].

Another revolution is currently undertaken: 3D printing manufacturing. Cutting, grinding, and polishing, such as photolithography and etching are subtractive methods that remove unwanted material to give a final device. The 3D printing is an additive method, because it fabricates a device layer by layer. It also has the great advantages to use a compact hardware and to be computer-controlled and integrated with several simulation softwares.

All discussed techniques are also well established for the fabrication of diffractive elements in the THz range. In particular, 3D-printing prototyping is often suitable at THz [151], [158], [159] because, in line of principle, only roughness higher than $\lambda/10$ can interfere with lens properties. It gives more tolerances than fabrication constrains in optics or X-rays regions. However, currently, materials suitable for 3D printing have absorptions at central THz frequencies larger than cyclo-olefins or HRFZ-Si [142]. Such absorptions could compromise lenses performance in that applications in which THz power is an important feature to preserve.

Another strategy for mass production of THz lenses is micro-powder compression [98]. This technique is very fast and cheap, but lens properties are not exactly repeatable, because they could locally change from device to device according to impurities and material powder distribution.

CHAPTER III

Methods for numerically design and fabricate polymeric zone plates

1. Introduction

Zone plates are able to focus electromagnetic radiation by diffraction. They are highly chromatic lenses and are suitable for all those applications in which the main issues are (i) the achievement of the lowest radiation attenuation in the focal area, (ii) a good resolution, and (iii) the integration in compact devices.

Phase-reversal ZPs can be a good choice in the THz range. In particular, binary ZPs have a low diffraction efficiency (of about 40.5%), but are simple to fabricate. On the other hand, in multilevel ZPs several rings of different thickness and width are fabricated as sub-zones. These sub-zones all together perform the phase shift of two adjacent rings in a binary ZP, and an efficiency of 68.4% or more is obtained, as illustrated in *Fig. 8*. In a multilevel ZP with four levels, diffraction efficiency is 81.1%. However, manufacturing becomes complicated as the number of levels increases. Moreover, multilevel ZPs are more susceptible to damage than binary ZPs.

For these reasons, a new configuration of ZP in the THz range has been devised and investigated in this work. It consists of a stacked version of two binary ZP. In general, when two ZPs are placed within each other’s near field zone, they act as a single lens. For this reason, in this work, this kind of ZP has been realized on the same device, by reproducing a binary ZP on both sides of a substrate plate. This configuration will be called ‘phase reversal double-sided ZP’, or simply ‘double-sided ZP’.

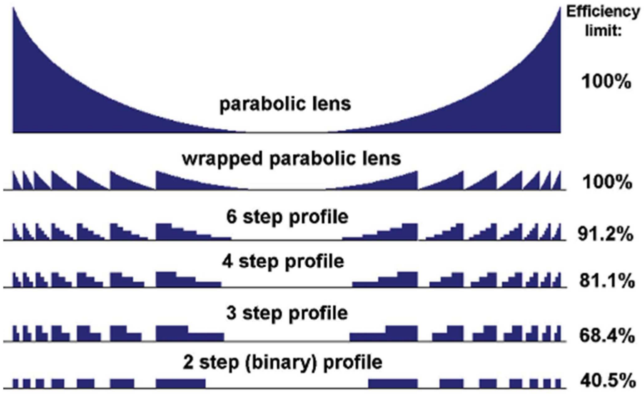

Fig. 8 Diffraction efficiency by increasing the number of discretization of zones phase step [117].

A ZP stacking and a double-sided ZP have been already employed for focusing X-rays with the aim to increase the field intensity in the first-order focus area [160]. However, this device has not been considered yet at THz frequencies. The main difference between stacked or double-sided ZPs known in the scientific literature and this new one for THz applications is in the zone thickness, *i.e.* in the phase shift introduced by zones. The THz double-sided ZP is made by two binary phase reversal ZPs and each ZP introduces a π/2 phase difference between polymeric material and air. The idea is that the first ZP shifts the phase of π/2 and the second ZP, placed in previous ZP near field, introduces another shift of π/2. In this way, the total phase shift of the incident radiation at the end of double-sided ZP stays π. On the contrary, in stacked and double-sided ZPs from literature, the total retardation at the end of the device is higher than π. Moreover, the ZPs for X-rays in the stacked configuration are sometimes metallic Fresnel ZP and not dielectric phase reversal ZPs.

From now on, we shall refer to binary and multilevel ZPs by assuming they are all phase reversal binary and multilevel ZPs, for need of brevity. The aim of the present work is to investigate the focusing properties of a THz double-sided ZP and to compare its lens behavior with a binary ZP and a four-levels (multilevel) ZP. For doing that, a thorough numerical investigation of the proposed lenses is needed for the design and their optimization (Sec. 3). On the basis of numerical results, some ZP prototypes have been fabricated by employing a suitable technique, as discussed in section 4.

2. Numerical methods in computational electromagnetic

Any numerical analysis or optimization has the goal to achieve a sufficient accuracy with a minimum effort, where the effort is usually the computational cost in terms of computational time and memory requirements.

In general, there are several aspects that could influence the choice of a computational method: (i) the electromagnetic problem may involve boundary conditions difficult to treat; (ii) materials could have nonlinear, anisotropic, or non-homogeneous characteristics; (iii) the problem could have a length scale of several wavelengths in vacuum; (iv) the problem could contain a combination of length scales due to its physics or geometry; (vi) the excitation can be non-stationary; (vii) the material can be frequency dispersive [161].

In some situations, one method could be competitive for a portion of the problem and, at the same time, another algorithm could be better suited for the remaining parts. In these situations, for example, a so-called hybrid method could be developed and applied. However, such methods are challenging to construct while preserving all important properties of Maxwell's equations.

For modeling electrically large systems, *i.e.*, systems in which the extension in the 3-D space corresponds to many wavelengths, it could be useful to compare how the number of floating-point operations and the memory requirements scales with the electromagnetic frequency f. *Table 6* summarizes the scaling with frequency for a given computational domain size for two main class of computational methods.

Table 6 Dependence of the number of operations to the frequency f and the number of iterations N_{it} [161].

	Differential equation methods	**Integral equation methods**
2-D space	f^3	$N_{\mathrm{it}} f^2$
3-D space	f^4	$N_{\mathrm{it}} f^4$

Differential equation methods solve Maxwell's equations in their differential formulation. They can be used for computations in frequency-domain as well as in time-domain. This choice does not influence the relationship between the number of operations and the frequency of the problem. However, the time-domain method requires a higher computation time than the frequency-domain method but it returns a complete frequency spectrum analyses. Conversely, a standard frequency-domain method returns only one computation, *i.e.* for a single frequency value. For broadband studies, the frequency domain method needs to be applied to a set of chosen frequencies. An example of a method based on the solution of differential equations is the finite element method (FEM) that will be briefly introduced in the following section.

Integral equation methods are based on the integral representation of Maxwell's equations. They are characterized by a lower number of unknowns than differential methods and are particularly suitable for electromagnetically large problems. Moreover, they are preferable choices when $N_{\mathrm{it}} < O(f^2)$ [161]. A typical example of integral equation method is the method of moments (MoM) [162].

Moreover, as already introduced, numerical methods can be applied in time-domain (TD) or in frequency-domain (FD). The TD methods usually feature a Cartesian grid and an explicit time integration scheme. The electromagnetic field propagation through a structure is computed by means of multiplications between a matrix vector and a specific time step. The larger the time step, the shorter the simulation time. The simulation time and the memory requirement are linearly proportional to the number of mesh points. For these reasons, TD solvers are usually employed for solving electrically large structures, with several geometrical details. Additionally, TD methods allow the derivation of FD information by applying Fourier transforms to the time domain signals. It is possible to obtain fields for various frequencies in one simulation run.

Conversely, FD solvers usually have an approach based on a large system of linear equation. The computational domain can be discretized for obtaining the solution at one value of frequency, but the presence of a structured or unstructured grid is not important as in TD methods. There are two main approaches for solving the equation system: direct and iterative solvers. A direct solver works directly on the system of equations coming from the domain discretization. It allows for a parallelization of the computation, reducing the calculation times. However, the memory requirements are very high because they are proportional to the square value of the number of elements in which the domain is discretized. Iterative solvers require reduced memory availability, but the computation time increases. Frequency domain solvers are suited to solve infinite periodic problems, thanks to the availability of periodic boundary conditions.

A summary of the main subdivisions of the computational electromagnetic problems is presented in *Fig. 9*. In the next section, such methods are discussed in the specific context of the numerical design of diffractive lenses.

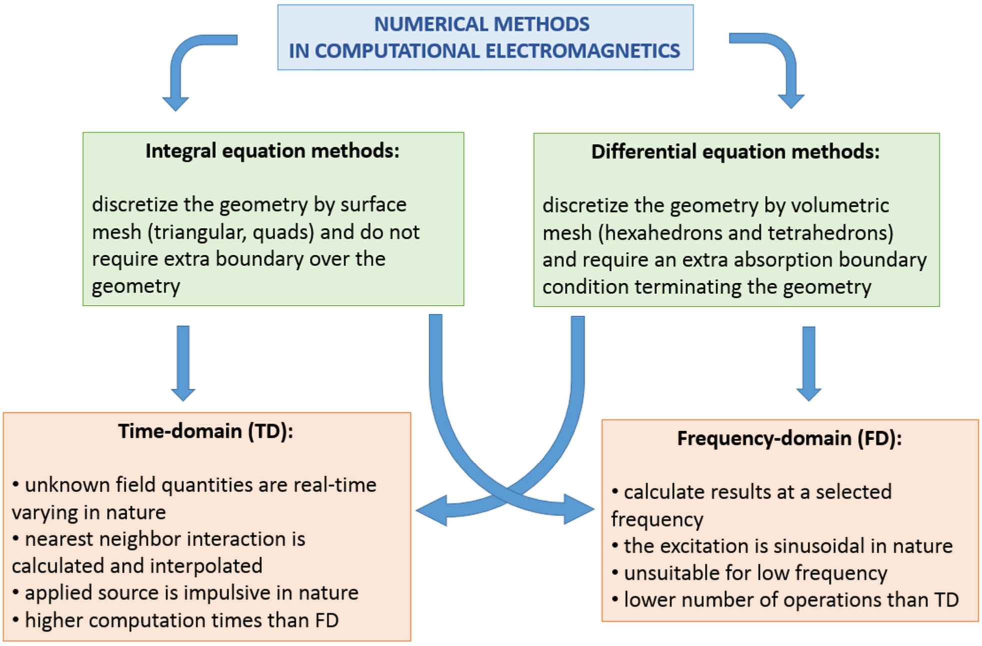

NUMERICAL METHODS IN COMPUTATIONAL ELECTROMAGNETICS

Integral equation methods:

discretize the geometry by surface mesh (triangular, quads) and do not require extra boundary over the geometry

Differential equation methods:

discretize the geometry by volumetric mesh (hexahedrons and tetrahedrons) and require an extra absorption boundary condition terminating the geometry

Time-domain (TD):

- unknown field quantities are real-time varying in nature
- nearest neighbor interaction is calculated and interpolated
- applied source is impulsive in nature
- higher computation times than FD

Frequency-domain (FD):

- calculate results at a selected frequency
- the excitation is sinusoidal in nature
- unsuitable for low frequency
- lower number of operations than TD

Fig. 9 Overview of the numerical approaches to the electromagnetic problems.

3. Numerical investigation of zone plates for terahertz focusing

Numerical simulations are performed with the aim to take into account material losses and geometrical tolerances due to the ZP fabrication process (for details about fabrication, see Ch. III Sec. 4). In fact, it is difficult to investigate the ZPs behavior in presence of such constrains by only theoretical formulas presented in chapter II section 4.

The ZPs are simulated by COMSOL Multiphysics® [163], a commercial software which employs a finite element method (FEM) of simulation in the FD. All ZPs investigated have a radial symmetry: it makes it possible to simulate the full-wave propagation through the lens structure employing a simplified 2D-axisymmetric model. After the ZP, a free space 50 mm long is accounted for wave propagation. At the frequency of 1 THz, thanks to the radial symmetry, the computational domain is a 2-D space of about $43\lambda_0 \times 167\lambda_0$, where λ_0 is the wavelength in the vacuum. For this reason, a workstation with 64 GB of main RAM has been needed for performing the ZPs numerical simulations.

In a FEM, the object under investigation is divided into subdomains. Each subdomain is described by a set of simple equations. All these equations are, then, recombined into a global system of equations that is solved starting from initial values of the whole system and taking into account boundary conditions of the electromagnetic problem.

Moreover, for validating the 2D-axisymmetric assumption, the 2-D FEM simulation has been compared with a 3-D full-wave simulation by means of another commercial software, CST Microwave Studio® [164], employing a finite integration technique (FIT) to numerically solve electromagnetic field problems in TD.

The major advantage of a FEM is its high geometrical flexibility for modeling complex geometries with discontinuous media parameters. However, FEM discretization requires large storage memory due to the number of unknowns. On the contrary, a FIT is simple to implement and it is able to perform an efficient parallel computing. However, the time step depends on the grid size. For those applications, in which a very small mesh size is required, the time step becomes significantly small. It results in longer simulation time.

It also has to take into account that COMSOL Multiphysics® employs a method in FD, while in CST Microwave Studio® a TD solver is selected for lenses simulation. As discussed above, with TD computation, only one simulation is required for a broadband solution with a fine frequency resolution. However, diffractive lenses are chromatic devices and do not need of broadband studies, which are time consuming.

About RAM occupancy, for example, in a 8 GB RAM workstation, it is possible to solve an electromagnetic problem of about 40 wavelengths in each directions by employing a TD technique, while a frequency method is restricted to about 10 wavelengths [165].

In ZP lenses design, some numerical studies have been considered: (i) the choice of the right material; (ii) the choice of the number of zones; (iii) the behavior at frequencies different, but close, to the design one; (iv) the comparison with a conventional refractive lens.

3.1 Material choice

The starting point of the numerical study is the choice of a suitable material. The only commercially available binary ZPs are made of HRFZ-Si [166]. It is a material with very low absorption at THz and simple to process by photolithography and etching. However, wafers are expensive due to energy and time consuming crystal growth process. Furthermore, 43.9 µm deep trenches need to be etched to provide π phase difference at 1 THz. These are usually made by deep reactive ion etching (RIE) in a suitable plasma (typically a mixture of CF_4 and SF_6), which is material, time and energy intensive process. Moreover, its refractive index of 3.416 at 1 THz is quite far from the refractive index of air, which is close to 1. Hence, a ZP made of HRFZ-Si needs of an antireflection coating to limit Fresnel losses. The solution devised in this work employs a polymeric material (i) with a lower refractive index, (ii) lower cost, (iii) easy to process, and (iv) with very low absorption at 1 THz. Zeonex® E48R is a specialty cyclo-olefin by Zeon Corporation which satisfies the above requirements. In fact, it has a refractive index of 1.516 at 1 THz. A 2 mm thick slab of this material has a transmittance larger than 0.8 up to 1 THz. In practice, it behaves in the THz range nearly as well as glass does in the visible range.

However, minor absorption losses do exist at the targeted frequency. So a pure phase-control behavior cannot be assumed. Hence, a FEM simulation has been performed in order to compare the focusing properties of two binary ZPs with same geometry, but made by different materials: one by Zeonex® and one by HRFZ-Si. Both Fresnel and absorption losses are fully accounted for either cases.

3.2 Number of zones

Another important characteristic of a ZP is the number of zones. It influences the focal length as well as the focal spot resolution. A binary ZP, with a fixed external diameter of 25.4 mm corresponding to a typical size for common 1” lens holders, is evaluated by changing the number of rings from 9 to 42. All these FEM simulations are performed at 1 THz, which corresponds to a wavelength of about 300 µm. All ZPs are excited under the same condition of plane wave illumination. When a binary ZP is made of 9 zones, the smallest ring width is larger than the wavelength of focused radiation. According to theory (compare Ch. II Sec. 4), it determines a poor lens resolution. By increasing the number of rings, the resolution increases.

3.3 Frequency behavior

All ZP lenses have been designed at the frequency of 1 THz. The main reason of this choice is in the definition of "THz gap" itself, already discussed in chapter I. In fact, the most challenging band of the THz field in terms of technological development is between 1 and 3 THz because it falls in the border between the electronic-based and the optical-based technological fields (*Fig. 10*).

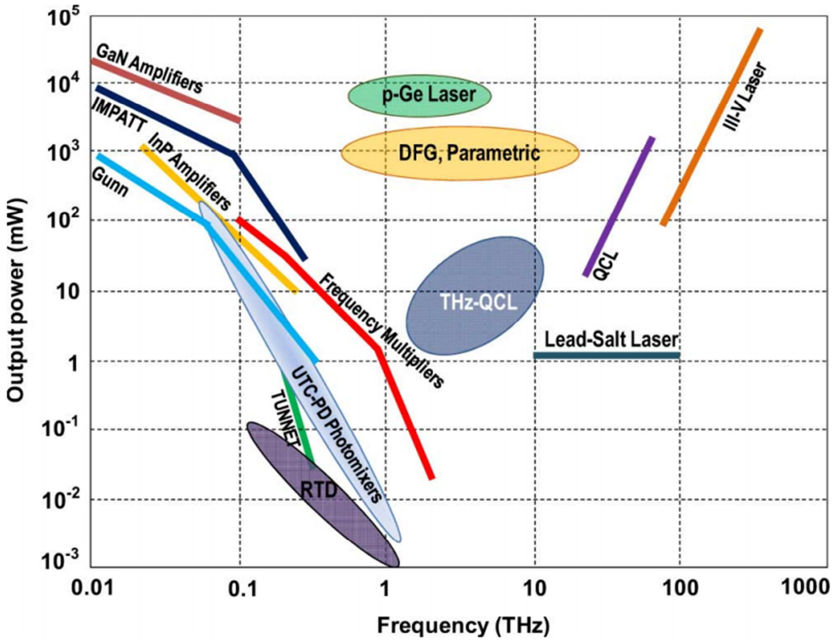

Fig. 10 Comparison between sources in terms of frequency and output power. This plot is from [5] and it is based on data until the year 2011. For additional information about THz sources until the year 2017, compare *Table 1*.

For this reason, the development of lenses working at 1 THz with an improved resolution if compared to the state-of-art and with an affordable production cost could be considered as an effort to contribute to the filling of the gap. In fact, from this point of view, lenses are devices often employed to improve antenna sources directivity, *i.e.*

lenses are able to concentrate the power density of the emitted radiation in a single direction.

Moreover, ZPs have a design perfectly scalable at almost every frequency value, as discussed in chapter II. Thus, the choice of a working frequency of 1 THz could be also considered as the select of a round number for easily conveying the design concept. Some examples of devices based on the ZP and operating at frequency values different from 1 THz can be found in chapter VII.

A method in the FD, such as the one employed by COMSOL, has been selected for the numerical analysis of the ZPs at the frequency of 1 THz. It is a reasonable choice for evaluating the behavior of diffractive planar elements, which are highly chromatic and work in a narrow band of frequencies, centered in their design frequency (compare Ch.II Sec. 4.3). However, an additional investigation of ZPs behavior from 500 GHz to 1.2 THz with a step of 100 GHz has been performed.

3.4 Comparison with a conventional refractive lens

The behavior of a refractive lens and a binary ZP can be numerically obtained by FEM simulations. It will help to understand focusing properties of a ZP by directly comparing it with a conventional refractive lens. The refractive and the diffractive devices have both the same maximum thickness of 2 mm and are illuminated by a plane wave at the frequency of 1 THz.

4. Fabrication

The fabrication process has been selected on the base of the ZP design and the numerical optimization process. In optics, the lens fabrication can be operated by employing machining or non-machining techniques [167]. Single point diamond turning (SPDT), slow tool servo (STS), fast tool servo (FTS), and three-axis micro-milling (MM) are machining techniques able to produce high quality optical devices. In particular, SPDT is a two-axis lathe technique and needs a manual positioning over the third axis. STS and FTS are fully automated techniques, but are limited by diamond tool relief angle. MM overcomes most limitations on lens geometries. It makes it possible to produce several shapes including aspheres, asymmetric lenses and other freeform optics, but it is a slow technique. These techniques can be compared to non-machining ones (see *Table 7*), such as grayscale lithography, thermal reflow, inkjet printing, and non-cutting techniques, as laser direct writing and deep lithography with protons.

Table 7 Comparison between lenses fabrication techniques [167].

Fabrication technique	**Automatic**	**Arbitrary shapes**	**Sag limit (mm)**	**Dimensions limit (mm)**	**Edge slope (°)**	**Fabrication rate**
SPDT	No	Yes	No	No	0-90	5-25 mm/min
STS	Yes	Yes	No	No	0-40	0.1 mm/min
FTS	Yes	Yes	0-6	No	0-40	0.25 mm/min
MM	**Yes**	**Yes**	**No**	**No**	**0-90**	**0.4-1.25 mm/min**
Thermal reflow	Yes	No	0-2	0.005-2	0-90	0.5 min
Microjet printing	Yes	No	0-5	0.02-5	0-180	0.5-5 mm/min
Grayscale lithography	Yes	Yes	0-0.06	>0.0006	0-90	1.33 min

A three-axis milling technique is chosen for ZPs fabrication because it offers a shape control with tolerances suitable for THz frequencies. In fact, ZPs are designed for working at a wavelength of 300 μm and errors in geometrical dimensions lower than 30 μm do not influence lenses performance. Furthermore, only few ZP prototypes are fabricated and the slow rate of the milling process is not an issue for research purposes. For these reasons, all polymeric ZP lenses subject of this work have been fabricated by milling a 2 mm thick slab of Zeonex®. In particular, it is a subtractive method of fabrication, in which a rotatory cutter removes material from a workpiece on fixed structure. Milling cutters can advance in every direction and at every angle. Cutters can be of very different sizes and shapes, according to the material and the final machined profiles. A set of high-speed steel (HSS) milling cutters with end diameters from 1.4 mm to 0.2 mm have been employed for THz ZPs manufacturing (*Fig. 11*).

This technique can produce structures with a tolerance of about 10 μm, in the plane perpendicular to the cutter axis, and of about 5 μm, in the parallel direction.

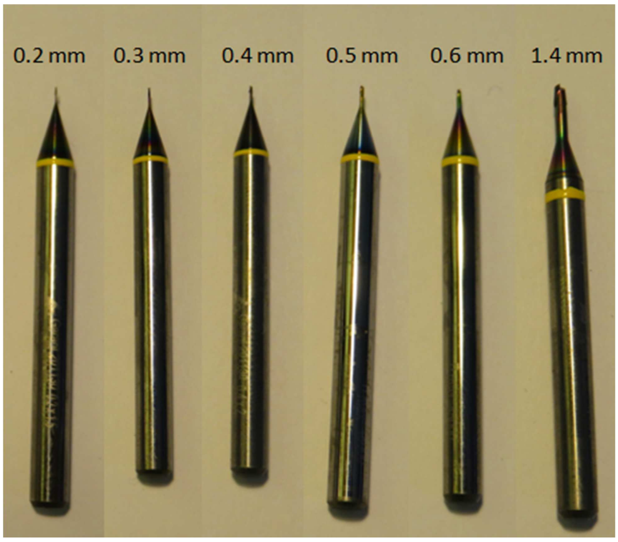

Fig. 11 Milling cutters used throughout this work for ZP fabrication. The diameter of each cutter is indicated.

CHAPTER IV

Numerical investigation and fabrication of terahertz zone plates

1. Material choice

Two binary ZP made of different materials (*i.e.*, one of Zeonex E48R and one of HRFZ-Si) are numerically compared, as shown in *Fig. 12*. The two ZP have same geometrical constrains except for zone thickness, which depends on material refractive index. Material losses, already discussed in Ch. II Sec. 5, are included.

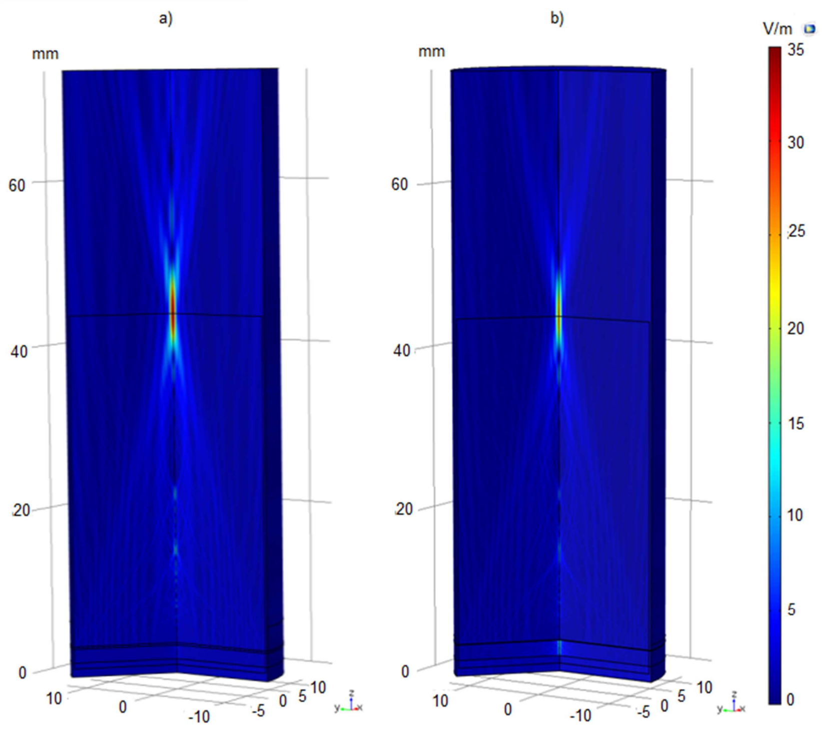

Fig. 12 Comparison between the focusing properties of a binary ZP made of a) Zeonex E48R and b) HRFZ-Si. A plane wave of 1 V/m is incident perpendicularly to both lenses. The E-field modulus is represented in a 3-D space, filled by air. Both ZPs, ending at z = 2 mm, have same external diameter, number of zones and thickness.

Most of the focusing parameters are the same for both ZP. From *Fig. 13*, ZPs have a focal length of 40 mm, for the primary focus. They also show two secondary foci at 10 mm and 17.5 mm from their external surface. The ZPs depth of field can be considered as the full width half maximum (FWHM) of the curves representing the square module of the E-field at 1 THz along the optical axis. It is equal to 5.3 mm ± 0.1 mm for both lenses.

The main difference is in the value of the E-field square modulus: at the focus of the Zeonex® ZP, it is twice as high as for the HRFZ-Si ZP, thanks to the lower refractive index of the polymer and lacks of antireflection coatings. Zeonex E48R is affordable, easy to processing, has low absorption at THz, and does not need a coating for avoiding reflection losses due to refractive index mismatch with air. It is perfectly suitable for the fabrication of THz devices and, in this situation, it results a better choice than HRFZ-Si.

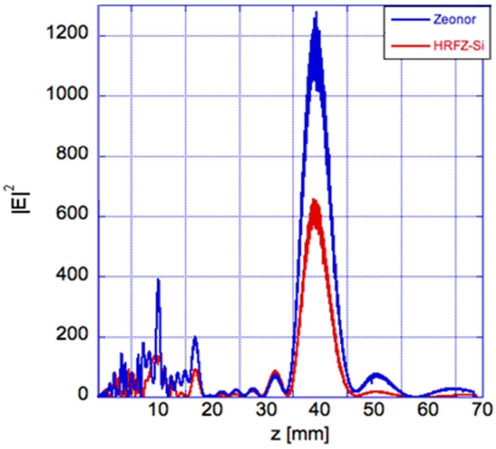

Fig. 13 Comparison between the focusing properties of a binary ZP made of Zeonex E48R (blue line) or HRFZ-Si (red line). A plane wave of 1 V/m is incident perpendicularly to both lenses. *z*-axis is the perpendicular one to the ZP plane. *z* = 0 mm corresponds to the end of the lens, where a free space, filled by air, starts. Both ZPs have the same external diameter, number of zones and thickness.

2. Number of zones

The number of zone is chosen by taking into account: (i) resolution, linked to the width of the most external zone, (ii) easy fabrication, and (iii) losses due to a high number of zones with dimensions comparable to operation wavelength. Moreover, as discussed in Ch. II Sec. 4.3, there is a limit in the number of zones due to the introduction of third order aberrations. Zones number has to be less than 16 for a binary ZP with a design focal length of 40 mm at 1 THz.

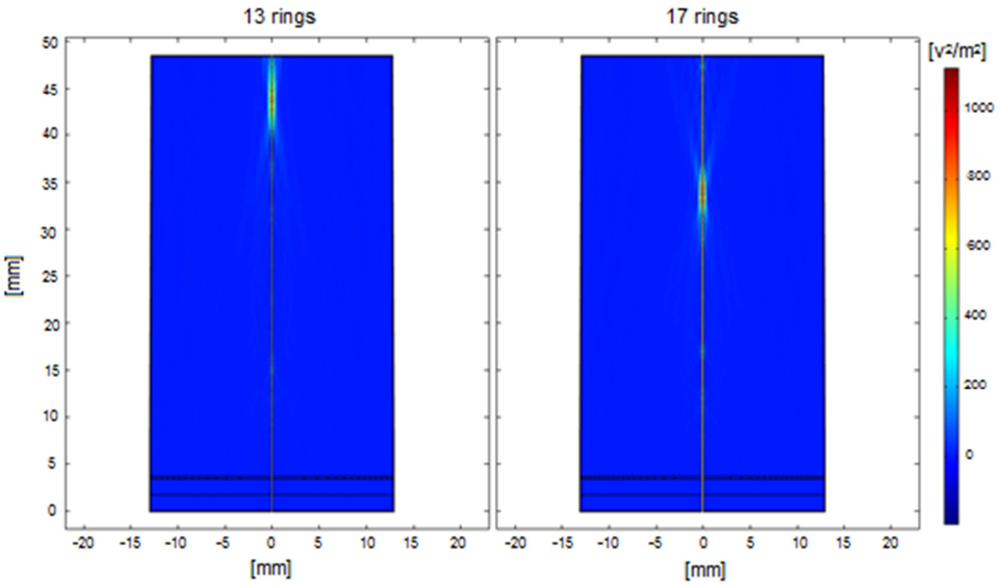

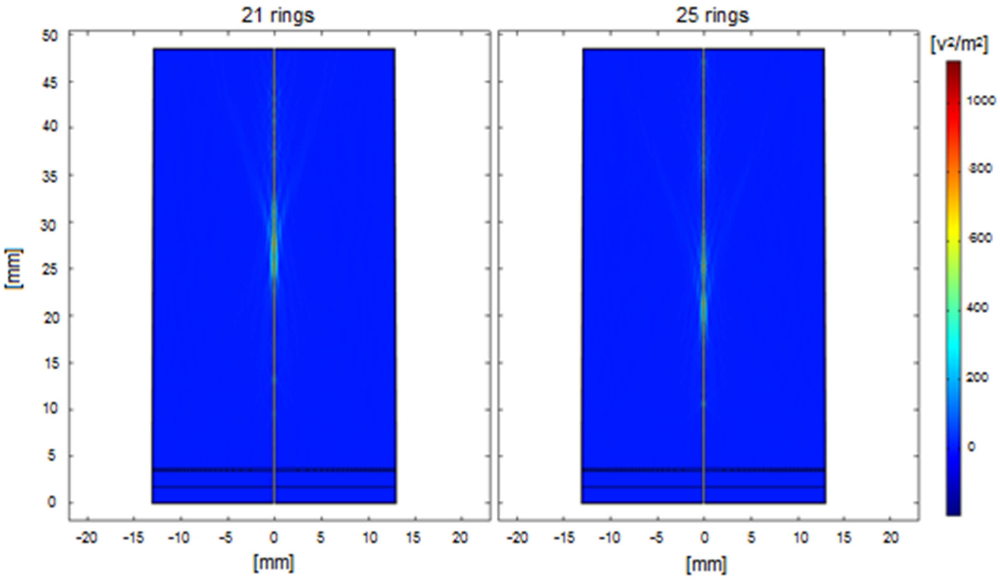

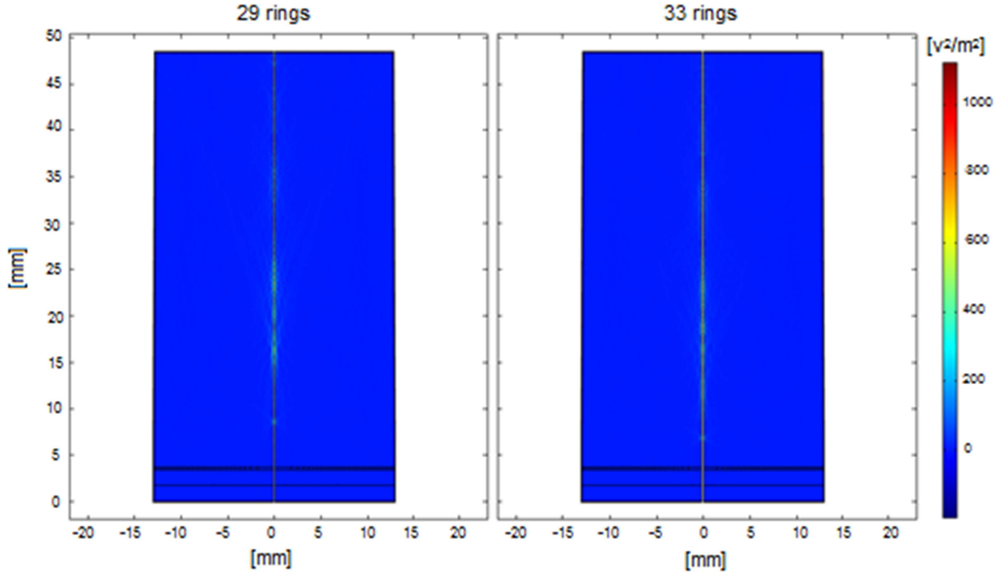

Fig. 14 Focusing behavior of a binary ZP with a fixed diameter and an increasing number of ring zones. A plane wave of 1 V/m is incident perpendicularly to the lens. All color maps represents ZP central section and optical axis, *z*, where THz radiation, coming from *z* = 0, is focused.

Because of these constrains, a suitable number of zones is 13. In fact, the resolution decreases when the number of zones is below 13, while the lens introduces losses and aberrations above it.

A numerical study of a binary ZP is performed by fixing the external diameter at 25.4 mm and increasing the number of zones, with the aim to elucidate how the number of zones can affect the ZP focusing behavior. The THz power density in the plane perpendicular to the lens and passing through the optical axis is shown in *Fig. 14*. The focal length decreases by increasing the zone number, but the ZP is no longer able to focus incident radiation.

3. Frequency behavior

The ZPs are highly chromatic lenses. Their frequency behavior depends on the number of rings and on the central frequency at which they work (for more details, see Ch. II), but it is independent from the ZP configuration, *i.e.* binary, multilevel or double-sided. The ZP configuration influences the lens resolution and its diffraction efficiency. The numerical study of the multilevel ZP designed for operation at 1 THz is presented in

Fig. 15 for the frequency band 0.5 – 1.1 THz, which has been sampled with a step of 100 GHz. Chromatic behavior is confirmed: each wavelength of the incident THz radiation is focused at a different focal length, with a different intensity in focal area, and with a different depth of field.

For this reason, a ZP can be also seen as a spatial and frequency filter [168].

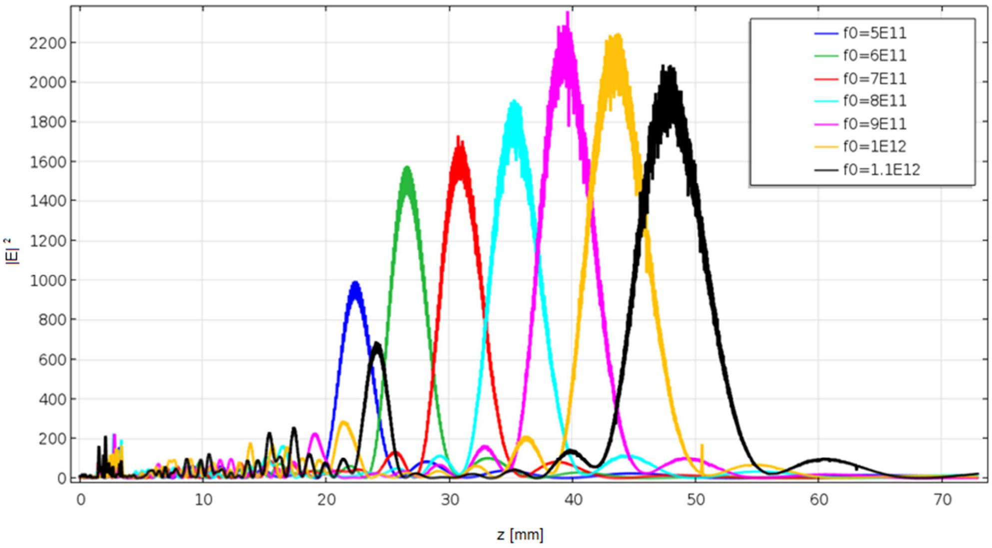

Fig. 15 Frequency behavior of a multilevel ZP from 0.5 THz to 1.1 THz with a step of 0.1 THz. z-axis is the perpendicular one to the ZP plane. Minor peaks in the square modulus of the E-field for z from 1 mm to 3 mm are related to multiple reflections within the 2 mm thick slab in which ZP is fabricated (no antireflection coating is used). For $z < 1$ mm and $z > 3$ mm, a free space filled by air for THz waves propagation is considered.

4. Comparison with a conventional refractive lens

A biconvex lens is numerically studied for evaluating the behavior of a ZP in focusing THz radiation instead of a more conventional refractive lens. The biconvex lens is designed with the constraint that its maximum thickness is equal to ZP thickness, *i.e.* 2 mm. Biconvex lens material is Zeonex E48R and material losses are taken into account, as done for the simulation of the multilevel ZP.

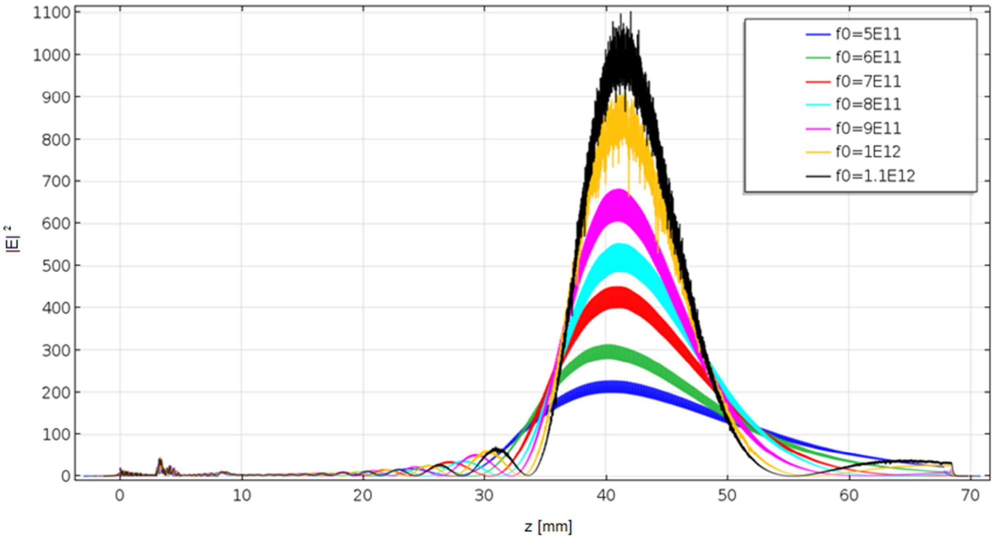

Fig. 16 Frequency behavior of a biconvex refractive lens from 0.5 THz to 1.1 THz with a step of 0.1 THz. z -axis is the lens optical axis. Extremely short peaks in the square modulus of the E-field for z from 2 mm to 4 mm are related to few multiple reflections inside the lens. For $z < 2$ mm and $z > 4$ mm, a free space, filled by air, for THz waves propagation is considered.

As can be seen by comparing *Fig. 15* and *Fig. 16*, a biconvex lens is able to focus THz waves with different wavelength at the same focal length. Moreover, it has a higher focal depth, which is more than 9 mm at 1 THz instead of 5.3 mm of the multilevel ZP. On the other side, the multilevel ZP is able to concentrate THz radiation in the focus with an intensity that is twice as high as for a biconvex lens. It makes ZPs a more valid lens than a conventional refractive lens for THz narrowband applications.

5. Conclusions about the numerical investigation and zone plates fabrication

As a result of the numerical studies already discussed, a ZP configuration which consists of 13 Fresnel zones has been selected as a promising diffractive lens structure. Moreover, the Zeonex E48R has been revealed as a very suitable material for THz lenses.

The ZP lenses prototypes are fabricated with the 3-D MM technique described in chapter III section 4 and are shown in *Fig. 17*. They have an external diameter of 25.4 mm (1 inch) and consist of 13 rings for the two binary configurations (*b)* and *c)* in

Fig. 17) and 28 rings at four different levels of deepness for the multilevel ZP (*a)* in *Fig. 17*).

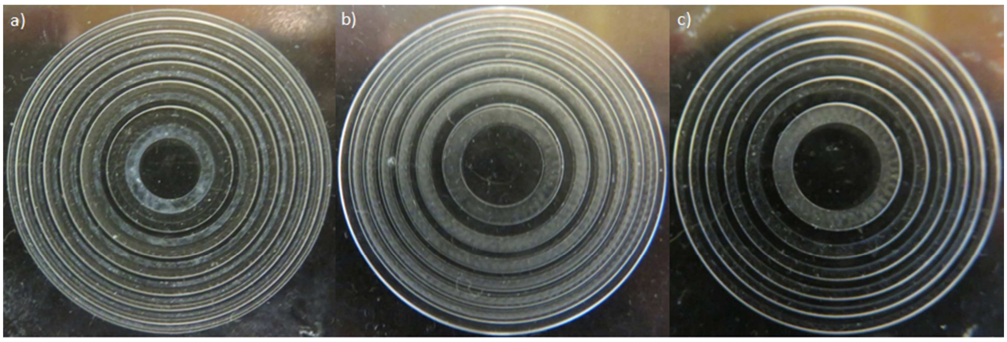

Fig. 17 Fabricated ZP lenses: a) multilevel ZP, b) double-sided ZP, c) binary ZP. The little roughness perceived in visible light is introduced by milling process, but it does not affect the lens behavior at THz because it is several orders of magnitude below the wavelength at 1 THz.

In the following chapter, some methods required for the experimental characterization of such ZP prototypes will be outlined and deeply discussed.

CHAPTER V

Methods for the experimental characterization of diffractive lenses at terahertz frequencies

1. Introduction

The numerical studies discussed in the previous chapter have been instrumental in the design of ZPs with the specific aim of elucidating the elements that contribute to the increase of their performances with respect to currently used diffractive lenses. It is worth reminding that, in contrast to lenses designed for the visible range where losses are comfortably neglected, for THz range these must be taken in the account. Hence, the lossless formula provided in chapter II section 4 are not fully adequate.

Nevertheless, simulations could not fully describe the real operational conditions. In fact, some idealizations are usually necessary to keep the problem within computational manageable limits. In the specific case, a linearly polarized plane wave, impinging normally to the lens, is used as excitation both in the analytical and numerical problems discussed in the previous chapters. On the other hand, the experimental conditions are far less simple because the wavefront of the incident radiation is not an ideal plane wave. Hence, the lens performance cannot be confirmed without a prior knowledge of this wavefront.

In this chapter, the calibration of the set-up available for ZPs characterization is presented after a brief overview on experimental set-ups for THz measurements. The calibration consists in the acquisition of shape, dimensions and intensity distribution of the THz beam emitted by the photoconductive antenna and its hemispherical silicon lens. As a matter of fact, upon specific requests made to the instrument manufacturers, they explicitly replied that the radiation pattern of the emitting THz antenna was unknown to them. This additional experimental step influenced the way in which it was more convenient to perform the measurements on ZP lenses. Moreover, a detailed description of the experimental configurations and methods employed in the ZPs characterization will be outlined.

2. Set-ups for terahertz metrology

In chapter I, several THz sources, detectors and components have been introduced and discussed. On the basis of them, a variety of set-ups for THz spectroscopy had been developed from both microwave and optics communities (*Fig. 18*). The main distinction that can be operated between available THz spectrometers is between TD and FD set-ups. In fact, some THz set-ups employ spectroscopic techniques which allow for conducting measurements directly in the FD via, *e.g.*, frequency sweeping or broadband exposure. Examples of set-up for measurements in FD are vector network analyzers (VNAs) or IR-Vis-UV spectrometers. Conversely, measurements in the TD can be performed: (i) indirectly, via interferometry, as made by Fourier-transform infrared spectrometers (FTIRs), or (ii) directly, such as the THz TDS, which is based on a sampling with an ultrafast laser pump-probe configuration [169].

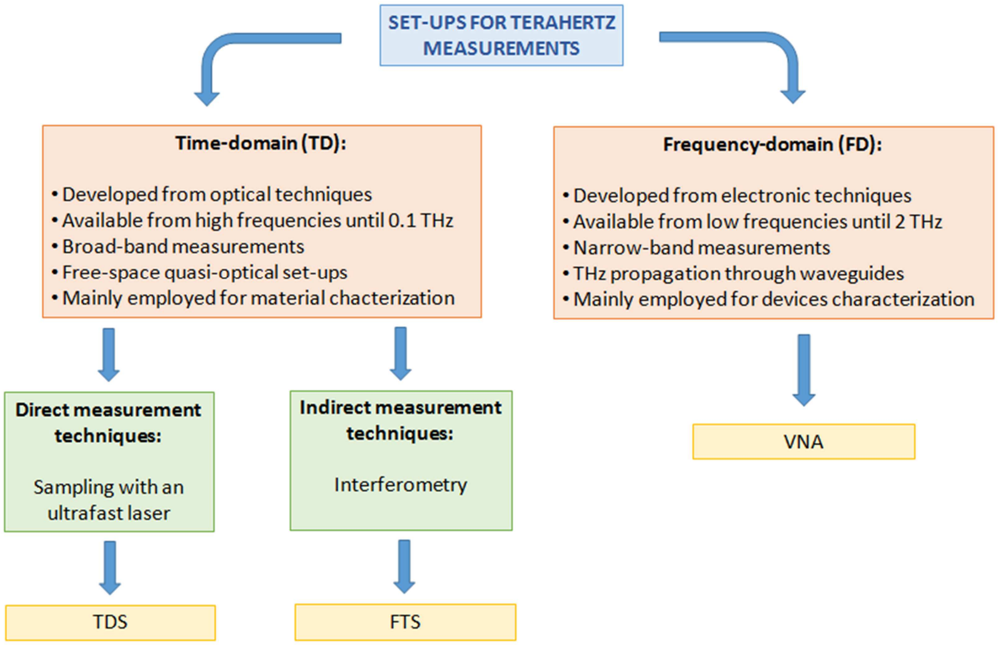

Fig. 18 Overview of the experimental approaches to the THz measurements.

2.1 Set-ups employing time-domain methods

The TDS is the premier technique for THz measurements due to its high dynamic range (compare *Table 3* for specifications about the commercially available TDSs) and its ability to detect both amplitude and phase of the transmitted THz radiation. In material science, for example, these informations can be translated in the measurement of the absorptions and the refractive index [170]. However, they could be also useful in the characterization of quasi-optical devices (introduced in Ch. I Sec. 4.2). Even if a detailed description of a TDS set-up will be made in section 3, it could be of interest to anticipate a brief explanation of a pump-probe TDS. The THz TDS system is triggered by an ultrafast laser with pulses of duration usually shorter than 100 fs. The laser beam is split into two: the majority of the power is employed in THz generation; a minor fraction is used as a probe. The probe pulses can be arranged for temporally and spatially overlapping the THz pulses, in the way to recombine with them on the detector (coherent detection). The resulting measured signal is proportional to the product between the probe pulses intensity and the THz field [171].

THz TDS emitters and detectors could be of photoconductive type or of optical rectification type [170]. Any combination of them between emitter and detector may be employed; however, commercial set-ups (as the ones compared in *Table 3*) mostly have photoconductive emitters and detectors.

The Fourier transform spectroscopy (FTS) operates over a larger bandwidth and has a higher frequency resolution than TDS. However, it enables only the acquirement of the optical intensity and its dynamic range is significantly smaller than TDS [170]. The FTS is an older and more established technique than TDS, but it is employed mainly for measurements at frequencies above 15 THz.

2.2 Set-ups employing frequency-domain methods

VNAs employ a radically different measurement modality from the TD spectrometers. In fact, VNAs are usually configured for measuring the complex scattering of electromagnetic signals impinging on a test device. For doing that, the VNA utilizes ports, *i.e.*, interfaces through which the signal going to and coming from the element under test can flow. The VNA measures the magnitude and phase of the signals at each port and operates a ratio of these quantities, presenting the scattering coefficients for a structure under test. These coefficients are often called scattering parameters or S-parameters. The measurement of the S-parameters allows a direct computation of other parameters. For example, the propagation delay through the test object can be obtained by differentiating the transmission phase with respect to the frequency [171].

The VNAs for THz frequencies are usually instruments with two ports. It means that they are useful for measuring the reflection and transmission behavior of one-port and two-port THz structures, such as antennas, filters, amplifiers and signal-transmission structures. In fact, VNAs are mainly employed for testing devices at THz frequencies, while TDSs are usually devoted to materials characterization.

Even if the VNAs manage THz radiation in propagation mode through a waveguide (see Ch. I Sec. 4.1), they can also operate with THz beams in free space. In this configuration, the VNAs can operate measurements similar to TDSs [172]. A comparison between a free-space VNA and the TDS performance in the measurement of the complex relative permittivity in the frequency range 0.22 – 0.33 THz can be found in [173]. The VNA employs a method in FD and the limitations in the measurements frequency depend on the waveguide size. Conversely, the TDS operates in TD and can operate measurements in a broad frequency range. Moreover, VNA time resolution is worse than TDS and the VNA may result unsuitable for precisely separating multiple reflections in the material under test. On the other hand, in the low THz range, the TDS shows a SNR worse than the VNA, resulting in a lower accuracy of TDS measurements. Authors suggest to select the measurement method by essentially considering the accuracy and the frequency range of the measurement. However, according to their data, the maximum difference between the two methods was less than 0.22 in relative permittivity and less than 0.17 in dielectric loss when a R1661 glass 486.5±0.5 μm thick is employed as a test material.

In [174], a VNA operating in waveguide configuration in the frequency band of 0.14 – 0.22 THz and a TDS working at 0.1 – 4 THz are compared measuring the complex relative permittivity of two petroleum jellies at 0.2 THz. Measurements show an agreement within the estimated uncertainties for each system. However, authors underline the importance of the sample material on the measurement accuracy. The material for the comparison between the two techniques has to be homogeneous (free from air bubbles) and semi-solid (capable of completely filling both a TDS sample cell and a section of a VNA hollow waveguide). In absence of these qualities, experimental data from both FD and TD methods are difficult to compare each other due to measurement artifacts.

3. Terahertz diffractive lenses characterization: measurements set-up

In this work, the available set-up for ZP characterization at the frequency of 1 THz was a commercial TDS by Menlo Systems (Germany) [175], the TERA K15, a state-of-art product. It is a compact, fiber-coupled device with a usable range of 0.2 – 3.5 THz with a maximum frequency resolution of 1.2 GHz. The frequency resolution is limited by the dynamic range of the delay line. It might be argued that for the characterization of lenses with a highly chromatic behavior, a FD set-up could represent the most natural choice. However, as discussed in the previous section, FD and TD techniques lead to comparable experimental results. Thus, a TD system is also a suitable alternative, but more efforts have been done in the experiments design and in the resulting data processing, as it will be deeply analyzed in the following.

The employed TDS set-up consists of a 1560 nm wavelength fiber laser, coupled by means of a 2.5 m optical fiber patch cord to a photoconductive antenna. At the end of the fiber, emitted pulses are shorter than 90 fs and imping onto a biased high-resistivity semiconductor inside the antenna, in correspondence of a gap between two electrodes. Photons excite electrons across the electronic bandgap of the semiconductor into the conduction band. Photocarriers generated increase semiconductor conductivity in the sub-picosecond time scale. Photogenerated current is accelerated by a bias field applied by electrodes on the semiconductor. Carriers start to recombine, trap, or scatter emitting radiation with a frequency in the THz range. Subsequently, the conductivity decreases from sub-picosecond to nanosecond time scale according to the semiconductor properties [176], [177].

Femtosecond pulses generated by the laser are split off in two beams. The first beam travels in a fixed distance and excites the emitting antenna. The second beam travels a variable distance and excites a detector photoconductive antenna. An optical delay line is used to vary the timing of these detection pulses and synchronize them with the incoming THz radiation [178].

Photoconductive antennas are usually dipole antennas and they are coupled to a hemispherical HRFZ-Si lens. This lens collects the emitted electromagnetic field and gives directivity to the beam. A narrow radiated beam is possible thanks to the large refractive index of HRFZ-Si (compare Ch. II Sec. 5). In fact, total internal reflection angle of THz rays is low if the difference of refractive index between hemispherical lens material and air is high. However, radiation patterns of the photoconductive antenna with silicon lens are frequency dependent. At large distances, only a central lobe propagates forward with a Gaussian-like distribution. However, it diverges with an angle proportional to the wavelength: at a fixed distance from the antenna, the FWHM of the emitted radiation decreases as the beam frequency increases [179].

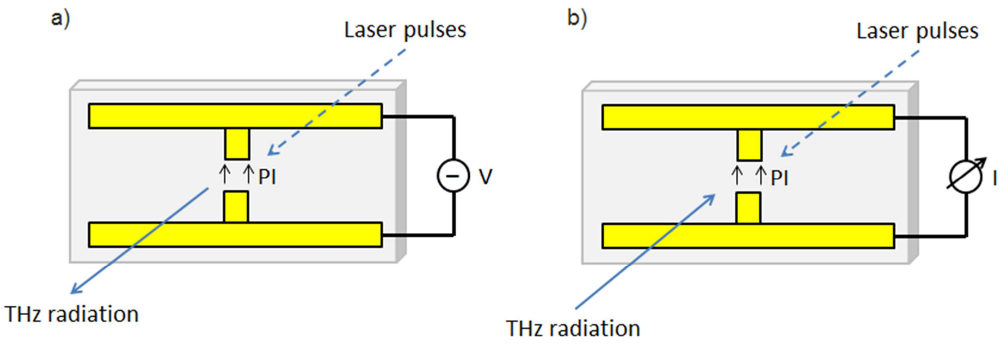

Fig. 19 Schematic representation of photoconductive antennas in their a) emitting and b) receiving configuration. PI is the photogenerated current.

In the standard configuration of the TDS delivered by Menlo Systems (*Fig. 20*), the presence of two convex-plane (L_1 and L_3) and two plano-convex lenses (L_2 and L_4), made by TPX and with a diameter of 38.1 mm (1.5 inches), are useful in most measurements. The lens L_1 has to collimate the beam coming from the hemispherical lens on the emitting antenna (PAT). The choice of the L_1 lens focal length is fundamental due to the divergent nature of the emitted radiation: the longer the focal length, the wider the beam diameter at each frequency. The lens L_2 has to focus radiation on the sample; L_3 collects the radiation passing through the sample, collimating the THz beam; L_4 focuses again the radiation on a receiving antenna.

Receiving THz antennas (such as PAR of *Fig. 20*) are photoconductive antennas with a structure close to emitting ones, but they do not receive a biasing from an external circuit (*Fig. 19 b)*). The detector is biased by the THz signal itself, focused on the antenna, where interacts with detection pulses. THz field drives a current between antenna electrodes. This electrical signal depends on whether the detection pulse arrives when the electric field of the THz pulse is low or high. A transimpedance amplifier receives the photogenerated current, which corresponds to the THz field strength, and amplifies it, converting to a usable voltage.

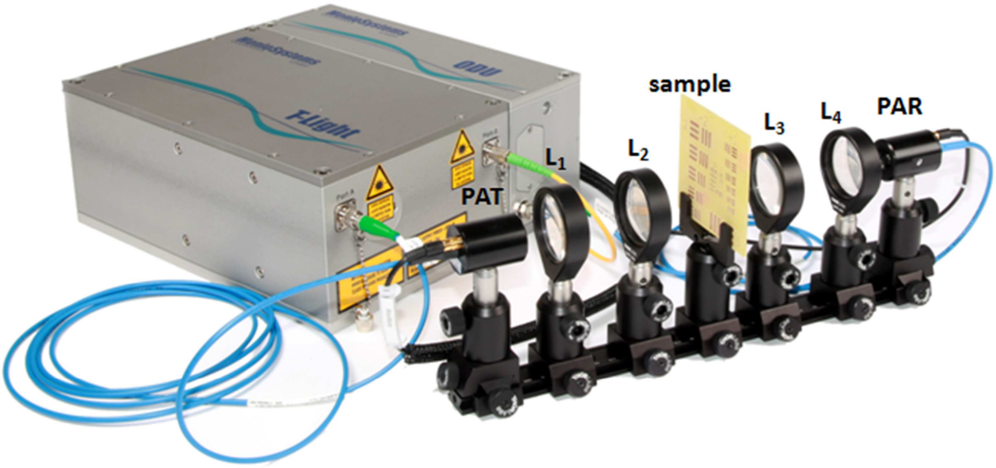

Fig. 20 Standard configuration of the commercial TDS TERA K15 by Menlo Systems. PAT: photoconductive antenna in transmission mode; L_1 and L_3: convex-plane lenses; L_2 and L_4: plano-convex lenses; PAR: photoconductive antenna in receiving mode [180].

As was previously pointed out, the TERA K15 TDS set-up was the only available instrument for the experimental characterization of the focusing properties of designed and fabricated ZP lenses. However, ZP design has been numerically studied assuming the THz excitation as an ideal one: a linearly polarized plane wave. Unfortunately, the wavefront after neither the TPX lens nor after the hemispherical HRFZ-Si lens is unknown to the manufacturer of the instrument. Hence, for comparing numerical and experimental data, it has arisen the need to carefully characterize the radiation emitted by the photoconductive antenna and collimated by the TPX lens (L_1 of *Fig. 20*). This is the real excitation of the ZPs.

In the following section, the methods employed for the beam characterization will be described. These methods have regarded the imaging of the THz beam emitted by the set-up source as well as the THz beam focused by the ZP lens. Thus, they will be discussed with regard of both experimental situations.

4. Terahertz beam characterization: knife-edge technique

The method employed for the beam characterization is the imaging on a plane perpendicular to the ZPs optical axis by means of knife-edge measurements. They consist of the gradual eclipsing of the THz beam by a sharp knife-edge. The blade translates in the direction perpendicular to the optical axis thus intersecting the beam, while the PAR measures the total intensity of the unmasked portion of the radiation. When the beam is spatially described by a Gaussian line shape, the detector measures an electric field sigmoidal profile along the blade translation direction. The spatial derivative of the measured signal yields the two-dimensional Gaussian field profile across the imaging plane and its FWHM represents the focal spot diameter.

4.1 Knife-edge set-up

In every knife-edge measurement, it was made sure that the edge of the blade employed has a roughness and a waviness well below 1 µm by careful inspection with a diffraction limited optical microscope (resolution less than 0.3 µm). Smoothness down to the deepest subwavelength level guarantees that no artifact is introduced by the blade itself. The blade has been fixed on the top of linear stage and was always perpendicular to the wave propagation direction. The translation stage carrying the blade has been bolted onto a graduated rotation stage, which has allowed for setting the angle at which translation can be operated. The rotation axis has coincided with the THz set-up optical axis.

The linear and rotation stages from Newport Corporation© [181] are motorized and can be controlled by a software provided by manufacturer. The linear stage has a weight of less than 1 kg and moves 25 mm. Rotation stage can rotate above 360° and it is also possible to manually control it, with a precision of 1°. When stages are driven by the software, they can move with a sensitivity of 0.1 µm, for the linear one, and with a 0.001° resolution and 0.05° absolute accuracy, for the rotation stage.

Knife-edge measurements for the TDS emitted beam characterization have been performed with the set-up configurations illustrated in *Fig. 21*. Three planar surfaces have been imaged. All of them are planes perpendicular to THz waves propagation direction. Plane 1 (*Fig. 21 a)*) and 2 (*Fig. 21 b)*) have been set at 3 mm and 9 mm from the hemispherical lens on the emitting photoconductive antenna, respectively. Plane 3 (*Fig. 21 c)*) has been located at the position past the lens L_1 where the ZPs will be later placed.

The blade has been scanned 16.2 mm across plane 1 and 2 with a 0.18 mm step, and 25 mm across plane 3 with a step of 0.125 mm. For each plane, the scans and acquisitions have been repeated for eight angular positions with a step of 22.5°.

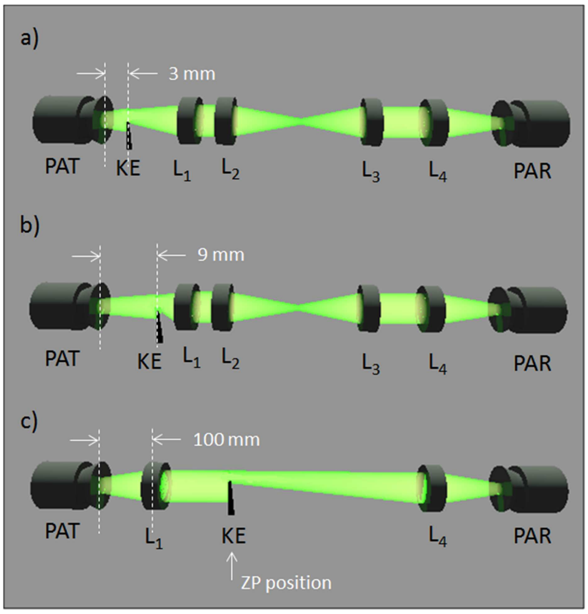

Fig. 21 TDS set-up configurations for the characterization of the THz beam emitted by the lens antenna (PAT). Three planes are imaged by knife-edge technique: a) plane 1, at a distance of 3 mm from the PAT; b) plane 2, at a distance of 9 mm from the PAT; c) plane 3, at the position in which the test ZPs will be located. PAT: photoconductive antenna in transmission mode; L_1 and L_3: convex-plane lenses; L_2 and L_4: plano-convex lenses; KE: knife-edge blade; PAR: photoconductive antenna in receiving mode.

In fact, if the focal spot is ideally circular, a knife-edge measurement for only one angle of scanning is necessary and sufficient for the beam characterization. However, in this experimental study, both the focal spot and the wavefront of the wave impinging ZPs have been assumed *a priori* unknown. Hence, an accurate beam characterization demands repeating knife-edge measurements for different angles between the knife-edge translation direction and THz field polarization direction.

The ZPs' focal plane has been characterized employing a modified version of the knife-edge technique already discussed. The THz TDS set-up is shown in *Fig. 22*. The ZP has been illuminated by THz radiation emitted by photoconductive antenna (PAT) and passing through a collimating convex-plane lens (L_1). At a distance matching the focal length, a razor blade (KE) has been mounted on a linear stage. After the blade, the uncovered radiation has been collected by a convex-plane TPX lens (L_3) and, then, focused on the receiving antenna (PAR) by a plano-convex TPX lens (L_4).

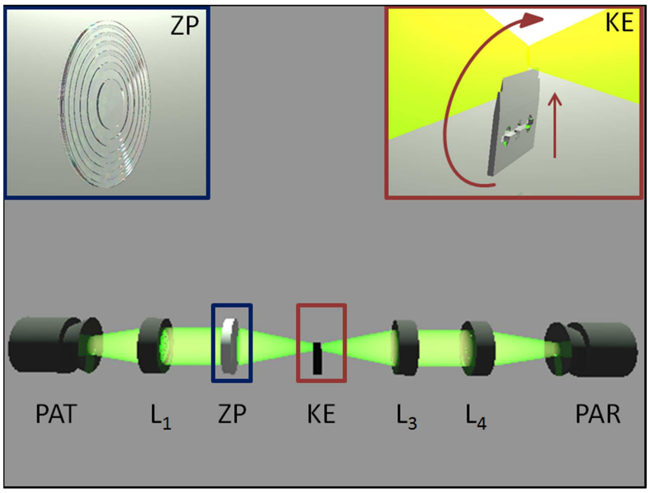

Fig. 22 Schematic representation of a THz TDS for focal spot measurements. PAT: photoconductive antenna in transmission mode; L_1 and L_3: convex-plane lenses; L_4: plano-convex lens; KE: knife-edge blade; PAR: photoconductive antenna in receiving mode.

A practical implementation of this scheme is illustrated in *Fig. 23*. The ZP has been positioned on a 1” circular mount and it has been centered with respect to the set-up optical axis to cut away radiation with a beam diameter larger than 25.4 mm. A stainless steel razor blade (KE) has been fixed on the translation stage start position, in which all the emitted radiation at 1 THz arrived on the detector, to an end position, in which the whole beam was stopped.

In general, when an ideal THz source is assumed, the standard knife-edge set-up configuration is the most conventional choice for the focal plane imaging. In fact, if the THz radiation incident on test ZP is uniform, all distortions in the ZP focus spot size, position and shape are introduced only by the ZP lens. On the other hand, the knife-edge technique could be performed in a different way if the THz radiation impinging on the ZP shows asymmetries due to reflections in optical path before the test lens. In this second set-up configuration, the blade is again on the translation stage and linearly moves, gradually covering the focal spot. However, it is the ZP lens that rotates, while the blade never changes its angle. The knife-edge always translates with a direction parallel to the polarization of incident THz radiation. In this way, results do not depend on set-up asymmetries but only on ZP lens, for every angle of measurement. This needs only to be carefully centered and normal to the propagation direction.

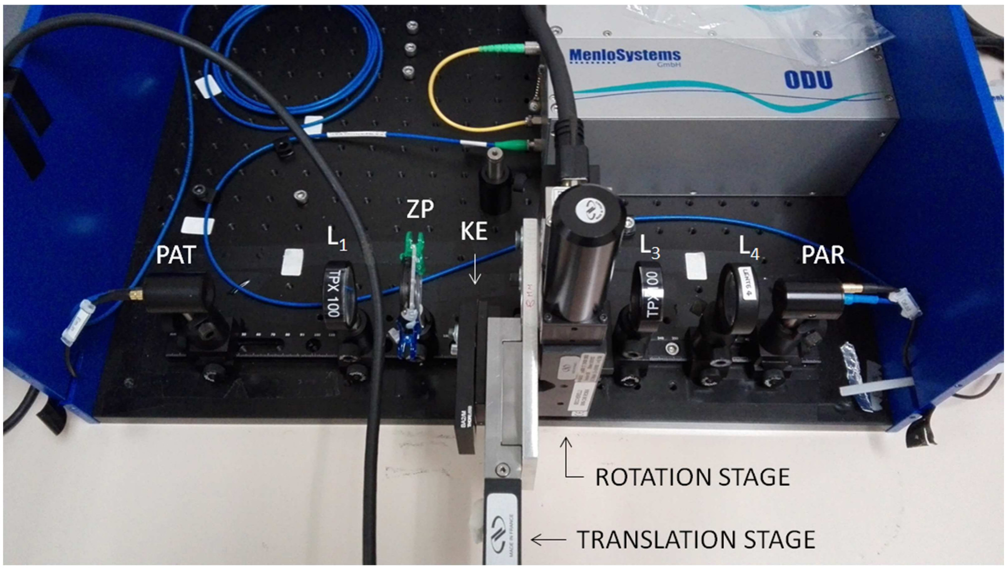

Fig. 23 Experimental set-up for standard knife-edge measurements. PAT: photoconductive antenna in transmission mode; L_1 and L_3: convex-plane lenses; L_4: plano-convex lens; KE: knife-edge blade; PAR: photoconductive antenna in receiving mode.

4.2 Knife-edge measurements automation

A program with LabVIEW System design software from National Instruments^{TM} [182] has been developed throughout this work for measurements automation. It allows for a synchronization between knife-edge movements and THz TDS pulses acquisition at every blade position. The final program is realized by employing instruments drivers provided by Newport and Menlo and displays a graphic user interface in which several parameters belonging to Newport stages and to Menlo TDS can be chosen, as shown in *Fig. 24*.

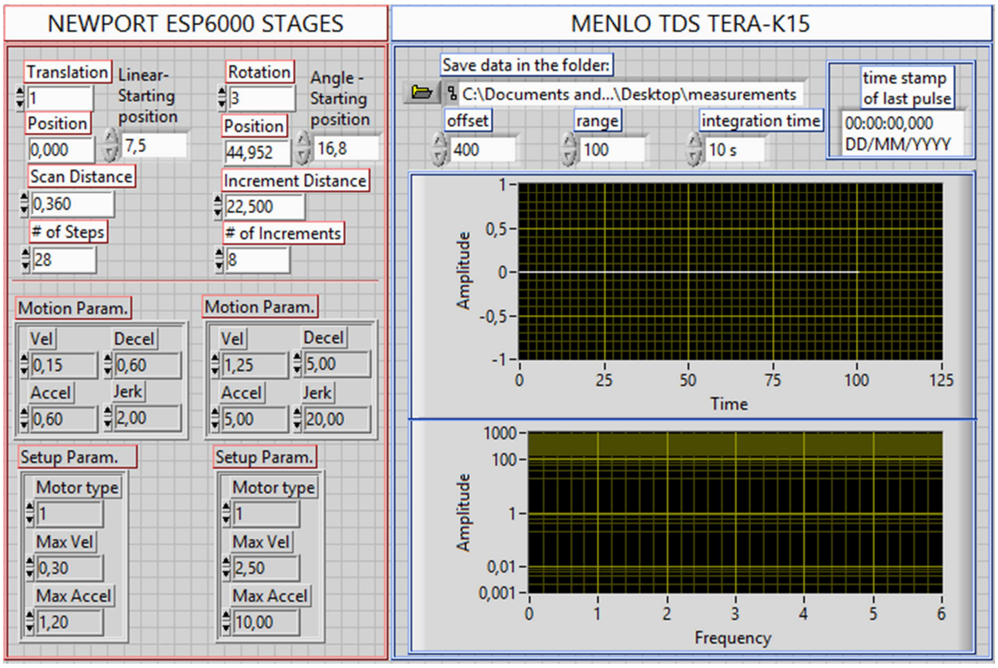

NEWPORT ESP6000 STAGES

Translation: 1
Position: 0,000
Linear-Starting position: 7,5
Scan Distance: 0,360
# of Steps: 28

Rotation: 3
Position: 44,952
Angle - Starting position: 16,8
Increment Distance: 22,500
# of Increments: 8

Motion Param.: Vel 0,15; Decel 0,60; Accel 0,60; Jerk 2,00
Motion Param.: Vel 1,25; Decel 5,00; Accel 5,00; Jerk 20,00

Setup Param.: Motor type 1; Max Vel 0,30; Max Accel 1,20
Setup Param.: Motor type 1; Max Vel 2,50; Max Accel 10,00

MENLO TDS TERA-K15

Save data in the folder: C:\Documents and...\Desktop\measurements
offset: 400
range: 100
integration time: 10 s
time stamp of last pulse: 00:00:00,000 DD/MM/YYYY

Fig. 24 LabVIEW front panel for knife-edge measurements automation. It employs drivers for the instruments and puts them in communication. The user can choose several parameters. Program also shows an updated plot of saved data and blade position.

The program has been designed for working in the following way:

1) Linear and rotation stages are reset in their zero position. This is determined by the manufacturer as a physical limit for the translation stage, while the rotation stage has an optical stop.
2) Both stages move towards a start position for knife-edge measurements. It can be set from the program user interface.
3) TDS starts the acquisition of THz pulse. Integration time, pulse duration, and starting temporal point can be set from the program user interface.
4) THz temporal pulse and its Fourier transform are saved as text files in a specific desktop folder, chosen by the user.
5) Linear stage moves the blade for a fixed distance, set according to the Nyquist criterion.

6) Steps 3, 4, and 5 are repeated until the last position of the blade for that angle is reached. It can be set from the program user interface.
7) Rotation stage moves a predetermined angular step the linear stage and the blade above it. The angular step can be set from the program user interface.
8) Steps 3, 4, 5, 6 and 7 are repeated until the last position of the blade for the last angle is reached.

4.3 Post-processing of data from knife-edge measurements: terahertz imaging

Once knife-edge measurements have been acquired and saved, resulting data can be plotted as total measured THz electric field (total $|E|$), which is the amplitude of total field passing through the uncovered area at every blade position. They appear as sigmoidal-like curves. To extract the variation of the total $|E|$ collected along the direction of blade translation, it is necessary to compute the first derivative of the acquired data plot with respect to the blade scan direction. This curve has a Gaussian-like shape. Gaussian representation can be seen as a projection of the $|E|$ distribution corresponding to a specific angle of view [183].

It is possible to reconstruct an image of the focal spot by increasing the number of projections at different angles of view. In this way, the image is constructed by an iterative process. Image quality depends on the number of the angle acquired.

From a mathematical point of view, each projection is a Radon transform [184], RT, of the $|E|$ distribution along a straight line L in the focal plane xy, $e(\boldsymbol{l})$:

$$\mathrm{RT}(L) = \int_L e(\boldsymbol{l})\, |d\boldsymbol{l}| \qquad \text{(III.1)}$$

If the straight line L is parametrized with respect to arc length z,

$$l = \big(x(z), y(z)\big) = \big((z\,\mathrm{sin}\alpha + d\,\mathrm{cos}\alpha), (-z\,\mathrm{cos}\alpha + d\,\mathrm{sin}\alpha)\big) \qquad \text{(III.2)}$$

where d is the distance between the line L and the optical axis (*i.e.*, the axis origin) and α is the angle between the vector normal to line L and the x axis. Radon transform can be expressed in the form

$$\mathrm{RT}(d,\alpha) = \int_{-\infty}^{\infty} e\big((z\,\mathrm{sin}\alpha + d\,\mathrm{cos}\alpha), (-z\,\mathrm{cos}\alpha + d\,\mathrm{sin}\alpha)\big)\, dz \qquad \text{(III.3)}$$

Hence, the Inverse Radon transform can be used to reconstruct the $|E|$ field distribution from projection curves. Inverse Radon transform is also called filtered back-projection formula:

$$e(\boldsymbol{l}) = \int_0^{\pi} \left(\mathrm{RT}(\cdot,\theta) * \hat{h}\right)(\langle \boldsymbol{l}, \boldsymbol{n}_\theta \rangle)\,d\theta \tag{III.4}$$

where $\hat{h}$ is the convolution kernel, a matrix used for filtering the image.

5. Iris sampling method: focal length characterization

The focal length is usually well estimated analytically or numerically, because depends on the operating wavelength, the number of zones and the most external radius of the ZP (compare Ch. II Sec. 4). Conversely, the spot shape and diameter (*i.e.*, the lens resolution) are influenced by the fabrication process and some differences between the numerical and the experimental data are usually unavoidable. Hence, starting from the standard TDS set-up previously discussed, other optical elements have been introduced in the THz beam path for characterizing the ZP lenses focal length, as shown in *Fig. 25*.

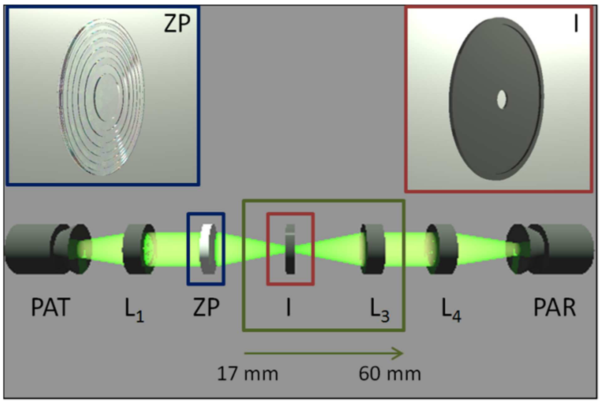

Fig. 25 Schematic representation of a THz TDS for focal length measurements. PAT: photoconductive antenna in transmission mode; L_1 and L_3: convex-plane lenses; L_4: plano-convex lens; I: iris; PAR: photoconductive antenna in receiving mode.

Terahertz radiation is emitted from the photoconductive antenna PAT. After the L_1 lens, which collimates the THz radiation emitted by the photoconductive antenna PAT, the ZP under investigation is positioned. The iris aperture is set equal to 3 mm (i.e., ~10 λ). It was verified that such aperture is wider than the focal spot width: all focused radiation passes through the aperture and can be detected by the photoconductive antenna PAR. Thus, a 3-mm aperture iris is scanned from 17 mm after the lens to 20 mm past the estimated focus to confirm its actual position. The ZP focal length corresponds to the position of the iris that results in the maximum THz electric field amplitude.

The TPX lens L_3 with a 54 mm focal length follows the iris in the optical path. This lens has the role to collect radiation coming from iris aperture and to parallelize the THz beam. Collimated THz radiation is focused by the last plano-convex lens on the receiving antenna.

The experiment has been performed as follows. The iris and the lens L_3 have been translated jointly by maintaining their separation equal to the lens focal length, *i.e.*, 54 mm. The range of distance scanned by iris is 17 mm to 60 mm past the ZP lens, with a step of 1 mm. These distances are chosen by taking into account: (i) information about ZPs behavior from numerical study (compare Ch. IV), (ii) (ii) the distance of the set-up’s antennas, related to the delay line’s optical fiber length, and (iii) the space physically occupied by elements in the optical axis, such as post holders and their bases.

6. Terahertz spectrometer calibration

Several commercial TDSs have the emitting antenna coupled with the hemispherical HRFZ-Si lens that radiates a broadband THz radiation with a frequency dispersive beam diameter. However, the frequency dependence of beam diameter is not declared by the Menlo TERA K15 manufacturers. Hence, it has been necessary to perform a careful characterization of the TDS set-up itself. Experimental data have been acquired over the entire spectrum (an intrinsic feature on any TDS technique) and have been fully processed in detail at 1 THz. This step fundamentally constitutes a calibration of the TDS set-up for the characterization of the lenses.

The planar surfaces defined in *Fig. 21 a)* (plane 1) and *b)* (plane 2) have been selected for the imaging of the radiation emitted by lens antenna PAT, while the imaging of the surface selected in *Fig. 21 c)* (plane 3) has allowed a calibration of the radiation impinging on the ZPs under test.

6.1 Near-field antenna images on cross-sections of emitted radiation

The THz field distribution at plane 1 and 2 is shown in *Fig. 26*. At plane 1, the pattern of emitted THz beam is almost circular with a diameter here assumed as the FWHM of the electric field, namely 4.68 mm. At plane 2, the pattern has an irregular shape with a FHWM equal to 5.76 mm and 6.3 mm along the directions perpendicular and parallel to electric field polarization, respectively. This indicates that the pattern of the emitted THz field has a divergence of 5.1°, in the direction perpendicular to electric field polarization, and of 7.7°, in the direction parallel to electric field polarization.

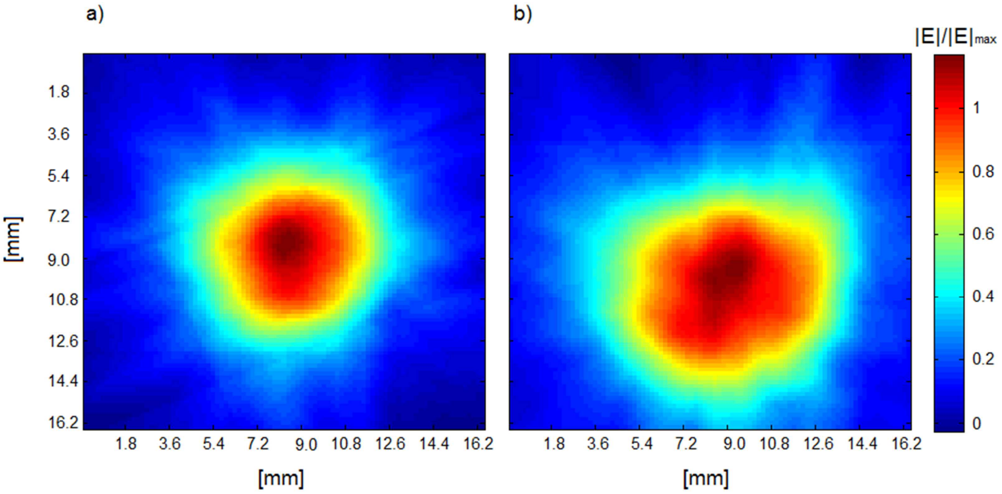

Fig. 26 Field distribution at 1 THz at a) 3 mm and b) 9 mm from the hemispherical lens of the emitting photoconductive antenna.

6.2 Distribution of the field intensity employed as lenses excitation

The ZPs have been fabricated to fit a standard 1” mount, *i.e.*, with a total diameter of 25.4 mm. The incident radiation should have a width equal or higher than ZPs’ one, which is of about 25 mm. A TPX refractive lens with a focal length of 100 mm has been chosen as L_1 to collimate the emitted beam. An image of the radiation profile at plane 3 is presented in *Fig. 27*.

The THz beam does not show a homogeneous distribution on the plane, but it has two zones in which the electric field has a maximum and two other zones in which radiation is 0.65 times the maximum electric field value. One of them is in the middle of the beam area. One of the reasons of a non-uniform distribution of the THz field could be due to reflections of the THz radiation introduced by the polymeric lens of the set-up.

The THz beam coming from photoconductive antenna shows irregular shape and intensity distribution just after 9 mm from the antenna. Thus, the field distribution after the collimating lens placed at a distance of about 100±4 mm from the emitting antenna cannot be considered ideal.

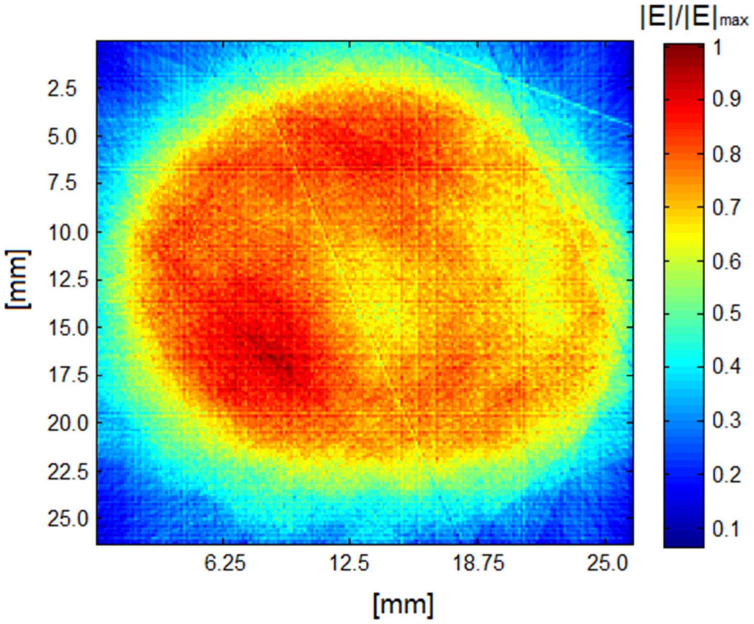

Fig. 27 THz field distribution collimated by a commercial lens and imaged on a planar surface by knife-edge technique.

However, all THz field with a modulus equal or higher than the half maximum is concentrated in a spot of approximately elliptical shape, with a minor axis of about 24 mm and a major axis of more than 25 mm. For this reason, it has been employed as the incident excitation for ZPs characterization. In order to avoid errors owing to the asymmetric distribution of the incident radiation in the imaging of the ZPs focal plane, the knife-edge technique has been performed by rotating the lenses under test, without changing the blade angle.

A plano-convex lens with a longer focal length, suitably placed further away from the emitting antenna would have allowed to fully cover the ZP. However, the range of allowable distances between the antennas is ruled by the delay line. The minimum distance is ruled by the polarization maintaining optical fibre patch cords. This is carefully glued by the manufacturer onto the antenna to maintain the femtosecond laser polarization. Unfortunately, the instrument in the knife-edge configuration of *Fig. 23* does not allow for inserting a lens L_1 with a focal length longer than 100 mm and it has been considered not advisable to modify the instrument internal configuration.

CHAPTER VI

Experimental characterization of polymeric zone plates

1. Introduction

A suitable material for THz devices has been analysed and compared to a more typical one by means of ZPs numerical studies. A number of 13 zones is found to be a good compromise, following theory and simulations.

Besides to a convenient lens design, it is also important to find experimental configurations suitable for characterization and comparison of the properties of three different fabricated ZP configurations. Uniformity in the incident radiation is one of the most important starting point for measurements. For this reason, THz radiation emitted by photoconductive antenna has to be collimated by a plano-convex TPX lens with a diameter of 1.5” and a focal length of 100 mm. In this situation, the radiation pattern a 1 THz is fairly paraxial with a 25 mm waist and it is able to illuminate ZPs completely.

Moreover, preliminary knife-edge measurements have been performed on the TDS set-up in order to evaluate the asymmetries in the emitted radiation due to the coupling between photoconductive antenna, its hemispherical silicon lens and the collimating TPX lens. It has allowed for developing a modified version of the knife-edge technique for the characterization of the ZP lenses.

2. Zone plates focal length

All measurements are made in air leading to the manifestation of water vapor absorption at several THz frequencies [185]. The most critical, in this experimental characterization, is the absorption peak at 1.1 THz due to its vicinity to the design frequency of the lenses. Hence, averaging acquired data in a frequency band 100 GHz wide centered in 1 THz is found the most appropriate choice to both filter noise and avoid very high losses associated with water absorption. Moreover, as discussed in chapter II section 4.3, there is a frequency band in which a ZP is achromatic which corresponds to about 71 GHz for ZPs working at 1 THz. Thus, the filtered data are marginally influenced by the lenses frequency dispersive behavior.

The ZP focal length was simulated and experimentally evaluated. It does not depend on the ZP configuration because the number of zones and the external diameter is the same for all investigated ZPs (compare equation II.2). *Fig. 28* displays simulated and experimental values of the average electric field amplitude $|E|_m$ in presence of the focusing ZP, normalized to the average amplitude $|E|_m^{\mathrm{air}}$ obtained when the ZP is removed and only a portion of the collimated beam passes through the iris aperture. In this way, the magnification effect of the ZP on the electric field amplitude in the focal area is evaluated.

The core part of the experimental set-up is also transposed in the COMSOL modeling environment. In the model, a circular aperture 3 mm wide is added after the lens and it is translated along the optical axis with a 2 mm step from 17 mm after the lens to 20 mm past the focus, as performed during the experiment. Still, the numerical results are obtained under idealized conditions, as some features of the experimental set-up cannot be transposed in the numerical model: (i) the field profile of the real source radiated from the antenna and silicon lens assembly does not correspond to a plane wave, (ii) imperfections in the employed metallic iris may result in diffraction and scattering, (iii) the TPX lenses of the set-up as well as the silicon lens of PAT and PAR are not included in the numerical model, thus ignoring possible reflections within them, and (iv) the coupling between TPX lenses, the silicon lens of the PAR and the PAR itself is not taken into account in the numerical study. This partially explains the differences between simulated and experimental data which can be seen in *Fig. 28*.

In addition, since the Menlo TERA K15 THz TDS is a fiber-coupled device, when femtosecond THz pulses propagate from the laser to the photoconductive antenna the fiber material is subject to a temperature increase and some temporal drift is observed as well as some amplitude modulation. This phenomenon does not reach a steady-state even if the instrument has been on for more than 12 hours and it cannot be taken into account in the simulation layout.

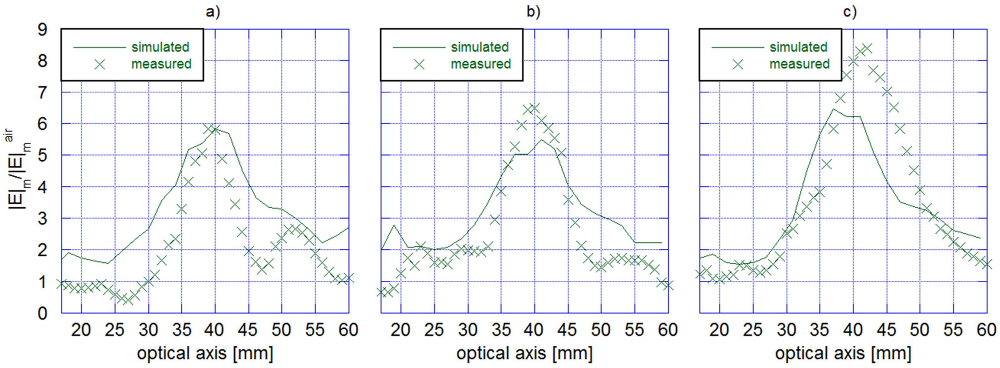

Fig. 28 Experimental and numerical evaluation of the focal length of three ZPs by means of the optical axis sampling of a) binary ZP, b) double-sided ZP, and c) multilevel ZP. Measurements are performed with the iris sampling method, which is also reproduced in the simulation environment.

Despite some differences between numerical and experimental values, *Fig. 28* shows some very interesting results. All ZPs are able to focus THz waves with a focal length of 40±1 mm, as targeted. The binary ZP is able to increase the THz field in the focal area by a factor of 5.8 (*Fig. 28 a)*). This factor increases to 6.5 (*Fig. 28 b)*), for a double-sided ZP, and to 8.4 (*Fig. 28 c)*) for a multilevel ZP. The measured depth of field is 8±1 mm for the binary ZP, 10±1 mm for the double-sided ZP, and 15±1 mm for the multilevel ZP. Hence, the experimental evidence demonstrates that the double-sided ZP possesses improved focusing properties than its conventional counterpart.

3. Zone plates focal plane

The modified knife-edge technique is employed for the characterization of the ZPs focal plane. The razor blade translates with 0.12 mm step, which is less than λ/2 at 1 THz. It satisfies the Nyquist criterion for signals sampling. The blade travels for a total length of 3 mm. The angular sampling has been performed with a fixed step of 10° by rotating the lens, for a total rotation of 180°. The blade is set always parallel to the incident THz field polarization.

The acquired data are represented by the sigmoidal curves of *Fig. 29*. Such curves are not perfectly monotonic, due to the presence of diffraction and scattering among passive components in the optical path. Sigmoidal curves start from different values because the three ZPs have different focusing capabilities: the double-sided ZP (*Fig. 29 b)*) has an intermediate focusing behavior between a binary ZP and a multilevel ZP. In fact, the mean value of the electric field in the whole focal spot for the double-sided ZP is greater than for a conventional ZP, but lower than for a multilevel ZP, validating the conclusion that the double-sided ZP outperforms the standard binary ZP.

The Gaussian-like curves of *Fig. 29* are the difference quotient of the acquired data, thus showing some negative values due to reflections among components of the THz set-up. The Gaussian-like curves can be seen as a projection of the |E|-field distribution corresponding to a specific angle of view. The electric field amplitudes are normalized with respect to their maximum value for each lens. This allows for better evaluating and comparing the focal spot size and shape without considering the focusing efficiency of each lens configuration. In the |E|-field projections, some secondary peaks, with a height less than a half of the main peak, especially for the binary ZP, are present (*Fig. 29 a)*). Moreover, the binary ZP is more influenced by the alignment to the experimental set-up optical axis than the others ZP configurations. The alignment of the ZP in the lens holder has an uncertainty deeply subwavelength, in the order of few micrometers. However, the field distribution slightly changes when different angles of view are selected. This does not occur for the other two ZP configurations.

Resulting images for the lenses under test are depicted in the inserts of *Fig. 29*. The focus spots (from yellow to red in *Fig. 29 g)-i)*, whose diameter is the FWHM of the Gaussian-like curves) are fairly circular, with a diameter of 0.7±0.12 mm for the binary ZP, of 0.65±0.12 mm for the double-sided ZP, and of 0.55±0.12 mm for the multilevel ZP. These sizes are comparable to 2λ at 1 THz.

On the other hand, from the comparison of reconstructed images of the focal spots, the binary ZP appears the only ZP with the maximum of the focus coinciding with the geometrical center, *i.e.* with the optical axis. The focuses of the double-sided ZP and multilevel ZP show a 0.12 and 0.06 mm offset above the optic axis, respectively. *Fig. 29 d)-f)* clearly shows that, above $|E|/|E|_{\max} = 0.5$, the curves for double-sided and multilevel ZPs are not completely symmetric. This influences image reconstruction showed in *Fig. 29 g)-i)* with an offset in the maximum field value position. However, the position of the center of the focus may be influenced by the manual alignment of the ZP under test in its lens holder, performed under a diffraction limited optical microscope.

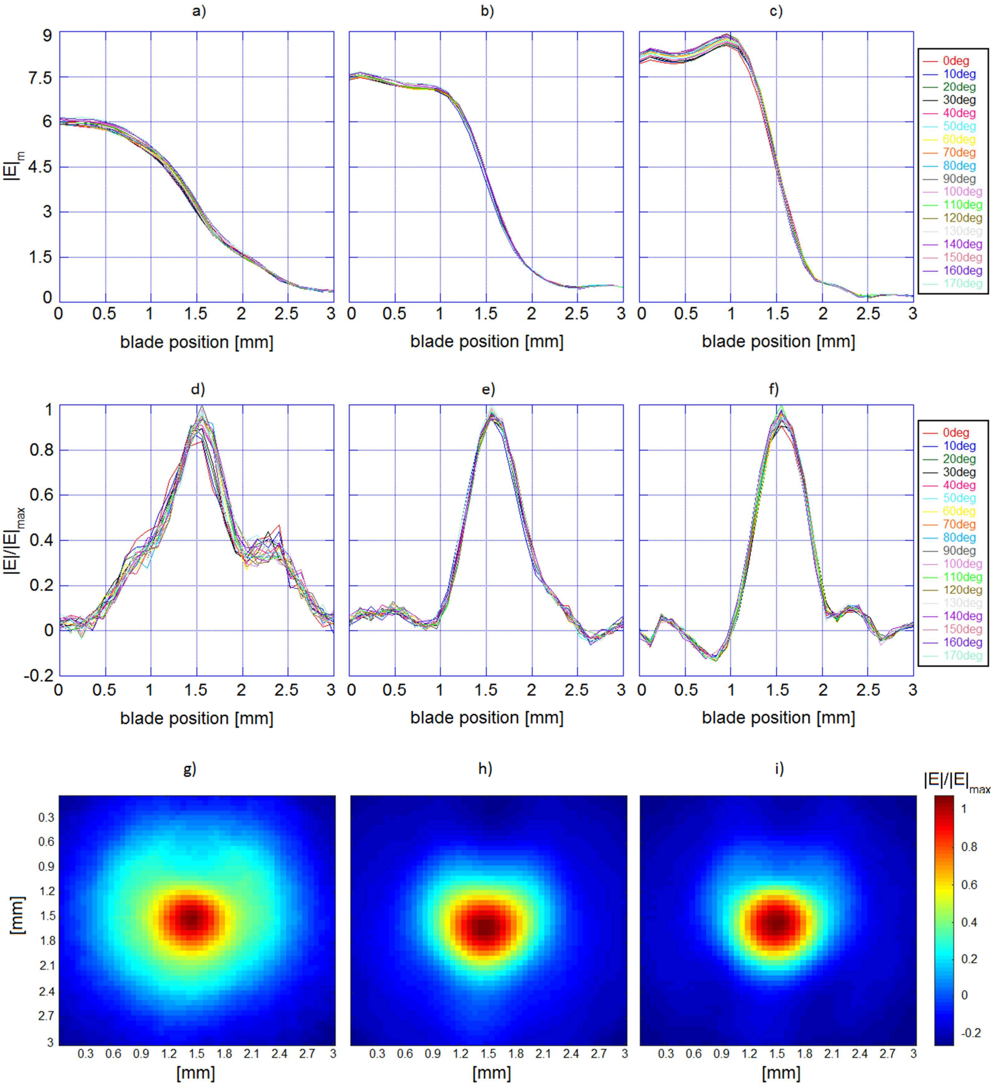

Fig. 29 Acquired data for a) a conventional binary ZP, b) a double-sided ZP, and c) a multilevel ZP; their difference quotient for d) a conventional binary ZP, e) a double-sided ZP, and f) a multilevel ZP; and focal plane images obtained by knife-edge measurements for g) a conventional binary ZP, h) a double-sided ZP, and i) a multilevel ZP. Negative values of the $|E|/|E|_{\max}$ are due to diffraction and scattering among the components in the THz optical path.

4. Focal plane experimental comparison between ideal and real illumination: multilevel zone plate case of study

All experimental data presented in *Fig. 29* are obtained by employing the modified knife-edge technique, *i.e.*, minimizing the influence of the THz source asymmetries on the devices characterization. As discussed in chapter V section 4, in a standard knife-edge technique, it is the blade that rotates, creating the real image of the focus. However, all changes in incident radiation, due to a non-ideal THz source and non-ideal behavior of THz optical components (compare Ch. V), compromise the focus quality. On the other hand, in the modified knife-edge technique, all data are collected by fixing the blade angle with respect to the THz field polarization and by rotating the lens. It has the advantage of obtaining a lens characterization in which excitation dishomogeneities do not affect the acquisition of the distribution of the field amplitude in the focal plane.

To the best of the author's knowledge, this modified knife-edge technique has not been discussed so far. Thus, to prove the effectiveness of the modified technique, a direct comparison can be made between the normalized |E|-field distribution in the four-level ZP focal plane, as imaged by the standard and modified knife-edge technique (*Fig. 30*). It is clear that, instead of a circular shape, the ZP focus area is irregular. The whole THz electric field is no more collected in a zone of maximum dimension of 1.2 mm, but radiation fringes of a 35% of the maximum field are present over an area of more than 6 mm of dimensions.

The situation presented in *Fig. 30* is strongly influenced by the diffractive nature of the test lens, which amplifies differences between the real incident THz field and an ideal plane wave. It also underlines the importance of the THz source characterization. In general, it is not appropriate to assume that the radiation emitted by a photoconductive antenna has a Gaussian-like distribution nor to approximate it as a plane wave.

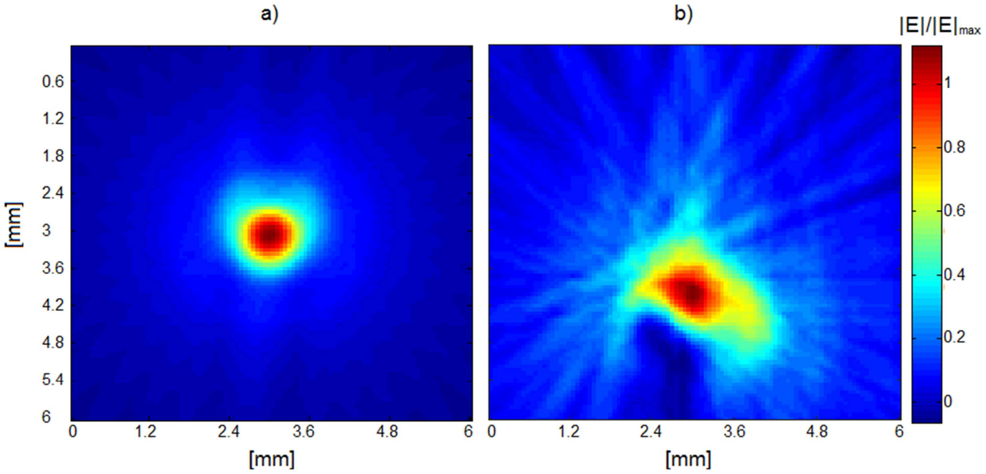

Fig. 30 Normalized amplitude of the electric field in the focal plane for the multilevel ZP acquired with knife-edge technique by rotating a) the lens, or b) the blade.

5. Conclusions

All investigated ZP configurations show good properties in focusing THz waves. The new double-sided ZP lens proposed and investigated in this work is a binary ZP, in which the total zone thickness is split in two halves. This new THz diffractive lens is simple and cheap to fabricate, can be realized by milling both sides of a polymeric substrate and delivers better performances than conventional ZPs.

By comparing its focalizing properties with ones of a conventional binary ZP, a double-sided ZP shows (i) an efficiency of 1.12 times higher (*Fig. 28*), (ii) a depth of field of approximately 7λ longer (*Fig. 28*), (iii) a resolution increased of (1/6)λ (*Fig. 29 g)* and *h)*), (iv) the total electric field is completely contained in a circle of confusion with a diameter of 1.4±0.12 mm instead of 2.6±0.12 mm (*Fig. 29 g)* and *h)*). Focal spots have both a circular shape.

Although the double-sided ZP performances do not fully match those delivered by the four-levels ZP, double-sided ZP is simpler to fabricate, is less susceptible to damage, and can be an interesting alternative for increasing the ZPs resolution.

CHAPTER VII

Future perspectives in developing planar diffractive lenses

1. Introduction

The development of THz applications and a market thereof is hampered by limitations of the available components. Limitations for sources and detectors were briefly addressed in chapter I. Among the pending issues for passive components for the manipulation of THz radiation, the fabrication costs and the lack of tunability are of particular relevance.

Hence, this chapter presents a design of a tunable diffractive lens by means of liquid crystal cells. It also presents a design of a focusing device working in reflection mode. This is based on a metal Fresnel ZP and is much lighter, smaller and cheaper than a conventional parabolic mirror. Some preliminary numerical results and new ideas for diffractive focusing elements will be shown in following sections.

2. Tunable zone plates

The focal length is the most appealing lens property to tune. However, the only way to tune a ZP focal length is by changing the number of zones. In fact, from equation II.2 (compare Ch. II):

$$l = \frac{r_{\mathrm{m}}^2}{m\lambda} \tag{VII.1}$$

where r_{m} is the radius of the whole ZP, m is the zone number, and λ is the wavelength. In most applications, the ZP external radius and the operational wavelength are fixed. It could be interesting to find a way to change the distance at which a ZP is able to focus THz waves. A successfully demonstated solution is to photoinduce an electron plasma ZP pattern on a silicon wafer [186]. Thus, a virtual ZP can be optically tuned by changing the electron plasma distribution. However, this solution requires an additional laser beam and a metal ZP masks. Every mask has to be projected on the silicon wafer and needs to be manually changed for obtaining different electron plasma patterns.

On the other side, an alternative can be offered by electro-optical tuning by means of liquid crystals (LCs). Several typologies of LC tunable lenses are successfully fabricated in the visible range [187]–[191]. At THz, LCs are employed in many devices, but only one tunable LC refractive lens prototype [192] and no diffractive lenses with LC have been proposed yet. However, exploiting the design rules of the double-sided ZPs, a change in ZP focal length is ideally feasible by electro-optical control and it will be numerically demonstrated.

2.1 Material with tunable properties: liquid crystals

LCs are materials that exhibit a solid crystalline phase, a liquid phase and intermediate phases in which they flow like a liquid, but show a preferred orientation. These intermediate phases are called mesophases. It is possible to distinguish several mesophases by changing temperature, concentration, constituents, substituents, or other LCs or environmental properties [193].

LCs can be also classified in lyotropic, thermotropic and polymeric, according to the physical parameters that control the existence of the liquid crystalline phases. Lyotropic LCs can be obtained when a suitable concentration of a material, usually amphiphilic molecules, is dissolved in a solvent, like water. This kind of LCs is of interest in biological field [194]. Thermotropic LCs are the most extensively studied LCs. They exhibit different mesophases as temperature increases. There are three main classes of thermotropic LCs: nematic, cholesteric, and smectic. Polymeric LCs are produced from monomers showing a liquid-crystal phase. These monomers are polymerized trough main chain or side chain reactions into a LC polymer. They have, in general, higher viscosity than other LC monomers due to bonds between polymeric chains [193]. Due to their excellent thermal and mechanical properties and low electromagnetic losses, they are also used as microwave substrates [195].

Materials constituted by molecules with an anisotropic shape could reveal mesophases. For this reason, it is common to refer to LCs as rod-like or disk-like molecules [196]. Thermotropic LCs have rod-like molecules. When the thermotropic LC is in a nematic phase (*Fig. 31 a)*), its rod molecules have a random position. It could remind a liquid; however, LC molecules are aligned in the same direction defined by a unit vector called director. In most cases, nematic molecules have a permanent dielectric dipole and the rods are arranged in a way that the resulting dipole moment of the bulk material vanishes. In fact, nematic LC molecules are centrosymmetric [193].

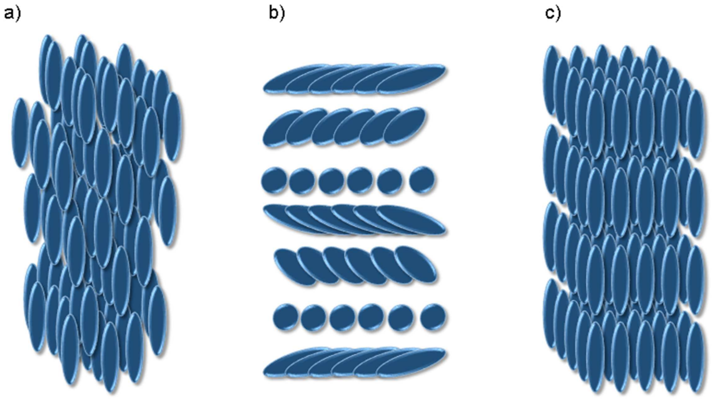

Fig. 31 Liquid crystals mesophases: a) nematic, b) cholesteric, and c) smectic.

Cholesterics (*Fig. 31 b)*) are also called chiral nematic LCs. They are nematic LC in which the alignment follow a helical arrangement. Smectic LCs (*Fig. 31 c)*), unlike nematics and cholesterics, have a positional order too: LC molecules are located in an ordered pattern. According to the configuration of rods positions, the smectic phase can be divided in subphases [196].

The amount of order in a LC can be measured by the scalar order parameter. It is a weighted average of the molecular orientation angles θ_{m} between the long molecular axes and the director [197]:

$$S = \frac{1}{2}\langle 3\cos^2\theta_{\mathrm{m}} - 1\rangle \tag{VII.2}$$

where the chevrons represents a thermal or statistical average. LCs in equilibrium state have usually a positive order parameter, which can change from $S_{\mathrm{eq}} = 0$, in the isotropic state (high temperature), to $S_{\mathrm{eq}} = 1$ in the crystalline phase (low temperature). A nematic LC has usually $S_{\mathrm{eq}} = 0.6$ at the temperature of operation [152].

2.1.1 Effects of an external electric field on nematic liquid crystals

When an external perturbation field is applied on LCs in nematic phase, they are subjected to deformation, as a solid. However, in a solid, the stress produces a translational displacement of molecules while, in LCs, molecules rotate in direction of the force without any displacement in their centre of gravity.

In general, in nematic LCs subjected to an external electric field, the director vector experiments a torque force. LCs respond to this external force with a reorientation of their long axis, which is influenced by several factors.

Thermotropic nematic LC layers are usually employed in a confined geometry, called "cell", *i.e.*, a cavity in which the top and bottom walls are covered with thin layers of polymeric material, typically a polyimide or polyamide. In free space optics, the edges are usually neglected as these lie outside the useable area of the device. This thin layer undergoes a mechanical[198] or optical [199] process able to align the polymer chains in a same direction (planar homogeneous alignment). When the nematic LC is in contact with this layer, it is energetically favourable that LC director has the same direction of polymer chains. In this way, the first layer of rods is considered anchored to the cell walls. The second layer follows the alignment pattern of the first layer, but experiments a lower anchoring, and so on. When LC molecules are strongly anchored to a boundary, surface interactions are not considered in the evaluation of rod molecules motion in nematic LCs due to external field interactions [193].

Moreover, the electronic response of LCs to an external electric field is characterized by its dielectric constants (or refractive indices), as well as electrical conductivities. These physical parameters are dependent to the direction of the external field and to its frequency: the dielectric permittivity is a tensor and its elements are, in general, complex numbers. Rod-like molecules are usually uniaxial LCs and the permittivity tensor is:

$$\bar{\bar{\varepsilon}} = \begin{bmatrix} \varepsilon_\perp & 0 & 0 \\ 0 & \varepsilon_\perp & 0 \\ 0 & 0 & \varepsilon_\parallel \end{bmatrix} \qquad \text{(VII.3)}$$

and similarly for the conductivity tensor. However, pure organic LCs are highly purified nonconductive materials (*i.e.* $\sigma = 0$), though may become conductive by adding ions and impurities. Electrical conductivity influences director orientation, chemical degradation and LCs lifetime.

Regarding dielectric permittivity, in most cases, $\varepsilon_{\parallel} > \varepsilon_{\perp}$ due to molecular structure and constituents. This condition is called positive anisotropy, *i.e.* $\Delta\varepsilon = \frac{(\varepsilon_{\parallel} - \varepsilon_{\perp})}{S_{\mathrm{eq}}} > 0$, where S_{eq} is the order parameter under equilibrium condition. In general, the elements in dielectric permittivity tensor are frequency dispersive and some LCs could change their anisotropy from negative to positive by increasing external field frequency [193].

When an external electric field E is applied, if its strength is more than a critical value E_F, called Freedericksz transition [200], LC director rotates by an angle θ with respect to its rest position, trying to align itself with the field direction:

$$E_{\mathrm{F}} = \frac{\pi}{d}\left(\frac{K}{\Delta\varepsilon}\right)^{1/2} \qquad \text{(VII.4)}$$

or

$$V_{\mathrm{F}} = \pi\left(\frac{K}{\Delta\varepsilon}\right)^{1/2} \qquad \text{(VII.5)}$$

where d is the distance between the electrodes which apply the field, and K is a local field factor. K takes into account the Frank elastic constants describing LCs director deformation: the splay modulus k_{11}, the twist modulus k_{22}, and the bend modulus k_{33} [196]. Under the condition of strong anchoring, if the external field induces a reorientation of the director from parallel to perpendicular with respect to electrodes plane (*Fig. 32*):

$$K = k_{11} + \frac{1}{4}\left(k_{33} - 2\,k_{22}\right) \qquad \text{(VII.6)}$$

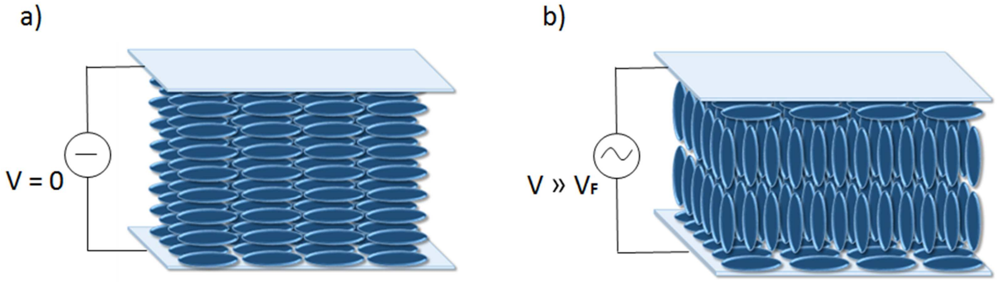

Fig. 32 Orientation of rod-like molecules in a nematic LC cell without any applied voltage or in presence of a voltage with strength higher than Freedericksz threshold. Typically, an alternating voltage in the few kilohertz range is chosen for preventing electrochemical degradation.

The rod molecules reorientation determines a change in a LC dielectric permittivity as well as in its refractive index. In fact, as discussed above, in absence of external fields, LC permittivity is expressed by equation VII.3. For values of applied voltage higher than the Freedericksz transition, it becomes:

$$\bar{\bar{\varepsilon}} = \begin{bmatrix} \varepsilon_{\parallel} & 0 & 0 \\ 0 & \varepsilon_{\perp} & 0 \\ 0 & 0 & \varepsilon_{\perp} \end{bmatrix} \tag{VII.7}$$

An equivalent notation that will be useful in following sections is:

$$\bar{\bar{\varepsilon}} = \varepsilon_0 \begin{bmatrix} \varepsilon_e & 0 & 0 \\ 0 & \varepsilon_o & 0 \\ 0 & 0 & \varepsilon_o \end{bmatrix} \tag{VII.8}$$

where the dielectric permittivity is considered as the product of the vacuum permittivity ε_0 and the extraordinary relative permittivity ε_e of the LC, when the director is parallel to the applied field, and it is the product of the vacuum permittivity ε_0 and the ordinary relative permittivity ε_o of the LC, when the director is perpendicular to the applied field.

2.1.2 Q-tensor formulation

Freedericksz transition provides a static description of LCs by introducing a threshold behaviour. However, a rigorous study of LC orientation in confined geometries requires the development of a model which involves the minimization of the LC free energy. It can be carried out following the Q−tensor formulation [197] that allows for the numerical study of edge effects, defect singularities, and order parameter variations.

In the more general case of a biaxial nematic LC, a symmetric traceless matrix, which represents the LC tensor order parameter, can be introduced as [201]:

$$\bar{\bar{Q}} = S_1\,(\boldsymbol{n} \otimes \boldsymbol{n}) + S_2\,(\boldsymbol{m} \otimes \boldsymbol{m}) - \frac{1}{3}(S_1 + S_2)\bar{\bar{I}} = \begin{pmatrix} q_1 & q_2 & q_3 \\ q_2 & q_4 & q_5 \\ q_3 & q_5 & -q_1-q_4 \end{pmatrix} \tag{VII.9}$$

where S_1 is the parameter order of the molecular axis with director $\boldsymbol{n}$, S_2 is the parameter order of the molecular axis with director $\boldsymbol{m}$, and $\bar{\bar{I}}$ is the identity matrix so that the trace of $\bar{\bar{Q}}$ is zero. The eigenvalues of the Q-tensor are [197]:

$$\lambda_1 = \frac{1}{3}(2\,S_1 - S_2) \tag{VII.10}$$

$$\lambda_2 = -\frac{1}{3}(S_1 + S_2) \tag{VII.11}$$

$$\lambda_3 = \frac{1}{3}(2\,S_2 - S_1) \tag{VII.12}$$

If the LC is uniaxial, two of these eigenvalues are equal and the Q-tensor is [201]:

$$\bar{\bar{Q}} = S\left[(\boldsymbol{n} \otimes \boldsymbol{n}) - \frac{1}{3}\bar{\bar{I}}\right] \tag{VII.13}$$

The total free energy of a bulk LC, under the condition of strong surface anchoring, is given by the contribution of thermotropic, elastic and electromagnetic energy density functions. The thermotropic energy density function is [201]:

$$F_{\mathrm{th}} = a_{\mathrm{th}}\,\mathrm{tr}\left(\bar{\bar{Q}}^2\right) + \frac{2b_{\mathrm{th}}}{3}\,\mathrm{tr}\left(\bar{\bar{Q}}^3\right) + \frac{c_{\mathrm{th}}}{2}\left[\mathrm{tr}\left(\bar{\bar{Q}}^2\right)\right]^2 \tag{VII.14}$$

where a, b and c are the thermotropic coefficients, *i.e.*, a temperature dependent coefficients, and *tr(·)* indicates the trace of a matrix.

The elastic energy density is the energy due to a distortion of the LC molecules, *i.e.* of a variation of the Q-tensor in the space [201]:

$$F_{\mathrm{d}} = \sum_{i,j,k=1,2,3}\left[\frac{L_1}{2}\left(\frac{\partial Q_{ij}}{\partial x_k}\right)^2 + \frac{L_2}{2}\frac{\partial Q_{ij}}{\partial x_j}\frac{\partial Q_{ik}}{\partial x_k}\right] + \sum_{i,j,k,l=1,2,3}\left[\frac{L_6}{2}\,Q_{lk}\frac{\partial Q_{ij}}{\partial x_l}\frac{\partial Q_{ij}}{\partial x_k}\right] \tag{VII.15}$$

L_1, L_2 and L_6 are elastic parameters related to Frank elastic constants k_{11}, k_{22} and k_{33}.

The electromagnetic energy density in presence of only an external electric field $\boldsymbol{E}$ is given by the electrostatic energy:

$$F_{\mathrm{em}} = -\int \boldsymbol{D} \cdot \mathrm{d}\boldsymbol{E} \tag{VII.16}$$

where the electric displacement field $\boldsymbol{D} = \varepsilon_0\tilde{\varepsilon}_{\mathrm{r}}\boldsymbol{E} + \boldsymbol{P}$ depends on the spontaneous polarization vector $\boldsymbol{P}$ and the LC permittivity tensor that, for a nematic LC, can be also expressed in terms of the Q-tensor:

$$\tilde{\varepsilon}_r = \Delta\varepsilon\,\bar{\bar{Q}} + \varepsilon_{eq}\,\bar{\bar{I}} \tag{VII.17}$$

where $\Delta\varepsilon$ is the dielectric anisotropy and $\varepsilon_{eq} = (\varepsilon_{\parallel} + 2\varepsilon_{\perp})/3$.

Spontaneous polarization derives from asymmetries in shape of LC molecules and can be written in terms of Q-tensor. The i$^{\mathrm{th}}$ components is given by:

$$P_i = p_1 \sum_{j=1,2,3}\frac{\partial Q_{ij}}{\partial x_j} + p_2 \sum_{j,k=1,2,3} Q_{ij}\frac{\partial Q_{jk}}{\partial x_k} \tag{VII.18}$$

with p_1 and p_2 that are polarization coefficients [197].

The Q-tensor formulation is based on the minimization of the free energy density function $F_{\mathrm{b}} = F_{\mathrm{th}} + F_{\mathrm{d}} + \mathrm{F}_{\mathrm{em}}$ via the solution of a system of five equations (i = 1 … 5):

$$\sum_{j=1}^{3} \frac{\partial}{\partial x_j}\left(\frac{\partial F_{\mathrm{b}}}{\partial q_{i,j}}\right) - \frac{\partial F_{\mathrm{b}}}{\partial q_i} = 0 \qquad \text{(VII.19)}$$

in which $q_{i,j} = \partial q_i/\partial x_j$. Equations VII.19 represent the LC static equations and can be solved together with suitable boundary conditions. In a strong anchoring regime, Dirichlet conditions are commonly employed: the Q-tensor at boundaries has a specified value defined by chosen alignment. In a weak anchoring regime, however, a surface energy density has to be added in the evaluation of the total free energy density of the LC [197].

When the study of the dynamic evolution of the Q-tensor is required, equations VII.19 become:

$$\sum_{j=1}^{3} \frac{\partial}{\partial x_j}\left(\frac{\partial F_{\mathrm{b}}}{\partial q_{i,j}}\right) - \frac{\partial F_{\mathrm{b}}}{\partial q_i} = \gamma \frac{\partial D}{\partial \dot{q}_i} \qquad \text{(VII.20)}$$

where D is the dissipation function $D = \mathrm{tr}\left(\left(\partial\bar{\bar{Q}}/\partial t\right)^2\right)$, γ is the ratio between the standard viscosity of the nematic LC and the order parameter obtained when the viscosity is measured, and $\dot{q}_i = \partial q/\partial x_i$.

By means of equations VII.20, it is possible to study the switching dynamics of devices employing LCs as well as the tunable properties of such devices. Equilibrium order parameter, standard viscosity, polarization coefficients, dielectric permittivity tensor elements, Frank elastic constants, and thermotropic coefficients change according to LC mixture chosen: their values will be indicated during the discussion of specific applications (compare Ch. VII Sec. 2.2 and Ch. IX). In the next section, the Q-tensor formulation has been employed in the numerical study of an electro-optical controlled planar diffractive lens able to switch between two different focal lengths.

2.2 Double-sided zone plate with two focal lengths

There are two main technological issues that have so far hampered LC-based electro-optical tunable phase-reversal ZPs at THz frequencies. The first one dwells in the thickness of a LC layer able to introduce a phase difference of π in the incident THz waves path (see equation II.5). As discussed in the previous subsection, a layer of LCs in a nematic phase is able to change its dielectric permittivity, *i.e.* its refractive index, according to a voltage externally applied to the LCs layer. In order to obtain a phase-reversal ZP dynamically tuned by means of the electro-optical effect of LCs, it is necessary to employ electrodes with alternative conductive and nonconductive annular zones shaped as ZP. Three configurations are possible. In a first configuration, the top and bottom are equally patterned and aligned. In a second configuration, only the electrodes on one substrate are pattern, whereas the other substrate is uniformly conducting. In a third configuration, only the electrodes on one substrate are pattern, and there is no electrode on the other substrate. Different director profiles result from these configurations.

However, an issue arises when an electrode is ZP-patterned. In fact, the electric field could short-circuit between two adjacent conductive rings of the same electrode when their distance is comparable to the separation between the top and bottom electrodes, *i.e.*, with the thickness of the LC cell. It involves that the LCs above non-conductive zones could change the refractive index together with the LCs above conductive zones. Consequently, the most external rings of the phase-reversal ZP could become a wide single zone and the ZP pattern is lost.

The second configuration is illustrated in *Fig. 33 a)*. The LC behavior is numerically investigated with the Q-tensor formulation discussed in the previous section by implementing it in a FEM model (described in Ch. III Sec. 2). This model provides the solution of the dynamic equations VII.19. A voltage of 70 V is applied between the two electrodes, which have a distance of about 386 μm. The distance between the top and bottom electrodes corresponds to the thickness of the phase-reversal ZP. The thickness is evaluated from equation II.5 by substituting the difference of refractive index between the polymer and the air with the LC birefringence $\Delta n = n_e - n_o$. All the other ZP geometrical parameters match with the ones of the polymeric binary phase-reversal ZP described in chapter III.

The selected LC material 1825 has been synthesized by the Military University of Technology of Warsaw and has complex ordinary and extraordinary refractive indices equal to $n_o = 1.554 - j0.018$ and $n_e = 1.941 - j0.022$ at 1 THz, low-frequency (1.5 kHz) permittivities $\varepsilon_o = 4.7$ and $\varepsilon_e = 21.7$, Frank elastic constants $k_{11} = 12.5$ pN, $k_{22} = 7.4$ pN, $k_{33} = 32.1$ pN, and viscosity $\gamma = 311.55$ mPa·s [202], [203]. This nematic mixture has been selected because it exhibits a high birefringence at THz and moderate losses [152] and it is available through an established collaboration.

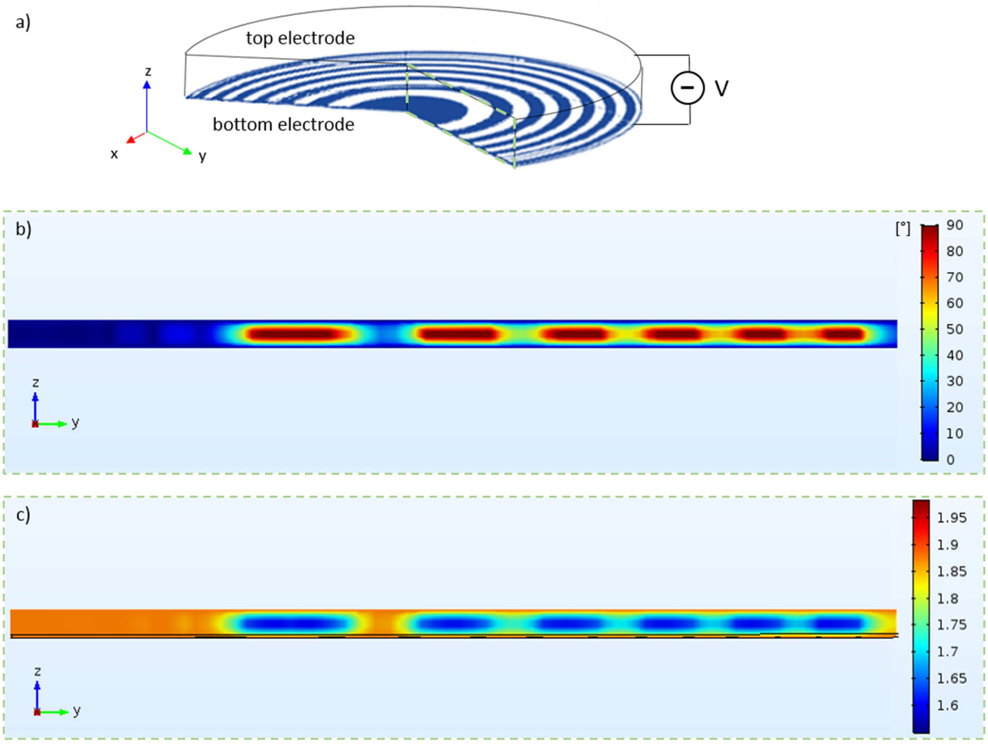

Fig. 33 a) A ZP configuration with a uniform electrode on top and a ZP-patterned electrode on bottom substrate. The rest condition of the LC is tilted 2° from the *y*-axis. b) tilt angle and c) *y*-component of refractive index tensor distributions in a LC cell 387 µm thick, 2 ms after the application of a 70 V step voltage (steady state).

In absence of applied voltage, the LC director is parallel to the electrode plane, with a pretilt angle of 2°. When the voltage is applied, the LCs show a switching behavior. After 2 ms from voltage switching (*i.e.*, in the steady state), the director has a tilt angle of 90° in the middle of the LC cell (*Fig. 33 a)*). Here, in fact, the anchoring forces do not influence the director orientation. An angle of 90° corresponds to a director orientation perpendicular to the electrode plane. However, LC is tilted only 55° − 60° between the most external adjacent electrodes in correspondence of a nonconductive ring. As it can be seen from (*Fig. 33 b)*), it corresponds to a *y*-component refractive index of about 1.6 – 1.65 in direction parallel to the polarization direction of the applied electric field. However, *Fig. 33* shows that the transition of the refractive index component from the fully switched and fully unswitched zones is not sharp. It gets significantly blurred for the outer rings where the thickness approaches the cell gap and the fringe field effects rule. Hence, the diffractive effect is reduced and the device becomes ineffective as a tunable lens.

Clearly, the fringe field effects play a detrimental role. Ideally, these should be reduced or avoided altogether. One way to reduce them is by recalling that, for double-sided phase-reversal ZPs, the phase shift introduced by each binary phase-reversal ZP is π/2 instead of π (see Ch. II). When this concept is transferred to a LC phase-reversal ZP, each LC cell needs to provide only half the overall retardation. Hence, the cell can be thinner and the fringe field effects can be reduced. As a straightforward example, a half thickness cell, 193 µm thick, is here considered.

The LC switching behavior can be numerically evaluated by applying a voltage of 35 V and employing the same electrode configuration of the one presented in *Fig. 33 a)*.

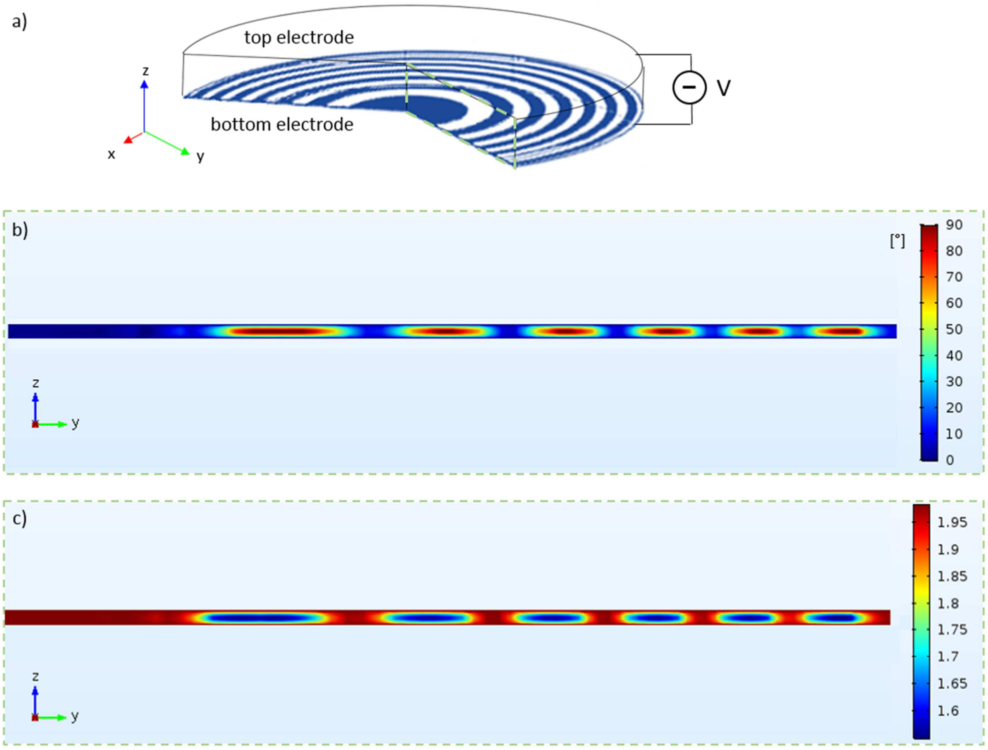

Fig. 34 a) A ZP configuration with a uniform electrode on top and a ZP-patterned electrode on bottom substrate. The rest condition of the LC is tilted 2° from the *y*-axis. b) tilt angle and c) *y*-component of refractive index tensor distributions in a LC cell 193 µm thick, 2 ms after the application of a 35 V step voltage (steady state).

The LC director tilt angle and refractive index in direction parallel to the polarization direction of the applied electric field for the half-thick cell are presented in *Fig. 34*. The maximum tilt angle of LC director in the middle of the cell above nonconductive rings is now always below 25°. It follows that the *y*-component of the refractive index differs appreciably from its rest value in the most external non-conductive ring and it is equal to about 1.9. This suggests that a double-sided LC phase-reversal ZP is a better candidate as electro-optical tunable diffractive lens than conventional binary phase-reversal ZP. Additionally, thinner LC devices require a lower driving voltage for the same switching time. More importantly, in real devices, the quality of the alignment is usually better, especially for 100s µm thick devices.

As a confirmation of this idea, a tunable LC double-sided phase-reversal ZP has been designed and numerically investigated. At the beginning of this chapter, it was argued that the only way to dynamically tune ZP focal length is by changing the number of Fresnel zones. Here, it is proposed that if two lenses with a different number of rings are stacked and one of them is electro-optically controlled, it is possible to change between two focal lengths simply by applying a voltage. In fact, when the voltage is turned off, the first ZP, which is a polymeric phase-reversal ZP as described in chapter III, is able to focus the incident THz radiation with its own focal length. When the LC is switched on, the waves passing through the first polymeric phase-reversal ZP are re-focused with a focal length corresponding to the number of zones of the LC phase-reversal ZP. In *Fig. 35*, a cross section perpendicular to the lens plane is shown and some geometrical parameters and materials information are presented. The numerical model has a radial symmetry and includes materials losses at 1 THz. However, this is a preliminary investigation and the LC is considered to have an asymptotic behavior, *i.e.*, its *y*-component switches from a uniform profile of n_e to a uniform profile of n_o.

The behavior of the dual-focus double-sided phase-reversal ZP is presented in *Fig. 36*. The *z*-direction is the one parallel to the ZP lens optical axis. When no voltage is applied to the LC, the lens focuses the 1 THz radiation 59.5 mm past the lens. The FWHM, which could be considered as the depth of field of the lens, is 9.2 mm approximately.

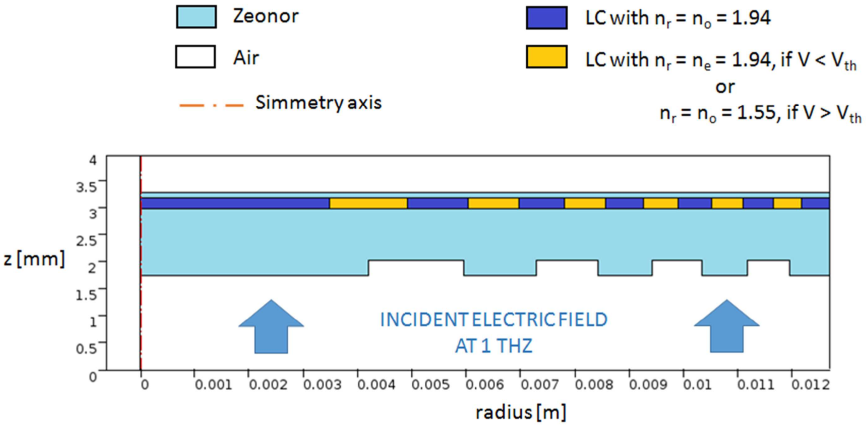

Fig. 35 Cross section of geometrical radial-symmetric model and data for the materials chosen for a dual-focus double-sided ZP. The ZP is symmetric and only the profile along the radius of the lens is represented in the picture.

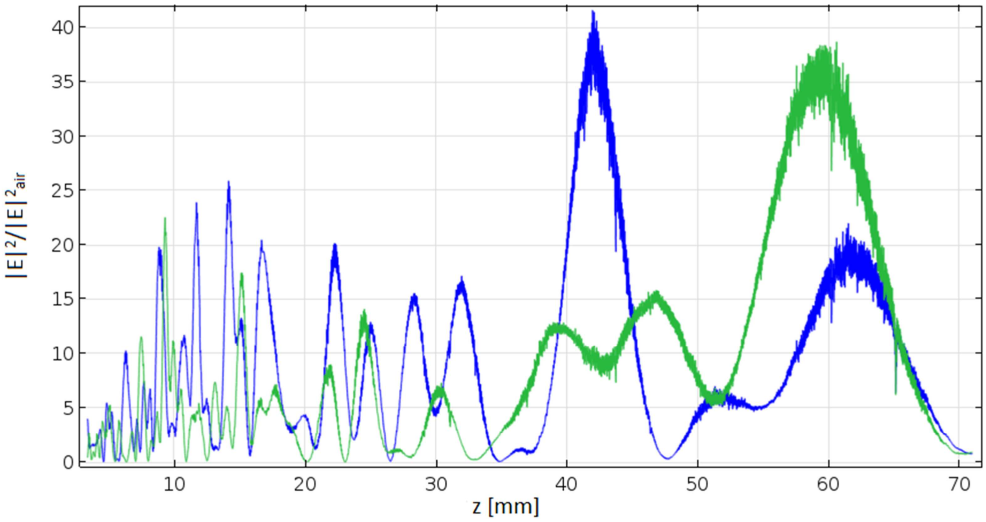

Fig. 36 Computed square modulus of the electric field component along the optical axis (*z*-component) at 1 THz for a dual-focus double-sided phase-reversal ZP lens. The green line is for zero applied voltage (rest), while the blue line is for LC molecules parallel to the lens optical axis (V_∞).

When the LC molecules are aligned in the *z*-direction, the focal length switches in ~2 ms to 42.1 mm approximately. The FWHM also changes to 4.5 mm.

The square modulus of the electric field in the focus area is about 35.5 times larger than the square modulus of the incident electric field on the lens, when the lens is switched off, and about 39 times larger, when the lens is switched on. However, several ripples are also present along the optical axis. These peaks are due to multiple reflections between the polymer facets. They disappear by changing the thickness of the polymer between the two ZPs. However, this distance is fundamental in the double-sided ZP design and could not be varied without changing the lens focusing properties. Further investigation is needed to suppress these peaks due to reflections and optimize the design. Moreover, an additional study is required for exploiting the dual-focus behavior when the asymptotic profile of the LC refractive index is substituted with the one computed by the Q-tensor model and presented in *Fig. 34 c)*.

The dual-focus double-sided phase-reversal ZP here described shows a switchable focal length and could offer a good starting point for developing ZP stacks optimized for working at different focal lengths by means of the electro-optical control of the LC orientation. It is a device simple to integrate in compact instruments, flat, and ideally suitable for miniaturization.

The main problem in the experimental demonstration of such devices is linked to the second technological issue in the development of tunable and compact devices at THz frequencies: the availability of a highly transparent conductive material for electrodes fabrication. In the visible range, indium tin oxide (ITO) is ubiquitously used [204]. However, it is opaque at THz frequencies. One of the most promising conductive polymer for transparent electrodes at THz is the poly(3,4-ethylenedioxythiophene):poly(4-styrenesulfonate) (PEDOT:PSS). However, the conductivity of a PEDOT:PSS film is usually no more than 10 S cm^{-1}. It is not completely suitable for replacing ITO, because it has, typically, a conductivity of about 4000 S cm^{-1} [205]. Several methods can be applied for improving PEDOT:PSS conductivity, such as treatments with acid solutions or the addition of organic compounds. However, only films with conductivity no more than 1000 S cm^{-1} allows for a PEDOT:PSS transmittance at THz comparable with ITO transmittance in the visible range (*i.e.* ~ 90%) [205].

An alignment film of polyimide decreases THz transmittance of about 10%, but the homogeneity of this effect does not compromise LC-ZP performance. In fact, the main problem due to the presence of a non-transparent ZP-patterned electrode is that it behaves as a Fresnel ZP itself. It implies that, in a dual-focus double-sided ZP, the polymeric phase-reversal ZP performance is affected by the LC electrode and the incident radiation will be focused at both focal lengths, losing power in the focus area. A thorough optimization of the devices is required which takes into account both the phase modulation and the exact effect of the conductive layer on the THz field.

Different formulations of PEDOT:PSS exist; some have been supplied for this work and have been preliminarily tested. However, the extraction of the real and imaginary component of PEDOT:PSS at THz is a challenging and still unaccomplished task. It would require a very elaborated ellipsometric technique because practical films are submicron, *i.e.*, roughly one thousandth the wavelength.

For this reason, the fabrication and experimental investigation of proposed LC switchable diffractive lens have not been planned yet, even if double-sided ZPs significantly reduce the problem of the LC thickness and should provide an effective solution for the dynamic focusing of THz radiation.

3. Metal zone plates

Fresnel ZPs can be also investigated at THz frequencies. As discussed in chapter II, a phase-reversal ZP has a higher efficiency than a Fresnel ZP due to the fact that all the incident radiation passes through the device. According to the zone construction, a portion of incident radiation is phase shifted and constructively interferes with the other portion, inducing a concentration of radiation in a small area, *i.e.*, the focus. However, some losses occur because of low efficiency of the diffraction mechanism and absorptions in the material.

In a Fresnel ZP, there is no phase shift of the radiation which destructively interferes to the focus construction. This part of the incident radiation is stopped by adding a patterned mirror. Hence, the transmitted wave suffers from losses to reflection. These losses sum up with those due to diffraction efficiency and material absorptions. Therefore, the Fresnel ZP lens shows a lower focusing efficiency than a phase-reversal ZP.

Interestingly, all reflected radiation is in phase and create virtual foci (*Fig. 7*). Thus, it is possible to combine synergistically the power transmitted with the power reflected from the Fresnel ZP in a novel device working in reflection mode with maximum efficiency. This device encompasses a homogenous mirror on the other side of the substrate on which the Fresnel ZP is patterned. The distance between the Fresnel ZP and the mirror must be equal to $\lambda/4$ in the material [206]. In this way, the main focus is superposed to the virtual focus with an increasing of the THz field strength in the focus area.

Fresnel ZP lenses working in reflection mode do not already exist at THz frequencies. This is on the side of the plane wave source. At the design frequency, this device behaves very similarly to a bulky parabolic mirror, but is very thin (50 μm for operation at 1 THz with a dielectric with a 1.5 refractive index). However, they have been often employed as lens antennas at millimeter-waves and at microwaves.

3.1 Zone plates in reflection mode

The performance of a Fresnel ZP working in reflection mode can be numerically compared with the behavior of the same Fresnel ZP working in transmission mode. Again, Zeonor is chosen as lens substrate for its low THz absorption (for material properties, compare Ch. II Sec. 5). However, the design was made for the available 100 μm foils due to the current unavailability of 50 μm thick foils working a λ/4 waveplates. This rules that the working frequency is about 0.5 THz.

A FEM model (as discussed in Ch. III Sec. 2) of both lenses has been developed under the condition of normal incidence of a plane wave. Both ZPs have 25 Fresnel zones made with an aluminum layer thicker than the skin depth at 0.5 THz. The thinnest zone is 610 μm and the lens diameter is 25.4 mm (*i.e.*, 1 inch). In the ZP reflector model, an aluminum film thicker than the skin depth at 0.5 THz is considered on the opposite side of the Zeonor substrate. The permittivity of aluminum is described by Drude model:

$$\varepsilon_{\mathrm{Al}} = 1 - \frac{\omega_{\mathrm{p}}^2}{\omega^2 - j\omega\gamma_{\mathrm{s}}}$$

where $\omega_{\mathrm{p}} = 2.243 \cdot 10^{16}$ rad/s is the plasma frequency and $\gamma_{\mathrm{s}} = 1.243 \cdot 10^{14}$ rad/s is the scattering frequency [207].

Fig. 37 shows a comparison between the square modulus of the electric field at 0.5 THz of the two Fresnel ZP lenses. The THz power in the focus area is about 5 times higher if the ZP works in reflection mode instead of transmission mode.

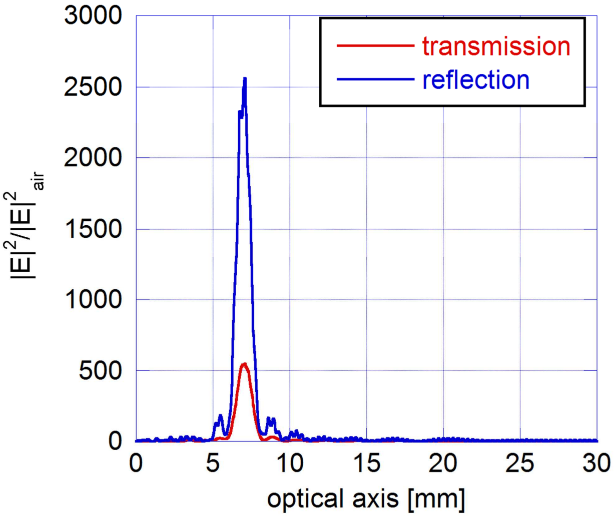

Fig. 37 Computed normalized square modulus of the *z*-component of the electric field at 0.5 THz along the optical axis of a Fresnel ZP working in transmission (red) or in reflection mode (blue).

Moreover, the power of a reflector Fresnel ZP lens in the focus and along the optical axis is higher than the one focused by a phase-reversal multilevel ZP with 28 subzones optimized for 0.5 THz, as shown in *Fig. 38*. However, ZPs in reflection mode are thinner and easier to fabricate than a multilevel phase-reversal ZPs.

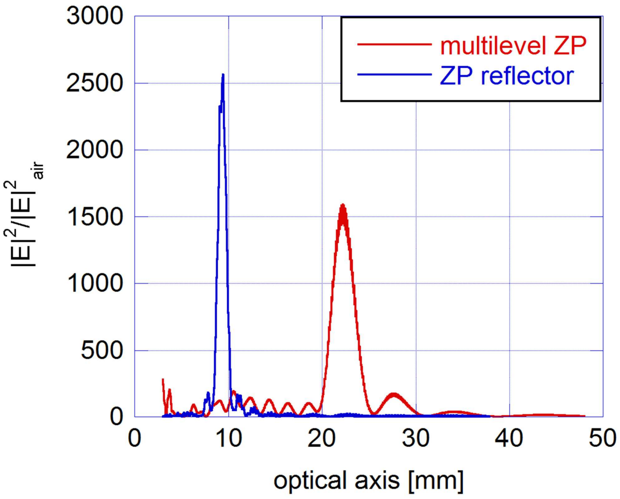

Fig. 38 Comparison between the computed square module of the electric field normalized to the square module of the incident electric field, at 0.5 THz, along the optical axis of a Fresnel ZP reflector and a multilevel phase-reversal ZP (compare Ch. IV).

ZP reflectors are much thinner and easier to fabricate than parabolic mirrors. They are also thinner than a multilevel phase-reversal ZPs. It could open to innovative applications, especially if they are linked to the possibility to consider ZP reflectors as THz antennas. Currently, lens designs for a 45° incident THz plane waves are under investigation.

CHAPTER VIII
Leaky-wave antennas for terahertz far-field applications

1. Introduction

In the previous chapter, the possibility to develop planar THz antennas based on patterned metallic surfaces was introduced. Only few examples of Fresnel ZP antennas already exist at THz frequencies (for example, [127], [208], [209]): new configurations can be implemented and tested, such as the stacked diffractive zone plate. However, a structured study about the design of this device and its radiating performance goes beyond the scope of this thesis.

On the other side, as discussed in chapter I, there is a growing interest toward THz communications, connected to the possibility to have access to Tbps wireless links. For this reason, it could be useful to develop antennas, which (i) could be fabricated with low-cost materials, (ii) are light and simple to integrate, (iii) could be conformable, and (iv) may exhibit reconfigurable properties.

In the field of planar antennas obtained by covering grounded dielectric slabs with patterned metallic screens, leaky-wave antennas (LWAs) are promising devices at THz frequencies. LWAs are travelling-wave antennas successfully employed as radiating systems at microwaves from decades. In LWAs, radiation phenomena are interpreted as the ‘energy leakage’ of a wave that propagates in a partially open structure and progressively loses its energy due partly to the losses (if any) in the medium and partly to the radiation losses [210]. Leaky waves are characterized by a generally complex propagation wavenumber, due to the energy leakage: $k_z = \beta_z - j\alpha_z$, where β_z is the phase constant and α_z is the attenuation constant. Moreover, in order to effectively radiate [211], [212], the leaky wave propagating in the structure has to be a fast wave, *i.e.*, characterized by $|\beta_z| < k_0$, where k_0 is the free-space wavenumber. Therefore, the operation of a LWA is quite different from a slow-wave or a surface-wave type of antenna, for which radiation mainly takes place at discontinuities (*e.g.*, at the edge of the structure) [213]. In the absence of ohmic losses, α_z takes into account only power losses due to radiation and it is called “leakage constant”: it represents the rate of decreasing of the aperture field due to the leakage mechanism of radiation.

The main advantages of LWAs dwell in the easiness of fabrication and design, the simple feeding network, as well as in the ubiquity of leaky-wave phenomena from microwaves, which are the historical starting point of the leaky-wave theory, to nano-optics, thanks to the current developments in metasurfaces and nanostructured materials. For this reason, they are perfectly suitable for being scaled at THz frequencies.

2. Historical path in the development of a leaky-wave theory

At the end of 1930’s, Hansen proposed an antenna made of a rectangular waveguide, in which there was a longitudinal cut for letting leaking away the guided electromagnetic power [214]. It was a very simple and promising device. However, it was only during 1950’s that it was re-examined, but first experimental attempts failed because leaky-wave theoretical fundamentals were unclear. About it, in 1984 Oliner, one of the pioneer of leaky-wave theory, wrote [215]: “It was […] recognized that the leaking waveguide possessed a complex propagation constant, with the usual phase constant and an attenuation constant due to the leakage (in addition to an attenuation constant due to wall losses). The field struggled with two basic problems:

1) Was the leaky wave truly real?

2) How should one determine the leakage constant theoretically?

Since it was obvious that leakage was being produced, why did people question the reality of the leaky wave? If one recalls simply that the squares of the wavenumbers in the three orthogonal directions must sum to the square of the free-space wavenumber, then, if there is decay longitudinally, corresponding to power leakage, the wave amplitude must increase in the transverse (or cross-section) plane. Since the cross section outside of the waveguide is unbounded, this implies that the leaky wave must increase transversely to infinity, yielding an unphysical result. The state of skepticism and uncertainty was so great that the Ohio State group, under V. H. Rumsey, made direct probe measurements [216]. They found that near to the waveguide the field did indeed increase transversely, but that some distance away it dropped off rather suddenly. […] Many people actually expressed surprise on learning that the wave type really exists, but its reality was no longer questioned. Still at issue, however, was how to compute the complex nature of the wave's properties. Several different methods, mostly perturbation approaches, were tried by various people, but most of them were incorrect, and they yielded poor results when they were applied to antenna structures."

Theoretical basis of leaky-wave theory comes from Marcuvitz's work about waveguides [217]. When a system is closed and lossless, any electromagnetic field distribution, which satisfies the boundary conditions, can be expressed as a superposition of eigenmodes. These eigenmodes form a spectrum of modes that is complete, orthogonal and is characterized by finite energy in every direction. Marcuvitz [218] rigorously proved that, when the system is not completely close, *i.e.* it is a waveguide open in one or two directions, the eigenmodes correspond to complex poles of the Green's function of the system. However, this Green's function is located on the incorrect ('improper') Riemann sheet [219] of the transverse wavenumber plane. In fact, a branch point arises when the system is open to infinity in, at least, one dimension, and two sheets are present on the Riemann surface. On one sheet, the 'improper' one, the waves grow at infinity in the transverse direction; on the other sheet, they decay moving to infinity when a small loss is introduced. This second sheet represents the spectral 'proper' solution of the field modes, while the leaky poles occur on the first sheet [215].

This theoretical contribution was important for two reasons [220]: (i) it solved the dispute about the unphysical behavior of the exponential growth at infinity of leaky modes; (ii) the leaky-mode wavenumbers could be considered as solution of the same dispersion equation of any other bound waveguide mode. Consequently, the analytical techniques available for the guided modes study can be also employed for leaky modes. One of this technique is the transverse resonance technique, based on transverse equivalent networks (TENs), which was developed and started to be employed during the Second World War years by Schwinger, Marcuvitz, and other researchers at the MIT Radiation Laboratory [217], [221].

During the late 1950's and the 1960's, the role of leaky waves in several physical phenomena was investigated. Some examples are the Smith-Purcell radiation, the

Cherenkov radiation, Wood’s anomalies on optical gratings, and prism and grating couplers for integrated optics [215].

Since the 1970’s, several radiating structures based on leaky-waves have been designed and deeply studied and a detailed account of them can be found in [210], [220], [222]. However, it is important to just mention that, starting approximately from the new millennium and up to present, LWAs based on metamaterials, metasurfaces, and reconfigurable materials opened new possibilities and new operative frequency ranges. This will be deeply discussed in chapter IX and X.

3. Classification of leaky-wave antennas

Leaky-wave antennas can be divided in several categories, according to their geometrical structure and their principle of operation [222]. A first distinction can be made between one-dimensional (1-D) and two-dimensional (2-D) LWAs. This has influence on the radiation features: a 1-D antenna usually produces fan beams, while a 2-D structure mainly irradiates pencil beams or fully conical beams.

Then, LWAs can also be divided, according to their structure, in uniform, quasi-uniform and periodic antennas. This distinction can affect the antenna scanning characteristics. In fact, a uniform LWA usually scans inside the forward spatial quadrant by varying the operating frequency, while a periodic LWA can scan the radiation beam in both forward and backward quadrants.

However, some exceptions could exist. A brief overview of these categories will be made in the following subsection.

3.1 One-dimensional uniform leaky-wave antennas

In 1-D LWAs, the antenna guiding structure is essentially one-dimensional: the structure supports a wave that travels in only one direction. A rectangular waveguide with a longitudinal slit (see *Fig. 39*), which allows the radiation, is an example of 1-D LWA [223]. It can also be considered a uniform LWA because the transverse cross section does not change along the longitudinal axis. In general, a 1-D LWA is characterized by a length equal to several wavelengths, while the cross section is usually in the order of the wavelength. A 1-D LWA radiates along its length L and its radiating behavior is comparable with the one of a conventional 1-D aperture antenna [224]. The main difference is that the aperture field of a LWA is dominated by the distribution of the relevant leaky mode of the structure [220], and thus has an exponentially-decaying profile.

In *Fig. 39*, a ground plane is employed as wave deflector; on it, a very narrow slot can be etched at one lateral end of the structure. It is equivalent to an infinite magnetic line current flowing in free space in the direction coinciding with the propagation direction of electromagnetic waves, *i.e.*, the z-direction of *Fig. 39*. If the LWA has a finite length, the line source is of finite length. The corresponding radiation pattern has the form of a cone with the axis coinciding with the z-axis: the radiation is limited to the forward quadrant ($z > 0$). As the angle between the cone and the z-axis approaches 90°, the radiated beam comes near to a broadside beam with a narrow-beam donut broadside pattern.

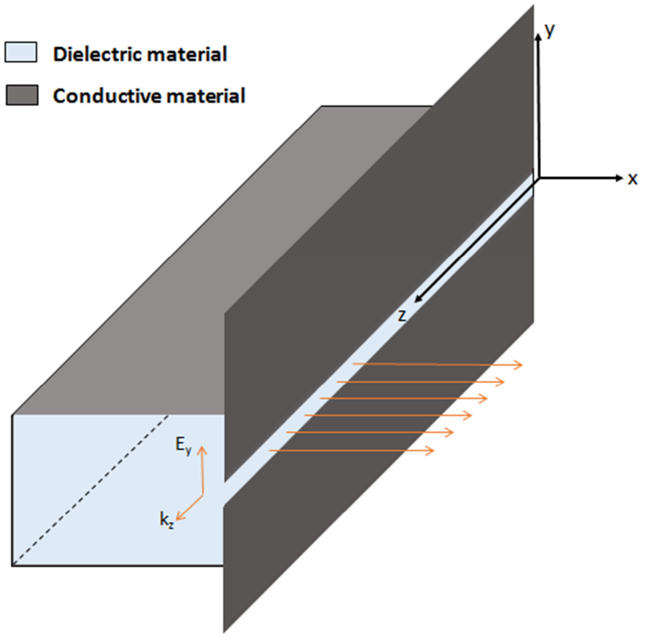

Fig. 39 A rectangular waveguide, as an example of 1-D uniform LWAs. The electromagnetic field propagates in z-direction. An infinite ground plane surrounds the slot [222].

However, if a 1-D uniform LWA is fed at one end, it can difficultly obtain a beam at broadside. A broadside beam can be achieved by feeding the antenna at both ends, or at the center of the structure. In this way, two beams are created, each pointing close to broadside but on opposite sides of it, shaping a single broadside beam [222].

Moreover, the range of scanning can include both forward and backward quadrants if nonconventional materials, such as ferrites or metamaterials, are loaded in 1-D uniform structures [225].

3.2 One-dimensional periodic leaky-wave antennas

An example of periodic 1-D LWA is the structure illustrated in *Fig. 40*. It is a 1-D antenna because the waves propagate in one direction, even if the width of the antenna, in the perpendicular direction with respect to the propagation direction, is large. Because of the width of the structure, this antenna can irradiate a fan beam or a pencil beam [222]. However, the beam can scan only one plane, *i.e.*, the forward quadrant, unless the unloaded structure is fed from both ends.

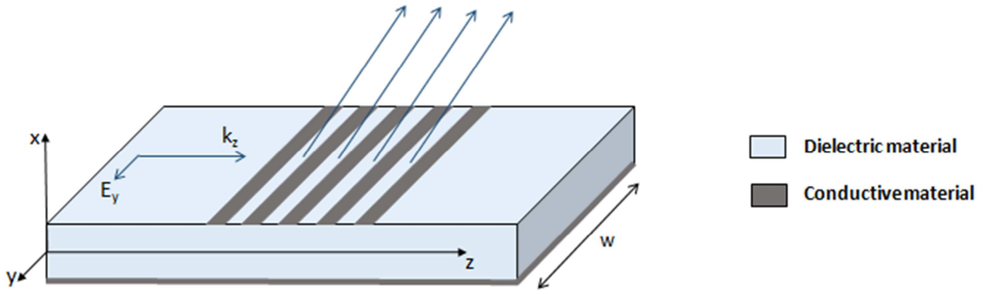

Fig. 40 An example of periodic 1-D LWA. This antenna configuration has a width, *w*, larger than the operative wavelength. The electric field is in y-direction and the electromagnetic wave propagates in *z*-direction.

In general, a periodic 1-D LWA derives from a dielectric waveguide periodically loaded by perturbations. The unperturbed waveguide usually supports an operating guided mode as a surface wave, which is slow ($\beta_z < k_0$), and is not able to radiate. A suitable periodic loading of the guide permits to describe the overall field in terms of a series expansion of Floquet’s modes or space harmonics with phase constants:

$\beta_{z,n} = \beta_z + 2\pi\, m/p$, where m is an integer and p is the period. Typically, in open structures, one of these space harmonics (usually the $m = -1$) becomes a fast wave (*i.e.*, a leaky-wave with $\beta_z > k_0$). The phase constant of the leaky wave could assume positive and negative values as the operating frequency changes: this LWA allows for radiation both in the forward and in the backward quadrant. However, the scanning region of simple LWA geometries, as the one in *Fig. 40*, usually shows a degradation in the radiation efficiency around broadside; specific more complex geometrical periodic patterns could be introduced for avoiding it [220], [222], [226].

The periodic LWAs considered above are characterized by a period comparable with the operating wavelength. Conversely, when the period is $p < \lambda/4$, the fast harmonic can be obtained for $m = 0$. These structures are called homogenizable periodic LWAs [220] or, similarly, quasi-uniform LWAs [222]. These antennas are structures based, *e.g.*, on metamaterials and metasurfaces, and can work both in 1-D and 2-D configuration.

3.3 Two-dimensional leaky-wave antennas

Two-dimensional LWAs are 2-D open waveguiding structures where a single source excites partially-guided electromagnetic fields [222]. An example of this LWA category is shown in *Fig. 41*, which represents a planar multilayered dielectric structure based on substrates and superstrates.

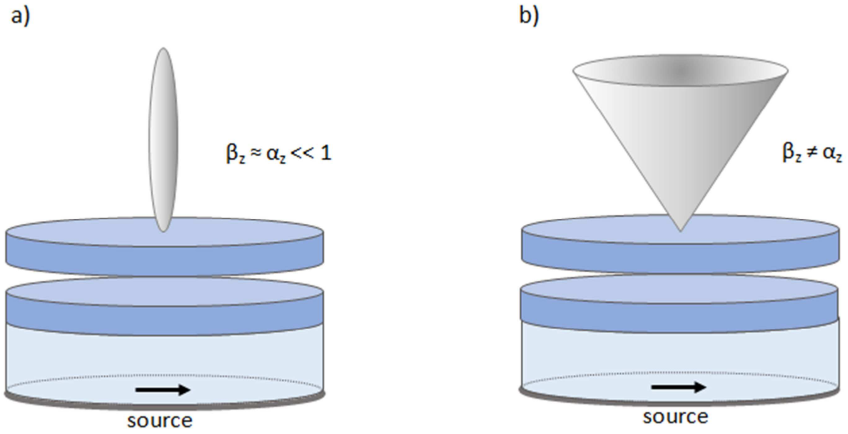

Fig. 41 An example of a 2-D LWA: the substrate-superstrate LWA. It can produce a) a pencil beam at broadside or b) a conical beam with an angle θ with respect to the broadside direction.

When a 2-D LWA is centrally fed, a cylindrical leaky wave is excited and radially propagates in the structure. Therefore, the leaky wave is characterized by a radial complex wavenumber, $k_r = \beta_r - j\alpha_r$, and the leakage mechanism in the upper space is associated with an outward wave propagation. Radiation features are derived by exploiting the cylindrical symmetry: the radiated beam usually has a conical shape (*Fig. 41 b)*) with an elevation main-beam pointing angle that continues to be regulated by the leaky-wave phase constant, while the attenuation constant affects the beam width [220].

However, if the normalized phase and leakage constants are almost equal and much less than unity, a pencil beam at broadside is achievable (*Fig. 41 a)*). In this regard, several techniques can be employed for controlling the leakage mechanism, such as the arrangement of substrate–superstrate layers (as in distributed Bragg reflectors (DBRs) [227]), the use of partially reflecting surfaces with periodic perturbations, the introduction of artificial homogenizable structures, and the use of special complex media, such as plasmas or graphene [210]. More details about 2-D LWAs will be given in the following chapters, where a substrate-superstrate 2-D LWA (Ch. IX) and several designs for a metasurface 2-D LWA (Ch. X) are developed and widely analyzed at THz frequencies.

4. Operation principles of leaky waves

A simple case of an aperture can be considered for evaluating the electromagnetic field behavior in a LWA (for example, compare *Fig. 39*) [222]. In correspondence of the aperture, *i.e.*, $x = 0$, the electric field $E_y(x, z)$ is

$$E_y(0, z) = Ae^{-jk_z z} \qquad \text{(VIII.1)}$$

where A is an arbitrary constant and the leaky-wave wavenumber is complex: $k_z = \beta_z - j\alpha_z$.

In the air region above the aperture, *i.e.*, $x > 0$, the electric field is

$$E_y(x, z) = Ae^{-jk_z z}e^{-jk_x x} \qquad \text{(VIII.2)}$$

where the vertical wavenumber is $k_x = \sqrt{k_0^2 - k_z^2}$, with k_0 being the wavenumber of the free space. It means that

$$\beta_z \alpha_z = -\beta_x \alpha_x \qquad \text{(VIII.3)}$$

When a wave is forward, $\beta_z > 0$ and $\alpha_z > 0$. If it is propagating away from the structure, in vertical direction, it follows from equation VIII.3 that $\alpha_x < 0$, and the wave propagating in the air region is exponentially increasing. Therefore, even if the wave is decaying in the propagation direction (z-direction) due to leakage losses, it exponentially increases in the surrounding air region. For this reason, the leaky wave is called ‘improper’ [222].

At a first glance, as said, it could seem an unphysical behavior. However, its physical meaning can be explained by considering a ray diagram [211], [212], as the one in *Fig. 42*.

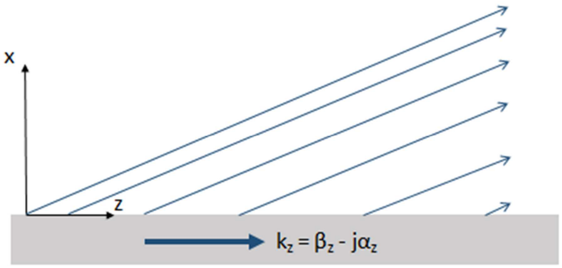

Fig. 42 Ray diagram of a forward leaky-wave. The intensity of the field is given by arrows separation: closer arrows correspond to a stronger field [222].

For an inhomogeneous plane wave, such as a leaky-wave, the power flow is in the direction of the phase vector, which is the real part of the complex wavenumber vector:

$$\boldsymbol{\beta} = \hat{\boldsymbol{x}}\beta_x + \hat{\boldsymbol{z}}\beta_z = Re(\boldsymbol{k}) = Re(\hat{\boldsymbol{x}}\beta_x + \hat{\boldsymbol{z}}\beta_z) \qquad \text{(VIII.4)}$$

The angle between the z-axis and the phase vector is

$$\tan(\theta_0) = \frac{\beta_x}{\beta_z} \qquad \text{(VIII.5)}$$

It can be approximated to

$$\cos(\theta_0) = \beta / k_0 \qquad \text{(VIII.6)}$$

if the attenuation constant α is small. Equation VIII.6 is a very useful relation for evaluating the beam angle in several practical problems.

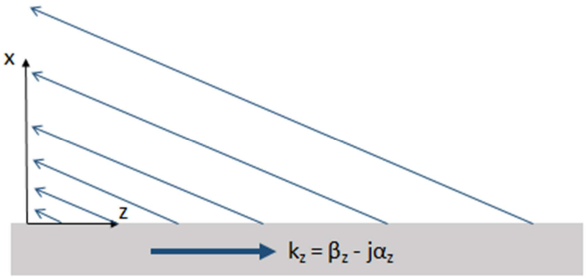

Fig. 43 Ray diagram of a backward leaky-wave. The intensity of the field is given by arrows separation: closer arrows correspond to a stronger field [222].

In the situation in which the leaky wave is a backward wave, the phase and group velocities are in opposite directions. In *Fig. 43*, it is assumed that the group velocity, that has generally the same direction of the power flow (an exception is represented by anomalous dispersive media [228]), is in the positive *z*-direction and the phase velocity has the negative *z*-direction: therefore, $\beta_z < 0$. Because the phase front increases away from the aperture, $\beta_x > 0$ and, according to equation VIII.3, $\alpha_x > 0$. The field associated to the leaky-wave decays exponentially in vertical direction from the aperture and the leaky wave is considered a 'proper' wave. A uniform LWA usually only supports a forward wave, while a periodic LWA can support either wave type [222]. The consideration about the physical and unphysical behavior of the field associated to leaky-waves has to be always taken into account in the analysis of a LWA structure.

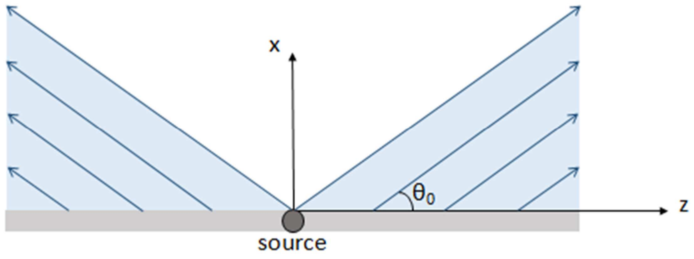

Fig. 44 Ray diagram of a leaky-wave excited by a source located in z = 0 [222].

However, in the previous discussion, an infinite propagation along the *z*-axis (*i.e.*, $-\infty < z < +\infty$) is considered. In a practical situation, the leaky wave is excited by a source located in a point of the structure and is not able to exist in the whole range. If the source is located in $z = 0$ and the wave is excited equally in both directions, the field on the aperture is:

$$E_y(0, z) = \mathrm{A}e^{-jk_z|z|} \qquad \text{(VIII.7)}$$

In this situation, the wave exponentially decays in both negative and positive z-direction. If the wave is a forward wave, the ray diagram (*Fig. 44*) is symmetric with respect to the x-axis (in the following, only the $z > 0$ part of the structure is considered). Moreover, a shadow region is defined at $|\theta| < \theta_0$, beyond which there is approximately no field, while a field comparable with that of the infinite leaky wave (*Fig. 42*) is confined in the region with $|\theta| < \theta_0$. It means that, moving away from the aperture in vertical direction, the field strength exponentially increases until the leakage shadow region and, then, above this limit, rapidly decreases. Consequently, the field does not increase indefinitely in the x-direction and does not violate the radiation condition at infinity: it has a physical meaning. The interested reader can refer to [210], [220]–[222], [229] for a rigorous mathematical description of the physical meaning of leaky waves.

5. Leaky-wave antenna analysis and design techniques overview

Nowadays, electromagnetic commercial CAD tools (compare Ch. III) allows for accurate full-wave analyses of complex structures. However, alternative methods for the design of LWAs are still of interest, because most of them enables an intuitive and efficient antenna characterization. Moreover, the general-purpose numerical methods show limitations and high computation times, especially when electrically large LWA structures are studied with high accuracy [220].

An efficient theoretical and numerical characterization of LWAs is usually based on the evaluation of the phase and attenuation constants of the dominant leaky mode that describes the aperture field. Methods based on the dispersion analysis of the propagating modes are able to furnish a very useful insight into the physical phenomena involved in such structures. In particular, the analysis of LWAs can be based on the evaluation of the generally complex eigensolutions of open waveguides by means of the study of their physical parameters involved, such as the geometrical features and the frequency behavior. Commonly, it is achievable through numerical methods [230].

As discussed in chapter III with regard to the design of diffractive lenses, the most appropriate choice depends on several factors related to the computational features of the methods, the geometry of the open structures, and so on [230]. Among numerical tools, the integral equation techniques are interesting approaches for the analysis of planar antennas, such as LWAs. Moreover, FD approaches are suited for the derivation of the eigensolutions in planar and printed structures [220], [230]. The method of moments (MoM) [230] is an integral equation technique that makes possible to include the description of the periodic conditions and the background geometry in the periodic Green’s functions (PGF) of the problem [231], [232]. Several kinds of Green’s functions can be defined: a mixed-potential integral equation (MPIE) formulation is usually implemented for spatial-domain MoM [233], in combination with acceleration techniques and interpolation procedures for increasing method efficiency [234].

Differential equation techniques can be also employed. In particular, methods based on a finite difference time domain (FDTD) technique [235], [236] can be used to calculate the dispersion diagram of leaky modes supported by 1-D and 2-D periodic structures.

Since the 1950’s, one of the most employed approaches for the evaluation of leakage phenomena in open waveguides is based on the transverse resonance technique (TRT) [220], [224], [230]. This method is still applied because it permits both a rigorous and an approximate LWA evaluation. In the TRT, a suitable equivalent transmission-line network (TEN) is developed for describing the cross-section geometry of the structure and is numerically solved in terms of transverse eigenvalues and physical parameters. Several works are present in the literature, mainly based on the representation of the equivalent apertures in partially open metallic waveguides [220], [237], [238].

For the analysis of periodic LWAs, the unit-cell approach [239] is an efficient method. It enables the derivation of the behavior of the whole antenna simply considering only one geometrical period and the effects due to the external environment. In a TEN, this study can be implemented changing the description of the radiation termination for a periodic environment (infinite number of linear elements) and calculating an active admittance, which describes the external radiating region as a function of the scan angle and the geometrical parameters [240]. When an accurate characterization of periodic structures is needed, the electromagnetic problem is formulated, discretized, and solved inside the unit cell by applying Floquet periodic boundary conditions along the directions of periodicity.

All of these computational techniques are essential tools in the development of efficient and accurate analysis of leakage phenomena on several different LWA structures. Among the methods outlined in this brief list, the TRT will be illustrated with more detail in the following subsection.

5.1 Transverse resonance technique

A standard method for the analysis of complex structures is: (i) to formulate the general solution of Maxwell's equations in a homogeneous region of the domain of interest; (ii) to apply the boundary conditions; (iii) to enforce the determinant of the coefficients to 0; (iv) to find the complex roots of the resulting equation, which is called dispersion equation. This procedure can be time consuming, especially if the domain of interest is composed by more than one medium.

In the situation in which only the determination of the eigenvalues is of interest, the transverse resonance technique represents an appropriate tool. In fact, the eigenvalues of a waveguide problem correspond to pole singularities of a suitable characteristic Green's function in the complex plane of the propagation wavenumber. This Green's function can be identified as the voltage (or current) on a transmission line along one of the transverse direction of the waveguide axial direction [221], [223]. The pole singularities correspond to the TEN model resonances and are usually computed using analytical methods.

A general form of terminated TEN is given in *Fig. 45*.

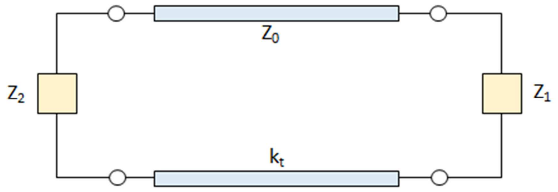

Fig. 45 Terminated equivalent network representing a waveguide cross-section [223].

The transverse wavenumber k_t that corresponds to source-free fields in the waveguide can be derived from the solution of the resonance equation:

$$Z(k_\mathrm{t}) = \vec{Z}(k_\mathrm{t}) + \overleftarrow{Z}(k_\mathrm{t}) \quad \text{or} \quad Y(k_\mathrm{t}) = \vec{Y}(k_\mathrm{t}) + \overleftarrow{Y}(k_\mathrm{t}) \qquad \text{(VIII.8)}$$

where $\vec{Z}$, $\vec{Y}$, $\overleftarrow{Z}$, and $\overleftarrow{Y}$ are the impedances or admittances from the left and the right of an arbitrary reference plane. A closed-form analytical solution to this resonance equation does not generally exist, except for very simple canonical examples, such as the parallel-plate waveguide.

In the simple situation in which the leaky wave can be seen as a perturbation of a mode in a closed waveguide [223], the transverse wavenumber can be considered as:

$$k_\mathrm{t} = k_\mathrm{t0} + \Delta k_\mathrm{t} \qquad \text{(VIII.9)}$$

where k_t0 is the wavenumber of the unperturbed mode and Δk_t is the perturbation. If the cross-section is homogeneous, the resonance equation can be written in terms of normalized impedances (admittances), expanded in the point $k_\mathrm{t} = k_\mathrm{t0}$:

$$Z'(k_\mathrm{t0}) + \left(\frac{dZ'(k_\mathrm{t})}{dk_\mathrm{t}}\right)_{k_\mathrm{t}=k_\mathrm{t0}} \Delta k_t \approx 0 \qquad \text{(VIII.10)}$$

according to which:

$$\Delta k_\mathrm{t} \approx -\frac{Z'(k_\mathrm{t0})}{\left(\frac{dZ'(k_\mathrm{t})}{dk_\mathrm{t}}\right)_{k_\mathrm{t}=k_\mathrm{t0}}} \quad \text{or} \quad \Delta k_\mathrm{t} \approx -\frac{Y'(k_\mathrm{t0})}{\left(\frac{dY'(k_\mathrm{t})}{dk_\mathrm{t}}\right)_{k_\mathrm{t}=k_\mathrm{t0}}} \qquad \text{(VIII.11)}$$

where $Z' = Z/Z_0$ is the normalized impedance, and $Y' = Y/Y_0$ is the normalized admittance.

However, the TEN has to be adapted to the specific structure under examination. Some practical examples can be found in chapter IX and X, where the TEN of two 2-D LWAs are developed with different techniques.

6. Leaky-wave antennas at terahertz frequencies

As discussed above, leaky phenomena are valid for a large range of frequencies, from microwaves to optics. For this reason, LWAs working at THz frequencies are feasible and some examples of devices are already present in the scientific literature. A summary of the main proposed types in the frequency range from about 0.3 THz to 3 THz is presented in *Table 8*.

Table 8 Leaky-wave antennas typologies and examples, working in the frequency range of 0.3 - 3 THz. In the headers, *f* is the frequency at which the antennas are investigated, while η is the radiation efficiency.

	Measured device?	**Materials**	**Feeding**	***f* [THz]**	**Directi-vity [dB]**	**η [%]**	**Beam width [°]**	**Ref.**
Lens antenna	yes	Si, SiN_x, Au, Al	wave-guide	0.3 – 2.8 (discrete values)	< 42.1	< 75	-	[241]–[246]
Periodic corrugated metallic wire	no	PEC	-	0.9655 – 0.9829	-	90	22	[247]
Flat corrugated antenna	yes	gold	slot	0.566	16	-	7	[248], [249]
Composite right/left-handed metamaterial waveguide	yes	$GaAs/Al_{0.15}Ga_{0.85}As$ + Cr/Au + Ni + Ti/Au/Ni	metal-metal QCL cavity	2.48 and 2.59	-	-	10 (at 2.48 THz) 15 (at 2.59 THz)	[250]
Metasurface antennas	no	*see Table 9*						
Tunable antennas	*see Table 10*							

The choice of this specific frequency band is linked to the technological issues already discussed in chapter I: even if the border between millimeters waves and far-IR has not been delimited yet, below 0.3 THz, facilities developed for the millimeter waves are available, while, above 3 THz, the mechanisms connected to the description of far-IR radiation are predominant.

The most studied THz LWA is a leaky-wave waveguide coupled with a hemispherical silicon lens. It is able to operate at a fixed value of frequency [241], [246] or in a frequency band of 0.2 THz [242] until 1.4 THz [243]–[245] wide. When the device works at a single frequency, it can show a very high directivity; for example [241], of 42.1 dB. Lens LWAs able to operate in a frequency band wider than 1 THz can be employed for practical applications, such as THz detectors (described in Ch. I, Sec. 3). However, independently from the operating frequencies of the antenna, the radiation efficiency is always below 75%, due to losses introduced by the coupling with a silicon lens (see Ch. V).

Table 9 Metasurfaces FPC-LWAs in the frequency range 0.3 - 3 THz. In the headers, *f* is the frequency at which the antennas are investigated, while *η* is the radiation efficiency.

	Materials	**Feeding**	***f* [THz]**	**Gain (max) [dBi]**	***η* [%]**	**3-dB gain Bandwidth [%]**	**Ref.**
5x5 square patches array	GaAs + metal	open-ended slotline or an array of 5 slit	0.34 - 0.4	9.8 (single feed) 15.5 (feed array)	69 (single feed) 73 (feed array)	16 (single feed) 17.3 (feed array)	[251]
7x7 circular patches array	GaAs + metal	open-ended slotline	0.315	11.3	72	3	[252]
7x7 ring patches array	GaAs + metal	open-ended slotline	0.315	11.4	75	22.5	[252]
7x7 circular hole array	GaAs + metal	open-ended slotline	0.318	15.3	60	1.3	[252], [253]

Another class of LWAs, widely employed at THz frequencies, is that of Fabry-Perot cavity (FPC) LWAs. They are 2-D LWAs inspired by the Fabry-Perot concept: the radiation phenomenon is interpreted in terms of multiple reflections between a ground plane and a partially reflective sheet (PRS). In this kind of LWAs, the maximum radiated power at broadside is connected to the resonance condition of the multiple reflections. For this reason, they usually work at a single frequency, *i.e.* at the resonance frequency of the FPC. The PRS can assume several forms. In *Table 9*, the performances of FPC-LWAs with different metasurface geometries are compared. A metasurface is, in general, a metallic patterned surface, in which the geometrical elements composing the pattern have dimensions deeply below the operative wavelength. It means that this surface can be considered as a homogeneous surface with properties depending on the specific geometrical pattern chosen for the metasurface synthesis. Even if several geometries have been investigated in the THz range as PRS for FPC-LWAs, none of them has been fully characterized yet. However, they show advantages common to many LWAs, such as the suitability to miniaturization and integration on complex devices or the scalability at every THz frequency value of operation. In addition, they are also: (i) simple to fabricate, (ii) with an affordable fabrication cost, and (iii) suitable for mass production. The radiation efficiencies, computed for the structures presented in *Table 9*, do not go beyond the

75%, but the high number of degrees of freedom in the metasurfaces design may allow for higher values.

Table 10 Leaky-wave antennas with a reconfigurable pointing angle, working in the frequency range between about 0.3 THz and 3 THz. In the headers, f is the frequency at which the antennas are investigated, η is the radiation efficiency, and $\Delta\theta$ is the maximum variation of the pointing angle.

	Measured device?	Materials	Feeding	f [THz]	η [%]	$\Delta\theta$ [°]	Beam-width [°]	Ref.
Microstrip-based periodic antenna	yes	cyclic olefin polymer + copper	wave-guide	0.235 - 0.325	-	38	4	[254], [255]
Graphene antenna based on a grating structure	no	quartz + SiN_x + graphene sheet	-	1.5	-	56.3	-	[256]
Fabry-Perot cavity graphene antenna	no	SiO_2 + PEDOT + HfO_2 + graphene	dipole-like on a ground plane	0.922 - 1.062	29 - 70	18 - 90	20.20 - 35.27	[257], [258]
Graphene antenna	no	SiO_2 + polysilicon + graphene	-	2	19	82.9	-	[259], [260]
Substrate-superstrate graphene antenna	no	SiO_2 + HfO_2 + graphene	dipole-like on a ground plane	1.14	-	45	6.75 - 22.46	[258], [261]

An interesting opportunity offered by FPC-LWAs is the possibility to develop a THz antenna with a reconfigurable pointing angle at a fixed frequency (see *Table 10*, *rows 2-5*). The only way, currently present in literature in the frequency band of interest, to steer the beam is by employing a graphene sheet as a PRS [256]–[262]. In fact, the electronic and optical properties of graphene can be tuned by applying a control voltage to the material sheet. At THz frequencies, graphene surface conductivity, which is the parameter that completely characterizes its electromagnetic properties, due to the mono-atomic layer structure, becomes mostly reactive [263]. The main advantage of graphene antennas is that they can theoretically steer the beam over the whole angular range by simply applying an external DC voltage. However, none of them has been fabricated and characterized in the THz band yet. Moreover, the antenna properties, especially in terms of radiation efficiency and reconfigurability, are deeply influenced by the graphene quality mainly determined by the synthesis technique and the interaction with the substrate, as well.

An alternative way to steer the beam is to change the operating frequency. An example is presented in *Table 10*, *row 1*, where a microstrip LWA with periodic elements is investigated as a THz radar and show a beam steering over an angular range of 38°, with a very narrow radiated beam. However, this kind of device has a limited application as radar to a short range object detection [254].

Other forms of PRS for FPC-LWAs working in the THz range will be widely analyzed in chapter IX and X, where a reconfigurable multilayered structure as well as some metasurface geometries will be designed and numerically investigated.

7. Conclusions

Leaky-wave antennas are fast traveling-wave antennas, in which radiation occurs thanks to a power leakage during the wave propagation. They are antennas characterized by a high directivity and by the possibility to be employed as radiating systems at microwaves as well as at optical frequencies.

For these reasons, LWAs seem to be particularly suitable for being integrated in THz systems. Among the several existing LWAs typologies, FPC-LWAs are attractive structures because they allow for tuning the radiation beam steering by applying an external voltage.

In the next chapters, two different FPC-LWAs will be designed and deeply investigated as promising devices for THz far-field applications.

CHAPTER IX

Fabry-Perot cavity leaky-wave antennas based on liquid crystals for terahertz beam-steering[2]

1. Introduction

Two-dimensional (2-D), bidirectional, quasi-uniform LWAs are a class of 2-D LWAs obtained as a perturbation of a metallic parallel-plate waveguide, where the upper plate is replaced by a PRS to allow radiation. Among them, FPC-LWAs are characterized by two features: (i) the thickness of the slab constituting the antenna substrate is close to half a wavelength in the medium; (ii) the PRS can be described by a single homogenized impedance. In fact, PRSs can take several forms, such as: a denser dielectric superstrate [264], a graphene sheet [262], a metamaterial or a metasurface, etc.. For most of PRSs constituted by a periodic arrangement of sub-resonant elements, homogenization formulas can be derived [265]–[267], permitting to derive the homogenized impedance of the PRS.

In this chapter, a PRS based on a metamaterial is introduced. The metamaterials are artificial materials obtained by the combination of different materials, present in nature, with spacing and geometrical features below the wavelength dimension. Since metamaterials can show values of dielectric permittivity and permeability that are impossible for natural materials, they allow for a considerable control of the electromagnetic radiation, helping in the development of interesting applications [268], [226].

---

[2] Most of information reported in this chapter is with courtesy of Dr. Walter Fuscaldo and was born from a collaboration with him. More details about theoretical background in the development of Fabry-Perot cavity leaky-wave antennas for THz applications can be found in his PhD thesis: “Advanced radiating systems based on leaky waves and nondiffracting waves”.

Even if several metasurface designs already exist for microwave applications [269]–[271], only few implementations have been proposed in the THz range [272], [273]. In this chapter, the possibility to develop an electro-optically tunable metasurface LWA is investigated. In fact, as discussed in chapter VII, LCs can be employed for the realization of different THz devices, such as, for example, composite free-space materials [274]–[276] as well as guided-wave THz phase shifters [277], [278]. However, only few works have considered the possibility of designing LCs reconfigurable THz LWAs. In the following sections, a THz FPC-LWA based on LCs is discussed in terms of theoretical and numerical modeling, underlining the conditions at which a device fabrication is feasible.

2. Liquid crystals for the design of a tunable leaky-wave antenna

As discussed in chapter VII, the application of a voltage to LCs change the direction of the molecules director, tuning the LCs dielectric properties. Therefore, the phase constant of the leaky-wave modes changes too, causing the radiation beam-steering at a fixed frequency. Among the different kinds of LC mixtures, the uniaxial nematic LCs, already employed in the numerical study of LC tunable diffractive lenses (see Ch. VII), is considered because of its high birefringence and moderate losses at THz frequencies [152].

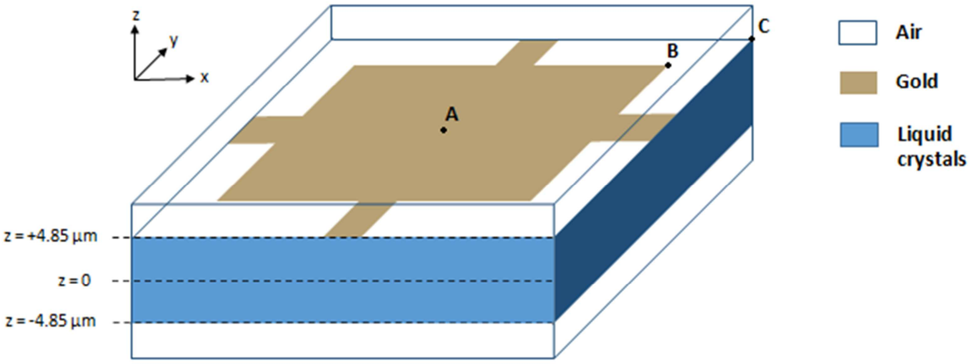

Fig. 46 LC cell driven by a gold fishnet electrode.

Thanks to the Q-tensor analysis (described in Ch. VII Sec. 2.1.2), values of all components of permittivity tensor can be numerically evaluated by changing the voltage from zero until the threshold value. For this computation, the LC cell, as presented in [152] and reported in *Fig. 46*, has a total thickness of 9.7 μm and its threshold voltage can be set equal to 7 V. Differently from the dual-focus diffractive lens which works in the absence of external voltage or with a voltage above the threshold, in this situation the device is designed for operating at every value of voltage from zero until the threshold.

As can be seen from *Fig. 47*, the ordinary value of the real part of LC dielectric permittivity is $\mathrm{Re}(\varepsilon_{\mathrm{o}}) \cong 2.42$, while the real part of extraordinary permittivity is $\mathrm{Re}(\varepsilon_{\mathrm{e}}) \cong 3.76$. Moreover, the LC director does not change along the *y*-direction and it is possible to consider $\varepsilon_y = \varepsilon_{\mathrm{o}}$.

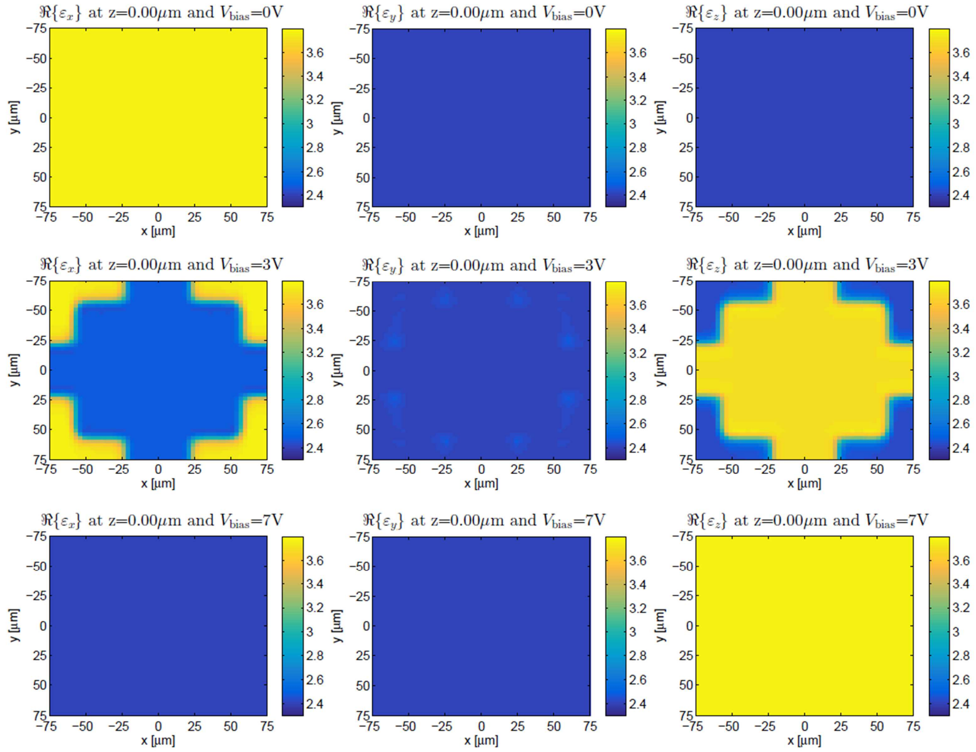

Fig. 47 Real part of the three main components of the LC permittivity tensor mapped in the *xy*-plane, in the middle of the LC cell (*z* = 0). The LCs behavior is show in absence of an external field (first row), for a voltage above the threshold (last row), and for an intermediate value of driving voltage (middle row) [with courtesy of Dr. W. Fuscaldo].

It is worth to stress that the chosen mixture contains uniaxial LCs. This would allow for a simplified electromagnetic description of LC layers in the equivalent circuit model (compare Ch. VIII Sec. 5.1). On the contrary, when the LC is not uniaxial, off-diagonal components of the permittivity tensor are no longer negligible and more complicated equivalent networks have to be considered [279].

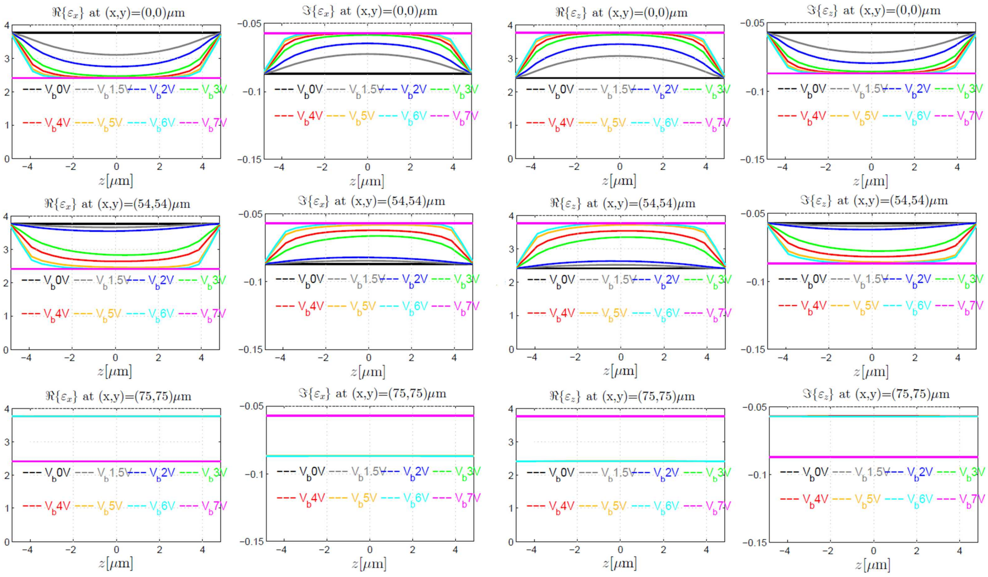

Fig. 48 Real and the imaginary part of the LC dielectric permittivity along a line perpendicular to the *xy*-plane and passing through three selected points of the LC cell [with courtesy of Dr. W. Fuscaldo].

In addition to the real permittivity map of the *xy*-plane of the LC cell, it is also important to know the permittivity profile in *z*-direction for values of voltage from 0 V until the threshold, *i.e.*, 7 V. Three different points, as indicated in *Fig. 46*, are chosen: A ((x_0, y_0) = (0, 0) µm) is in the middle of the electrode, B ((x_0, y_0) = (54, 54) µm) is at the edge of the electrode, and C ((x_0, y_0) = (75, 75) µm) is outside the electrode. The plot of the real and the imaginary part of the LC dielectric permittivity along a line perpendicular to the *xy*-plane and passing through these three points is shown in *Fig. 48*, with regard of the ε_x and ε_z components. The variation is quite uniform in correspondence of the middle and the edge of the electrode: anchoring forces change permittivity profile in the first micrometer of thickness in contact with boundaries; however, away from boundaries, the applied voltage is completely able to pilot the LC molecules, determining a uniform permittivity profile. No variation is seen outside the fishnet, where there is no applied electric field. As expected from uniaxial LC physics,

ε_x and ε_z exhibit a specular nonlinear variation as the bias changes from 0 V (unbiased state) to 7 V (fully biased state).

For the sake of brevity, in the design of a tunable FPC-LWA, only averaged values of LC layers permittivity and the two limiting voltage cases (*i.e.*, unbiased and fully-biased states) are studied to investigate the maximum tunability range of the THz LWA.

3. Tunable Fabry-Perot cavity leaky-wave antenna design

The proposed THz FPC-LWA consists of a multistack of materials: high-permittivity dielectric material layers, such as the alumina (Al_2O_3), are alternated with low-permittivity material layers, such as the LCs described in the previous section.

The multistack of alternating layers could be interpreted as a distributed Bragg reflector (DBR), meaning that it is a periodic electronic bandgap (EBG) structure operating in a stopband [280]. A leaky-wave explanation of the phenomenon is provided in [281].

Material layers in the multistack need to have a thickness equal to the odd multiples of a quarter wavelength in their respective media. In this way, the alternation of such layers allows for obtaining a narrow radiated beam at broadside [281]. The multistack is placed above a grounded dielectric slab (GDS), as shown in *Fig. 49*. The material chosen for the substrate layer is the Zeonor because, in the THz range, the real part of its dielectric permittivity (~2.3) is almost matched with the real part of the ordinary dielectric permittivity (~2.42) of the LC mixture [152], [203]. It is required to properly enhance the resonance condition in a FPC [281]. Moreover, Zeonor is a low absorption material at THz frequencies and introduces negligible losses overall (for a discussion of Zeonor properties, see Ch. II Sec. 5).

In the proposed device, the innovating feature is represented by the use of LCs as low-permittivity layers, which leads to the beam-steering at a fixed THz frequency.

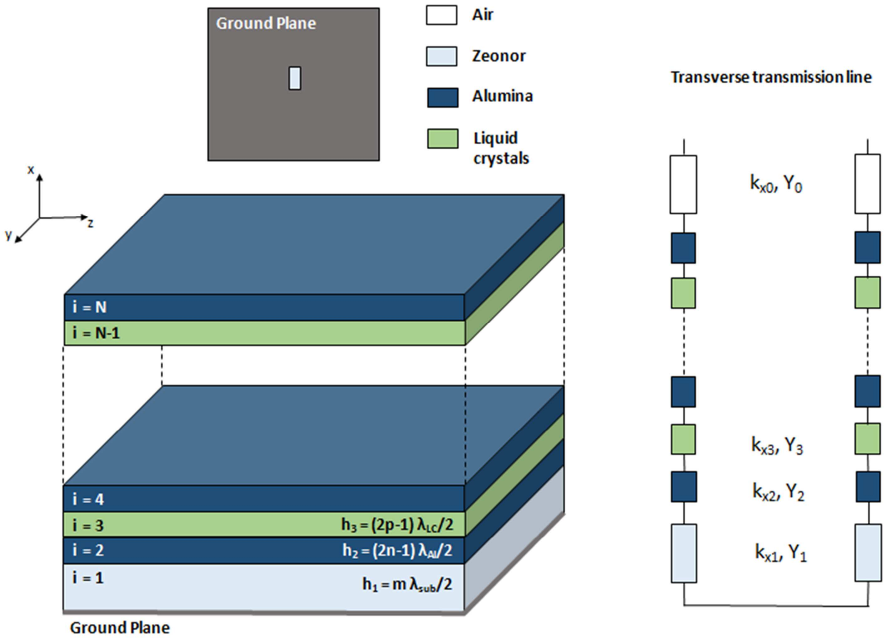

Fig. 49 Schematic representation of the proposed FPC-LWA and its equivalent transmission line model.

A circuit model of the proposed device is shown in *Fig. 49*. It takes into account the anisotropy of LC layers considering:

$$\bar{\bar{\varepsilon}}(V) = \begin{bmatrix} \varepsilon_x(V) & 0 & 0 \\ 0 & \varepsilon_o & 0 \\ 0 & 0 & \varepsilon_z(V) \end{bmatrix} \qquad \text{(IX.1)}$$

According to the reference frame shown in *Fig. 49*, when no bias is applied, LC molecules are aligned along the horizontal *z*-axis and $\varepsilon_z(V=0) = \varepsilon_e$. When a sufficiently large driving voltage (V_∞) is applied to LC molecules, their director is reoriented along the vertical *x*-axis and $\varepsilon_x(V = V_\infty) = \varepsilon_e$.

With regard to the transverse transmission line model (*Fig. 49*), the characteristic admittances, Y_3, and the normal wavenumbers, k_{x3}, of the LC layers for both transverse-electric (TE) and transverse-magnetic (TM) polarizations (with respect to the *xz*-plane) are functions of the bias voltage. Their expression is given by:

$$Y_3^{\mathrm{TE}} = \frac{k_x}{\omega\mu_0} \quad \text{and} \quad Y_3^{\mathrm{TM}} = \frac{\omega\varepsilon_0\varepsilon_z^2(V)}{k_x} \qquad \text{(IX.2)}$$

$$k_{x3}^{\mathrm{TE}} = \sqrt{k_0^2\varepsilon_y - k_z^2} \quad \text{and} \quad k_{x3}^{\mathrm{TM}} = \sqrt{\frac{\varepsilon_z(V)}{\varepsilon_x(V)_0}\, k_0^2\varepsilon_x(V) - k_z^2} \qquad \text{(IX.3)}$$

where k_0 is the vacuum wavenumber, k_x is the radiation wavenumber in *x*-direction, k_z is the radiation wavenumber in *z*-direction, ε_0 is the vacuum dielectric permittivity, and μ_0 is the vacuum permeability.

However, the selected LC mixture is uniaxial and ε_y does not depend on the applied voltage: only the fundamental TM leaky mode is affected by the external bias and, thus, the TE leaky mode is not of interest in this investigation. It also allows for showing the LWA radiation features only in the E-plane (*i.e.*, the *xz*-plane, with respect to the reference system in *Fig. 49*), that is the plane affected by the TM leaky mode [282].

The dispersion equation relates the frequency and the complex longitudinal wavenumber. The dispersion equation can be obtained by applying the transverse resonance technique to the transverse equivalent network of *Fig. 49*. As discussed in chapter VIII, this method consists of considering the sum between the admittance looking upwards Y_{up} and downwards Y_{dw} at an arbitrary cross section and to equal it to zero:

$$Y_{\mathrm{up}} + Y_{\mathrm{dw}} = 0 \tag{IX.4}$$

Equation IX.4 evaluated at the cross section correspondent to $x = h_1$ is:

$$Y_{\mathrm{in},i} - jY_0^{\mathrm{TM}} \cot\left(k_{x,0} h_0\right) = 0 \tag{IX.5}$$

where the input admittance of the *i*-th layer can be written as:

$$Y_{\mathrm{in},i} = Y_i^{\mathrm{TM}} \frac{Y_{\mathrm{in},i+1} \cos\left(k_{x,i} h_i\right) + Y_i^{\mathrm{TM}} \sin\left(k_{x,i} h_i\right)}{Y_i^{\mathrm{TM}} \cos\left(k_{x,i} h_i\right) + Y_{\mathrm{in},i+1} \sin\left(k_{x,i} h_i\right)} \tag{IX.6}$$

where Y_i^{TM} is the characteristic admittance of the *i*-th layer, $k_{x,i}$ is the transverse wavenumber of the *i*-th layer, and h_i can be considered as the *i*-th layer thickness.

4. Terahertz implementation of a Fabry-Perot cavity leaky-wave antenna with liquid crystals: numerical results

The dispersion curves for an ideal layout (Layout 1) can be derived as a proof-of-concept of the proposed antenna at the frequency of 0.59 THz. In this design, the number of layers, *N*, is set equal to four and the layers are made with lossless materials (the effect of losses on antenna performance will be examined further). Relevant parameters for the antenna designs are listed in *Table 11*.

Table 11 Design parameters for different THz FPC-LWA layouts.

Layout	N	h_1 [µm]	h_2 [µm]	h_3 [µm]	f_0 [THz]
1	4	167	127	82	0.59
2	8	167	127	82	0.56
3	6	100	75	145	1.00
4	4	188	127	82	0.56

For the evaluation of materials thickness, (compare design rules in *Fig. 49*), the wavelength in the media is considered as: $\lambda_{\mathrm{LC}} = \lambda_0/\sqrt{\varepsilon_{\mathrm{o}}}$, for LC layers; $\lambda_{\mathrm{Al}} = \lambda_0/\sqrt{\varepsilon_{r,\mathrm{Al}}}$, for alumina layers; and $\lambda_{\mathrm{sub}} = \lambda_0/\sqrt{\varepsilon_{r,\mathrm{sub}}}$, for the substrate of Zeonor; where λ_0 is the vacuum wavelength, *i.e.*, the wavelength corresponding to the design frequency. Moreover, m, n, and p, appearing in *Fig. 49*, are integer values that indicate which odd multiple of the quarter wavelength is considered. $m = 1$, $n = 2$, and $p = 1$ are chosen in Layout 1; for higher values of m, n, and p higher-order modes may appear in certain frequency ranges, and possibly degrade the antenna performance. Finally, in Layout 1, the choice of a design frequency, f_0, of 0.59 THz is due to the minimum commercially available thickness for alumina layers (127 µm). At 0.59 THz, alumina exhibits a relative permittivity $\varepsilon_{r,\mathrm{Al}} = 9$ and a loss tangent of about $\tan\delta_{\mathrm{Al}} \cong 0.01$ [283].

4.1 Dispersion analysis of fundamental leaky modes: lossless case of study

Dispersion curves of the fundamental TM leaky mode for the frequency range 0.50–0.75 THz are presented in *Fig. 50*. They are a family of curves obtained gradually changing the voltage between zero (red curve) and the threshold voltage V_∞ (blue curve). For the proposed LC cell thickness, values below 20 V are sufficient to cover almost the complete switching range. For simplifying the analysis, it is assumed that LC relative permittivity linearly varies with the applied voltage. For this reason, the unbiased and biased states are always correctly predicted. Conversely, the dynamic variation of $\hat{\beta}_z = \beta_z/k_0$ and $\hat{\alpha}_z = \alpha_z/k_0$, corresponding to voltage values between 0 and 20 V, could change if the voltage-dependence of LC permittivity is completely predicted by Q-tensor computations (compare Ch. VII Sec. 2.1.2).

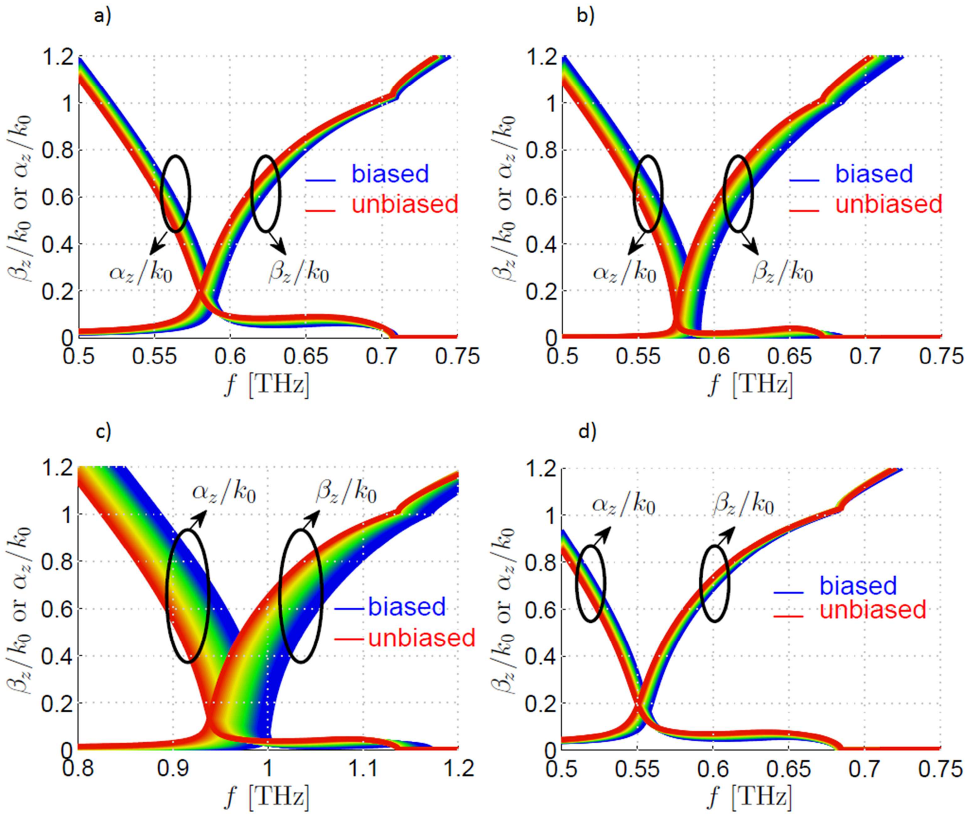

Fig. 50 Dispersion curves of the fundamental TM for different THz FPC-LWA with LC: a) Layout 1, b) Layout 2, c) Layout 3, d) Layout 4. Colors gradually shade from blue to red as the applied external voltage decreases from V_∞ to zero [with courtesy of Dr. W. Fuscaldo].

The frequency at which the splitting condition $\hat{\beta}_z \cong \hat{\alpha}_z$ is achieved can be considered as the operating frequency. For this application, the operative frequency is fixed by the value obtained when the voltage is equal to V_∞ (blue curve), which corresponds to the design frequency. In fact, once the operating frequency is fixed, it is possible to change the value of the normalized phase constant $\hat{\beta}_z$ by simply decreasing the external voltage. On the contrary, the value of the normalized attenuation constant $\hat{\alpha}_z$ remains almost the same, such that $\hat{\beta}_z > \hat{\alpha}_z$. This would allow the steering of the THz beam with a quasi-constant beamwidth (because it is proportional to $\hat{\alpha}_z$ that does not change with the voltage) at a fixed frequency. Some relevant radiating features for the Layout 1 are reported in the first row of *Table 12*.

Table 12 Figure of merits for radiating performance of different layouts of a FPC-LWA with LCs: beam reconfigurability (θ_p^M), directivity (D_0) and beamwidth ($\Delta\theta$).

Layout	β_z^M/k_0	α_z/k_0	θ_p^M [°]	D_0 [dB]	$\Delta\theta$ [°]	f_{op} [THz]
1	0.37	0.16	22	17.87	26	0.59
2	0.44	0.05	26	27.98	8	0.59
3	0.65	0.08	40	23.90	13	1.00
4	0.34	0.17	20	17.35	34	0.56

The maximum pointing angle is given from:

$$\theta_p^M \cong \arcsin\sqrt{\left(\frac{\beta_z{}^M}{k_0}\right)^2 - \left(\frac{\alpha_z}{k_0}\right)^2} \qquad \text{(IX.7)}$$

and the half power beamwidth (HPBW) is [282]:

$$\begin{cases} \Delta\theta = \text{HPBW} = 2\dfrac{\alpha_z^{\text{TM}}}{k_0}\csc\theta_0 & \text{for } \beta_z \gg \alpha_z \\ \Delta\theta = \text{HPBW} = 2\sqrt{2}\dfrac{\alpha_z^{\text{TM}}}{k_0} & \text{for } \beta_z \cong \alpha_z \end{cases} \qquad \text{(IX.8)}$$

where $\beta_z \cong \alpha_z$ represents the condition in which the beam points at broadside. The directivity at broadside is approximated by the formula:

$$D_0 = {}^{4\pi}\!/_{\Delta\theta^2} \qquad \text{(IX.9)}$$

Since equation IX.8 is derived for a LWA in the limit of an infinite aperture, the radiation pattern does not exhibit sidelobes (the diffraction from edges is neglected). Thus, the directivity is well approximated by equation IX.9, which considers only the width of the main beam. It is also worth noting that equation IX.9 assumes that the HPBW is equal along the principal planes of the antenna. Since in FPC-LWAs radiation on the E(H)-plane is determined by the TM(TE) leaky mode, equation IX.9 is accurate as long as TE and TM leaky modes exhibit almost the same dispersion. This condition is fulfilled by FPC-LWAs as those studied here (numerical simulations, not reported here, corroborate the concept).

As shown in *Table 12*, the HPBW remains relatively high ($\Delta\theta \cong 26°$) when the LC permittivity changes. It is due to a relatively high leakage rate ($\hat{\alpha}_z \cong 0.16$). Because the HPBW at broadside is greater than the maximum pointing angle, the radiated power density never decreases below –3 dB during the steering of the THz beam.

Therefore, some designs can be developed with the aim to improve the scanning range or reduce the beamwidth of the proposed THz FPC-LWA. Two solutions are possible:

(i) increasing the number of material layers (Layout 2 of *Table 11*), or (ii) employing thicker LC cells (Layout 3 of *Table 11*).

As presented in *Fig. 50 b)*, the attenuation constant of Layout 2 is considerably reduced, whereas the range of tunability is almost the same. On the other hand, in Layout 3 (see *Fig. 50 c)*), the attenuation constant is slightly reduced, but the achieved range of tunability is wider than Layout 1. However, in Layout 3, the thickness of alumina layers is reduced to 75 μm. Consequently, the operating frequency is 1 THz and the design of the FPC-LWA is achieved with a higher-order leaky-wave mode (m=1, n=2, and p=2). Unfortunately, the fabrication of devices with features as those presented in Layout 2 and Layout 3 is extremely challenging. Therefore, an additional design, *i.e.*, Layout 4, is considered. It has the same configuration of Layout 1, but the thickness of the Zeonor substrate is increased to the closest commercially available one. This choice will simplify the fabrication of the device. According to the geometrical parameters, the most noticeable differences between Layout 1 and 4 are: (i) the operative frequency shift from 0.59 to 0.56 THz, and (ii) a reduced range of tunability.

4.2 Terahertz Fabry-Perot cavity leaky-wave antenna radiation patterns: lossless case of study

Radiating patterns on the E-plane of all the proposed layouts can be evaluated on the basis of the dispersion analysis. The antenna excitation is modelled with a horizontal magnetic dipole (HMD) placed on the ground plane (see *Fig. 53*). HMD source can be used to model a slot etched in the ground plane and back-illuminated by a coherent THz source (compare Ch. I Sec. 2), such as QCLs or photomixers.

For deriving radiating patterns, two methods are used: (i) taking into account only the contribution of the relevant leaky mode (*LWA theory*), and (ii) by invoking the reciprocity theorem (*Reciprocity*).

In the *LWA theory*, the tangential electric field distribution of a forward leaky wave over an aperture plane can be Fourier-transformed, obtaining the array factor (AF) of the antenna. It allows for discretizing the LWA radiating behavior and taking into account only the contribution of the relevant leaky mode. If the antenna structure can be considered infinite in the *y*- and *z*-directions, the AF assumes the following expression:

$$\mathrm{AF}(\theta) = \frac{-2jk_z\cos(\theta)}{k_z^2 - k_0^2\sin^2(\theta)} \tag{IX.10}$$

For *Reciprocity*, an in-house MATLAB code is developed for deriving the one-dimensional Green's functions of the transverse equivalent network (TEN) model by means of the ABCD-matrix formalism [284]. Afterward, the reciprocity theorem is applied for calculating the *E*-plane far field radiation patterns. The far-field intensity at a given angle θ can be considered equivalent to the magnetic field excited at the source position by a plane wave, incident with the same angle θ and coming from a testing dipole source [285].

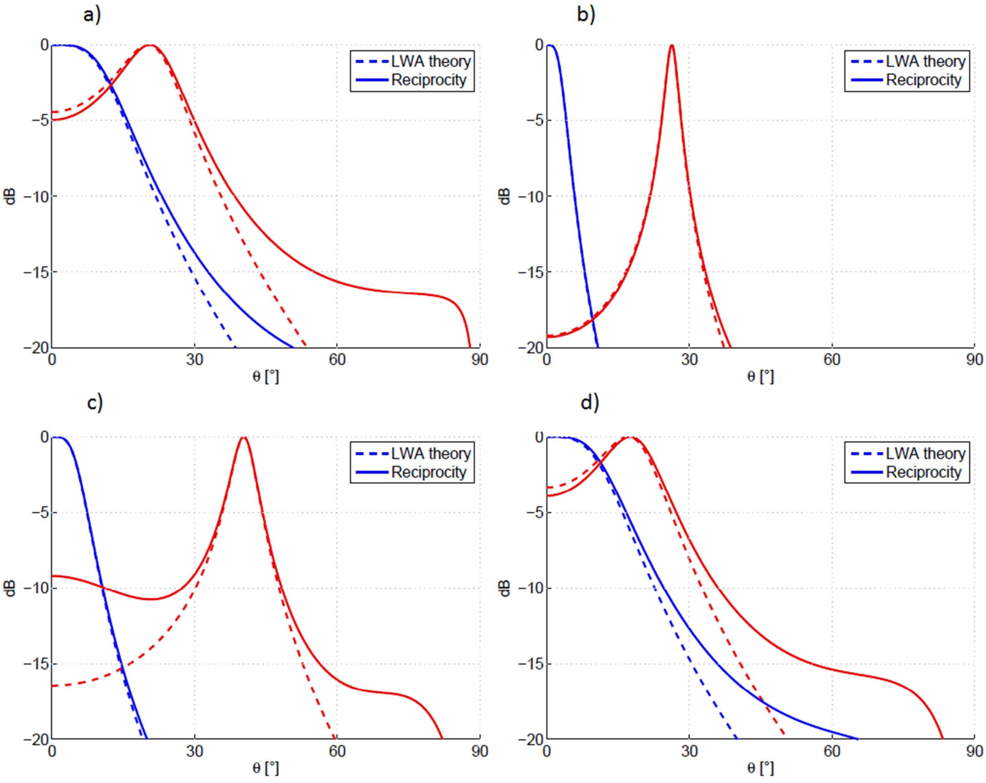

Fig. 51 Radiation patterns predicted by leaky-wave theory (dashed lines) or by means of reciprocity theorem (solid lines): a) Layout 1, b) Layout 2, c) Layout 3, and d) Layout 4 (see Table 3.5). The condition of the THz beam pointing at broadside (blue lines) and the radiation at the maximum pointing angle (red lines) are presented [with courtesy of Dr. W. Fuscaldo].

Radiation patterns are reported in *Fig. 51* for all discussed layouts. *Fig. 51 a), b),* and *d)*, show a very good agreement between *LWA theory* and *Reciprocity*. However, in

Fig. 51 c), the LWA theory does not provide an accurate evaluation. This is probably because Layout 3 is developed with a higher-order design and a higher-order leaky-wave mode could be present, increasing the sidelobe level. Reciprocity, however, correctly predicts this effect.

Some relevant radiating features are listed in *Table 12*. Layout 2 considerably improves the directivity and, consequently, the beamwidth of the THz FPC-LWA. On the other side, the proposed device, designed according to Layout 3, has an increased reconfigurable capability. In fact, a higher thickness of the LC layers in Layout 3 extends the range of tunability, but degrades the radiation patterns. Conversely, a higher number of material layers, as presented in Layout 2, increases the antenna directivity, but the structure becomes difficult to fabricate and could suffer from non-negligible dielectric and ohmic losses.

4.3 Terahertz Fabry-Perot cavity leaky-wave antenna: dispersion curves and radiation patterns in the case of materials with dielectric losses

Dispersion properties of the fundamental TM leaky-wave modes in the lossy case are investigated for evaluating the effect of losses on the proposed THz FPC-LWAs.

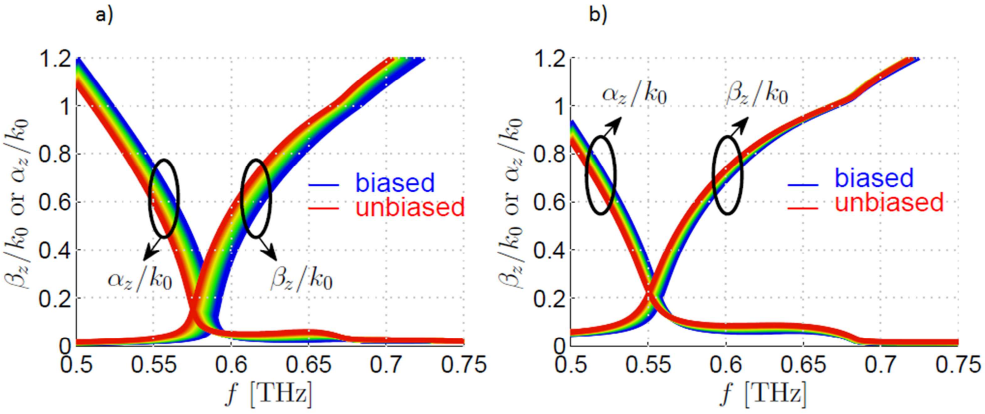

Fig. 52 Dispersion curves of the fundamental TM when losses of the materials are taken into account: a) Layout 2, and b) Layout 4. Colors gradually shade from blue to red as the applied external voltage decreases from V_∞ to zero [with courtesy of Dr. W. Fuscaldo].

In particular, the performance of Layout 2, which has a better directivity than the other layouts, is compared with Layout 4, which is easier to fabricate than the other discussed layouts. However, only dielectric losses are taken into account. At a first approximation, ohmic losses due to LCs electrodes could be neglected if PEDOT:PSS is employed as conductive material (compare Ch. VII Sec. 2.2).

The value of $\hat{\alpha}_z$ increases when dielectric losses are introduced (*Fig. 52*), determining a deterioration of the FPC-LWA performance in terms of both HPBW and directivity.

For the lossy case, full-wave numerical simulations are performed for Layout 2 and 4 employing CST Microwave Studio (compare Ch. III Sec. 2) together with reciprocity. This setting can be modelled in CST [286] as represented in *Fig. 53*: a unit cell of period *p* is excited with a waveguide port at the distance h_{air}.

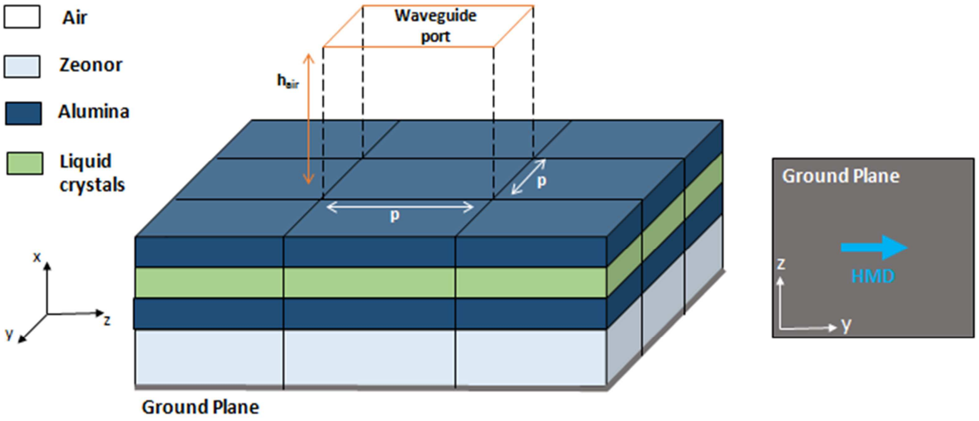

Fig. 53 THz FPC-LWA unit cell model, as implemented in CST full-wave simulation. A probe for evaluating the tangential magnetic field at the ground plane is added as a light blue arrow.

The FPC-LWA is electrically large in the transverse plane and could be assumed transversely infinite: Floquet boundary conditions can be applied to the unit cell. If λ_{op} is the wavelength that corresponds to the operative frequency, the period of the unit cell is $p = \lambda_{\text{op}}/4$ and the distance between the unit cell and the waveguide port is $h_{\text{air}} = \lambda_{\text{op}}/2$, in order to prevent the excitation of higher-order Floquet modes [287]. LC layers are modelled as layers of anisotropic material in the two limit cases of LC director aligned along *x*- and *z*-axis.

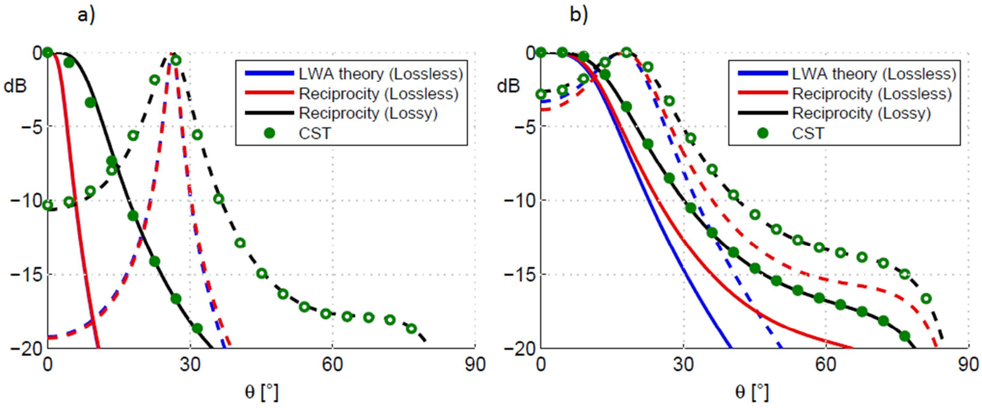

Fig. 54 Radiation patterns of a) Layout 2 and b) Layout 4 for radiation at broadside (solid) and at the maximum pointing angle (dashed). Radiation patterns are calculated by means of reciprocity theorem in the lossless (in red) and the lossy (in black) case. Patterns from leaky-wave theory are also shown (blue). Full-wave simulations with CST are reported, in the lossy case, for radiation at broadside (filled green circles) and at the maximum pointing angle (empty green circles) [with courtesy of Dr. W. Fuscaldo].

A rigorous application of the reciprocity theorem helps to get an accurate evaluation of the radiating performance of Layout 2 and 4 for the proposed antennas. In *Fig. 54*, it is possible to notice that the introduction of dielectric losses in the model has a negative effect in terms of the directivity of the antennas: the beam is wider. This is especially true for Layout 2, because the number of lossy layers is higher than in Layout 4 (*Table 13*).

Table 13 Comparison between radiation properties of Layout 2 and 4, with and without dielectric material losses.

Layout	β_z^M/k_0	α_z/k_0	θ_p^M **[°]**	D_0 **[dB]**	$\Delta\theta$ **[°]**	η **[%]**	f_{op} **[THz]**
2 (lossless)	0.44	0.05	26	27.98	8	100	0.59
2 (lossy)	0.44	0.13	26	19.26	21	40	0.59
4 (lossless)	0.34	0.17	20	17.35	34	100	0.56
4 (lossy)	0.34	0.21	20	15.52	27	80	0.56

In fact, directivity is governed by the attenuation constant, which accounts for both radiation and dielectric losses. Consequently, as the number of layers increases, dielectric losses influence the increment of beamwidth. For this reason, a simple design, such as the one presented for Layout 4, could be a good compromise between reconfigurable performances and easiness of fabrication.

5. Conclusions

In this chapter, a FPC-LWA containing material layers with reconfigurable electro-optical properties is investigated at THz frequencies. Specifically, different multistacked Fabry-Perot cavity-like configurations have been considered for the design of a THz radiator with a tunable pointing angle. The benefits and drawbacks of ideal designs against those of more practical configurations have been carefully addressed. Ideal designs show excellent radiating features, but are not easy to fabricate, whereas practical designs show a considerably reduced performance, but are very straightforward to fabricate. Moreover, even if material losses are taken into account, a practical multistack LWA design shows a radiation efficiency higher of a 10% or more than the state-of-art reconfigurable graphene FPC-LWAs (compare *Table 10* and *Table 13*).

The proposed multistack FPC-LWA can be considered as a promising solution for the current requirement of tunable THz antennas for THz wireless links. The antenna fabrication and characterization will start to be performed in a short time.

CHAPTER X
Terahertz leaky-wave antennas based on homogenized metasurfaces

1. Introduction

In the previous chapter, a FPC-LWA with a tunable pointing angle by means of electro-optical control is introduced as a promising device for THz beam-steering. It is constituted by a grounded dielectric slab with a PRS above, in the form of a distributed Bragg Reflector (DBR) [93]. In this chapter, another kind of PRS for FPC-LWAs is investigated, *i.e.*, the metallic patterned metasurface[3]. These periodic PRSs are studied in the situation in which the period is much smaller than the wavelength, that is called homogenization limit [288]. Under this condition, a single impedance boundary condition is sufficient to accurately describe the electromagnetic response of the PRS as a whole.

In the following sections, the effect of a unit cell's geometrical parameters on the value of the homogenized impedance is shown for three different topologies: the patch, the strip, and the fishnet [266], [288], [289]. The aim of the analysis is to identify the design with the highest reflectivity to improve the FPC-LWA directivity. However, differently from patches and strips for which homogenization formulas exist [266], no analytical expressions have been reported so far for fishnet PRSs. This motivates a deeper study of this PRS topology.

---

[3] The topic, described in this chapter, was developed in collaboration with Dr. Walter Fuscaldo, who is the main author of the work.

2. Design constraints of terahertz metasurface leaky-wave antennas

The PRSs, studied in this chapter, are characterized by a periodic arrangement of sub-resonant lossless elements, *i.e.*, elements with a period $p \ll \lambda_0$. Under this hypothesis, the homogenized PRS can be modeled as a purely imaginary impedance: $Z_\mathrm{s} = jX_\mathrm{s}$. Ohmic losses are not taken into account because the metal is treated as a perfect electric conductor (PEC). However, as discussed further, ohmic losses can be also neglected by employing a high-conductive metal layer, as copper or aluminum, of suitable thickness.

The directivity at broadside of a LWA with a PRS described by a surface impedance $X_\mathrm{s} \ll \eta_0$, where $\eta_0 = 120\pi$ is the vacuum impedance, is inversely proportional to the square of X_s [290]:

$$D_0 \cong \frac{\pi^2\eta_0^2}{\sqrt{\varepsilon_r^3 X_\mathrm{s}^2}} \qquad \text{(X.1)}$$

where ε_r is the dielectric permittivity of the substrate material.

On the contrary, the fractional bandwidth (FBW), *i.e.*, the range of frequency, normalized to the operating frequency, for which the radiated power density at broadside has not decreased more than 3 dB, is directly proportional to the square X_s:

$$\mathrm{FBW} = 2\frac{X_\mathrm{s}^2}{\pi\eta_0^2}\sqrt{\varepsilon_\mathrm{r}} + \tan\delta_\mathrm{e} \qquad \text{(X.2)}$$

where $\tan\delta_\mathrm{e}$ is the loss tangent of the substrate material.

For this reason, lower impedance values lead to highly-directive FPC-LWA designs working in a narrow bandwidth, whereas higher impedance values lead to moderately-directive FPC-LWA designs working in a considerable bandwidth.

Furthermore, the FPC-LWAs have to be optimized for working in the THz range. This adds some technological constrains: (i) the availability of low-loss THz materials, (ii) the accessibility to efficient THz sources, (iii) the mechanical tolerances in the fabrication process. With regard to (i), a commercially available substrate of Zeonor, with a thickness $h = 100\ \mu m$, is considered (compare Ch. II Sec. 5). For the antenna excitation, a slot can be etched in y-direction on the ground plane, as for the LWA in chapter IX. A suitable dimension for the slot could be $200 \times 100\ \mu m^2$. In fact, considering a guided-wave excitation, such dimension is comparable with the cross section of commercial THz waveguides operating in the 0.9−1.4 THz range [80]; if a free-space excitation is considered, this dimension could provide a good energy coupling with THz beams focalized by commercial lenses. As discussed in previous chapters, the focus area of a commercial focusing device at about 1 THz has a diameter of around 1 mm, with an approximately bidimensional Gaussian profile. Moreover, the suggested dimensions allow for modeling the slot as a resonant HMD source, as required for exciting a pair of TE-TM leaky modes in a FPC-LWAs [282]. Finally, the period of the PRS unit cell can be set to $p = \lambda_0/5 = 60\ \mu\text{m}$ to facilitate the manufacturing process. It is important to underline that p should not preferably be set greater than $\lambda_0/4$ for fulfilling the homogenization limit [266]. The smallest detail commonly allowed in a standard photolithographic process should be greater than 3 μm to avoid fabrication issues in a low-cost large-area production [291].

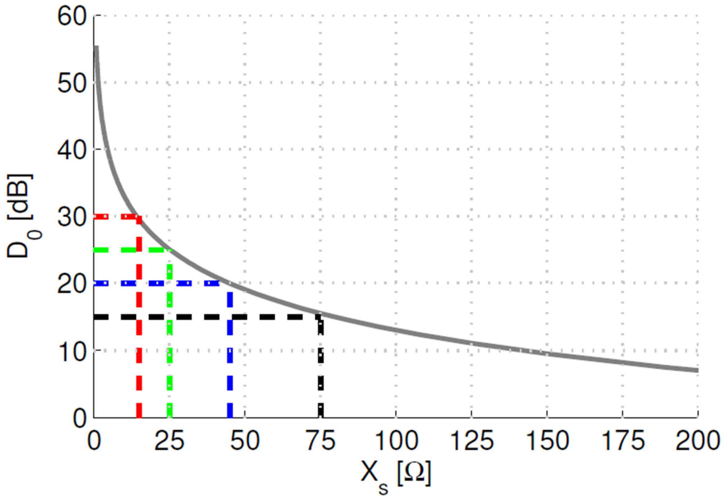

Fig. 55 Directivity at broadside as a function of the characteristic impedance of a PRS (see equation X.1). Black, blue, green, and red dashed lines selects the reactance values required for achieving theoretical directivities of 15, 20, 25 and 30 dB, respectively.

Equation X.1 is represented in *Fig. 55* as a function of the characteristic reactance X_s. The four directivity values correspond to theoretical directivities at broadside of 15, 20, 25, and 30 dB, and can be reachable by employing PRSs with a reactance value of 75, 45, 25, and 15, respectively. However, the curve in *Fig. 55* does not accurately describe the relationship between directivity and reactance when X_s increases, because equation X.1 is given for $X_s \ll \eta_0$. For high values of reactance, the theoretical curve in *Fig. 55* should be intended as an upper bound.

The method for the impedance synthesis is based on the extraction of the surface impedance of the PRS from a full-wave simulation [266], [282]. Differently from the literature, the presence of the ground is neglected because it is supposed to not affect the actual value of the PRS impedance due to a plate separation of $h = 0.5\,\lambda_0/\sqrt{\varepsilon_r}$. The unit cell (*Fig. 56*) is excited from the top with a Floquet-wave impinging on the PRS with a normal angle of incidence $\theta = 0°$ for evaluating radiation at broadside.

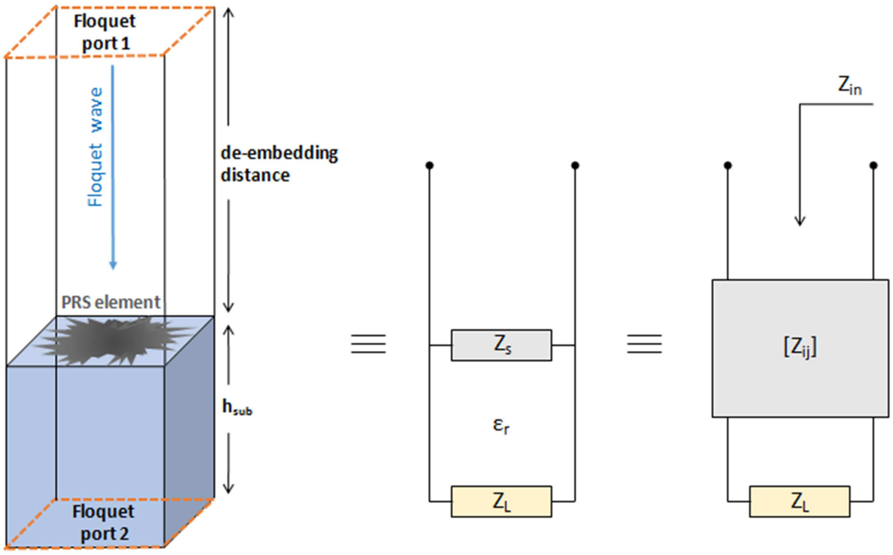

Fig. 56 A model for evaluating the surface impedance of a periodic PRS. A Floquet wave impinges on the PRS. The impedance matrix is obtained in correspondence of the PRS, fixing a suitable de-embedding distance. An equivalent circuit model can be derived for retrieving the value of the surface impedance from the impedance matrix parameters.

The PRS is deposited on a dielectric substrate that terminates with another Floquet port. In this configuration, the surface impedance is:

$$Z_{\mathrm{s}} = (Z_{\mathrm{in}}^{-1} - Z_L^{-1})^{-1} \qquad \text{(X.3)}$$

where Z_{in} is the input impedance [284]:

$$Z_{\mathrm{in}} = Z_{11} - \frac{Z_{12}Z_{21}}{Z_{22} - Z_L} \qquad \text{(X.4)}$$

$Z_{i,j},\ i,j = 1{,}2$ are the elements of the impedance matrix of the two-port network (see *Fig. 56*) and Z_L is the characteristic impedance of the Floquet port in the substrate:

$$Z_L = Z_0/\sqrt{\varepsilon_r} \qquad \text{(X.5)}$$

The proposed method has a considerable advantage with respect to the one proposed in [266], [282], where a short-circuit termination replaces the Floquet port in the modeling of the ground plane. In this situation, $Z_L = j\eta_0/\sqrt{\varepsilon_r}\tan(k_0\sqrt{\varepsilon_r}h_{\mathrm{sub}})$ and the argument of the tangent introduces some resonances in the surface impedance, when simulations are performed over more than one octave frequency band. On the contrary, the method proposed in [266], [282] should be preferred when the PRS is above an extremely thin substrates, *i.e.*, when $h_{\mathrm{sub}} \ll \lambda_0$. However, this situation is of scarce interest for THz applications. In such conditions, the capacitive effect introduced by the ground plane may alter the electromagnetic response of the PRS and the short-circuit termination in the unit-cell is required for an accurate modeling. Such a model is accurate only for a given value of substrate thickness: it limits the use of this method to specific problems.

3. Impedance synthesis of three partially reflective sheet geometries

Full-wave simulations are carried out for obtaining the surface reactance of the PRS, which has a period $p = \lambda_0/5 = 60$ µm, at the frequency of 1 THz.

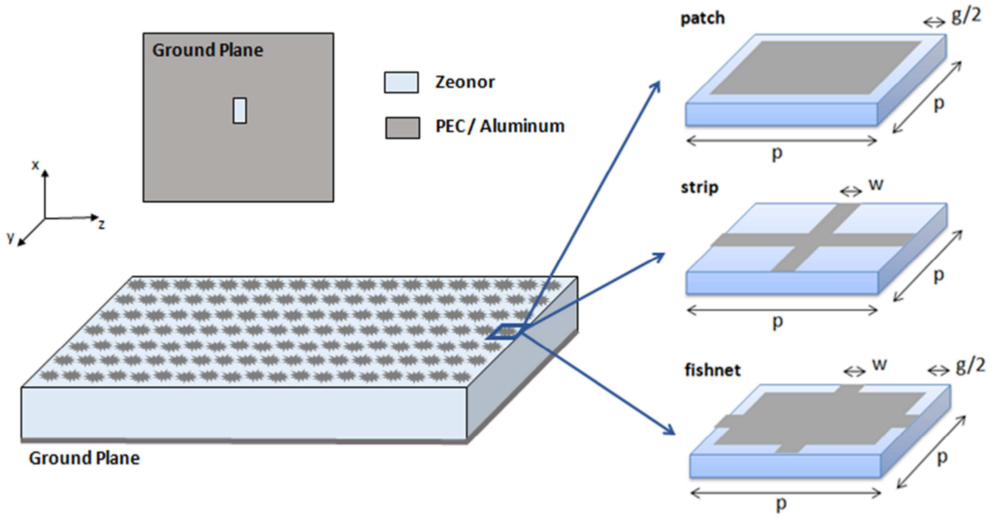

Fig. 57 Illustrative example of a FPC-LWA based on PRS with three different elements geometry.

As shown in *Fig. 57*, the PRS unit cell can take various forms, such as a square patch, a strip or a fishnet element. The proposed fishnet geometry can be considered as the superposition of the other two elements: the patch and the strip. All elements are symmetric along the principal planes (*viz.*, the *xz*-, and the *yz*-plane, *i.e.*, the E- and H-plane, respectively). The reactance X_s is evaluated by employing commercial software based on a FEM (compare Ch. III Sec. 2).

A wide variation of their relevant geometrical parameters is considered: the gap, *g*, for the patches, the width, *w*, for the strips, and the combination of both *g* and *w*, for the fishnet. Specifically, *g* and *w* are varied from 0.05*p* to 0.4*p*, with a step of 0.05*p*. These values represent the lower and upper constrains due to the fabrication tolerances and the homogenization limit. The simulations are carried out at the single frequency of 1 THz since, as long as $X_s \ll \eta_0$, the operating frequency does not differ much from the design frequency of 1 THz.

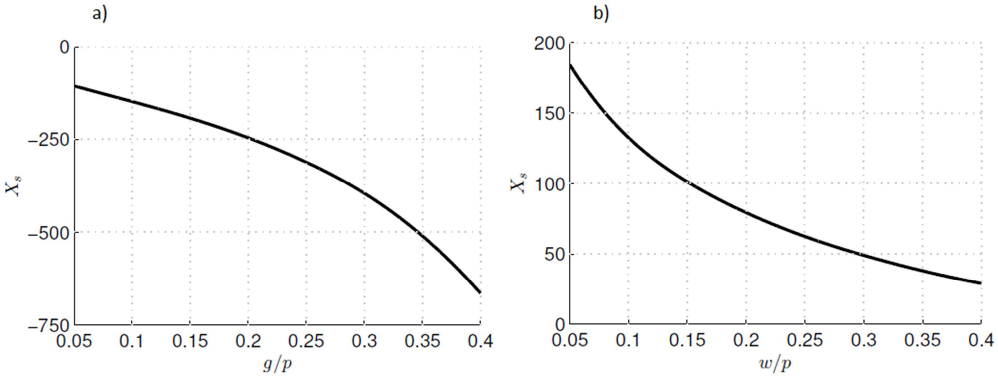

Fig. 58 Surface reactance X_s of a) a patch-based PRS, as a function of the normalized gap *g* between the patches, and b) a strip-based PRS, as a function of the normalized width *w* of the strips.

The simulated surface reactance for the three PRS configurations is reported in *Fig. 58* and *Fig. 59* as a function of the relevant geometrical parameters. The reactance of the patch-based PRS is negative (see *Fig. 58 a)*) because the capacitive behavior is dominant. Moreover, the absolute value of the impedance decreases as the gap decreases, due to an increment of the capacitive effect. On the other side, the reactance of the strip-based and fishnet-based PRS is positive because the inductive behavior is dominant (see *Fig. 58 b)* and *Fig. 59*).

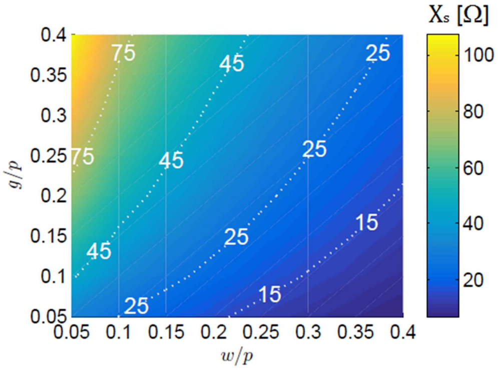

Fig. 59 Surface reactance X_s of a fishnet-based PRS as a function of both *g* and *w*. The iso-lines of the reactance at 15, 25, 45, and 75 Ω are reported in white dashed lines.

It is also possible to notice that the absolute value of X_s for a patch-based PRS is never lower than 100 Ω. It reveals that the patch geometry is not suitable for the design of a directive THz FPC-LWA (compare the directivity curve in *Fig. 55*). However, it is possible to decrease the impedance value of an arrangement of patches employing a double-sheeted array of patches as in [292]. This, however, goes beyond the scope of this work.

On the contrary, the strip-based PRS can achieve values of X_s as low as 30 Ω, if the width of the strips is large with respect to the period. It means that theoretical directivities greater than 25 dB are not achievable. The fishnet-like element spans values of X_s from 100 Ω to few ohms in the same parameter space (*Fig. 59*). Consequently, a suitable combination of *g* and *w* values allows for the design of a highly directive FPC-LWA. Since the fishnet element has a two-valued space parameter, any pair of *g* and *w* lying on the iso-lines at 15, 25, 45 and 75 Ω of *Fig. 59* satisfies the corresponding impedance value. Moreover, differently from the strip-based PRS, a very low value of X_s, such as 15 Ω, can be synthesized without an extreme parameter variation.

If the three PRSs are evaluated in terms of filling factor (FF), the fishnet PRS has a FF larger than that of the strip and patch equivalent designs. It is an interesting property of the fishnet-based PRS because it may open to the possibility of employing this PRS configuration as electrode for an electro-optical tunable material, such as LCs (compare Ch. VII and Ch. IX). It would not be possible in a patch-based PRS with a comparable filling factor, due to the intrinsic topology of patches, which are not interconnected elements.

It is also important to evaluate if the PRS with fishnet-like elements exhibits frequency and spatial dispersion. In general, when a dense array of elements is modeled in the homogenization limit, the dependence on the angle of incidence (spatial dispersion) and on the frequency (frequency dispersion) has to be taken into account. The grid impedance of patches for TE polarization and the grid impedance of strips for TM polarization, as a consequence of Babinet principle (invoked because the strips array is the complementary structure of the patches array) [293], exhibit a spatially-dispersive character.

In *Fig. 60* the surface reactance X_s of a fishnet-like unit cell of period $p = \lambda_0/10$, and geometrical parameters $g = w = p/10$ is presented. The unit cell is simulated with a commercial software employing a FEM, in the frequency range between 0.5 THz and 1.5 THz, for angles of incidence varying from 0° (blue curve of *Fig. 60*) to 80° (red curve of *Fig. 60*). These numerical simulations show that the fishnet PRS surface impedance is essentially spatially nondispersive. This property might be of particular interest in the future perspective of developing a FPC-LWA based on a metasurface, with tunable radiation properties (as already proposed for the multilayered FPC-LWA described in Ch. IX).

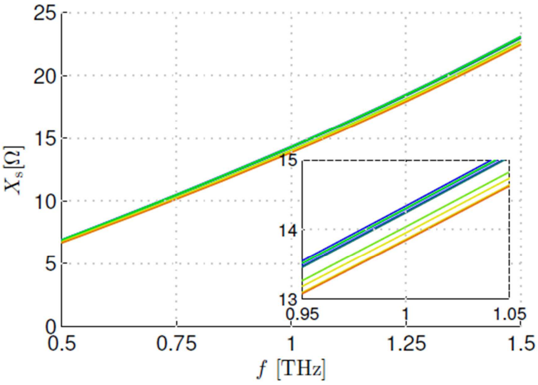

Fig. 60 Surface reactance of a fishnet-like unit cell as a function of frequency. The family of curves is obtained changing the angle of incidence from 0° to 80° (the color shades from blue to red, respectively).

According to the impedance analysis, the fishnet-like PRS (i) allows for a high directivity, in combination with a flexible choice in its geometrical parameters, and (ii) is suitable for the design of a FPC-LWA with a reconfigurable pointing angle (compare Ch. IX). In the following section, the radiating properties of four FPC-LWAs based on four different fishnet-based PRSs are fully characterized.

4. Radiating behavior of Fabry-Perot cavity leaky-wave antennas based on fishnet-like metasurface

Four different pairs of w and g are selected among those lying on the same iso-line of *Fig. 59*, with the aim to develop PRSs with impedances of 15, 25, 45 and 75 Ω (for details, see *Table 14*). The choice of a specific pair of parameters is mainly due to the easiness of fabrication and to the good fulfillment of the homogenization limit. In fact, all the pairs lying on the same iso-reactance line lead to the same antenna performance. The surface impedance is characterized over a frequency range from 0.5 THz to 1.5 THz, to have a frequency-dispersive model of the four fishnets. As shown in *Fig. 61 a)*, almost all designs lead to a reactance with a linear frequency dependence: it is a consequence of the dominant inductive behavior of the PRS.

Table 14 Relevant geometrical parameters and radiating properties of the FPC-LWAs based on the considered PRSs with fishnet-like elements.

X_s [Ω]	g/p	w/p	$f_{o\rho}^{\mathrm{TE(TM)}}$ [THz]	$\mathrm{BW}^{\mathrm{TE(TM)}}$ [GHz]	$\alpha_\rho^{\mathrm{TE(TM)}}$	α_{loss}	$e_{r,\infty}$ [%]	e_r [%]	D_0 [dB]	G [dB]	$\Delta\theta^{\mathrm{H(E)}}$ [°]
15	0.2	0.4	0.982 (0.982)	2.34 (2.34)	0.051 (0.052)	0.013	75	69	27.74	26.13	8.25 (8.42)
25	0.2	0.25	0.967 (0.967)	5.72 (5.72)	0.079 (0.082)	0.008	90	88	23.34	22.96	12.73 (13.25)
45	0.3	0.2	0.949 (0.950)	12.90 (12.90)	0.115 (0.123)	0.005	96	95	20.23	19.78	18.67 (19.98)
66	0.3	0.1	0.925 (0.926)	29.65 (29.68)	0.167 (0.186)	0.003	98	98	17.04	16.26	27.09 (30.12)

An exception is the design represented by the black solid line of *Fig. 61 a)*, which seems to show a quadratic behavior. This can be explained by considering the geometrical parameters of the layout: $g/p = 0.3$ and $w/p = 0.1$. Such values reveal a geometry with very narrow strips and a lower filling factor ($\mathrm{FF} = 0.61$) that the layout chosen for an impedance of 15 Ω ($\mathrm{FF} = 0.8$). Consequently, the inductive behavior is less dominant and the impedance is high: the design has a lower directivity and a higher fractional bandwidth than the other proposed layouts.

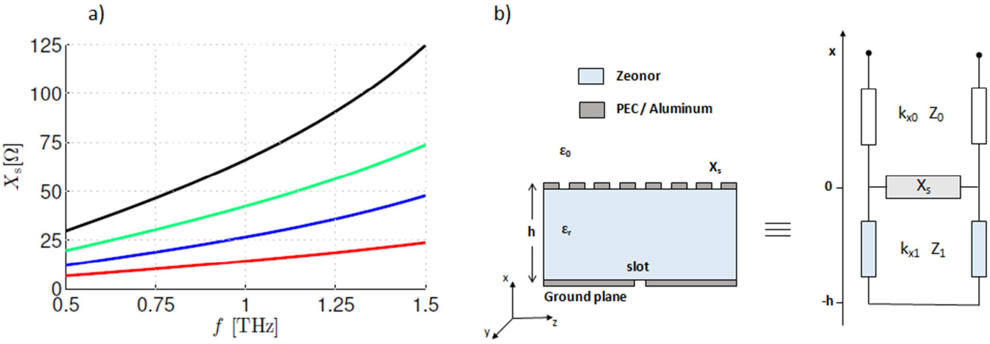

Fig. 61 a) Surface reactance as a function of the frequency for the four layouts presented in *Table 14*: behavior at 15 Ω is in red, at 25 Ω is in blue, at 45 Ω is in green, and at 66 Ω is in black. b) Section of the proposed FPC-LWA and its equivalent circuit model. Z_0 and Z_1 are the modal impedances in the air and in the medium, respectively, whereas k_{x0} and k_{x1} are the vertical wavenumbers in the air and in the medium, respectively.

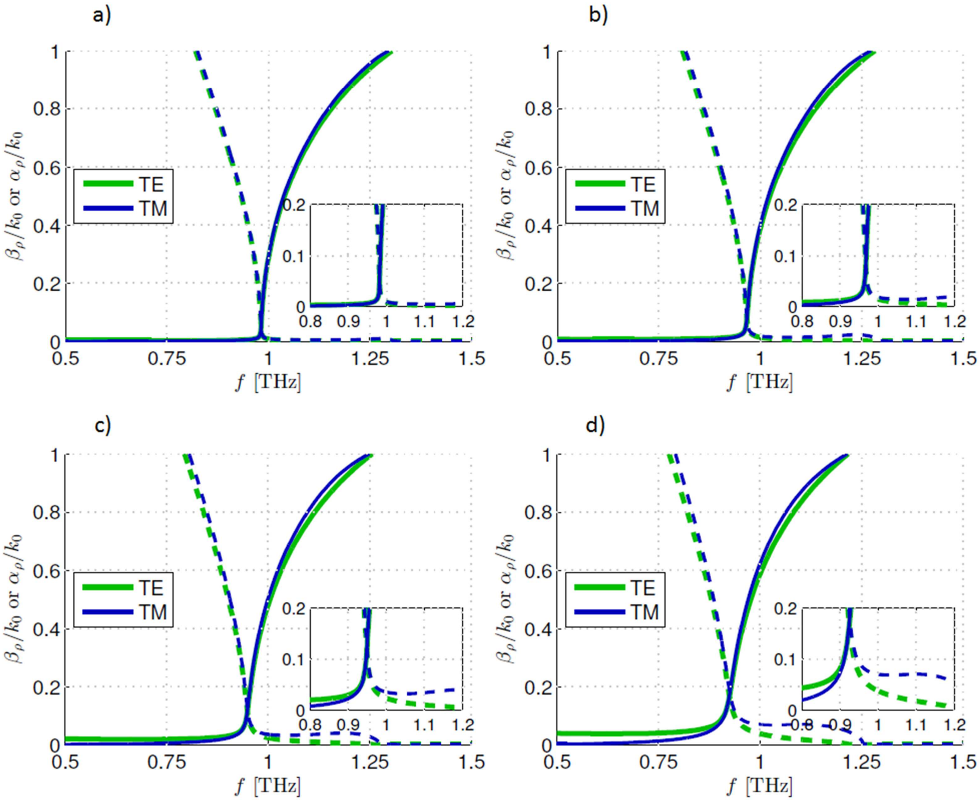

Fig. 62 Dispersion curves β_z/k_0 (solid lines) and α_z/k_0 (dashed lines) as a function of the frequency. In the insets, the frequency range is limited to 0.8 – 1.2 THz to highlight the behavior around the operative frequency of the dominant leaky modes for both TE (in green) and TM (in blue) polarizations.

Because the PRS with fishnet elements is spatially nondispersive (compare *Fig. 60*), the surface impedance $Z_s(f)$ can be modeled as a function of the sole frequency, without including the dependence on the wavenumber, which is supposed to be almost constant for all designs. The $Z_s(f)$ is then implemented in an equivalent circuit model (as in *Fig. 61 b)*) and the dispersion analysis of the radiating structure is performed [294].

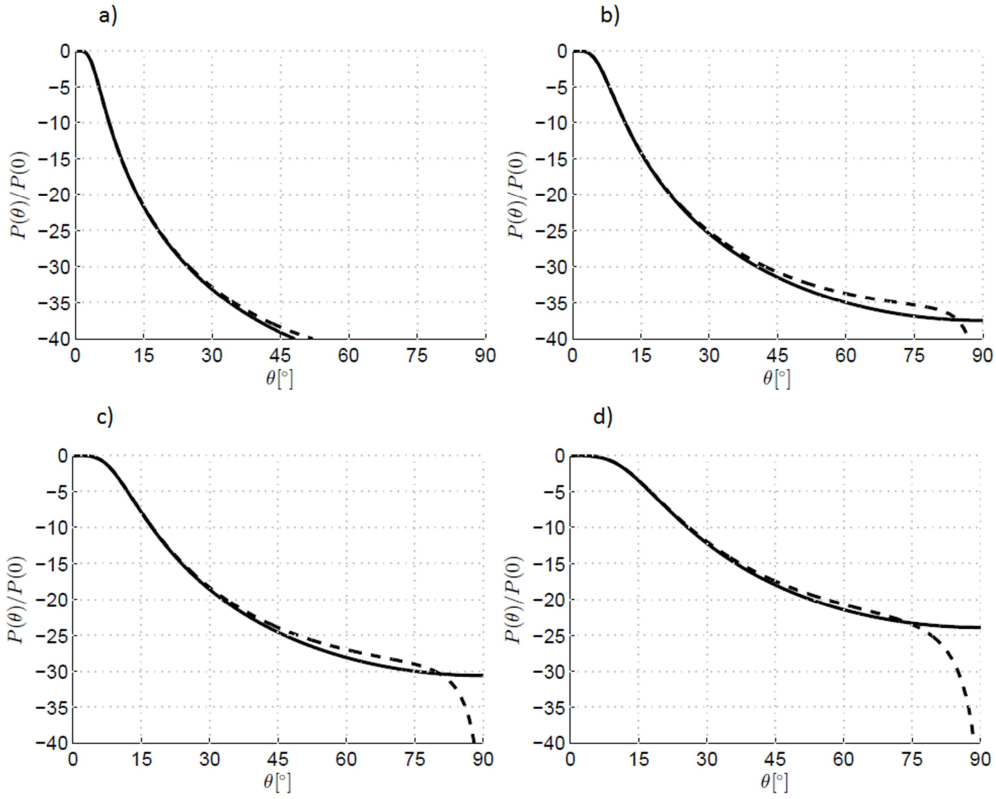

Fig. 63 Radiation patterns normalized to broadside radiation calculated with the leaky-wave approach (black solid lines) and reciprocity theorem (black dashed lines) are reported over the *E*-plane for the four layouts of *Table 14*.

Numerical results for the four FPC-LWAs are reported in *Fig. 62*: the behavior of the complex-mode normalized phase (solid lines) and attenuation constants (dashed lines) is presented in the frequency range 0.5 – 1.5 THz for both TE (green) and TM (blue) polarizations. It is possible to notice from *Fig. 62* that, as the impedance increases, as well as the operating frequency differs from the design frequency of 1 THz (compare *Table 14*). This circumstance determines a non-negligible disequalization of the radiating performance over the E- and H-planes, as shown in *Fig. 63* and *Fig. 64*.

However, when $X_s \ll \eta_0$, the change in the operating frequency can be analytically predicted with good accuracy by [290]:

$$\frac{f_{\mathrm{op}}-f_0}{f_0} = \frac{1}{\pi}\operatorname{arccot}\left(\frac{\eta_0}{\sqrt{\varepsilon_r}X_s(f_{\mathrm{op}})}\right) \qquad \text{(X.6)}$$

In addition, a higher impedance value increases the normalized attenuation constant value in correspondence of the operative frequency: this effect is predictable, due to a weaker reflectivity of a higher impedance value.

Consequently, as the impedance value increases, the radiation patterns at broadside of the corresponding LWA have wider beamwidths and reduced directivities. Both leaky-wave theory [222] and reciprocity theorem [285] confirm this behavior, as shown in *Fig. 63* for the *E*-plane (primarily determined by the TM leaky mode) and in *Fig. 64* for the *H*-plane (primarily determined by the TE leaky mode). Some relevant radiating properties for all layouts are listed in *Table 14*.

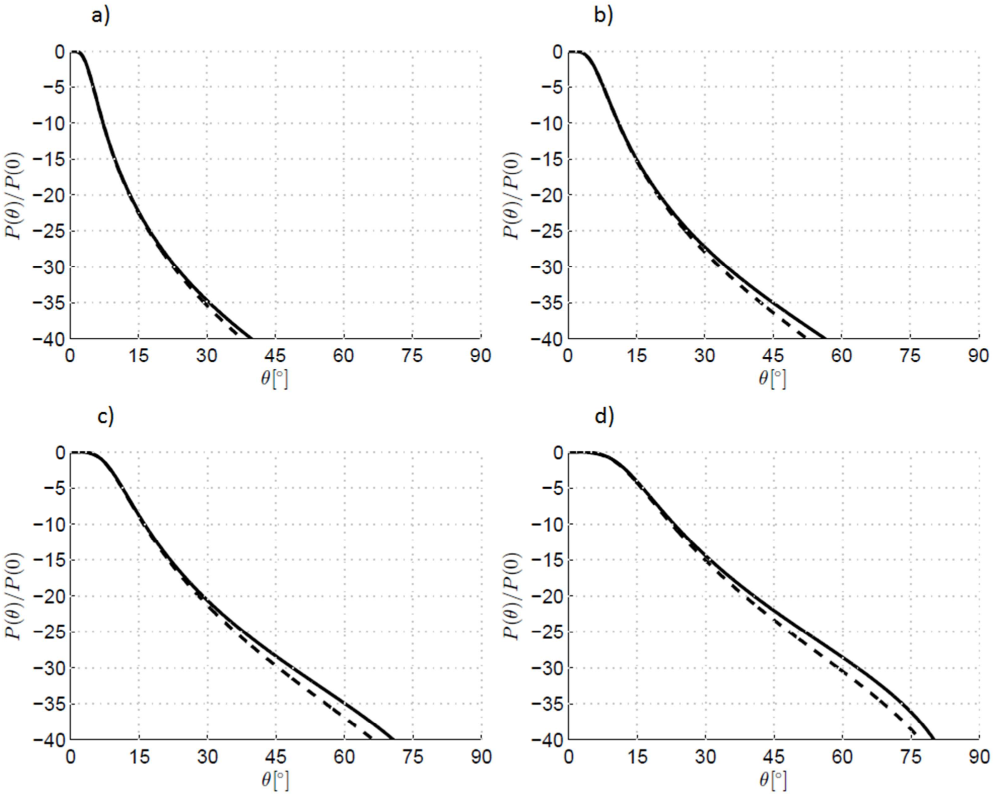

Fig. 64 Radiation patterns normalized to broadside radiation calculated with the leaky-wave approach (black solid lines) and reciprocity theorem (black dashed lines) are reported over the H-plane for the four layouts of *Table 14*.

With regard to the efficiency of these devices, the loss tangent of the Zeonor (see Ch. II Sec. 5 for a comparison between THz suitable materials properties) contributes to raise the leakage rates in all layouts. Hence, the amount of leakage due to radiation $\hat{\alpha}_{\mathrm{rad}}$ and due to absorption $\hat{\alpha}_{\mathrm{loss}}$ can be determined for calculating the efficiency as proposed in [295]:

$$e_r = e_{r,\infty}\eta_r = \frac{\alpha_{\mathrm{rad}}}{\alpha_\rho}\left(1 - e^{-\alpha_\rho L}\right) \qquad \text{(X.7)}$$

where $\hat{\alpha}_\rho = \hat{\alpha}_{\mathrm{rad}} + \hat{\alpha}_{\mathrm{loss}}$, L is the dimension of the structure in *y*- and *z*-direction, $e_{r,\infty} = \lim_{L\to\infty} e_r$ is the efficiency contribution due to the substrate losses, and η_r is the efficiency contribution due to the finiteness of the structure. The values of $e_{r,\infty}$ and e_r are reported in *Table 14* for $L = 20\lambda_0$ which allows to have $\eta_r > 90\%$ for all layouts. The gain can be calculated as $G = e_r D_0$. It results just few dB lower than the predicted theoretical directivities, confirming the remarkable radiating performance of FPC-LWAs based on the metasurfaces with fishnet elements. The impact of the substrate loss is more evident for highly-directive layouts: it leads to a reduction of the efficiency of 20% more than the layouts with a lower directivity.

4.1 Full-wave analysis of the truncated structure

Full-wave simulations of the truncated FPC-LWAs based on PRSs with fishnet-like elements are performed by employing CST Microwave Studio (compare Ch. III Sec. 2), with the aim to evaluate the effect of diffraction from edges. The structure is excited by modeling a *y*-oriented HMD (compare Ch. IX) with a slot of lateral dimensions $\lambda_0/2$ and $\lambda_0/4$ along the *y*- and *x*-axis, respectively.

As shown in *Fig. 65 a)-b)* and *Fig. 66 a)-b)*, the effect of the lateral truncation ($L = 20\lambda_0$) is almost negligible due to the weak contribution of the field at the edge of the structure ($\eta_r > 90\%$).

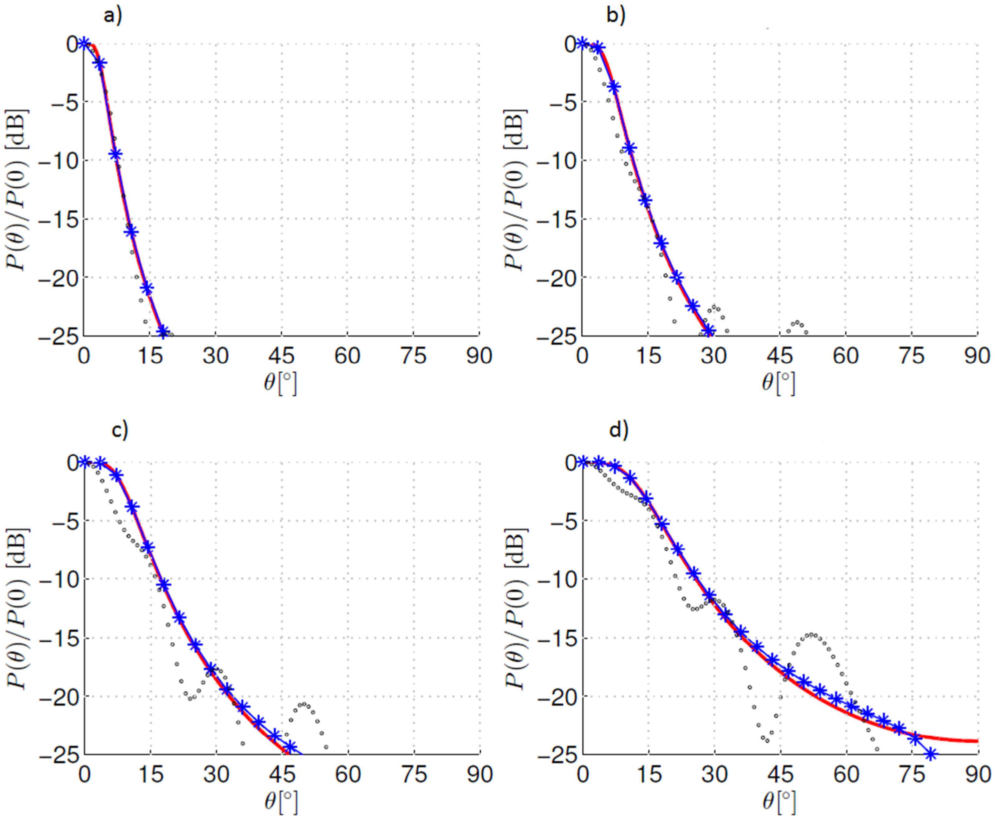

Fig. 65 Radiation patterns normalized to broadside radiation calculated with the leaky-wave approach (red solid lines) and reciprocity theorem (blue asterisks), and validated with full-wave simulations (black circles) are reported over the *E*-plane for the four layout of *Table 14*.

The agreement between full-wave simulations (small black circles of *Fig. 65* and *Fig. 66*), the leaky-wave approach (red solid lines of *Fig. 65* and *Fig. 66*), and the reciprocity theorem (blue asterisks of *Fig. 65* and *Fig. 66*) is remarkably good. Some differences can be just observed on the E-plane for the last two layouts (*Fig. 65 c)-d)*), probably due to a weaker validity of the homogenization hypothesis. A period of $\lambda_0/10$ for the unit cell could lead to a closer agreement. However, for that value of the period, the mask details for the PRS fabrication are at the limit of the standard tolerances for the targeted low-cost large area photolithographic process.

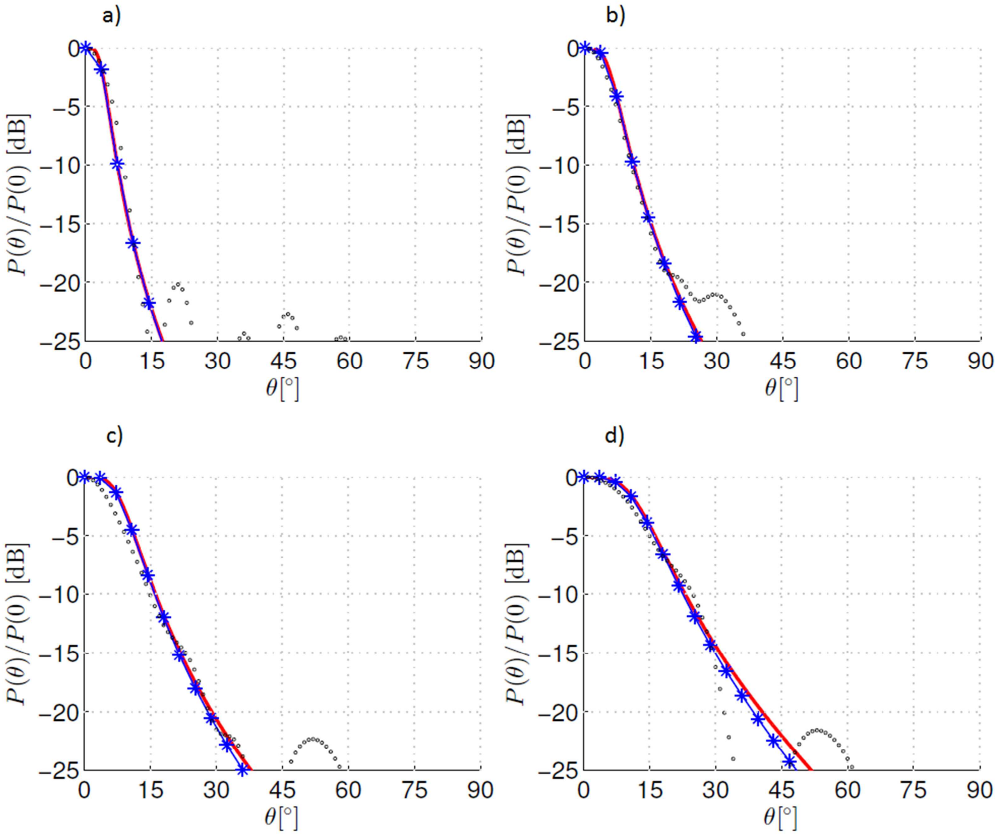

Fig. 66 Radiation patterns normalized to broadside radiation calculated with the leaky-wave approach (red solid lines) and reciprocity theorem (blue asterisks), and validated with full-wave simulations (black circles) are reported over the H-plane for the four layout of *Table 14*.

Finally, the same simulations have been performed: (i) by assuming a lossy layer of aluminum, with a thickness larger than its skin depth at 1 THz, in place of the ideal PEC modeling the metallic part of the fishnet-like element; (ii) by considering possible errors due to fabrication process, such as the misalignment of the slot with respect to the center of the structure, a rotation of the slot with respect to the *xy*-plane, and so on. Corresponding numerical results are not shown because they do not present appreciable differences if compared to data in *Fig. 65* and *Fig. 66*. The only exception is when the slot has a misalignment of 10 μm in the transverse plane and a rotation around the vertical axis of about 15 mrad. This configuration barely affects the symmetry of the radiation pattern below the level of the sidelobes (around -20 dB), showing a further confirmation of the validity of the homogenization limit.

5. Conclusions

The proposed fishnet-like PRS has interesting features with respect to other existing PRSs. At first, it provides a very low purely imaginary impedance in the THz range without an extreme variation of its geometrical parameters, as is required for the design of similar homogenized metasurfaces, such as patches or strips [38]. Consequently, a FPC-LWA based on a fishnet PRS can have a very high directivity.

Secondly, this PRS has a high filling factor, *i.e.*, a high ratio between the area covered by the metal and the unit-cell area. Moreover, the fishnet is a topologically-connected geometry and its surface impedance is spatially nondispersive: the fishnet PRS is an attractive candidate as top electrode in a FPC-LWA filled with an electro-optically tunable material, such as LCs.

Finally, differently from patches and strips, for which already exist homogenization formulas [266], no analytical expressions have been reported so far for such PRSs, thus motivating the in-depth study carried out on this PRS geometry.

REFERENCES

[1] B. Ferguson and X.-C. Zhang, “Materials for terahertz science and technology,” *Nat. Mater.*, vol. 1, no. 1, pp. 26–33, 2002.

[2] E. Pickwell and V. P. Wallace, “Biomedical applications of terahertz technology,” *J. Phys. Appl. Phys.*, vol. 39, no. 17, pp. R301–R310, 2006.

[3] T. Nagatsuma, “Terahertz technologies: Present and future,” *IEICE Electron. Express*, vol. 8, no. 14, pp. 1127–1142, 2011.

[4] T. Nagatsuma *et al.*, “Terahertz wireless communications based on photonics technologies,” *Opt. Express*, vol. 21, no. 20, pp. 23736–23747, 2013.

[5] G. Chattopadhyay, “Technology, capabilities, and performance of low power terahertz sources,” *IEEE Trans. Terahertz Sci. Technol.*, vol. 1, no. 1, pp. 33–53, 2011.

[6] M. Tonouchi, “Cutting-edge terahertz technology,” *Nat. Photonics*, vol. 1, no. 2, pp. 97–105, 2007.

[7] P. H. Siegel, “Terahertz technology,” *IEEE Trans. Microw. Theory Tech.*, vol. 50, no. 3, pp. 910–928, 2002.

[8] M. White, D. Scott, and J. Silk, “Anisotropies in the cosmic microwave background,” *Annu. Rev. Astron. Astrophys.*, vol. 32, pp. 319–70, 1994.

[9] E. F. Nichols, “A method for energy measurements in the infra-red spectrum and the properties of the ordinary ray in quartz for waves of great wave length,” *Phys. Rev. Ser. I*, vol. 4, no. 4, pp. 297–313, 1897.

[10] H. Rubens and E. F. Nichols, “Heat rays of great wave length,” *Phys. Rev. Ser. I*, vol. 4, no. 4, pp. 314–323, 1897.

[11] M. F. Kimmitt, “Restrahlen to T-Rays – 100 Years of Terahertz Radiation,” *J. Biol. Phys.*, vol. 29, no. 2–3, pp. 77–85, Jun. 2003.

[12] W. S. Boyle and K. F. Rodgers, “Performance Characteristics of a New Low-Temperature Bolometer,” *JOSA*, vol. 49, no. 1, pp. 66–69, Jan. 1959.

[13] S. J. Fray and J. F. C. Oliver, “Photoconductive detector of radiation of wavelength greater than 50 μ,” *J. Sci. Instrum.*, vol. 36, no. 4, p. 195, 1959.

[14] F. J. Low, “Low-Temperature Germanium Bolometer,” *JOSA*, vol. 51, no. 11, pp. 1300–1304, Nov. 1961.

[15] E. H. Putley, “Solid state devices for infra-red detection,” *J. Sci. Instrum.*, vol. 43, no. 12, p. 857, 1966.

[16] M. A. C. S. Brown and M. F. Kimmitt, “Far-infrared resonant photoconductivity in indium antimonide,” *Infrared Phys.*, vol. 5, no. 2, pp. 93–97, Jun. 1965.

[17] M. Bass, P. A. Franken, J. F. Ward, and G. Weinreich, “Optical Rectification,” *Phys. Rev. Lett.*, vol. 9, no. 11, pp. 446–448, Dec. 1962.

[18] K. Aoki, J. Savolainen, and M. Havenith, “Broadband terahertz pulse generation by optical rectification in GaP crystals,” *Appl. Phys. Lett.*, vol. 110, no. 20, p. 201103, May 2017.

[19] K. H. Yang, P. L. Richards, and Y. R. Shen, “Generation of Far-Infrared Radiation by Picosecond Light Pulses in LiNbO3,” *Appl. Phys. Lett.*, vol. 19, no. 9, pp. 320–323, Nov. 1971.

[20] L. R. Elias, J. Hu, and G. Ramian, “The UCSB electrostatic accelerator free electron laser: First operation,” *Nucl. Instrum. Methods Phys. Res. Sect. Accel. Spectrometers Detect. Assoc. Equip.*, vol. 237, no. 1, pp. 203–206, Jun. 1985.

[21] M. B. Ketchen *et al.*, “Generation of subpicosecond electrical pulses on coplanar transmission lines,” *Appl. Phys. Lett.*, 19860324.

[22] U. Frisk *et al.*, “The Odin satellite - I. Radiometer design and test,” *Astron. Astrophys.*, vol. 402, no. 3, pp. L27–L34, May 2003.

[23] “EOS MLS.” [Online]. Available: https://mls.jpl.nasa.gov/index-eos-mls.php. [Accessed: 31-Aug-2017].

[24] “Orbiter Instruments.” [Online]. Available: http://sci.esa.int/rosetta/35061-instruments/?fbodylongid%EF%BB%BF=%EF%BB%BF1641. [Accessed: 31-Aug-2017].

[25] S. S. Dhillon *et al.*, “The 2017 terahertz science and technology roadmap,” *J. Phys. Appl. Phys.*, vol. 50, no. 4, p. 043001, 2017.

[26] L. Huang, S. G. Lambrakos, A. Shabaev, N. Bernstein, and L. Massa, *Passive and Active Millimeter-Wave Imaging XVII*, vol. 9078. 2014.

[27] J. O. Richardson *et al.*, “Investigation of terahertz vibration–rotation tunneling spectra for the water octamer,” *J. Phys. Chem. A*, vol. 117, no. 32, pp. 6960–6966, Aug. 2013.

[28] Y. D. Wu, T. Zhou, Z. W. Yao, and J. C. Cao, “Theoretical and experimental investigation of terahertz absorption spectra for water clusters (H2O)n (n = 4, 5, 6) in the atmosphere,” *J. Appl. Spectrosc.*, vol. 83, no. 3, pp. 362–366, Jul. 2016.

[29] I. F. Akyildiz, J. M. Jornet, and C. Han, “Terahertz band: Next frontier for wireless communications,” *Phys. Commun.*, vol. 12, pp. 16–32, Sep. 2014.

[30] T. S. Rappaport, J. N. Murdock, and F. Gutierrez, “State of the art in 60-GHz integrated circuits and systems for wireless communications,” *Proc. IEEE*, vol. 99, no. 8, pp. 1390–1436, Aug. 2011.

[31] R. Miles, X.-C. Zhang, H. Eisele, and A. Krotkus, *Terahertz Frequency Detection and Identification of Materials and Objects*. Springer Science & Business Media, 2007.

[32] R. Gente and M. Koch, “Monitoring leaf water content with THz and sub-THz waves,” *Plant Methods*, vol. 11, p. 15, Mar. 2015.

[33] N. Q. Vinh, M. S. Sherwin, S. J. Allen, D. K. George, A. J. Rahmani, and K. W. Plaxco, “High-precision gigahertz-to-terahertz spectroscopy of aqueous salt solutions as a probe of the femtosecond-to-picosecond dynamics of liquid water,” *J. Chem. Phys.*, vol. 142, no. 16, p. 164502, Apr. 2015.

[34] D. M. Leitner, M. Havenith, and M. Gruebele, “Biomolecule large-amplitude motion and solvation dynamics: modelling and probes from THz to X-rays,” *Int. Rev. Phys. Chem.*, vol. 25, no. 4, pp. 553–582, Oct. 2006.

[35] M. Hishida and K. Tanaka, “Long-range hydration effect of lipid membrane studied by terahertz time-domain spectroscopy,” *Phys. Rev. Lett.*, vol. 106, no. 15, p. 158102, Apr. 2011.

[36] B. B. Hu and M. C. Nuss, “Imaging with terahertz waves,” *Opt. Lett.*, vol. 20, no. 16, pp. 1716–1718, Aug. 1995.

[37] R. F. Haglund, J. Neev, R. F. Wood, and S. of P. I. Engineers, *Commercial and biomedical applications of ultrashort pulse lasers; laser plasma generation and diagnostics*. SPIE, 2001.

[38] V. p. Wallace *et al.*, “Terahertz pulsed imaging of basal cell carcinoma ex vivo and in vivo,” *Br. J. Dermatol.*, vol. 151, no. 2, pp. 424–432, Aug. 2004.

[39] E. Heinz *et al.*, “Passive 350 GHz video imaging systems for security applications,” *J. Infrared Millim. Terahertz Waves*, vol. 36, no. 10, pp. 879–895, Oct. 2015.

[40] M. R. Leahy-Hoppa, M. J. Fitch, X. Zheng, L. M. Hayden, and R. Osiander, “Wideband terahertz spectroscopy of explosives,” *Chem. Phys. Lett.*, vol. 434, no. 4, pp. 227–230, Feb. 2007.

[41] C. Mann, “First demonstration of a vehicle mounted 250 GHz real time passive imager,” presented at the Terahertz Physics, Devices, and Systems III: Advanced Applications in Industry and Defense, 2009, vol. 7311, p. 73110Q.

[42] R. Appleby and S. Ferguson, “Submillimetre wave imaging and security: imaging performance and prediction,” presented at the Millimetre Wave and Terahertz Sensors and Technology IX, 2016, vol. 9993, p. 999302.

[43] C. G. Soares, Y. Garbatov, A. Zayed, and G. Wang, “Influence of environmental factors on corrosion of ship structures in marine atmosphere,” *Corros. Sci.*, vol. 51, no. 9, pp. 2014–2026, Sep. 2009.

[44] W. Tu, S. Zhong, Y. Shen, and A. Incecik, “Nondestructive testing of marine protective coatings using terahertz waves with stationary wavelet transform,” *Ocean Eng.*, vol. 111, pp. 582–592, Jan. 2016.

[45] D. J. Cook, S. Lee, S. J. Sharpe, and M. G. Allen, “Accuracy and linearity of time-domain THz paint thickness measurements,” presented at the Terahertz Technology and Applications, 2008, vol. 6893, p. 68930H.

[46] J. B. Jackson *et al.*, “A survey of terahertz applications in cultural heritage conservation science,” *IEEE Trans. Terahertz Sci. Technol.*, vol. 1, no. 1, pp. 220–231, Sep. 2011.

[47] K. Krügener *et al.*, “Terahertz meets sculptural and architectural art: Evaluation and conservation of stone objects with T-ray technology,” *Sci. Rep.*, vol. 5, Oct. 2015.

[48] K. Fukunaga, T. Ikari, and K. Iwai, “THz pulsed time-domain imaging of an oil canvas painting: a case study of a painting by Pablo Picasso,” *Appl. Phys. A*, vol. 122, no. 2, p. 106, Feb. 2016.

[49] A. Borak, “Toward bridging the terahertz gap with silicon-based lasers,” *Science*, vol. 308, no. 5722, pp. 638–639, Apr. 2005.

[50] W. L. Chan, J. Deibel, and D. M. Mittleman, “Imaging with terahertz radiation,” *Rep. Prog. Phys.*, vol. 70, no. 8, p. 1325, 2007.

[51] J. M. Chamberlain, “Where optics meets electronics: recent progress in decreasing the terahertz gap,” *Philos. Trans. R. Soc. Lond. Math. Phys. Eng. Sci.*, vol. 362, no. 1815, pp. 199–213, Feb. 2004.

[52] B. S. Williams, “Terahertz quantum-cascade lasers,” *Nat. Photonics*, vol. 1, no. 9, pp. 517–525, Sep. 2007.

[53] H.-W. Hübers, S. G. Pavlov, and V. N. Shastin, “Terahertz lasers based on germanium and silicon,” *Semicond. Sci. Technol.*, vol. 20, no. 7, p. S211, 2005.

[54] B. A. Knyazev, G. N. Kulipanov, and N. A. Vinokurov, “Novosibirsk terahertz free electron laser: instrumentation development and experimental achievements,” *Meas. Sci. Technol.*, vol. 21, no. 5, p. 054017, 2010.

[55] D. W. Sprehn, C. L. Rettig, and N. C. Luhmann, “Phase locking and frequency locking of a 140 GHz klystron and a 280 GHz carcinotron,” *Rev. Sci. Instrum.*, vol. 63, no. 10, pp. 4685–4687, Oct. 1992.

[56] J. E. Walsh, J. H. Brownell, M. J. Goldstein, J. C. Swartz, J. Urata, and M. F. Kimmitt, “A new tunable coherent FIR-THz source,” *Opt. Photonics News*, vol. 9, pp. 51–52, Dec. 1998.

[57] P. H. Siegel, A. Fung, H. Manohara, J. Xu, and B. Chang, “Nanoklystron: A monolithic tube approach to THz power generation,” 2001.

[58] A. Maestrini *et al.*, “A frequency-multiplied source with more than 1 mW of power across the 900-GHz band,” *IEEE Trans. Microw. Theory Tech.*, vol. 58, no. 7, pp. 1925–1932, Jul. 2010.

[59] A. Maestrini *et al.*, “A 1.7-1.9 THz local oscillator source,” *IEEE Microw. Wirel. Compon. Lett.*, vol. 14, no. 6, pp. 253–255, Jun. 2004.

[60] “Frequency Multipliers.” [Online]. Available: http://vadiodes.com/en/frequency-multipliers. [Accessed: 18-Oct-2017].

[61] J. Lusakowski *et al.*, “Voltage tuneable terahertz emission from a ballistic nanometer InGaAs⁄InAlAs transistor,” *J. Appl. Phys.*, vol. 97, no. 6, p. 064307, Mar. 2005.

[62] A. Lisauskas, A. Rämer, M. Burakevič, V. Krozer, W. Heinrich, and H. G. Roskos, “Terahertz emission from large AlGaN/GaN field-effect transistors,” in *2016 41st International Conference on Infrared, Millimeter, and Terahertz waves (IRMMW-THz)*, 2016, pp. 1–1.

[63] G. Chin, “Optically pumped submillimeter laser heterodyne receivers: astrophysical observations and recent technical developments,” *Proc. IEEE*, vol. 80, no. 11, pp. 1788–1799, Nov. 1992.

[64] H.-P. Röser, “Heterodyne spectroscopy for submillimeter and far-infrared wavelengths from 100 μm to 500 μm,” *Infrared Phys.*, vol. 32, pp. 385–407, Jan. 1991.

[65] G. Dodel, “On the history of far-infrared (FIR) gas lasers: Thirty-five years of research and application,” *Infrared Phys. Technol.*, vol. 40, no. 3, pp. 127–139, Jun. 1999.

[66] J. M. Chamberlain and R. Miles, *New Directions in Terahertz Technology*. Springer Netherlands, 1997.

[67] M. Scheller, J. M. Yarborough, J. V. Moloney, M. Fallahi, M. Koch, and S. W. Koch, “Room temperature continuous wave milliwatt terahertz source,” *Opt. Express*, vol. 18, no. 26, pp. 27112–27117, Dec. 2010.

[68] X. L. Wu *et al.*, “Green light stimulates terahertz emission from mesocrystal microspheres,” *Nat. Nanotechnol.*, vol. 6, no. 2, pp. 103–106, Feb. 2011.

[69] N. T. Yardimci, S. H. Yang, C. W. Berry, and M. Jarrahi, “High-power terahertz generation using large-area plasmonic photoconductive emitters,” *IEEE Trans. Terahertz Sci. Technol.*, vol. 5, no. 2, pp. 223–229, Mar. 2015.

[70] S. Kono, M. Tani, P. Gu, and K. Sakai, “Detection of up to 20 THz with a low-temperature-grown GaAs photoconductive antenna gated with 15 fs light pulses,” *Appl. Phys. Lett.*, vol. 77, no. 25, pp. 4104–4106, Dec. 2000.

[71] D. Kuk, Y. J. Yoo, E. W. Rosenthal, N. Jhajj, H. M. Milchberg, and K. Y. Kim, “Generation of scalable terahertz radiation from cylindrically focused two-color laser pulses in air,” *Appl. Phys. Lett.*, vol. 108, no. 12, p. 121106, Mar. 2016.

[72] H. A. Hafez *et al.*, “Intense terahertz radiation and their applications,” *J. Opt.*, vol. 18, no. 9, p. 093004, 2016.

[73] K. A. McIntosh, E. R. Brown, K. B. Nichols, O. B. McMahon, W. F. DiNatale, and T. M. Lyszczarz, “Terahertz photomixing with diode lasers in low-temperature-grown GaAs,” *Appl. Phys. Lett.*, vol. 67, no. 26, pp. 3844–3846, Dec. 1995.

[74] A. J. Deninger *et al.*, "Precisely tunable continuous-wave terahertz source with interferometric frequency control," *Rev. Sci. Instrum.*, vol. 79, no. 4, p. 044702, Apr. 2008.

[75] R. A. Lewis, "A review of terahertz sources," *J. Phys. Appl. Phys.*, vol. 47, no. 37, p. 374001, 2014.

[76] N. M. Burford and M. O. El-Shenawee, "Review of terahertz photoconductive antenna technology," *Opt. Eng.*, vol. 56, no. 1, p. 010901, Jan. 2017.

[77] A. Rogalski and F. Sizov, "Terahertz detectors and focal plane arrays," *Opto-Electron. Rev.*, vol. 19, no. 3, pp. 346–404, 2011.

[78] F. Sizov and A. Rogalski, "THz detectors," *Prog. Quantum Electron.*, vol. 34, no. 5, pp. 278–347, Sep. 2010.

[79] H.-J. Song and T. Nagatsuma, *Handbook of Terahertz Technologies: Devices and Applications*. CRC Press, 2015.

[80] "Virginia Diodes, Inc - Application Notes." [Online]. Available: http://www.vadiodes.com/en/app-notes/app-notes. [Accessed: 02-Oct-2017].

[81] A. Barh, B. P. Pal, G. P. Agrawal, R. K. Varshney, and B. M. A. Rahman, "Specialty fibers for terahertz generation and transmission: a review," *IEEE J. Sel. Top. Quantum Electron.*, vol. 22, no. 2, pp. 365–379, Mar. 2016.

[82] S. R. Andrews, "Microstructured terahertz waveguides," *J. Phys. Appl. Phys.*, vol. 47, no. 37, p. 374004, 2014.

[83] L. Cao, A.-S. Grimault-Jacquin, N. Zerounian, and F. Aniel, "Design and VNA-measurement of coplanar waveguide (CPW) on benzocyclobutene (BCB) at THz frequencies," *Infrared Phys. Technol.*, vol. 63, pp. 157–164, Mar. 2014.

[84] Y. Kadoya, "THz wave propagation on strip lines: Devices, properties, and applications," in *2007 19th International Conference on Applied Electromagnetics and Communications*, 2007, pp. 1–4.

[85] K. Nielsen, H. K. Rasmussen, A. J. L. Adam, P. C. M. Planken, O. Bang, and P. U. Jepsen, "Bendable, low-loss Topas fibers for the terahertz frequency range," *Opt. Express*, vol. 17, no. 10, pp. 8592–8601, May 2009.

[86] A. Dupuis, A. Mazhorova, F. Désévédavy, M. Rozé, and M. Skorobogatiy, "Spectral characterization of porous dielectric subwavelength THz fibers fabricated using a microstructured molding technique," *Opt. Express*, vol. 18, no. 13, pp. 13813–13828, Jun. 2010.

[87] A. Hassani, A. Dupuis, and M. Skorobogatiy, “Porous polymer fibers for low-loss Terahertz guiding,” *Opt. Express*, vol. 16, no. 9, pp. 6340–6351, Apr. 2008.

[88] P. F. Goldsmith, “Quasi-optical techniques,” *Proc. IEEE*, vol. 80, no. 11, pp. 1729–1747, Nov. 1992.

[89] Y. Cai, I. Brener, J. Lopata, J. Wynn, L. Pfeiffer, and J. Federici, “Design and performance of singular electric field terahertz photoconducting antennas,” *Appl. Phys. Lett.*, vol. 71, no. 15, pp. 2076–2078, Oct. 1997.

[90] M. Reid, I. V. Cravetchi, and R. Fedosejevs, “Terahertz radiation and second-harmonic generation from InAs: Bulk versus surface electric-field-induced contributions,” *Phys. Rev. B*, vol. 72, no. 3, p. 035201, Jul. 2005.

[91] F. Yan, C. Yu, H. Park, E. P. J. Parrott, and E. Pickwell-MacPherson, “Advances in polarizer technology for terahertz frequency applications,” *J. Infrared Millim. Terahertz Waves*, vol. 34, no. 9, pp. 489–499, Sep. 2013.

[92] B. Vasić, D. C. Zografopoulos, G. Isić, R. Beccherelli, and R. Gajić, “Electrically tunable terahertz polarization converter based on overcoupled metal-isolator-metal metamaterials infiltrated with liquid crystals,” *Nanotechnology*, vol. 28, no. 12, p. 124002, 2017.

[93] M. Born and E. Wolf, *Principles of Optics: Electromagnetic Theory of Propagation, Interference and Diffraction of Light*. Elsevier, 2013.

[94] M. E. MacDonald, A. Alexanian, R. A. York, Z. Popovic, and E. N. Grossman, “Spectral transmittance of lossy printed resonant-grid terahertz bandpass filters,” *IEEE Trans. Microw. Theory Tech.*, vol. 48, no. 4, pp. 712–718, Apr. 2000.

[95] C. Winnewisser, F. Lewen, and H. Helm, “Transmission characteristics of dichroic filters measured by THz time-domain spectroscopy,” *Appl. Phys. A*, vol. 66, no. 6, pp. 593–598, Jun. 1998.

[96] N. R. Erickson, “A directional filter diplexer using optical techniques for millimeter to submillimeter wavelengths,” *IEEE Trans. Microw. Theory Tech.*, vol. 25, no. 10, pp. 865–866, Oct. 1977.

[97] Z. G. Lu, J. B. Tan, and Z. G. Fan, “Terahertz Fabry-Perot interferometer constructed by metallic meshes with micrometer period and high ratio of linewidth/period,” *Key Eng. Mater.*, vol. 437, pp. 286–290, 2010.

[98] B. Scherger, M. Scheller, C. Jansen, M. Koch, and K. Wiesauer, “Terahertz lenses made by compression molding of micropowders,” *Appl. Opt.*, vol. 50, no. 15, pp. 2256–2262, May 2011.

[99] Y. H. Lo and R. Leonhardt, “Aspheric lenses for terahertz imaging,” *Opt. Express*, vol. 16, no. 20, pp. 15991–15998, Sep. 2008.

[100] M. Wichmann *et al.*, “Terahertz plastic compound lenses,” *Appl. Opt.*, vol. 52, no. 18, pp. 4186–4191, Jun. 2013.

[101] M. Takai, K. Shibata, M. Uemoto, and S. Watanabe, “Spatial polarization variation in terahertz electromagnetic wave focused by off-axis parabolic mirror,” *Appl. Phys. Express*, vol. 9, no. 5, p. 052206, Apr. 2016.

[102] L. Minkevičius *et al.*, “Compact diffractive optical components for terahertz beam manipulation,” in *2015 40th International Conference on Infrared, Millimeter, and Terahertz waves (IRMMW-THz)*, 2015, pp. 1–2.

[103] A. Siemion *et al.*, “Diffractive paper lens for terahertz optics,” *Opt. Lett.*, vol. 37, no. 20, pp. 4320–4322, Oct. 2012.

[104] A. Siemion *et al.*, “Off-axis metallic diffractive lens for terahertz beams,” *Opt. Lett.*, vol. 36, no. 11, pp. 1960–1962, Jun. 2011.

[105] S. Wang and X.-C. Zhang, “Terahertz technology: Terahertz tomographic imaging with a Fresnel lens,” *Opt. Photonics News*, vol. 13, no. 12, pp. 59–59, Dec. 2002.

[106] J. L. Soret, “Ueber die durch Kreisgitter erzeugten Diffractionsphänomene,” *Ann. Phys.*, vol. 232, no. 9, pp. 99–113, Jan. 1875.

[107] E. Skudrzyk, *The Foundations of Acoustics*. Springer-Verlag, 1971.

[108] Lord Rayleigh, “Wave theory,” *Encycl. Br.*, p. 422, 1890.

[109] R. W. Wood, “LIII. Phase-reversal zone-plates, and diffraction-telescopes,” *Philos. Mag. Ser. 5*, vol. 45, no. 277, pp. 511–522, Jun. 1898.

[110] R. W. Wood, *Physical Optics*. The Macmillan Company, 1934.

[111] R. A. Houstoun, *A treatise on light*. London, New York etc.: Longmans, Green and co., 1930.

[112] M. Sussman, “Elementary diffraction theory of zone plates,” *Am. J. Phys.*, vol. 28, no. 4, pp. 394–398, Apr. 1960.

[113] O. E. Myers Jr., “Studies of transmission zone plates,” *Am. J. Phys.*, vol. 19, no. 6, pp. 359–365, Sep. 1951.

[114] A. V. Baez, “A study in diffraction microscopy with special reference to X-rays,” *JOSA*, vol. 42, no. 10, pp. 756–762, Oct. 1952.

[115] A. V. Baez, “Fresnel zone plate for optical image formation using extreme ultraviolet and soft X-radiation,” *JOSA*, vol. 51, no. 4, pp. 405–412, Apr. 1961.

[116] J. Kirz, “Phase zone plates for x rays and the extreme uv,” *JOSA*, vol. 64, no. 3, pp. 301–309, Mar. 1974.

[117] I. Mohacsi *et al.*, “High-efficiency zone-plate optics for multi-keV X-ray focusing,” *J. Synchrotron Radiat.*, vol. 21, no. 3, pp. 497–501, May 2014.

[118] S.-C. Gleber *et al.*, “Fresnel zone plate stacking in the intermediate field for high efficiency focusing in the hard X-ray regime,” *Opt. Express*, vol. 22, no. 23, p. 28142, Nov. 2014.

[119] R. Mirjalili and B. A. Parviz, “Microlight-emitting diode with integrated Fresnel zone plate for contact lens embedded display,” *J. MicroNanolithography MEMS MOEMS*, vol. 11, no. 3, pp. 033010–033010, 2012.

[120] T. B. Brown, “Microwave zone plates,” *Am. J. Phys.*, vol. 30, no. 1, pp. 55–60, Jan. 1962.

[121] R. Ruben, “An electronically scanned antenna using fresnel zone techniques,” in *1958 IRE International Convention Record*, 1966, vol. 14, pp. 244–251.

[122] G. S. Sanyal and M. Singh, “Fresnel zone plate antenna,” *IETE J. Res.*, vol. 14, no. 6, pp. 265–281, Jun. 1968.

[123] K. K. Dey and P. Khastgir, “A study of the characteristics of a microwave spherical zone plate antenna,” *Int. J. Electron.*, vol. 35, no. 1, pp. 97–103, Jul. 1973.

[124] H. D. Hristov, “Microwave Fresnel zone plate antenna runs at multiple terahertz frequencies,” presented at the Proceedings of the IASTED International Conference on Antennas, Radar and Wave Propagation, ARP 2010, 2010, pp. 9–13.

[125] H. D. Hristov, “Terahertz harmonic operation of microwave Fresnel zone plate lens and antenna: Frequency filtering and space resolution properties,” *Int. J. Antennas Propag.*, vol. 2011, p. e541734, Dec. 2011.

[126] J. M. Rodríguez, H. D. Hristov, and W. Grote, “Fresnel zone plate and ordinary lens antennas: Comparative study at microwave and terahertz frequencies,” presented at the European Microwave Week 2011: “Wave to the

Future", EuMW 2011, Conference Proceedings - 41st European Microwave Conference, EuMC 2011, 2011, pp. 894–897.

[127] H. D. Hristov, J. m. Rodriguez, and W. Grote, "The grooved-dielectric Fresnel zone plate: An effective terahertz lens and antenna," *Microw. Opt. Technol. Lett.*, vol. 54, no. 6, pp. 1343–1348, Jun. 2012.

[128] J. C. Wiltse, "Phase-correcting zone plate antennas at terahertz frequencies," presented at the Proceedings of SPIE - The International Society for Optical Engineering, 2003, vol. 5070, pp. 98–107.

[129] A. E. Torres-García, B. Orazbayev, R. Gonzalo, and I. Ederra, "A quasi-spiral antenna for THz - IR dual-band sensors," in *2016 Global Symposium on Millimeter Waves (GSMM) ESA Workshop on Millimetre-Wave Technology and Applications*, 2016, pp. 1–2.

[130] L. Minkevičius *et al.*, "Study of terahertz zone plates with integrated cross-shape apertures," in *2013 38th International Conference on Infrared, Millimeter, and Terahertz Waves (IRMMW-THz)*, 2013, pp. 1–2.

[131] L. Minkevičius *et al.*, "Terahertz zone plates with integrated laserablated bandpass filters," *Electron. Lett.*, vol. 49, no. 1, pp. 49–50, 2013.

[132] L. Minkevičius *et al.*, "On-chip integration solutions of compact optics and detectors in room-temperature terahertz imaging systems," 2015, vol. 9585, p. 95850M–95850M–6.

[133] L. Minkevičius, V. Tamošiunas, K. Madeikis, B. Voisiat, I. Kašalynas, and G. Valušis, "On-chip integration of laser-ablated zone plates for detection enhancement of inGaAs bow-tie terahertz detectors," *Electron. Lett.*, vol. 50, no. 19, pp. 1367–1369, Sep. 2014.

[134] L. Liu *et al.*, "Tunable and reconfigurable THz devices for advanced imaging and adaptive wireless communication," *Proceeding SPIE*, vol. 9934, pp. 993407-993407–13, 2016.

[135] M. I. B. Shams, Z. Jiang, J. Qayyum, S. Rahman, P. Fay, and L. Liu, "A terahertz reconfigurable photo-induced fresnel-zone-plate antenna for dynamic two-dimensional beam steering and forming," in *2015 IEEE MTT-S International Microwave Symposium*, 2015, pp. 1–4.

[136] V. E. Levashov and A. V. Vinogradov, "Analytical theory of zone plate efficiency," *Phys. Rev. E*, vol. 49, no. 6, pp. 5797–5803, Jun. 1994.

[137] D. J. Stigliani, R. Mittra, and R. G. Semonin, “Resolving power of a zone plate,” *JOSA*, vol. 57, no. 5, pp. 610–613, May 1967.

[138] G. Schmahl and D. Rudolph, “High power zone plates as image-forming systems for soft X-rays,” May 1977.

[139] M. Young, “Zone plates and their aberrations,” *JOSA*, vol. 62, no. 8, pp. 972–976, Aug. 1972.

[140] J. Dai, J. Zhang, W. Zhang, and D. Grischkowsky, “Terahertz time-domain spectroscopy characterization of the far-infrared absorption and index of refraction of high-resistivity, float-zone silicon,” *JOSA B*, vol. 21, no. 7, pp. 1379–1386, Jul. 2004.

[141] M. Naftaly and R. E. Miles, “Terahertz time-domain spectroscopy: A new tool for the study of glasses in the far infrared,” *J. Non-Cryst. Solids*, vol. 351, no. 40, pp. 3341–3346, Oct. 2005.

[142] S. F. Busch, M. Weidenbach, M. Fey, F. Schäfer, T. Probst, and M. Koch, “Optical properties of 3D printable plastics in the THz regime and their application for 3D printed THz optics,” *J. Infrared Millim. Terahertz Waves*, vol. 35, no. 12, pp. 993–997, Dec. 2014.

[143] D. Han, K. Lee, J. Lim, S. S. Hong, Y. K. Kim, and J. Ahn, “Terahertz lens made out of natural stone,” *Appl. Opt.*, vol. 52, no. 36, pp. 8670–8675, Dec. 2013.

[144] P. D. Cunningham *et al.*, “Broadband terahertz characterization of the refractive index and absorption of some important polymeric and organic electro-optic materials,” *J. Appl. Phys.*, vol. 109, no. 4, pp. 043505-043505-5, Feb. 2011.

[145] A. Siemion, P. Kostrowiecki-Lopata, A. Pindur, P. Zagrajek, and M. Sypek, “Paper on designing costless THz paper optics,” *Adv. Mater. Sci. Eng.*, vol. 2016, p. e9615698, Nov. 2016.

[146] Y.-S. Jin, G.-J. Kim, and S.-G. Jeon, “Terahertz dielectric properties of polymers,” *J. Korean Phys. Soc.*, vol. 49, no. 2, pp. 513–517, 2006.

[147] A. Podzorov and G. Gallot, “Low-loss polymers for terahertz applications,” *Appl. Opt.*, vol. 47, no. 18, pp. 3254–3257, Jun. 2008.

[148] P. A. George, W. Hui, F. Rana, B. G. Hawkins, A. E. Smith, and B. J. Kirby, “Microfluidic devices for terahertz spectroscopy of biomolecules,” *Opt. Express*, vol. 16, no. 3, pp. 1577–1582, Feb. 2008.

[149] M. Sypek *et al.*, “Highly efficient broadband double-sided Fresnel lens for THz range,” *Opt. Lett.*, vol. 37, no. 12, pp. 2214–2216, Jun. 2012.

[150] J. R. Middendorf, D. A. LeMaster, M. Zarepoor, and E. R. Brown, “Design of multi-order diffractive THz lenses,” in *2012 37th International Conference on Infrared, Millimeter, and Terahertz Waves*, 2012, pp. 1–2.

[151] S. F. Busch, M. Weidenbach, J. C. Balzer, and M. Koch, “THz optics 3D printed with TOPAS,” *J. Infrared Millim. Terahertz Waves*, vol. 37, no. 4, pp. 303–307, 2016.

[152] D. C. Zografopoulos and R. Beccherelli, “Tunable terahertz fishnet metamaterials based on thin nematic liquid crystal layers for fast switching,” *Sci. Rep.*, vol. 5, Aug. 2015.

[153] B. Scherger, M. Scheller, N. Vieweg, S. T. Cundiff, and M. Koch, “Paper terahertz wave plates,” *Opt. Express*, vol. 19, no. 25, pp. 24884–24889, Dec. 2011.

[154] J. Jahns, Q. Cao, and S. Sinzinger, “Micro- and nanooptics – an overview,” *Laser Photonics Rev.*, vol. 2, no. 4, pp. 249–263, Aug. 2008.

[155] “AF3-202E - velvia_100_datasheet.pdf.” [Online]. Available: http://www.fujifilm.com/products/professional_films/pdf/velvia_100_datasheet.pdf. [Accessed: 16-Aug-2017].

[156] W. B. Veldkamp and T. J. McHugh, “Binary optics,” *Sci. Am.*, vol. 266, no. 5, pp. 92–97, 1992.

[157] L. Kipp *et al.*, “Sharper images by focusing soft X-rays with photon sieves,” *Nature*, vol. 414, no. 6860, pp. 184–188, Nov. 2001.

[158] W. D. Furlan, V. Ferrando, J. A. Monsoriu, P. Zagrajek, E. Czerwińska, and M. Szustakowski, “3D printed diffractive terahertz lenses,” *Opt. Lett.*, vol. 41, no. 8, pp. 1748–1751, Apr. 2016.

[159] J. Suszek *et al.*, “3-D-printed flat optics for THz linear scanners,” *IEEE Trans. Terahertz Sci. Technol.*, vol. 5, no. 2, pp. 314–316, Mar. 2015.

[160] I. Mohacsi *et al.*, “High resolution double-sided diffractive optics for hard X-ray microscopy,” *Opt. Express*, vol. 23, no. 2, pp. 776–786, Jan. 2015.

[161] T. Rylander, P. Ingelström, and A. Bondeson, *Computational Electromagnetics*. Springer Science & Business Media, 2012.

[162] A. J. Poggio and E. K. Miller, *Integral Equation Solutions of Three-dimensional Scattering Problems*. MB Assoc., 1970.

[163] “COMSOL Multiphysics® Modeling Software.” [Online]. Available: https://www.comsol.com/. [Accessed: 09-May-2017].

[164] “CST.” [Online]. Available: https://www.cst.com/. [Accessed: 09-May-2017].

[165] T. Weiland, M. Timm, and I. Munteanu, “A practical guide to 3-D simulation,” *IEEE Microw. Mag.*, vol. 9, no. 6, pp. 62–75, Dec. 2008.

[166] “TYDEX Research&Industrial Optics.” [Online]. Available: http://www.tydexoptics.com/. [Accessed: 09-May-2017].

[167] B. McCall and T. S. Tkaczyk, “Rapid fabrication of miniature lens arrays by four-axis single point diamond machining,” *Opt. Express*, vol. 21, no. 3, pp. 3557–3572, Feb. 2013.

[168] F. Rui and W. Li, “A zone plate as a tunable terahertz filter,” *Chin. Phys. Lett.*, vol. 27, no. 6, p. 064201, 2010.

[169] W. Withayachumnankul and M. Naftaly, “Fundamentals of measurement in terahertz time-domain spectroscopy,” *J. Infrared Millim. Terahertz Waves*, vol. 35, no. 8, pp. 610–637, Aug. 2014.

[170] M. Naftaly, *Terahertz Metrology*. Artech House, 2015.

[171] M. Naftaly, R. G. Clarke, D. A. Humphreys, and N. M. Ridler, “Metrology state-of-the-art and challenges in broadband phase-sensitive terahertz measurements,” *Proc. IEEE*, vol. 105, no. 6, pp. 1151–1165, Jun. 2017.

[172] W. Sun, B. Yang, X. Wang, Y. Zhang, and R. Donnan, “Accurate determination of terahertz optical constants by vector network analyzer of Fabry–Perot response,” *Opt. Lett.*, vol. 38, no. 24, pp. 5438–5441, Dec. 2013.

[173] T. Tosaka, K. Fujii, K. Fukunaga, and A. Kasamatsu, “Development of complex relative permittivity measurement system based on free-space in 220 GHz range,” *IEEE Trans. Terahertz Sci. Technol.*, vol. 5, no. 1, pp. 102–109, Jan. 2015.

[174] M. Naftaly, N. Shoaib, D. Stokes, and N. M. Ridler, “Intercomparison of terahertz dielectric measurements using vector network analyzer and time-domain spectrometer,” *J. Infrared Millim. Terahertz Waves*, vol. 37, no. 7, pp. 691–702, Jul. 2016.

[175] “Menlo TERA K15.” [Online]. Available: http://www.menlosystems.com/products/thz-time-domain-solutions/all-fiber-coupled-terahertz-spectrometer/. [Accessed: 10-May-2017].

[176] E. Castro-Camus and M. Alfaro, “Photoconductive devices for terahertz pulsed spectroscopy: a review [Invited],” *Photonics Res.*, vol. 4, no. 3, pp. A36–A42, Jun. 2016.

[177] P. U. Jepsen, D. G. Cooke, and M. Koch, “Terahertz spectroscopy and imaging – Modern techniques and applications,” *Laser Photonics Rev.*, vol. 5, no. 1, pp. 124–166, Jan. 2011.

[178] P. R. Smith, D. H. Auston, and M. C. Nuss, “Subpicosecond photoconducting dipole antennas,” *IEEE J. Quantum Electron.*, vol. 24, no. 2, pp. 255–260, Feb. 1988.

[179] P. U. Jepsen and S. R. Keiding, “Radiation patterns from lens-coupled terahertz antennas,” *Opt. Lett.*, vol. 20, no. 8, pp. 807–809, Apr. 1995.

[180] “MENLO-SYSTEMS-Terahertz-Time-Domain-Solution-TERA-K15-THzStrecke-Extern-pr.jpg (2721×1814).” [Online]. Available: http://www.menlosystems.com/assets/PR/MENLO-SYSTEMS-Terahertz-Time-Domain-Solution-TERA-K15-THzStrecke-Extern-pr.jpg. [Accessed: 22-Oct-2017].

[181] “Motion Control.” [Online]. Available: https://www.newport.com/c/motion-control. [Accessed: 16-May-2017].

[182] “LabVIEW System Design Software - National Instruments.” [Online]. Available: http://www.ni.com/labview/i/. [Accessed: 16-May-2017].

[183] G. T. Herman, *Image Reconstruction from Projections*. Berlin: Springer, 1979.

[184] A. G. Lindgren and P. A. Rattey, “The inverse discrete radon transform with applications to tomographic imaging using projection data,” *Adv. Electron. Electron Phys.*, vol. 56, pp. 359–410, Jan. 1981.

[185] D. M. Slocum, E. J. Slingerland, R. H. Giles, and T. M. Goyette, “Atmospheric absorption of terahertz radiation and water vapor continuum effects,” *J. Quant. Spectrosc. Radiat. Transf.*, vol. 127, pp. 49–63, Sep. 2013.

[186] X. Wang *et al.*, “Focusing and imaging of a virtual all-optical tunable terahertz Fresnel zone plate,” *Opt. Lett.*, vol. 38, no. 22, pp. 4731–4734, Nov. 2013.

[187] P. Valley, M. R. Dodge, J. Schwiegerling, D. Mathine, G. Peyman, and N. Peyghambarian, “Flat liquid crystal diffractive lenses with variable focus and magnification,” presented at the Current Developments in Lens Design and

Optical Engineering XI; and Advances in Thin Film Coatings VI, 2010, vol. 7786, p. 77860H.

[188] H. Ren and S.-T. Wu, “Adaptive liquid crystal lens with large focal length tunability,” *Opt. Express*, vol. 14, no. 23, pp. 11292–11298, Nov. 2006.

[189] H. Ren, Y.-H. Fan, and S.-T. Wu, “Liquid-crystal microlens arrays using patterned polymer networks,” *Opt. Lett.*, vol. 29, no. 14, pp. 1608–1610, Jul. 2004.

[190] L.-C. Lin, H.-C. Jau, T.-H. Lin, and A. Y.-G. Fuh, “Highly efficient and polarization-independent Fresnel lens based on dye-doped liquid crystal,” *Opt. Express*, vol. 15, no. 6, pp. 2900–2906, Mar. 2007.

[191] B. Wang, M. Ye, and S. Sato, “Liquid crystal lens with stacked structure of liquid-crystal layers,” *Opt. Commun.*, vol. 250, no. 4, pp. 266–273, Jun. 2005.

[192] H. Li *et al.*, “Terahertz electrically controlled nematic liquid crystal lens,” *Infrared Phys. Technol.*, vol. 54, no. 5, pp. 439–444, Sep. 2011.

[193] I.-C. Khoo, *Liquid Crystals: Physical Properties and Nonlinear Optical Phenomena*. John Wiley & Sons, 2007.

[194] S. V. Shiyanovskii *et al.*, “Lyotropic chromonic liquid crystals for biological sensing applications,” *Mol. Cryst. Liq. Cryst.*, vol. 434, p. 259/[587]-270/[598], 2005.

[195] D. C. Thompson, O. Tantot, H. Jallageas, G. E. Ponchak, M. M. Tentzeris, and J. Papapolymerou, “Characterization of liquid crystal polymer (LCP) material and transmission lines on LCP substrates from 30 to 110 GHz,” *IEEE Trans. Microw. Theory Tech.*, vol. 52, no. 4, pp. 1343–1352, Apr. 2004.

[196] S. Chandrasekhar, *Liquid Crystals*. Cambridge University Press, 1992.

[197] N. J. Mottram and C. J. P. Newton, “Introduction to Q-tensor theory,” *ArXiv14093542 Cond-Mat*, Sep. 2014.

[198] D. W. Berreman, “Solid surface shape and the alignment of an adjacent nematic liquid crystal,” *Phys. Rev. Lett.*, vol. 28, no. 26, pp. 1683–1686, Jun. 1972.

[199] O. Yaroshchuk and Y. Reznikov, “Photoalignment of liquid crystals: basics and current trends,” *J. Mater. Chem.*, vol. 22, no. 2, pp. 286–300, Dec. 2011.

[200] V. Fréedericksz and V. Zolina, “Forces causing the orientation of an anisotropic liquid,” *Trans. Faraday Soc.*, vol. 29, no. 140, pp. 919–930, Jan. 1933.

[201] D. C. Zografopoulos, R. Beccherelli, and E. E. Kriezis, “Beam-splitter switches based on zenithal bistable liquid-crystal gratings,” *Phys. Rev. E*, vol. 90, no. 4, p. 042503, Oct. 2014.

[202] R. Dąbrowski, P. Kula, and J. Herman, “High birefringence liquid crystals,” *Crystals*, vol. 3, no. 3, pp. 443–482, Sep. 2013.

[203] M. Reuter *et al.*, “Highly birefringent, low-loss liquid crystals for terahertz applications,” *APL Mater.*, vol. 1, no. 1, p. 012107, Jun. 2013.

[204] R. Bel Hadj Tahar, T. Ban, Y. Ohya, and Y. Takahashi, “Tin doped indium oxide thin films: Electrical properties,” *J. Appl. Phys.*, vol. 83, no. 5, pp. 2631–2645, Mar. 1998.

[205] Y. Du, H. Tian, X. Cui, H. Wang, and Z.-X. Zhou, “Electrically tunable liquid crystal terahertz phase shifter driven by transparent polymer electrodes,” *J. Mater. Chem. C*, vol. 4, no. 19, pp. 4138–4142, May 2016.

[206] H. D. Hristov, *Fresnel Zones in Wireless Links, Zone Plate Lenses and Antennas*. Artech House, 2000.

[207] A. Ferraro, D. C. Zografopoulos, M. Missori, M. Peccianti, R. Caputo, and R. Beccherelli, “Flexible terahertz wire grid polarizer with high extinction ratio and low loss,” *Opt. Lett.*, vol. 41, no. 9, pp. 2009–2012, 2016.

[208] A. E. Torres-Garcia, B. Orazbayev, I. Ederra, and R. Gonzalo, “IR-Fresnel zone plate lens acting as THz antenna,” in *2017 10th Global Symposium on Millimeter-Waves*, 2017, pp. 129–131.

[209] C. H. Chan, K. B. Ng, and S. W. Qu, “Gain enhancement for low-cost terahertz fresnel zone plate lens antennas,” in *2015 International Workshop on Antenna Technology (iWAT)*, 2015, pp. 66–69.

[210] F. Monticone and A. Alù, “Leaky-wave theory, techniques, and applications: from microwaves to visible frequencies,” *Proc. IEEE*, vol. 103, no. 5, pp. 793–821, May 2015.

[211] T. Tamir and A. A. Oliner, “Guided complex waves. Part 1: Fields at an interface,” *Proc. Inst. Electr. Eng.*, vol. 110, no. 2, pp. 310–324, Feb. 1963.

[212] T. Tamir and A. A. Oliner, “Guided complex waves. Part 2: Relation to radiation patterns,” *Proc. Inst. Electr. Eng.*, vol. 110, no. 2, pp. 325–334, Feb. 1963.

[213] W. Croswell and F. J. Zucker, “Surface-wave antennas,” in *Antenna Engineering Handbook*, 4th ed., vol. Chap. 10, J. L. Volakis, Ed. New York: McGraw-Hill, 2007.

[214] W. W. Hansen, “Radiating electromagnetic wave guide,” US2402622 A, 25-Jun-1946.

[215] A. A. Oliner, “Historical perspectives on microwave field theory,” *IEEE Trans. Microw. Theory Tech.*, vol. 32, no. 9, pp. 1022–1045, Sep. 1984.

[216] J. N. Hines, V. H. Rumsey, and C. H. Walter, “Traveling-wave slot antennas,” *Proc. IRE*, vol. 41, no. 11, pp. 1624–1631, Nov. 1953.

[217] N. Marcuvitz, *Waveguide Handbook*. IET, 1951.

[218] N. Marcuvitz, “On field representations in terms of leaky modes or Eigenmodes,” *IRE Trans. Antennas Propag.*, vol. 4, no. 3, pp. 192–194, Jul. 1956.

[219] H. M. Farkas and I. Kra, *Riemann Surfaces*. Springer Science & Business Media, 2012.

[220] A. Galli, P. Baccarelli, and P. Burghignoli, “Leaky-Wave Antennas,” in *Wiley Encyclopedia of Electrical and Electronics Engineering*, J. G. Webster, Ed. John Wiley & Sons, Inc., 2016.

[221] L. B. Felsen and N. Marcuvitz, *Radiation and Scattering of Waves*. John Wiley & Sons, 1994.

[222] D. R. Jackson and A. A. Oliner, “Leaky-Wave Antennas,” in *Modern Antenna Handbook*, C. A. Balanis, Ed. John Wiley & Sons, Inc., 2008, pp. 325–367.

[223] L. Goldstone and A. Oliner, “Leaky-wave antennas I: Rectangular waveguides,” *IRE Trans. Antennas Propag.*, vol. 7, no. 4, pp. 307–319, Oct. 1959.

[224] C. H. Walter, *Traveling Wave Antennas*. Peninsula Publishing, 1990.

[225] F. Capolino, *Theory and Phenomena of Metamaterials*. CRC Press, 2009.

[226] C. Caloz and T. Itoh, *Electromagnetic Metamaterials: Transmission Line Theory and Microwave Applications*. John Wiley & Sons, 2005.

[227] G. Chartier, *Introduction to Optics*. Springer Science & Business Media, 2005.

[228] L.-G. Wang, N.-H. Liu, Q. Lin, and S.-Y. Zhu, “Superluminal propagation of light pulses: A result of interference,” *Phys. Rev. E,* vol. 68, no. 6, p. 066606, Dec. 2003.

[229] H. Shigesawa, M. Tsuji, and A. A. Oliner, “The nature of the spectral gap between bound and leaky solutions when dielectric loss is present in printed-circuit lines,” *Radio Sci.*, vol. 28, no. 6, pp. 1235–1243, Nov. 1993.

[230] R. Sorrentino, *Numerical Methods for Passive Microwave and Millimeter Wave Structures*. New York: IEEE Press, 1989.

[231] P. Baccarelli, C. D. Nallo, S. Paulotto, and D. R. Jackson, “A full-wave numerical approach for modal analysis of 1-D periodic microstrip structures,” *IEEE Trans. Microw. Theory Tech.*, vol. 54, no. 4, pp. 1350–1362, Jun. 2006.

[232] G. Valerio, P. Baccarelli, P. Burghignoli, and A. Galli, “Comparative analysis of acceleration techniques for 2-D and 3-D Green’s functions in periodic structures along one and two directions,” *IEEE Trans. Antennas Propag.*, vol. 55, no. 6, pp. 1630–1643, Jun. 2007.

[233] K. A. Michalski and J. R. Mosig, “Multilayered media Green’s functions in integral equation formulations,” *IEEE Trans. Antennas Propag.*, vol. 45, no. 3, pp. 508–519, Mar. 1997.

[234] G. Valerio *et al.*, “Efficient computation of 1-D periodic layered mixed potentials for the analysis of leaky-wave antennas with vertical elements,” *IEEE Trans. Antennas Propag.*, vol. 63, no. 6, pp. 2396–2411, Jun. 2015.

[235] P. Kosmas, A. P. Feresidis, and G. Goussetis, “Periodic FDTD analysis of a 2-D leaky-wave planar antenna based on dipole frequency selective surfaces,” *IEEE Trans. Antennas Propag.*, vol. 55, no. 7, pp. 2006–2012, Jul. 2007.

[236] T. Kokkinos, C. D. Sarris, and G. V. Eleftheriades, “Periodic finite-difference time-domain analysis of loaded transmission-line negative-refractive-index metamaterials,” *IEEE Trans. Microw. Theory Tech.*, vol. 53, no. 4, pp. 1488–1495, Apr. 2005.

[237] P. Lampariello and A. A. Oliner, “New equivalent networks with simple closed-form expressions for open and slit-coupled E-plane tee junctions,” *IEEE Trans. Microw. Theory Tech.*, vol. 41, no. 5, pp. 839–847, May 1993.

[238] M. Guglielmi and A. A. Oliner, “Multimode network description of a planar periodic metal-strip grating at a dielectric interface-II: small-aperture and small-obstacle solutions,” *IEEE Trans. Microw. Theory Tech.*, vol. 37, no. 3, pp. 542–552, Mar. 1989.

[239] R. E. Collin and F. J. Zucker, *Antenna Theory*. McGraw-Hill, 1969.

[240] P. Baccarelli *et al.*, “Full-wave analysis of printed leaky-wave phased arrays,” *Int. J. RF Microw. Comput.-Aided Eng.*, vol. 12, no. 3, pp. 272–287, May 2002.

[241] M. Alonso-delPino, T. Reck, C. Jung-Kubiak, C. Lee, and G. Chattopadhyay, “Development of silicon micromachined microlens antennas at 1.9 THz,” *IEEE Trans. Terahertz Sci. Technol.*, vol. 7, no. 2, pp. 191–198, Mar. 2017.

[242] N. Hussain and I. Park, “Optimization of a small lens for a leaky-wave slit dipole antenna at the terahertz band,” in *2016 International Symposium on Antennas and Propagation (ISAP)*, 2016, pp. 782–783.

[243] A. Neto, N. Llombart, J. J. A. Baselmans, A. Baryshev, and S. J. C. Yates, “Demonstration of the leaky lens antenna at submillimeter wavelengths,” *IEEE Trans. Terahertz Sci. Technol.*, vol. 4, no. 1, pp. 26–32, Jan. 2014.

[244] J. Bueno *et al.*, “Photon noise limited performance over an octave of bandwidth of kinetic inductance detectors for sub-millimeter astronomy,” in *2016 41st International Conference on Infrared, Millimeter, and Terahertz waves (IRMMW-THz)*, 2016, pp. 1–2.

[245] N. Llombart, J. Bueno, O. Yurduseven, J. Baselmans, and A. Neto, “Dual polarized leaky wave antenna coupled KIDs for THz space applications,” in *2014 39th International Conference on Infrared, Millimeter, and Terahertz waves (IRMMW-THz)*, 2014, pp. 1–2.

[246] N. Llombart, G. Chattopadhyay, A. Skalare, and I. Mehdi, “Novel terahertz antenna based on a silicon lens fed by a leaky wave enhanced waveguide,” *IEEE Trans. Antennas Propag.*, vol. 59, no. 6, pp. 2160–2168, Jun. 2011.

[247] I.-H. Chung, J. J. Wu, J. Q. Shen, and P. J. Huang, “Properties of transmission and leaky modes in a plasmonic waveguide constructed by periodic subwavelength corrugated metallic wire with open hollow rings in THz regime,” *Appl. Opt.*, vol. 54, no. 31, pp. 9120–9126, Nov. 2015.

[248] U. Beaskoetxea *et al.*, “Flat THz leaky wave antennas: Analysis and experimental results,” in *2014 8th International Congress on Advanced Electromagnetic Materials in Microwaves and Optics*, 2014, pp. 55–57.

[249] U. Beaskoetxea *et al.*, “Low profile THz periodic leaky-wave antenna,” in *Proceedings of 2014 Mediterranean Microwave Symposium (MMS2014)*, 2014, pp. 1–4.

[250] A. A. Tavallaee, P. W. C. Hon, Q.-S. Chen, T. Itoh, and B. S. Williams, “Active terahertz quantum-cascade composite right/left-handed metamaterial,” *Appl. Phys. Lett.*, vol. 102, no. 2, p. 021103, Jan. 2013.

[251] N. Hussain and I. Park, “Design of a wide-gain-bandwidth metasurface antenna at terahertz frequency,” *AIP Adv.*, vol. 7, no. 5, p. 055313, May 2017.

[252] N. Hussain, T. K. Nguyen, and I. Park, “Performance comparison of a planar substrate-integrated Fabry-Perot cavity antenna with different unit cells at terahertz frequency,” in *2016 10th European Conference on Antennas and Propagation (EuCAP)*, 2016, pp. 1–4.

[253] T. K. Nguyen, B. Q. Ta, and I. Park, “Design of a planar, high-gain, substrate-integrated Fabry–Perot cavity antenna at terahertz frequency,” *Curr. Appl. Phys.*, vol. 15, no. 9, pp. 1047–1053, Sep. 2015.

[254] K. Murano *et al.*, “Demonstration of short-range terahertz radar using high-gain leaky-wave antenna,” in *2016 41st International Conference on Infrared, Millimeter, and Terahertz waves (IRMMW-THz)*, 2016, pp. 1–2.

[255] K. Murano *et al.*, “Low-profile terahertz radar based on broadband leaky-wave beam steering,” *IEEE Trans. Terahertz Sci. Technol.*, vol. 7, no. 1, pp. 60–69, Jan. 2017.

[256] J. Li, M. He, C. Wu, and C. Zhang, “Radiation-pattern-reconfigurable graphene leaky-wave antenna at terahertz band based on dielectric grating structure,” *IEEE Antennas Wirel. Propag. Lett.*, vol. 16, pp. 1771–1775, 2017.

[257] W. Fuscaldo, P. Burghignoli, P. Baccarelli, and A. Galli, “Graphene Fabry-Perot cavity leaky-wave antennas: Plasmonic versus nonplasmonic solutions,” *IEEE Trans. Antennas Propag.*, vol. 65, no. 4, pp. 1651–1660, Apr. 2017.

[258] W. Fuscaldo, P. Burghignoli, P. Baccarelli, and A. Galli, “A reconfigurable substrate-superstrate graphene-based leaky-wave THz antenna,” *IEEE Antennas Wirel. Propag. Lett.*, vol. 15, pp. 1545–1548, 2016.

[259] J. Cheng, S. Jafar-Zanjani, and H. Mosallaei, “Real-time two-dimensional beam steering with gate-tunable materials: a theoretical investigation,” *Appl. Opt.*, vol. 55, no. 22, pp. 6137–6144, Aug. 2016.

[260] M. Esquius-Morote, J. S. Gómez-Diaz, and J. Perruisseau-Carrier, “Sinusoidally modulated graphene leaky-wave antenna for electronic

beamscanning at THz," *IEEE Trans. Terahertz Sci. Technol.*, vol. 4, no. 1, pp. 116–122, Jan. 2014.

[261] W. Fuscaldo, P. Burghignoli, P. Baccarelli, and A. Galli, "A graphene-loaded substrate-superstrate leaky-wave THz antenna," in *2016 10th European Conference on Antennas and Propagation (EuCAP)*, 2016, pp. 1–3.

[262] W. Fuscaldo, P. Burghignoli, P. Baccarelli, and A. Galli, "Complex mode spectra of graphene-based planar structures for THz applications," *J. Infrared Millim. Terahertz Waves*, vol. 36, no. 8, pp. 720–733, Aug. 2015.

[263] G. W. Hanson, "Dyadic Green's functions for an anisotropic, non-local model of biased graphene," *IEEE Trans. Antennas Propag.*, vol. 56, no. 3, pp. 747–757, Mar. 2008.

[264] D. R. Jackson and A. A. Oliner, "A leaky-wave analysis of the high-gain printed antenna configuration," *IEEE Trans. Antennas Propag.*, vol. 36, no. 7, pp. 905–910, Jul. 1988.

[265] A. B. Yakovlev, Y. R. Padooru, G. W. Hanson, A. Mafi, and S. Karbasi, "A generalized additional boundary condition for mushroom-type and bed-of-nails-type wire media," *IEEE Trans. Microw. Theory Tech.*, vol. 59, no. 3, pp. 527–532, Mar. 2011.

[266] O. Luukkonen *et al.*, "Simple and accurate analytical model of planar grids and high-impedance surfaces comprising metal strips or patches," *IEEE Trans. Antennas Propag.*, vol. 56, no. 6, pp. 1624–1632, Jun. 2008.

[267] S. Tretyakov, *Analytical Modeling in Applied Electromagnetics*. Artech House, 2003.

[268] A. Alù and N. Engheta, "Achieving transparency with plasmonic and metamaterial coatings," *Phys. Rev. E*, vol. 72, no. 1, p. 016623, Jul. 2005.

[269] S. Maci, G. Minatti, M. Casaletti, and M. Bosiljevac, "Metasurfing: Addressing waves on impenetrable metasurfaces," *IEEE Antennas Wirel. Propag. Lett.*, vol. 10, pp. 1499–1502, 2011.

[270] D. Blanco, E. Rajo-Iglesias, S. Maci, and N. Llombart, "Directivity enhancement and spurious radiation suppression in leaky-wave antennas using inductive grid metasurfaces," *IEEE Trans. Antennas Propag.*, vol. 63, no. 3, pp. 891–900, Mar. 2015.

[271] D. Di Ruscio, P. Burghignoli, P. Baccarelli, and A. Galli, “Omnidirectional radiation in the presence of homogenized metasurfaces,” *Prog. Electromagn. Res.*, vol. 150, pp. 145–161, 2015.

[272] T. Ao *et al.*, “Terahertz band-pass filters based on fishnet metamaterials fabricated on free-standing SiNx membrane,” *Opt. Commun.*, vol. 405, no. Supplement C, pp. 22–28, Dec. 2017.

[273] C. Jansen, I. A. I. Al-Naib, N. Born, and M. Koch, “Terahertz metasurfaces with high Q-factors,” *Appl. Phys. Lett.*, vol. 98, no. 5, p. 051109, Jan. 2011.

[274] J. A. Bossard *et al.*, “Tunable frequency selective surfaces and negative-zero-positive index metamaterials based on liquid crystals,” *IEEE Trans. Antennas Propag.*, vol. 56, no. 5, pp. 1308–1320, May 2008.

[275] I. C. Khoo, D. H. Werner, X. Liang, A. Diaz, and B. Weiner, “Nanosphere dispersed liquid crystals for tunable negative-zero-positive index of refraction in the optical and terahertz regimes,” *Opt. Lett.*, vol. 31, no. 17, pp. 2592–2594, Sep. 2006.

[276] G. Isić, B. Vasić, D. C. Zografopoulos, R. Beccherelli, and R. Gajić, “Electrically tunable critically coupled terahertz metamaterial absorber based on nematic liquid crystals,” *Phys. Rev. Appl.*, vol. 3, no. 6, p. 064007, Jun. 2015.

[277] C.-F. Hsieh, R.-P. Pan, T.-T. Tang, H.-L. Chen, and C.-L. Pan, “Voltage-controlled liquid-crystal terahertz phase shifter and quarter-wave plate,” *Opt. Lett.*, vol. 31, no. 8, pp. 1112–1114, Apr. 2006.

[278] Y. Garbovskiy *et al.*, “Liquid crystal phase shifters at millimeter wave frequencies,” *J. Appl. Phys.*, vol. 111, no. 5, p. 054504, Mar. 2012.

[279] R. E. Collin, *Field theory of guided waves*, 1st ed. New York: McGraw-Hill, 1960.

[280] M. Thevenot, C. Cheype, A. Reineix, and B. Jecko, “Directive photonic-bandgap antennas,” *IEEE Trans. Microw. Theory Tech.*, vol. 47, no. 11, pp. 2115–2122, Nov. 1999.

[281] D. R. Jackson, A. A. Oliner, and A. Ip, “Leaky-wave propagation and radiation for a narrow-beam multiple-layer dielectric structure,” *IEEE Trans. Antennas Propag.*, vol. 41, no. 3, pp. 344–348, Mar. 1993.

[282] A. Ip and D. R. Jackson, “Radiation from cylindrical leaky waves,” *IEEE Trans. Antennas Propag.*, vol. 38, no. 4, pp. 482–488, Apr. 1990.

[283] K. Z. Rajab *et al.*, "Broadband dielectric characterization of aluminum oxide (Al2O3)," *J. Microelectron. Electron. Packag.*, vol. 5, no. 1, pp. 2–7, Jan. 2008.

[284] D. M. Pozar, *Microwave Engineering*. Wiley India Pvt. Limited, 2009.

[285] T. Zhao, D. R. Jackson, J. T. Williams, and A. A. Oliner, "General formulas for 2-D leaky-wave antennas," *IEEE Trans. Antennas Propag.*, vol. 53, no. 11, pp. 3525–3533, Nov. 2005.

[286] M. Lorente-Crespo and C. Mateo-Segura, "Highly directive Fabry-Perot leaky-wave nanoantennas based on optical partially reflective surfaces," *Appl. Phys. Lett.*, vol. 106, no. 18, p. 183104, May 2015.

[287] B. H. Fong, J. S. Colburn, J. J. Ottusch, J. L. Visher, and D. F. Sievenpiper, "Scalar and tensor holographic artificial impedance surfaces," *IEEE Trans. Antennas Propag.*, vol. 58, no. 10, pp. 3212–3221, Oct. 2010.

[288] C. L. Holloway, E. F. Kuester, J. A. Gordon, J. O'Hara, J. Booth, and D. R. Smith, "An overview of the theory and applications of metasurfaces: The two-dimensional equivalents of metamaterials," *IEEE Antennas Propag. Mag.*, vol. 54, no. 2, pp. 10–35, Apr. 2012.

[289] F. Costa, A. Monorchio, and G. Manara, "Efficient analysis of frequency-selective surfaces by a simple equivalent-circuit model," *IEEE Antennas Propag. Mag.*, vol. 54, no. 4, pp. 35–48, Aug. 2012.

[290] G. Lovat, P. Burghignoli, and D. R. Jackson, "Fundamental properties and optimization of broadside radiation from uniform leaky-wave antennas," *IEEE Trans. Antennas Propag.*, vol. 54, no. 5, pp. 1442–1452, May 2006.

[291] A. Ferraro, D. C. Zografopoulos, R. Caputo, and R. Beccherelli, "Broad- and narrow-line terahertz filtering in frequency-selective surfaces patterned on thin low-loss polymer substrates," *IEEE J. Sel. Top. Quantum Electron.*, vol. 23, no. 4, pp. 1–8, Jul. 2017.

[292] W. Fuscaldo, G. Valerio, A. Galli, R. Sauleau, A. Grbic, and M. Ettorre, "Higher-order leaky-mode Bessel-beam launcher," *IEEE Trans. Antennas Propag.*, vol. 64, no. 3, pp. 904–913, Mar. 2016.

[293] R. F. Harrington, *Time-Harmonic Electromagnetic Fields*. Wiley, 2001.

[294] V. Galdi and I. M. Pinto, "A simple algorithm for accurate location of leaky-wave poles for grounded inhomogeneous dielectric slabs," *Microw. Opt. Technol. Lett.*, vol. 24, no. 2, pp. 135–140, Jan. 2000.

[295] C. Di Nallo, F. Frezza, A. Galli, and P. Lampariello, “Rigorous evaluation of ohmic-loss effects for accurate design of traveling-wave antennas,” *J. Electromagn. Waves Appl.*, vol. 12, no. 1, pp. 39–58, Jan. 1998.

LIST OF PUBLICATIONS

Journal papers

[J5] **S. Tofani**, D.C. Zografopoulos, R. Fastampa, M. Missori, and R. Beccherelli, “High resolution binary zone plate in double-sided configuration for terahertz radiation focusing,” *submitted.*

[J4] **S. Tofani**, D.C. Zografopoulos, M. Missori, R. Fastampa, and R. Beccherelli, “Terahertz focusing properties of polymeric zone plates characterized by a modified knife-edge technique,” *submitted*.

[J3] W. Fuscaldo, **S. Tofani**, D.C. Zografopoulos, P. Baccarelli, P. Burghignoli, R. Beccherelli, and A. Galli, “Systematic design of THz leaky-wave antennas based on homogenized metasurfaces,” IEEE *Trans. Antennas Propag.*, *Early access*, doi:10.1109/TAP.2018.2794393.

[J2] W. Fuscaldo, **S. Tofani**, D.C. Zografopoulos, P. Baccarelli, P. Burghignoli, R. Beccherelli, and A. Galli, “Tunable Fabry-Perot cavity THz antenna based on leaky-wave propagation in nematic liquid crystals,” *Antennas Wireless Propag. Lett.*, vol. 16, pp. 2046-49, Apr. 2017.

[J1] D.C. Zografopoulos, K.P. Prokopidis, **S. Tofani**, O. Chojnowska, R. Dąbrowski, E.E. Kriezis, and R. Beccherelli, “An ADE-FDTD formulation for the study of liquid-crystal components in the terahertz spectrum,” *Mol. Cryst. Liq. Cryst.*, vol. 619, pp. 49-60, Sep. 2015.

Conference proceedings

[P5] W. Fuscaldo, **S. Tofani**, P. Burghignoli, P. Baccarelli, A. Notargiacomo, S. Cibella, M. Pea, P. Carelli, N. Mishra, C. Coletti, and A. Galli, “Graphene-based Fabry-Perot cavity leaky-wave antennas: towards an experimental validation,” *European Microwave Week 2018, accepted*.

[P4] **S. Tofani**, W. Fuscaldo, D.C. Zografopoulos, P. Baccarelli, P. Burghignoli, R. Beccherelli, and A. Galli, "Spatial dispersion analysis of homogenized metafurfaces for terahertz leaky-wave antennas," *Eur. Conf. Antennas Propag. (EuCAP 2018), accepted.*

[P3] W. Fuscaldo, **S. Tofani**, P. Baccarelli, P. Burghignoli, D.C. Zografopoulos, R. Beccherelli, and A. Galli, "A reconfigurable multilayered THz leaky-wave antenna employing liquid crystals," *Eur. Conf. Antennas Propag. (EuCAP 2017)*, Paris, France, 19-24 Mar. 2017.

[P2] **S. Tofani**, D.C. Zografopoulos, M. Missori, and R. Beccherelli, "Polymeric zone plates for THz focusing," 41st International Conference on Infrared, Millimeter and Terahertz Waves, *IRMMW-THz 2016*, Bella Center Copenhagen, Denmark, 25-30 Sep. 2016.

[P1] W. Fuscaldo, **S. Tofani**, P. Baccarelli, P. Burghignoli, D. C. Zografopoulos, R. Beccherelli, and A. Galli, "Reconfigurable Fabry-Perot cavity leaky-wave antennas based on nematic liquid crystals for THz applications," *XXI RiNEm*, Parma, Italy, 12-14 Sep. 2016.

Doctoral school book and e-book contributions

[1] **S. Tofani**, W. Fuscaldo, A. Galli, and R. Beccherelli, "Static and tunable devices for terahertz focusing and beam steering," in *Quantum Nano-Photonics,* NATO Science for Peace and Security Series B: Physics and Biophysics, Springer Verlag, *in press*.

[2] **S. Tofani**, "Le nuove frontiere dell'Elettromagnetismo: come la creatività aiuta lo sviluppo tecnologico", *in press*.